Dissertation

submitted to the
Combined Faculties for the Natural Sciences and for Mathematics
of the University of Heidelberg, Germany
for the degree of
Doctor of Natural Sciences

Put forward by

Diplom-Mathematiker, Diplom-Physiker
Jan Fuhrmann
geb. am 29.04.1981 in Markranstädt

Date of oral examination:

06.08.2012

On a Minimal Model for the Initiation of Cell Movement

Advisors:

Prof. Dr. Angela Stevens
Prof. Dr. Heinrich Freistühler

Acknowledgements

I would like to express my gratitude to

- my advisors, Prof. Dr. Angela Stevens and Prof. Dr. Heinrich Freistühler, for encouraging me to step into the investigation of this topic, for providing support and advice whenever necessary, and for their scientific input,
- the German Federal Ministry of Education and Research (BmBF) for providing financial support via the Bernstein Center for Computational Neuroscience Mannheim/Heidelberg
- the German Science Foundation (DFG) for providing financial and organizational support through the Graduate College IGK 710 and the Heidelberg Graduate School MathComp,
- the member of all work groups involved for fruitful discussions and for making working at the University of Heidelberg such an enjoyable experience, in particular Dr. Ivano Primi,
- the staff of the Faculty of Mathematics and Computer Science and in particular of the Institute of Applied Mathematics at the University of Heidelberg for the organizational support,
- and finally my family and friends for their support in every respect and their patience.

Abstract

Actin-driven motility of eucaryotic cells plays a crucial role in many biological processes and has therefore been under intense experimental and theoretical investigation throughout several decades. In [10], we introduced a minimal model for the preparation of movement in a symmetric resting cell on a flat substrate. This system consists of at least four hyperbolic conservation laws describing the evolution of densities of actin filament tips and at least one parabolic equation for the actin monomer concentration. For this coupled hyperbolic-parabolic system, we shall now formulate a free boundary problem to allow for actual motion of the cell.

For this model with some specific boundary conditions, we will show short time well posedness and present several mechanisms by which the solutions might break down for large times. In particular, possible blow-up phenomena are described and investigated, both analytically and numerically. Moreover, we discuss how the cease of existence of solutions can be interpreted physically as the emergence of actin polymerization fronts.

Finally, different possible boundary conditions are presented, and their biological meanings are explained.

We furthermore reformulate the model under certain assumptions and derive a system of two parabolic equations describing the motion of two interacting species of filaments moving in opposite directions. This simplified model is investigated in part II where we ask for stability of particular steady states and construct traveling wave solutions. The existence of the latter can also be found in simulations, and we will discuss the type and velocity of the evolving wave profiles.

Particular attention will be paid to the remarkable differences between different types of nonlinearities describing the mutual interaction. Of special interest are the deviations from the predictions about stability and the traveling wave solutions obtained from the linearization of the model around its equilibria. These predictions are met quite well by some versions of the nonlinear terms whereas for others they are missed significantly. We are thus dealing with a quite minimalistic system of reaction advection diffusion equations whose behavior cannot be predicted by linearization but strongly depends on the particular nonlinearity.

Abstract

Aufgrund der großen Bedeutung für eine Vielzahl biologischer Prozesse ist die aktingetriebene Bewegung eukaryotischer Zellen seit mehreren Jahrzehnten Gegenstand intensiver experimenteller und theoretischer Forschung. Unter anderem wurde in [10] ein minimales Modell für die Polarisation des Aktinzytoskeletts einer symmetrischen, ruhenden Zelle auf einer ebenen Fläche vorgestellt, die sich auf einen äußeren Anstoß hin darauf vorbereitet, sich in Bewegung zu setzen. Dieses System besteht aus mindestens vier hyperbolischen Erhaltungsgleichungen für die Dichten der Enden von Aktinfilamenten und mindestens einer parabolischen Gleichung für die Konzentration der Aktinmonomere. Für dieses gekoppelte hyperbolisch-parabolische System wollen wir nun ein Problem mit freiem Rand herleiten, um der Zelle tatsächliche Bewegung zu erlauben.

Für dieses Problem mit einer spezischen Form der Randbedingungen soll zunächst die Wohlgestelltheit für kurze Zeiten gezeigt werden. Des weiteren werden wir einige Mechanismen beleuchten, die zum Zusammenbruch der Lösungen für große Zeiten führen können, wobei insbesondere die analytische und numerische Untersuchung von räumlich beschränkten Explosionen dieser Lösungen in den Blick genommen wird. Ferner werden wir erklären, wie der Kollaps der Lösungen als Ausbildung von Polymerisationsfronten physikalisch zu verstehen ist.

Schließlich werden wir noch weitere Randbedingungen vorstellen und deren biologische Interpretation beleuchten.

Außerdem werden wir das gegebene Modell unter gewissen Annahmen zu einem System aus zwei parabolischen Gleichungen reduzieren. Diese beschreiben die Bewegung zweier sich in entgegengesetzter Richtung bewegender und miteinander interagierender Sorten von Filamenten. Dieses reduzierte Modell soll in Teil II hinsichtlich der Stabilität bestimmter stationärer Zustände und des Auftretens wandernder Wellenfronten analysiert werden. Letztere werden auch in Simulationen beobachtet, und wir werden sowohl Form als auch die Geschwindigkeiten der auftretenden Wellen untersuchen.

Spezielles Augenmerk wird auf den Einfluss des nichtlinearen Interaktionsterms auf das Stabilitätsverhalten sowie auf die Art und Geschwindigkeit der wandernden Wellen zu legen sein. Von besonderem Interesse sind die Abweichungen für bestimmte Nichtlinearitäten von den Vorhersagen, die sich aus der Linearisierung des Systems an seinen Gleichgewichtspunkten ergeben. Für gewisse Formen des nichtlinearen Terms stimmt das beobachtete Verhalten der Lösungen mit diesen Vorhersagen sehr gut überein, während sich für andere Formen deutliche Unterschiede zeigen. Wir haben es also mit einem minimalistischen System von Reaktions-Advektions-Diffusionsgleichungen zu tun, deren Verhalten nicht ohne weiteres durch die Linearisierung vorhergesagt werden kann, sondern vielmehr stark von der speziellen Gestalt der Nichtlinearität abhängt.

Contents

Chapter 1

Introduction

1.1 The actin cytoskeleton

Practically all eucaryotic cells express some types of the proteins actin and myosin. Actin is a highly conserved protein with a molecular weight of approximately 43 kDa which can be found as monomer (globular or *G-actin*) or in elongated, helical polymers called filaments (*F-actin*). In addition, actin is an ATPase and thus occurs in three basic states, namely ATP-bound, $ADP+P_i$-bound and ADP-bound. Filamentous actin often forms meshworks by binding to crosslinker proteins and plays a vital role in shaping cells as part of the so called cytoskeleton. Red blood cells, for example, maintain there shape by a thin actin cortex directly underneath their plasma membrane.

Actin filaments are polar, meaning that their ends have very different properties. At the so called *barbed end* the affinity to (ATP-bound) actin monomers is high and under physiological conditions new monomers are readily added. At this end the filament therefore typically grows. Upon being incorporated into a filament the actin monomer quickly hydrolyses its ATP and after some time of aging releases the inorganic phosphate P_i to become ADP-bound. At the *pointed end* of a typical actin filament we thus find ADP-actin and the affinity to monomers is low. Since, in addition, ADP-actin readily dissociates from a filament, the latter preferentially shrinks at its pointed end.

These polymerization and depolymerization processes are tightly controlled by a large variety of actin related proteins which, for example,

- cap filament tips to inhibit association or dissociation of monomers (*capping*, e.g. CapZ),
- bind to actin monomers to enhance or reduce their binding affinity to filament tips (*sequestration*, e.g. profilin, thymosin-β4),
- bind to actin filaments and produce branching sites at which new barbed ends emerge (*branching*, e.g. ARP2/3),
- or weaken the bonds in ADP-F-actin which leads to faster depolymerization (*severing*, e.g. ADF/cofilin).

A good overview of the mechanisms controlling the actin turnover in vivo can be found in the review paper [2] and the references therein.

In contrast to actin of which very few and similar variants are known, myosin denotes a whole family of motor proteins having different shapes and sizes. Alone in humans over 40 different myosin subtypes can be found. Common to all of them is a conserved head domain binding to actin filaments and walking along them towards the barbed ends. The single steps are accomplished by conformational changes which are again driven by the hydrolysis of ATP. Depending on the subtype, there may be different tail domains attached to this head which can carry a variety of cargos by binding to different substrates. Some of the myosins tend to form dimers or even filamentous polymers.

The most prominent member of the myosin family is myosin II which occurs for example in muscle fibres where it forms filaments by attaching the tail domains of several monomers to each other. Each of these monomers has two heads and thus can bind to two actin filaments simultaneously. Due to the arrangement of these head domains the actin filaments being bound to one myosin II monomer are oriented to opposite directions and thus by walking along both of them the myosin makes them slide along each other into the direction of their pointed ends. This relative movement can be very fast and in the particular case of skeleton muscles leads to muscle contraction.

For a single actin filament the described mechanisms allow for a treadmilling behavior. Under certain physiological conditions the growth velocity at the barbed end may be as large as the shrinkage velocity at the pointed end such that the total length of the filament does not change. However, the filament will be displaced towards its barbed end just by growing and shrinking. This shift may be counteracted by myosin motors walking along this filament and being anchored somewhere else − say, at other parts of the cytoskeleton − and thereby pulling it backwards. If this pull back velocity equals the polymerization speed then the whole filament does not move at all but is constantly regenerated. This situation is depicted in figure 1.1. Note that each polymerization step and each step of a myosin motor costs one ATP equivalent of energy.

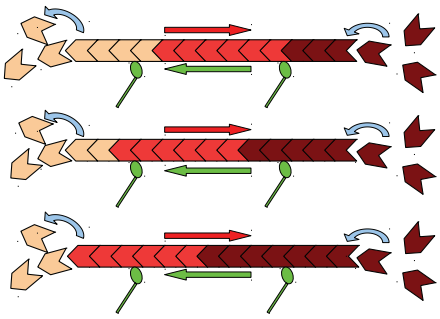

Figure 1.1: Treadmilling of a typical actin filament (*red*) with two myosin motors (*green*) attached to it. The red arrow denotes the displacement velocity due to polymerization and depolymerization, the green arrow stands for the pull back velocity.

As similar processes go on in most eucaryotic cells we can state that the before mentioned actin meshwork is under permanent reconstruction.

1.2 Actin driven cell motility

The growth of barbed ends of actin filaments together with the myosin driven contraction of actin fibres is able to drive the directed motion of cells. This cell motility plays a crucial role in a large variety of biological functions a short selection of which is presented in the following list.

- During wound healing, fibroblasts use their actin cytoskeleton to crawl into the wound where they can start their repair work.
- Axonal growth cones of neurons are driven by actin polymerization and guide the axon to its destination.
- Amebae crawl along various kinds of substrates to haunt and digest bacteria. The same mechanism is used by macrophages of the human immune system which hunt for invading microorganisms in the body.
- Cancer cells often show an enhanced motility allowing the tumor to penetrate the surrounding tissue and eventually form metastases.

In order to move or just maintain its shape, the cell has to coordinate actin polymerization and depolymerization as well as the binding of actin filaments to other parts of the cytoskeleton in a very sophisticated fashion. This is, among others, accomplished by the control mechanisms already mentioned above.

We will here only model the actin turnover at the filament tips explicitely, but we allow for variations of the reaction parameters in order to account for these regulation mechanisms. The particular effect of explicitely modeling barbed end capping as an example of polymerization modulation has already been discussed in [10].

Part I

Formulation and Analysis of the Free Boundary Problem

This first part is devoted to the examination of the full free boundary problem for the model derived in [10]. This basic system is comprised of four hyperbolic conservation laws describing the densities of actin filament tips and a parabolic equation for the actin monomer concentration. In chapter 2 we start with briefly recalling the derivation of the governing equations and describe how the boundary conditions are obtained. Then we calculate first estimates for the monomer concentration and resulting bounds on the end velocities in chapter 3. We will explicitely compute bounds for the boundary velocity and the concentration of monomers and show that the total actin amount remains conserved.

The analysis of the well posedness in chapter 4 starts with the examination of the linearized system with the monomer equation being decoupled from the equations for the filament end densities. We first investigate in section 4.1 well posedness for the case of constant coefficients and under the assumption of the hyperbolic part being strictly hyperbolic.

For the construction of a solution we require three steps. First, we find a unique solution to the parabolic free boundary problem for the monomer density and the boundary curves assuming given filament end densities. This solution is found as the fixed point of an appropriate operator which is shown to be a contraction for sufficiently small times. Then, using the method of characteristics, the hyperbolic equations for the filament tips are solved explicitely for given monomer concentration which only enters the velocity fields of the conservation laws. Finally, the estimates obtained for the solutions to both of these decoupled problems allow the construction of another contraction operator – again for sufficiently small times – whose unique fixed point is the solution to the full problem with constant coefficients.

Since the dynamics of the actin cytoskeleton strongly depend on regulatory mechanisms we also work out the differences arising in case the coefficients are varying in space and time. As long as the variation of the parameters is sufficiently smooth only the constants in the estimates for the solutions are affected and the time for which we can assert the existence of smooth solutions becomes smaller in the variable coefficient case.

In section 4.3 we also discuss the loss of strict hyperbolicity when at least two end velocities coincide. In that case, we will still find weak solutions by very similar arguments as in the strictly hyperbolic case. The main difference lies in the spaces where we look for solutions and the resulting estimates.

Then we are concerned with the problem of blow-up of the solutions in finite time in chapter 5. We shall discuss the possibility of degeneration of the end densities to measure valued solutions and the concomittant blow-up of the spatial derivative of the monomer density in the interior of the domain. For the full problem we find a particular type of exact solutions with DIRAC measure valued end densities and continuous, piecewise smooth monomer concentration. Moreover, we investigate the hyperbolic limit system without monomer diffusion and find some particular solutions with jumps in the monomer density. The biological relevance of these types of solutions as describing fronts of polymerizing actin filaments will be discussed as well.

We will finally give alternative boundary conditions leading to a problem with fixed boundary in chapter 6. Here, we find size structured equations for the end densities at the boundary.

In the end of this part, chapter 7 provides some numerical simulations for the system which shall demonstrate some of the behaviors being predicted by the analysis of the

prior chapters. In particular, some illustrations of the blow-up phenomena will be given. We shall for instance observe that the predicted δ-peaks in the end densities indeed emerge from smooth initial data within finite time. This phenomenon will be discussed as the emergence of actin polymerization fronts.

Chapter 2

Formulation of the Free Boundary Problem

2.1 Derivation and reformulation of the model equations

2.1.1 The original model

We briefly recall the ideas and notation that led to the model presented in [10]. From the biological point of view we consider a symmetric cell resting on a flat substrate. Upon some stimulus, this cell shall then be polarized into a particular direction. This leads to a well defined spatial axis along which the whole system is supposed to evolve.

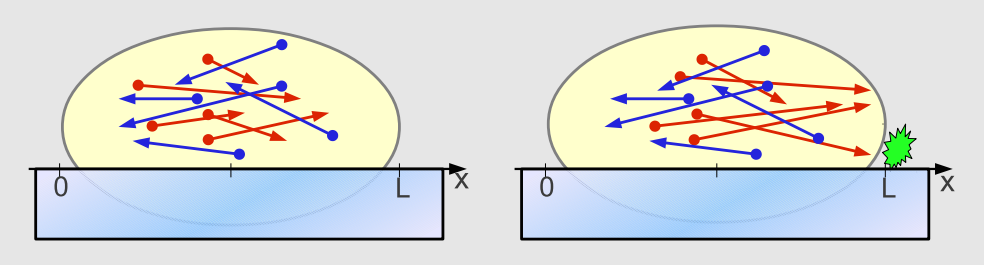

Figure 2.1: Sketch of a polarizable cell on a flat substrate. *Left*: symmetric unpolarized cell, *right*: polarization of the cytoskeleton upon some stimulus at the right edge. Actin filaments (*red*: right oriented, *blue*: left oriented) are depicted as arrows with arrow heads as barbed ends and bullet heads as pointed ends.

Inside the cell we consider actin monomers described by a concentration a and straight actin filaments whose barbed and pointed ends are given by densities B and P, respectively. Having a well defined spatial direction x we can distinguish between so called right and left oriented filaments. Here, a filament is called right oriented if its barbed end points to the right. The end densities are divided into right and left oriented as well and we find four distinct densities B_r, P_r, B_l, and P_l.

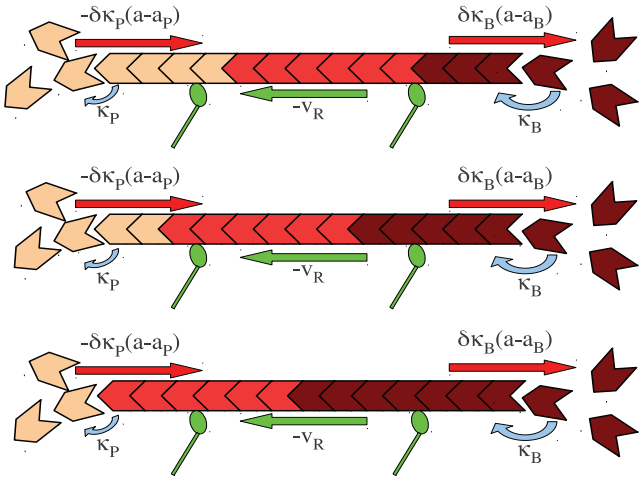

Figure 2.2: Treadmilling of a typical actin filament (*red*) with two myosin motors (*green*) attached to it. The red arrows denote the polymerization speed $\delta\kappa_B(a - a_B)$ at the barbed end and the depolymerization speed $\delta\kappa_P(a_P - a)$ at the pointed end, respectively. The green arrow shows the myosin-driven retrograde flow velocity v_R.

For the filament tips we derived a velocity as a combination of the myosin-driven retrograde flow velocity and the growth or shrinkage speed due to polymerization or depolymerization (cf. figure 2.2). The former is denoted by v_R and assumed to be constant. For the polymerization speed we consider first order reaction kinetics for the addition or removal of monomers to or from the filament tip, respectively.

As being described in the introduction, barbed ends show a high affinity to monomers and show fast reaction kinetics. These properties are reflected by a low critical concentration a_B and a high reaction rate constant κ_B. Given a local monomer concentration a, the mean polymerization rate is then given by

$$\kappa_B(a - a_B).$$

We note that for $a < a_B$ this rate is negative and then accounts for depolymerization. If we now denote the average length change of a filament upon addition of one monomer by δ we obtain a polymerization velocity of

$$v_{pol,B} = \delta\kappa_B(a - a_B). \tag{2.1}$$

For right oriented barbed ends, this velocity is counted in positive x-direction. The myosin driven retrograde flow velocity acts in the opposite direction and we obtain as velocity for right oriented barbed ends

$$v_B(t, x, a(t, x)) = -v_R + \delta\kappa_B(t, x)(a(t, x) - a_B(t, x)). \tag{2.2}$$

Very similarly we derive the pointed end velocity to be

$$v_P(t, x, a(t, x)) = -v_R - \delta\kappa_P(t, x)(a(t, x) - a_P(t, x)) \tag{2.3}$$

where $\kappa_P < \kappa_B$ is the reaction rate constant for (de-)polymerization at pointed ends and $a_P > a_B$ is the corresponding critical concentration.

For symmetry reasons, the velocities for the left oriented filament tips are the same but with opposite sign. These filament tip speeds will act as velocity field for hyperbolic

conservation laws describing the densities of right and left oriented barbed and pointed ends.

The monomers are assumed to undergo diffusion with constant diffusion coefficient D and to react with the filament tips according to the polymerization rates given above yielding a reaction diffusion equation for the monomer concentration.

In [10], an additional capping protein was introduced which can bind to barbed ends and prevent them from any interactions with actin monomers. This resulted in an additional reaction diffusion equation for the capping protein itself and two more conservation laws for the densities of capped barbed ends of either orientation. Moreover, the barbed end equations were supplemented by additional reaction terms taking into account the transition of active to capped barbed ends by capping and vice versa by dissociation of the capper from the filament.

These additional features do not change the basic character of the system and we therefore stick to the most basic version for the analysis.

After a certain rescaling (for details, please refer to [10]) this leads to the following model for the actin cytoskeleton of a motile cell:

$$\begin{aligned}
\partial_t B_r &= -\partial_x \left(v_B(a) B_r\right) && \text{(2.4a)}\\
\partial_t B_l &= \partial_x \left(v_B(a) B_l\right) && \text{(2.4b)}\\
\partial_t P_r &= -\partial_x \left(v_P(a) P_r\right) && \text{(2.4c)}\\
\partial_t P_l &= \partial_x \left(v_P(a) P_l\right) && \text{(2.4d)}\\
\partial_t a &= D\partial_{xx} a + R(a, B_r, B_l, P_r, P_l) && \text{(2.4e)}
\end{aligned}$$

with the reaction term in the monomer equation being given by

$$R(a, B_r, B_l, P_r, P_l) = -\delta\kappa_B(a - a_B)(B_r + B_l) - \delta\kappa_P(a - a_P)(P_r + P_l). \tag{2.5}$$

This system is now given in the space-time domain

$$Q_T := \{(t, x) \;\mid\; 0 < t < T,\; x \in \Omega_t \equiv (r(t), l(t))\} \tag{2.6}$$

where $l(t)$ and $r(t)$ describe the moving boundaries of the domain which are subject to the initial conditions

$$l(t) = 0 \qquad \text{and} \qquad r(t) = L$$

and whose evolution will be derived in section 2.2.

System (2.4a - 2.4e) shall also be equipped with non-negative initial conditions satisfying

$$\operatorname{supp}(B_r(0, \cdot) + B_l(0, \cdot) + P_r(0, \cdot) + P_l(0, \cdot)) = [0, L]. \tag{2.7}$$

This condition means, that the total density of filament tips is strictly positive almost everywhere in the initial spatial domain, and in particular there are filament tips in each neighborhood of the initial boundary.

2.1.2 Reformulation of the model and basic assumptions

As the most basic form of interaction of the cytoskeleton with the cell membrane one might consider a very soft membrane exerting no forces onto the filaments. Their tips

will thus just move with their free velocity.

To formulate the system itself and the boundary conditions in a more concise way we rewrite the densities and velocities as

$$u^1 := B_l \quad \text{and} \quad \lambda^1 := -v_B \equiv v_R - \delta\kappa_B(a - a_B) \tag{2.8a}$$
$$u^2 := P_r \quad \text{and} \quad \lambda^2 := v_P \equiv -v_R - \delta\kappa_P(a - a_P) \tag{2.8b}$$
$$u^3 := P_l \quad \text{and} \quad \lambda^3 := -v_P \equiv v_R + \delta\kappa_P(a - a_P) \tag{2.8c}$$
$$u^4 := B_r \quad \text{and} \quad \lambda^4 := v_B \equiv -v_R + \delta\kappa_B(a - a_B). \tag{2.8d}$$

Although we will often assume the reaction parameters $a_{B/P}$ and $\kappa_{B/P}$ to be constant we give the following conditions on the parameters for the case that they are variable in space and time.

Condition 2.1.1. *The parameters satisfy:*

(*i*) v_R *and* δ *are positive constants*

(*ii*) κ_B, κ_P, a_B, *and* a_P *(denoted as* variable parameters*) may in general depend on* (t, x) *and:*

a) belong to $C^{0+1}([0,T];\ C^\infty(\mathbb{R}))$.

b) are positive, bounded and bounded away from zero. In particular,

$$\inf_{t,x} a_B(t,x) \quad =: \quad \underline{a_B} > 0 \tag{2.9}$$
$$\sup_{t,x} a_P(t,x) \quad =: \quad \overline{a_P} < \infty. \tag{2.10}$$

(*iii*)
$$\sup_{t,x} a_B(t,x) =: \overline{a_B} < \underline{a_P} := \inf_{t,x} a_P(t,x) \tag{2.11}$$

(*iv*)
$$\sup_{t,x} \left(\kappa_B(t,x)(a_P(t,x) - a_B(t,x))\right) \ > \ \frac{v_R}{\delta}. \tag{2.12}$$

This condition guarantees that the velocity of right oriented barbed ends can take positive values.

We can now rewrite system (2.4a - 2.4d) in the compact form

$$\partial_t u + \partial_x(\Lambda(a)u) = 0 \tag{2.13}$$

where $u = (u^1, u^2, u^3, u^4)^T$ and $\Lambda = \mathrm{diag}(\lambda^1, \lambda^2, \lambda^3, \lambda^4)$. Assuming sufficiently smooth parameters and monomer density a, system (2.13) may be equivalently rewritten in transport form

$$\partial_t u + \Lambda\partial_x u = f(u) \equiv -\partial_x \Lambda u. \tag{2.14}$$

The equation for the monomers can also be rewritten in a more concise form:

$$\partial_t a - D\partial_{xx} a \ = \ -cua + \tilde{c}u \ \equiv \ R(a,\ u) \tag{2.15}$$

where

$$c \equiv (c_1,\ c_2,\ c_3,\ c_4) = \delta(\kappa_B,\ \kappa_P,\ \kappa_P,\ \kappa_B) \tag{2.16}$$

and

$$\tilde{c} \equiv (\tilde{c}_1,\ \tilde{c}_2,\ \tilde{c}_3,\ \tilde{c}_4) = \delta(\kappa_B a_B,\ \kappa_P a_P,\ \kappa_P a_P,\ \kappa_B a_B) \tag{2.17}$$

Remark 2.1. *If in addition to condition 2.1.1, the reaction parameters $\kappa_{B/P}$, $a_{B/P}$ are constant such that for some $a = a^{ss}$ the equality*

$$v_B(a^{ss}) = 0 = v_P(a^{ss}) \tag{2.18}$$

holds, then the characteristic velocities $\lambda^\alpha(a)\ldots$

(I) ... vanish if and only if $a = a^{ss}$.

(II) ... satisfy $\lambda^1(a) < \lambda^2(a) < 0 < \lambda^3(a) < \lambda^4(a)$ if and only if $a > a^{ss}$.

(III) ... satisfy $\lambda^4(a) < \lambda^3(a) < 0 < \lambda^2(a) < \lambda^1(a)$ if and only if $a < a^{ss}$.

2.2 Formulation of the boundary conditions

2.2.1 Boundary conditions for the hyperbolic equations

From the hyperbolic equations in transport form (2.14) we can easily read off the characteristic curves for the respective filament end densities u^α. Noting that the velocity matrix is diagonal we deduce the position of the α^{th} characteristic curve y^α starting at time $t = 0$ in $\xi \in [0, L]$ to be given by the initial value problem

$$\dot{y}^\alpha(t;\ \xi) = \lambda^\alpha(t, y^\alpha(t;\ \xi)) \qquad y^\alpha(0;\ x_0) = \xi \tag{2.19}$$

or equivalently by the Volterra type integral equation

$$y^\alpha(t;\ \xi) = \xi + \int_0^t \lambda^\alpha(\tau, y^\alpha(\tau;\ \xi))d\tau. \tag{2.20}$$

As a first approximation we assume a very soft membrane exerting no force on the filament ends and being displaced by any filament growing against it. This is modeled by a domain boundary moving freely with the outermost characteristic curves for the end densities. Let us therefore define the space-time domain

$$Q_T = \{(t, x) \mid 0 < t < T,\ l(t) < x < r(t)\} \tag{2.21}$$

where the left and right boundary curves are given by

$$l(t) := \min_{\alpha=1,\ldots,4} l^\alpha(t) \equiv \min_{\alpha=1,\ldots,4} y^\alpha(t;\ \xi_l^\alpha) \tag{2.22}$$

$$r(t) := \max_{\alpha=1,\ldots,4} r^\alpha(t) \equiv \max_{\alpha=1,\ldots,4} y^\alpha(t;\ \xi_r^\alpha). \tag{2.23}$$

Here, the initial points are given by

$$\xi_l^\alpha = \inf\{x \in (0, L) \mid u^\alpha(0, x) > 0\} \tag{2.24}$$

$$\xi_r^\alpha = \sup\{x \in (0, L) \mid u^\alpha(0, x) > 0\} \tag{2.25}$$

That is, the boundary curves r and l are just the characteristic curves emerging from the boundary points of the initial domain $\Omega_0 = (0, L)$ as long as we assume that each of the points 0 and L belongs to the support of at least one initial datum (which we always will, cf. section 2.3).

We also define the characteristic domains for each individual end density by

$$Q_T^\alpha := \{(t,x) \mid 0 < t < T,\ l^\alpha(t) < x < r^\alpha(t)\}\ , \qquad \alpha = 1, \ldots,\ 4 \tag{2.26}$$

and notice that

$$Q_T = \bigcup_{\alpha=1}^{4} Q_T^\alpha.$$

Let us furthermore introduce the notation

$$\Omega_t := \{x \in \mathbb{R} \mid l(t) < x < r(t)\} \equiv \{x \in \mathbb{R} \mid (t,x) \in \overline{Q_T}\}\ , \qquad t \in [0,T] \tag{2.27}$$

and

$$\Omega_t^\alpha := \{x \in \mathbb{R} \mid l^\alpha(t) < x < r^\alpha(t)\}\ , \qquad t \in [0,T] \tag{2.28}$$

for the spatial cross sections of Q_T and Q_T^α, respectively. Finally, let us denote by $\alpha_r(t)$ and $\alpha_l(t)$ the *leading* and *trailing* characteristic family at time t, respectively, namely that α defining the edge motion:

$$r^{\alpha_r}(t) = \max_{\alpha=1,\ldots,4} r^\alpha(t) \tag{2.29}$$

$$l^{\alpha_l}(t) = \min_{\alpha=1,\ldots,4} l^\alpha(t). \tag{2.30}$$

Note that these α_r and α_l are not necessarily unique for all times t. In the case of nonuniqueness we will under abuse of notation denote the set of all α's satisfying the above equalities by $\alpha_r(t)$ and $\alpha_l(t)$.

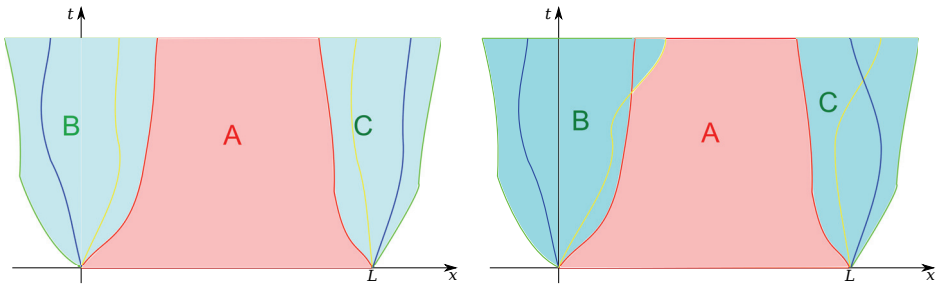

Figure 2.3: Decomposition of Q_T without (*left*) and with (*right*) crossing boundary curves. Colored curves designate the outer characteristics of the different end densities $u^1, \ldots,\ u^4$. The supports of the initial data are $[0,\ L]$

We now have to specify boundary conditions for each characteristic curve entering the domain Q_T from its lateral boundary. These are precisely those characteristics having not the smallest or largest velocity at the left or right boundary, respectively. As no filament ends are supposed to enter the domain from the outside, these will simply be

zero conditions.

In practice we will consider a characteristic boundary value problem on a decomposed domain domain where each end density u^α is only considered on its characteristic domain Q_T^α. Then, the lateral boundary coincides with the outer characteristic curve of the respective density and we only need to integrate the corresponding values along this characteristic without imposing any further boundary values.

The domain Q_T can thus be decomposed as indicated in figure 2.3 into

- $A = \{(t,x) \mid 0 < t < T,\ \max_\alpha l^\alpha(t) < x < \min_\alpha r^\alpha(t)\}$
- $B = \{(t,x) \mid 0 < t < T,\ l(t) < x < \max_\alpha l^\alpha(t)\}$
- $C = \{(t,x) \mid 0 < t < T,\ \min_\alpha r^\alpha(t) < x < r(t)\}$.

Now, to the subdomain A no characteristics enter from the lateral boundary and solving the hyperbolic part of the model system on this domain simply corresponds to solving the appropriate CAUCHY problem. The subdomains B and C are fan shaped characteristic domains in the sense of [18], chapter 4, paragraph 1.

By diagonality of the velocity matrix Λ we do not have to consider specific interface conditions along the characteristic curves inside B and C. It is sufficient to put each of the end densities to zero outside its characteristic domain.

Remark 2.2. *In case of constant reaction parameters satisfying the hypotheses of remark 2.1, the characteristic boundary curves of the different end densities cannot cross as long as $a(t,x) - a^{ss}$ has a sign in B and C, respectively. This situation is depicted in figure 2.3 on the left.*

For completeness, the right picture in figure 2.3 shows an example for the decomposition of Q_T where the characteristic boundaries for the different end densities cross each other.

2.2.2 Boundary conditions for the parabolic equation

For the reaction diffusion equation describing the monomer concentration we assume that monomers are reflected at the membrane and thus simply impose zero flux conditions on the lateral boundary of Q_T. In particular, we assume that G-actin can neither leave nor enter the cell through the membrane.

Notation. Adapting the nomenclature in [19] we use the following names for the parts of the boundary ∂Q_T of the space-time domain.

- the parabolic boundary

$$\mathcal{P}Q_T := \left\{(t,x) \in \partial Q_T \mid \forall \varepsilon > 0 :\ \mathrm{Cyl}_\varepsilon(t,x) \cap (\mathbb{R}^{1+1} \backslash Q_T) \neq \emptyset\right\}$$

  where the parabolic cylinder around a point (t,x) is defined as

$$\begin{aligned} \mathrm{Cyl}_\varepsilon(t,x) &:= \left\{(s,y) \in \mathbb{R}^{1+1} \mid s \leq t,\ \max\{\sqrt{t-s}, |x-y|\} < \varepsilon\right\} \\ &\equiv \left\{(s,y) \in \mathbb{R}^{1+1} \mid s \leq t,\ t-s < \varepsilon^2, |x-y| < \varepsilon\right\}. \end{aligned} \tag{2.31}$$

  Here, the value

$$|(t,x) - (s,y)|_P := \max\{\sqrt{t-s}, |x-y|\}$$

shall be called the parabolic distance between the space-time points (t, x) and (s, y), and the parabolic cylinder is just a semiball of radius ε beneath (t, x) with respect to this distance. The parabolic boundary is therefore that part of the boundary across which a parabolic equation can carry information into the domain and we have to provide this information by specifying initial and boundary conditions.

- the top (or open) boundary

$$\mathcal{T}Q_T := \partial Q_T \backslash \mathcal{P}Q_T.$$

Here, information can only leave the domain as locally Q_T lies below $\mathcal{T}Q_T$.

- the base (or bottom)

$$\mathcal{B}Q_T := \left\{(t, x) \in \mathcal{P}Q_T \mid \mathrm{Cyl}_\varepsilon(t + \varepsilon^2, x) \subset Q_T \text{ for some } \varepsilon > 0\right\}$$

which in our case coincides with

$$\overline{Q_T} \cap \{t = 0\}.$$

That means that all information emerging from this boundary is locally transported into the domain Q_T and we have to provide initial conditions.

- the lateral boundary

$$\mathcal{L}Q_T := \mathcal{P}Q_T \backslash \overline{\mathcal{B}Q_T}.$$

In our case, this part of the boundary is given by the outer characteristic curves of the hyperbolic part:

$$\mathcal{L}Q_T = \{(t, l(t)) \mid 0 < t < T\} \cup \{(t, r(t)) \mid 0 < t < T\}.$$

This lateral boundary receives information from the interior of the domain Q_T and simultaneously sends information into that domain via parabolic equations. We therefore have to provide boundary conditions which couple these information flows.

- the corners

$$\mathcal{C}Q_T := (\overline{\mathcal{B}Q_T} \cap \mathcal{P}Q_T) \backslash \mathcal{B}Q_T.$$

A space-time domain with the respective parts of the boundary being indicated is shown in figure 2.4.

Given the velocities of the boundary as above, we can now write the no flux conditions on the lateral boundary $\mathcal{L}Q_T$ as:

$$D\partial_x a(t, l(t)) + \dot{l}(t) a(t,\, l(t)) \;=\; D\partial_x a(t, r(t)) + \dot{r}(t) a(t,\, r(t)) \;=\; 0 \qquad \forall\, t \in (0, T). \tag{2.32}$$

To this end we should note that the boundary velocity can be expressed in terms of the monomer concentration itself and the model parameters. We thus in fact have

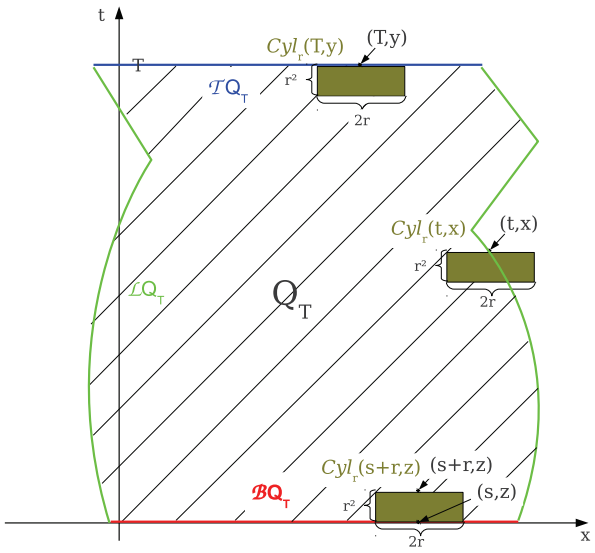

Figure 2.4: Sketch of a typical space-time domain. The respective parts of the domain boundary are indicated, and a parabolic cylinder of radius r is sketched for two boundary points. Note that beneath (T, y) there is some parabolic cylinder which has no point in common with the exterior of Q_T whereas any parabolic cylinder beneath (t, x) reaches beyond the boundary of Q_T.

nonlinear boundary conditions of the form

$$D\partial_x a(t,l(t)) + \vartheta(t,l(t))\ a(t,\ l(t)) + \varkappa(t,l(t))\ a(t,l(t))^2 \quad = \quad 0 \qquad (2.33)$$

$$D\partial_x a(t,r(t)) + \vartheta(t,r(t))\ a(t,\ r(t)) + \varkappa(t,r(t))\ a(t,r(t))^2 \quad = \quad 0 \qquad (2.34)$$

where $\varkappa$ is either of $\pm\delta\kappa_B$ or $\pm\delta\kappa_P$, and ϑ is the sum of $\pm v_R$ and either of $\pm\delta\kappa_B a_B$ or $\pm\delta\kappa_P a_P$.

2.3 Formulation of the initial conditions

On the base

$$\mathcal{B}Q_T = \overline{Q_T} \cap \{t = 0\} = \{(0, x) \mid 0 \leq x \leq L\} \tag{2.35}$$

of Q_T we have to specify initial conditions for the end densities as well as for the momomer concentration. Let us denote them by

$$a(0, x) = a_0(x) \quad \text{for } 0 \leq x \leq L \tag{2.36}$$

$$u^\alpha(0, x) = u_0^\alpha(x) \quad \text{for } 0 \leq x \leq L \quad \alpha = 1, \ldots, 4. \tag{2.37}$$

Now for reasons of compatibility with the boundary conditions we shall most often require the following assumptions.

Condition 2.3.1. *(Initial conditions for the hyperbolic equations)*

1. *For* $\alpha = 1, \ldots, 4$ *assume* $u_0^\alpha \in C^1((0, L)) \cap C^{0+1}([0, L])$.
2. *For* $\alpha = 1, \ldots, 4$ *assume* $u_0^\alpha(x) \geq 0$ *for* $x \in [0,\ L]$.
3. *For each* $\alpha = 1, \ldots, 4$ *assume:*

$$u_0^\alpha(0) = 0 = u_0^\alpha(L). \tag{2.38}$$

4. *If* $\lambda^\alpha(a(0, 0)) = \min_{\beta=1,\ldots,4} \lambda^\beta(a(0, 0))$ *then assume the existence of an* $\varepsilon > 0$ *such that*

$$u_0^\alpha(x) > 0 \quad \text{on } \ (0, \varepsilon). \tag{2.39}$$

5. *If* $\lambda^\alpha(a(0, L)) = \max_{\beta=1,\ldots,4} \lambda^\beta(a(0, L))$ *then assume the existence of an* $\varepsilon > 0$ *such that*

$$u_0^\alpha(x) > 0 \quad \text{on } \ (L - \varepsilon,\ L) \tag{2.40}$$

The last two conditions are motivated by physical considerations. As the outermost characteristic curve is supposed to support the membrane, the corresponding density of filament tips in each arbitrarily small neighborhood of the boundary should be positive.

The first condition can be without loss of physical relevance strengthened to

$$u_0^\alpha \in C^\infty([0, L]).$$

For the parabolic equation we require the following conditions.

Condition 2.3.2. *The initial conditions for the parabolic equation satisfy*

1. $a_B(0, x) \leq a(0, x) \leq a_P(0, x)$ *for each* $x \in [0, L]$
2. *compatibility with the boundary conditions at the left corner point:*

$$D\frac{d}{dx}a(0, 0) + \dot{l}(0)a(0, 0) = 0$$

3. compatibility at the right corner point:

$$D\frac{d}{dx}a(0,L) + \dot{r}(0)a(0,L) = 0$$

The first condition ensures that the initial monomer concentration lies in its natural range between the critical values a_B and a_P that will be derived in section 3.2. The other conditions ensure the compatibility at the corners of Q_T (cf. [16]) and are required if we want to hope for classical solutions.

2.4 Steady states for the free boundary problem

At this point, we shall make some remarks about steady state solutions to the problem established in this chapter. We first note that we can distinguish different notions of steady states corresponding to different behaviors of the modeled cell.

1. By a *strong steady state* we shall denote a solution $(u, a) : [0, L] \to \mathbb{R}^4 \times \mathbb{R}$ to the stationary problem

$$\frac{d}{dx}(\Lambda(a(x))u(x)) = 0 \tag{2.41}$$

$$D\frac{d^2}{dx^2}a(x) = -R(a(x), u(x)) \tag{2.42}$$

posed in $(0, L)$ and equipped with the boundary conditions

$$u(0) = 0 = u(L) \qquad a'(0) = 0 = a'(L). \tag{2.43}$$

This solution is called a *physical strong steady state* if it is non-negative and satisfies the following conditions

- For each $x \in [0, L]$ the filament density is non-negative:

$$\int_0^x u^2(y) - u^4(y)dy \geq 0, \qquad \int_0^x u^1(y) - u^3(y)dy \geq 0.$$

- Each of the boundaries is supported by at least one appropriate end density. That is, there exists some $\varepsilon > 0$ such that

$$u^1(\delta) + u^2(\delta) > 0 \qquad \text{and} \qquad u^3(L-\delta) + u^4(L-\delta) > 0$$

whenever $\delta \in (0, \varepsilon)$.

Such a steady state corresponds to a non-moving cell of constant size whose cytoskeleton is in a dynamic equilibrium.

2. By an *exterior steady state* we mean a solution (u, a, r, l) to the full problem that satisfies $\dot{r}(t) = \dot{l}(t) \equiv 0$ throughout the considered time interval $[0, T]$. This corresponds to a resting cell with global internal reorganization of the cytoskeleton and possible polarization.

3. An *interior steady state* will be a solution (u, a) to the stationary problem posed in point 1 on the whole real line. These do not correspond to any physical state of the cell but are mere mathematical tools to study the behavior of the solutions in the interior of the space-time cylinder. We note at this point that we will occasionally allow weak and even measure valued solutions to be interior steady states. Solutions with point measures for the hyperbolic equations may well be understood by thinking of sharp fronts of filament tips at some point in the cell.

4. A *moving steady state* shall be a solution (u, a, r, l) of the full initial boundary value problem with the property that $\dot{l}(t) = \dot{r}(t) \equiv v \neq 0$. This type of steady state should not be mixed up with the typical notion of steady state solutions in mathematics but is nevertheless quite useful as it accounts for a cell with an active cytoskeleton moving at constant speed.

5. Finally, a *moving interior steady state* is a (generalized) traveling wave solution (u, a) to the CAUCHY problem corresponding to (2.13), (2.15) on the whole real line, that is, a solution of the type

$$u(t, x) = U(x - ct), \qquad a(t, x) = A(x - ct).$$

   Again, we allow for measure valued solutions for u and weak solutions for a.

2.4.1 Strong steady states

This type of steady state corresponding to a resting cell with stationary cytoskeleton has already been investigated in [10] where we found a particular class of time independent solutions with homogeneous monomer concentration $a \equiv a^{ss}$. We recall that for these solutions to exist, the reaction parameters had to satisfy the compatibility condition

$$\kappa_B(a^{ss} - a_B) = \kappa_P(a_P - a^{ss}) \tag{2.44}$$

for some $a^{ss} \in (a_B, a_P)$ which then is the steady state monomer concentration. Both of these expressions had in addition to be equal to $v_R\delta^{-1}$ in order to make all end velocities vanish.

The end densities in these states have to satisfy the pointwise condition

$$u^1 + u^4 = u^2 + u^3 \tag{2.45}$$

which guarantees that the reaction term $R(a, u)$ vanishes for a equalling the steady state concentration a^{ss}. Apart from that and the usual physicality and regularity conditions, the end distributions can be chosen freely.

2.4.2 Interior steady states

When talking about interior steady states we mainly think of weak solutions $a \in H^{1,loc}(\mathbb{R}; [0, \infty))$ of the stationary problem (2.42) together with measure valued solutions $u \in \mathcal{M}_+(\mathbb{R})$ of (2.41), both on the whole real axis. The obvious reason to consider this type of solutions is the idea of polymerization fronts of filament tips as being ob-

served at the interface between the leading lamellipodium and the lamella of motile cells, as for example being observed experimentally by Ponti et al in [26].

Let us explain the relevance of these states by the following instructive example. We consider a cytoskeleton existing of a certain number of right oriented filaments, all of them having the same length l_0 and located at the same position. In mathematical terms, this filament distribution corresponds to a number of left oriented pointed ends at some position x_0,

$$u^2 = b_0 \delta_{x_0}$$

and the same number of right oriented barbed ends at $x_0 + l_0$,

$$u^4 = b_0 \delta_{x_0 + l_0}$$

where δ_{x_0} denotes the DIRAC measure concentrated at x_0.

The corresponding monomer concentration may then be given by

$$a(x) = \begin{cases} a_P^0 & \text{in } (-\infty, x_0] \\ a_P^0 + \frac{a_B^0 - a_P^0}{l_0}(x - x_0) & \text{in } (x_0, x_0 + l_0) \\ a_B^0 & \text{in } [x_0 + l_0, \infty) \end{cases} \tag{2.46}$$

where a_B^0 and a_P^0 are the concentrations at which the velocities of barbed and pointed ends, respectively, are zero (cf. section 3.1). These concentrations may be different for general reaction parameters, and we will for this example assume $a_P^0 > a_B^0$, the case which is depicted in the right graph of figure 3.1.

According to our ideas of the cytoskeleton, the pointed ends at position x_0 permanently produce monomers at rate

$$\delta \kappa_P (a_P - a_P^0) b_0$$

which are consumed by the barbed ends at position $x_0 + l_0$ at the rate

$$\delta \kappa_B (a_B^0 - a_B) b_0.$$

By the definitions of a_B^0 and a_0^P, both of these rates are equal to $v_R b_0$.

As monomers are produced at one point and consumed at another one, they have to be transported from x_0 to $x_0 + l_0$. The only way for monomers to move is by diffusion, and the diffusive flux is given by

$$-D \partial_x a = \frac{D}{l_0}(a_P^0 - a_B^0)$$

throughout the interval $(x_0, x_0 + l_0)$. Since this flux clearly has to balance the production at pointed ends and the consumption at barbed ends, we obtain a relation between the height b_0 and the distance l_0 of the peaks:

$$b_0 l_0 = \frac{D}{v_R}(a_P^0 - a_B^0) = \frac{D}{v_R}(a_P - a_B) - \frac{D}{\delta}\frac{\kappa_B + \kappa_P}{\kappa_B \kappa_P}. \tag{2.47}$$

For symmetry reasons we may add the mirror image of the described distributions,

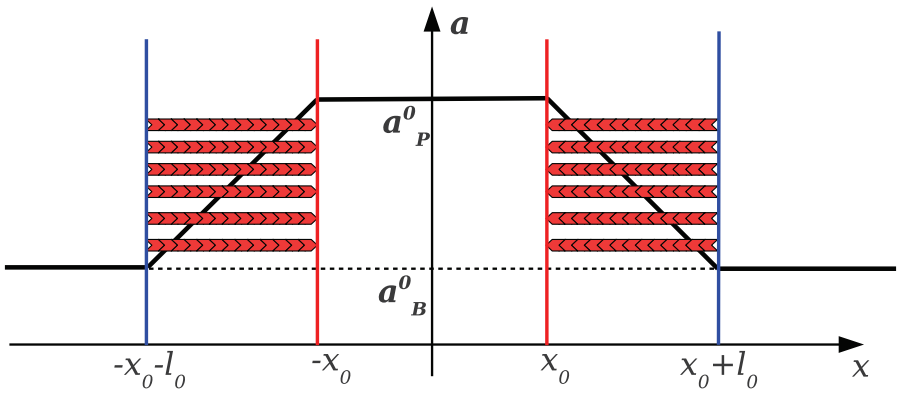

Figure 2.5: Sketch of measure valued interior steady states. The monomer density a (*black line*) is given by a_B^0 for large $|x|$, by a_P^0 for small $|x|$ and linearly interpolated in between. The end densities are DIRAC measures, sketched as *red* and *blue* bars for pointed and barbed ends, respectively.

namely the same number of left oriented filaments of length l_0 with pointed ends located at $-x_0$ and barbed ends concentrated at $-x_0 - l_0$. This particular situation is sketched in figure 2.5.

One may argue that this situation does not fit with our understanding of the pullback velocity v_R being caused by myosin motors pulling filaments along one another. However, we can easily adapt this steady state by interchanging the positions of left and right oriented pointed ends, respectively, to obtain an overlap of actin filaments as indicated in figure 2.6.

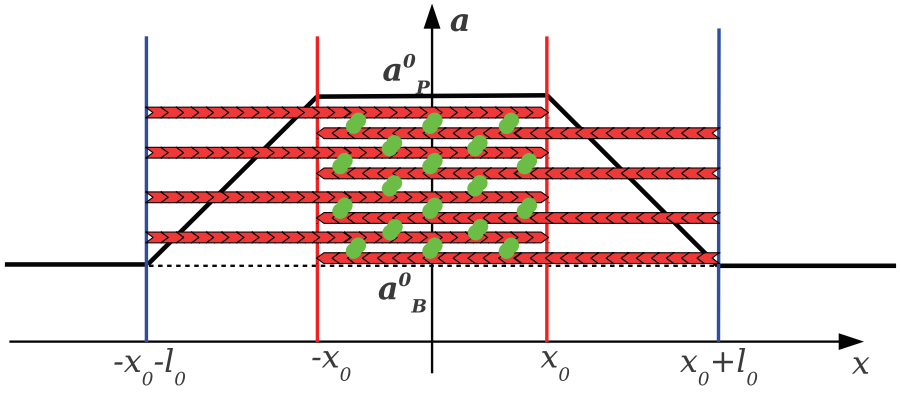

Figure 2.6: Sketch of measure valued interior steady states with overlapping filaments and myosin motors (green) between them. The *black line* denotes the monomer concentration, the *red* and *blue* bars denote the DIRAC measures for the pointed and barbed end densities, respectively.

Moving interior steady states

We may also think about this type of steady states with a given shape moving at constant velocity v_0. We therefore ask for two DIRAC measures $p_0\delta_{x_0+v_0t}$ and $b_0\delta_{x_0+v_0t+l_0}$ describing the end densities P_l and B_r, respectively. Moreover, the monomer density should be given by constant states on $\{x \leq x_0+v_0t\}$ and $\{x \geq x_0+v_0t+l_0\}$, respectively, and in between by a constant profile of the shape $a(t,x) = A(x-v_0t)$. That is, we want the monomer concentration to be of the form

$$a(t,x) = \begin{cases} a_l & \text{for } x \leq x_0 + v_0t \\ A(x-v_0t) & \text{for } x_0 + v_0t < x < x_0 + v_0t + l_0 \\ a_r & \text{for } x \geq x_0 + v_0t + l_0. \end{cases} \tag{2.48}$$

Here, the asymptotic densities a_r and a_l are determined by the requirements

$$-v_P(a_l) = v_0 = v_B(a_r).$$

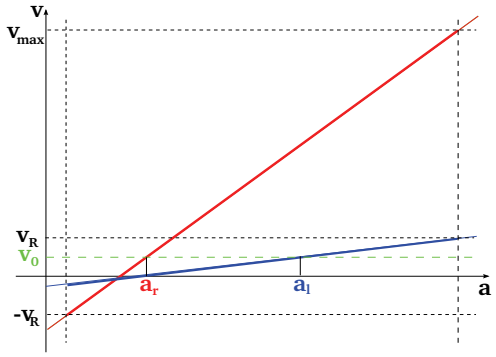

Figure 2.7: Filament end velocities v_B (*red*) and $-v_P$ (*blue*) depending on the monomer density a. Given a velocity v_0 between 0 and v_R, the figure shows how to determine the asymptotic densities a_r and a_l. For parameter values as indicated in this graph, the difference $a_l - a_r$ will always be positive if v_0 is. It should be noted that for different parameter settings and sufficiently small v_0, this difference may also become negative.

Writing the velocity v_0 as a multiple of the retrograde flow velocity,

$$v_0 = \theta v_R$$

with $|\theta| \in (0,1]$ we obtain the following values for the asymptotic monomer densities

$$a_l = a_P - \frac{v_R}{\delta\kappa_P}(1-\theta) = a_P^0 + \frac{v_R}{\delta\kappa_P}\theta \tag{2.49}$$

$$a_r = a_B + \frac{v_R}{\delta\kappa_B}(1+\theta) = a_B^0 + \frac{v_R}{\delta\kappa_B}\theta. \tag{2.50}$$

These values in fact only depend on the model parameters and the velocity the profile is supposed to move at. Figure 2.7 shows how the asymptotic densities are obtained from the velocity and why in general not all velocities are admissable.

The next observation is that upon the profile moving, the total number of monomers changes at rate

$$v_0(a_l - a_r).$$

This has to be balanced by the net production or consumption of monomers at the filament ends:

$$\theta(a_l - a_r) = (1-\theta)p_0 - (1+\theta)b_0. \tag{2.51}$$

Thus, we can express one of the peak heights for the ends in terms of the other one, say p_0 in terms of b_0:

$$\begin{aligned} p_0 &= \frac{1}{1-\theta}\left(\theta(a_l - a_r) + (1+\theta)b_0\right) \\ &= \frac{1}{1-\theta}\left(\theta(a_P - a_B) - \frac{\theta v_R}{\delta}\left(\frac{1-\theta}{\kappa_P} + \frac{1+\theta}{\kappa_B}\right)\right) + \frac{1+\theta}{1-\theta}b_0. \end{aligned}$$

We observe that for positive velocity $v_0 = \theta v_R$ and if the difference $a_l - a_r$ is positive (which will be the case for standard parameters, cf. figure 2.7), the number of pointed ends has to be larger than that of barbed ends.

It remains to calculate the distance of the peaks and the profile for the monomer density in between. The latter is done by plugging the ansatz $a(t,x) = A(x - v_0 t)$ into the monomer equation (2.15) and recalling that the reaction term vanishes due to the absence of filament ends outside the peaks. Therefore, A as a function of

$$\xi := x - v_0 t - x_0$$

satisfies the ordinary differential equation

$$v_0 A(\xi) + DA'(\xi) = C_1 \tag{2.52}$$

where C_1 is a constant of integration to be determined by the boundary conditions. The general solution to this equation is given by

$$A(\xi) = C_2 \exp\left[-\frac{\theta v_R}{D}\xi\right] + \frac{C_1}{\theta v_R}.$$

This leads to the following values for the integration constants

$$\begin{aligned} C_2 &= \frac{A(0) - A(l_0)}{1 - \exp\left[-\frac{\theta v_R}{D} l_0\right]} \\ C_1 &= \theta v R\left(A(0) - \frac{A(0) - A(l_0)}{1 - \exp\left[-\frac{\theta v_R}{D} l_0\right]}\right). \end{aligned}$$

Asking for continuous monomer densities we may impose the particular boundary conditions

$$A(0) = a_l \qquad \text{and} \qquad A(l_0) = a_r.$$

and subsequently obtain the following shape of the monomer profile

$$A(\xi) = a_l - \frac{a_l - a_r}{1 - \exp\left[-\frac{\theta v_R}{D} l_0\right]}\left(1 - \exp\left[-\frac{\theta v_R}{D}\xi\right]\right). \tag{2.53}$$

This profile, together with indicated DIRAC peaks for the end densities B_r and P_l, is sketched in figure 2.8.

Moreover, we know that the total flux of monomers into or out of the interface curves

$$x_0 + v_0 t \qquad \text{and} \qquad x_0 + v_0 t + l_0$$

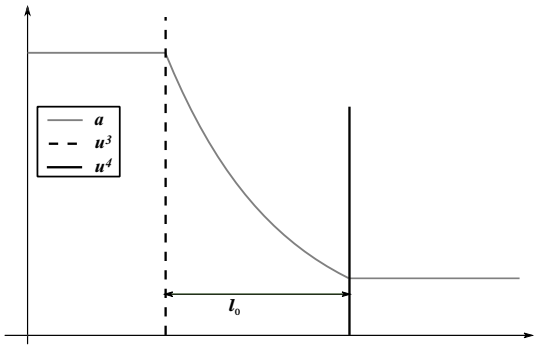

Figure 2.8: Sketch of a moving steady state profile with positive velocity v_0. The monomer concentration is drawn in *solid, grey*; the positions and masses of the DIRAC peaks for right oriented barbed ends (*solid, black*) and left oriented pointed ends (*dashed, black*) are shown as well.

(from both sides) has to be balanced by the consumption or production of monomers in these boundaries. This imposes two additional conditions:

$$\begin{aligned} \theta v_R a_l - DA'(0) - \theta v_R A(0) &= (1-\theta) v_R p_0 \\ \theta v_R a_r - DA'(l_0) - \theta v_R A(l_0) &= (1+\theta) v_R b_0. \end{aligned}$$

We calculate the derivative of A to be

$$\begin{aligned} A'(\xi) &= -C_2 \frac{\theta v_R}{D} \exp\left[-\frac{\theta v_R}{D}\xi\right] \\ &= -\frac{\theta v_R}{D} \frac{A(0) - A(l_0)}{1 - \exp\left[-\frac{\theta v_R}{D} l_0\right]} \exp\left[-\frac{\theta v_R}{D}\xi\right] \end{aligned}$$

and in particular at the boundary points:

$$\begin{aligned} DA'(0) &= -(A(0) - A(l_0))\theta v_R \frac{1}{1 - \exp\left[-\frac{\theta v_R}{D} l_0\right]} \\ DA'(l_0) &= -(A(0) - A(l_0))\theta v_R \frac{1}{\exp\left[\frac{\theta v_R}{D} l_0\right] - 1}. \end{aligned}$$

Again, for a continuous monomer concentration, we find

$$\begin{aligned} (a_l - a_r)\theta &= (1-\theta) p_0 \left(1 - \exp\left[-\frac{\theta v_R}{D} l_0\right]\right) \\ (a_l - a_r)\theta &= (1+\theta) b_0 \left(\exp\left[\frac{\theta v_R}{D} l_0\right] - 1\right). \end{aligned}$$

From the latter equality we may infer that l_0 shall be given by

$$l_0 = \frac{D}{\theta v_R} \log\left[1 + \frac{a_l - a_r}{b_0} \frac{\theta}{1+\theta}\right]. \tag{2.54}$$

The other flux condition together with the actin mass conservation condition (2.51) yields the same result.

We can also ask how the shape of the profile depends on the parameters. A good measure for the deviation from a linear interpolation is the weighted difference of the

derivatives $A'(0)$ and $A'(l_0)$:

$$\frac{|A'(0)-A'(l_0)|}{|A'(0)+A'(l_0)|} = \frac{\left|\frac{1}{1-\exp\left[-\frac{\theta v_R}{D}l_0\right]}-\frac{1}{\exp\left[\frac{\theta v_R}{D}l_0\right]-1}\right|}{\left|\frac{1}{1-\exp\left[-\frac{\theta v_R}{D}l_0\right]}+\frac{1}{\exp\left[\frac{\theta v_R}{D}l_0\right]-1}\right|}.$$

Now we use the particular value of the distance l_0 given by (2.54) and plug the argument of the logarithm into the above ratio:

$$\begin{aligned}\frac{|A'(0)-A'(l_0)|}{|A'(0)+A'(l_0)|} &= \frac{\frac{a_l-a_r}{b_0}\frac{\theta}{1+\theta}}{2+\frac{a_l-a_r}{b_0}\frac{\theta}{1+\theta}} \\ &= \frac{\theta(a_l-a_r)}{2(1+\theta)b_0+\theta(a_l-a_r)}.\end{aligned}$$

We conclude that we shall find an approximately linear profile of the monomer density if

- the velocity is small as compared to the retrograde flow velocity (corresponding to $\theta \ll 1$), or
- the difference $a_l - a_r$ is small as compared to the number b_0 of filament ends.

The former effect is consistent with the perfectly linear profile obtained for the limit case of a standing profile ($\theta = 0$), the second one will become later in an instant.

Finally, we mention that we will deal with another type of interior steady states which we only consider locally in space. This state will be given by a shock in the monomer densities violating even the mild regularity assumptions on a stated at the beginning of this subsection. We will discuss these states in chapter 5 on gradient blow-up for the monomer density.

2.4.3 A note on dimensional analysis of the model

In equation (2.54) we observe that the distance l_0 does not change at all if we increase or decrease the number b_0 of barbed ends and the diffusion coefficient D by te same factor. To make this observation more rigorous we will briefly check how our model system could be brought into dimensionless form and deduce the connection between the diffusion coefficient and the typical end densities.

We note that it is sufficient to consider the monomer equation together with the equations for one type of barbed and one type pointed ends since all parameters are already contained therein. As basic physical quantities we identify space and time

$$t = T\tau \qquad \text{and} \qquad x = X\xi$$

and two types of dimensionless entities which are given as densities, namely monomers $a = A\alpha$ and filament tips, $B_r = B\beta$ and $P_l = B\pi$. Applying these formal transforma-

tions to the equations (2.4a), (2.4d) and (2.15), we find the system

$$\begin{aligned}
\partial_\tau \beta + \partial_\xi \left(\left(-\frac{T}{X} v_R + \frac{\delta \kappa_B T}{X} (A\alpha - a_B) \right) \beta \right) &= 0 \\
\partial_\tau \pi + \partial_\xi \left(\left(\frac{T}{X} v_R + \frac{\delta \kappa_P T}{X} (A\alpha - a_P) \right) \pi \right) &= 0 \\
(\partial\tau - \partial_{\xi\xi})\alpha + T\delta\kappa_B \left(\alpha - \frac{a_B}{A} \right) B\beta + T\delta\kappa_P \left(a - \frac{a_P}{A} \right) B\pi &= 0.
\end{aligned}$$

With the natural choices

$$X = \frac{D}{v_R},\ T = \frac{D}{v_R^2}, \quad \text{and} \quad A = a_B,$$

where we chose the characteristic drift velocity to be v_R, this leads to the following dimensionless system

$$\begin{aligned}
\partial_\tau \beta + \partial_\xi \left((-1 + \gamma(\alpha - 1))\beta \right) &= 0 && (2.55) \\
\partial_\tau \pi + \partial_\xi \left((1 + \gamma\rho(\alpha - \sigma))\pi \right) &= 0 && (2.56) \\
(\partial_\tau - \partial_{\xi\xi})\alpha &= -\gamma(\alpha - 1)\beta - \gamma\rho(\alpha - \sigma)\pi && (2.57)
\end{aligned}$$

if we in addition define the non-dimensional parameters

$$\begin{aligned}
\gamma = \frac{\delta \kappa_B a_B}{v_R} \quad &\ldots \quad \text{ratio of typical polymerization and retrograde flow velocities} \\
\rho = \frac{\kappa_P}{\kappa_B},\ \sigma = \frac{a_P}{a_B} \quad &\ldots \quad \text{ratios of pointed vs. barbed end kinetics}
\end{aligned}$$

and take the characteristic end density to be

$$B = \frac{v_R}{D} a_B = \frac{1}{X} a_B$$

which also explains why the monomer profile is nearly linear for the number of filament ends being large as compared to the monomer density.

Recalling that in the derivation of the model we scaled the end densities by a factor of δ in order to more conveniently calculate the filament density (cf. [10]) we conclude that the characteristic true end density $b = \delta B$ scales as

$$b = \frac{\delta v_R}{D} a_B = \frac{\delta}{X} a_B.$$

That means that the typical invariance under a change in the diffusion coefficient and a concommitant rescaling of the characteristic time and length scales is in our case not granted since these scaling constants also occur in the relative densities of filament tips and monomers.

We see in particular that a variation of the diffusion coefficient does not change the behavior of the system at all if simultaneously all end densities are varied by the same factor and all other quantities are left unchanged. We will recover this finding in simulations as well. To put it differently that means that increasing the diffusion coefficient has the same effect as decreasing the end densities relative to the typical

monomer density.

This behavior can also be understood from physical considerations. By increasing the diffusion coefficient we increase the mobility of the monomers and the interaction of these with the filament tips is a relatively weakened as a driver of the monomer dynamics. If however simultaneously there are more filament ends present there influence is increased again. If we now note that the hyperbolic equations for the end densities neither see a change of the diffusion coefficient nor a variation of the end densities by a constant factor we can draw the same conclusion as from the formal calculations given above.

These considerations allow for the investigation of the dimension free model rather than the original one. For the numerical simulations in chapter 7 we will nevertheless use the model in its dimensional form in order to explicitely see the effect of changing the parameters within their physiological range.

Chapter 3

General Estimates for the Solutions

We begin this chapter by introducing the notion of a smooth solution to the free boundary problem established in chapter 2.

Definition 3.0.1. *Assume conditions 2.1.1. By a* smooth solution *(or* classical solution*) of problem (2.14), (2.15) we denote a pair*

$$(u,\ a) \in C_b^1\left(\overline{Q_T};\ [0,\infty)^n\right) \times \left(C_b^{2_x,1_t}(Q_T;\ (0\infty)) \cap C^{1_x,0_t}(\overline{Q_T};\ (0,\infty))\right)$$

such that u satisfies (2.14) and a satisfies (2.15) in Q_T which is given by (2.21).

In the above definition we denoted by $C_b^{2_x,1_t}(Q_T)$ the space of bounded continuous functions in Q_T having bounded continuous derivatives up to order two with respect to the spatial variable x and of first order with respect to time t. Similarly, $C^{1_x,0_t}(\overline{Q_T})$ denotes the space of continuous functions on the closure $\overline{Q_T}$ having continuous first derivatives with respect to space up to the boundary.

Remark 3.1. *Note that for physical reasons we will only consider solutions for which the left boundary is determined by the characteristic curves of u^1 or u^2 (corresponding to B_l and P_r, respectively) and for which the right boundary is given by u^3 or u^4 (i.e., P_l or B_r). With α_r and α_l defined by (2.29) and (2.30), respectively, this can be expressed by:*

$$\forall t \geq 0: \quad \alpha_l(t) \cap \{1,2\} \neq \emptyset, \quad \alpha_r(t) \cap \{3,4\} \neq \emptyset. \tag{3.1}$$

The physical interpretation is that the barbed ends of left oriented filaments have to be closer to the left boundary than their corresponding pointed ends, and similarly the barbed ends of right oriented filaments should be further to the right than right oriented pointed ends.

We will refer to such solutions as physical solutions.

3.1 Characteristic velocities

In remark 2.1 we already noted that for special reaction parameters all characteristic velocities are either zero or mutually different, depending on the value of the monomer density a. We will now give an overview of all possible combinations. First notice that by definition we always have

$$\begin{aligned} -\lambda^1(t,x) &= v_B(a(t,x)) &= \lambda^4(t,x) \quad (3.2)\\ \lambda^2(t,x) &= v_P(a(t,x)) &= -\lambda^3(t,x). \quad (3.3) \end{aligned}$$

This observation leaves us with the following cases.

1. $0 \neq |v_B| \neq |v_P| \neq 0$. In that case the hyperbolic part has four distinct eigenvalues given by $\pm v_B$ and $\pm v_P$, and is thus strictly hyperbolic. This is the generic case whereas all other cases require a particular value of the monomer concentration.

2. $v_B = v_P \neq 0$. That means we find two distinct, double eigenvalues $\pm v_B = \pm v_P$ with the corresponding eigenspaces being simply $\langle \mathbf{e}_2,\ \mathbf{e}_4\rangle$ and $\langle \mathbf{e}_1,\ \mathbf{e}_3\rangle$. This case occurs if the monomer concentration satisfies

$$a(t,x) = a^{ss} := \frac{\kappa_B(t,x)a_B(t,x) + \kappa_P(t,x)a_P(t,x)}{\kappa_B(t,x) + \kappa_P(t,x)}. \quad (3.4)$$

3. Either $v_B = 0$ or $v_P = 0$. That is, 0 is a double eigenvalue with associated eigenspace being either $\langle \mathbf{e}_1,\ \mathbf{e}_4\rangle$ or $\langle \mathbf{e}_2,\ \mathbf{e}_3\rangle$, and there are two further single eigenvalues of mutually opposite sign. The corresponding values of the monomer density are given by

$$\begin{aligned} v_B = 0: &\qquad a(t,x) = a_B^0 := a_B(t,x) + \frac{v_R}{\delta\kappa_B(t,x)} \quad (3.5)\\ v_P = 0: &\qquad a(t,x) = a_P^0 := a_P(t,x) - \frac{v_R}{\delta\kappa_P(t,x)}. \quad (3.6) \end{aligned}$$

4. $v_B = -v_P \neq 0$. Then we have two double eigenvalues $\pm v_B$ with $\langle \mathbf{e}_3,\ \mathbf{e}_4\rangle$ and $\langle \mathbf{e}_1,\ \mathbf{e}_2\rangle$ as corresponding eigenspaces, respectively. This will be true for the monomer concentration

$$a(t,x) = a^{BP} := \frac{2\frac{v_R}{\delta} + \kappa_B(t,x)a_B(t,x) - \kappa_P(t,x)a_P(t,x)}{\kappa_B(t,x) - \kappa_P(t,x)}. \quad (3.7)$$

5. $v_B = v_P = 0$. In that case there is only one eigenvalue of multiplicity four with the whole $\mathbb{R}^4$ as eigenspace. This case can only occur if the reaction parameters satisfy the compatibility condition

$$a_B(t,x) + \frac{v_R}{\delta\kappa_B(t,x)} = a_P(t,x) - \frac{v_R}{\delta\kappa_P(t,x)} \quad (3.8)$$

where both sides have to equal $a(t,x)$. The compatibility condition (3.8) can be rewritten to

$$\kappa_B(t,x)\kappa_P(t,x)\frac{a_P(t,x) - a_B(t,x)}{\kappa_P(t,x) + \kappa_P(t,x)} = \frac{v_R}{\delta}. \quad (3.9)$$

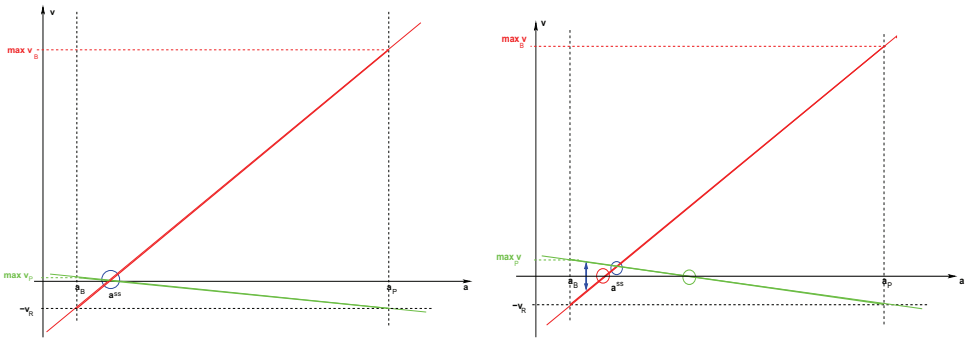

Figure 3.1: Characteristic velocities v_B (*red*) and v_P (*green*) in dependence of the monomer concentration a for parameters satisfying (*left*) or not satisfying (*left*) the compatibility condition (3.8). The slopes of the lines are κ_B and $-\kappa_P$, respectively. Note that by lemma 3.3, the dynamics are bound to the dashed rectangle.

Remark 3.2. *Provided the initial and boundary conditions are appropriate, the characteristic velocities are uniformly bounded by:*

$$\begin{aligned} -v_R &\leq v_B(t,x) \\ &\leq \delta \sup_{t,x}(\kappa_B(t\ x)(a_P(t,x) - a_B(t,x))) - v_R \\ &\leq \delta \sup_{t,x} \kappa_B(t,x)(\overline{a_P} - \underline{a_B}) - v_R, \end{aligned}$$

and

$$\begin{aligned} -v_R &\leq v_P(t,x) \\ &\leq \delta \sup_{t,x}(\kappa_P(t\ x)(a_P(t,x) - a_B(t,x))) - v_R \\ &\leq \delta \sup_{t,x} \kappa_P(t,x)(\overline{a_P} - \underline{a_B}) - v_R, \end{aligned}$$

respectively. This is obvious from the boundedness of a between $\underline{a_B}$ and $\overline{a_P}$ (cf. lemma 3.3). In particular, we can state

$$-v_{max} \leq \lambda^1, \ldots, \lambda^4 \leq v_{max}$$

where we introduced the maximal possible velocity

$$v_{max} := \max\left\{v_R, \delta \sup_{t,x} \kappa_B(t,x)(\overline{a_P} - \underline{a_B}) - v_R\right\}. \tag{3.10}$$

For given compatible (in the sense of (3.8)) parameters, the characteristic velocities v_B and v_P behave as indicated in figure 3.1 on the left whereas the right diagraph shows the case of incompatible parameters allowing no eigenvalue of multiplicity four.

Since v_B and v_P are affine functions of a and since κ_B is always assumed to be larger than κ_P, the values of a^{ss}, a_B^0, a_P^0, and a^{BP} are always unique for any fixed set of

parameters.

3.2 Reaction term and monomer density

Given any values for the monomer densities $u^1, \dots, u^4 \geq 0$ we can calculate for the reaction term in the monomer equation (2.4e):

$$R(a_P(t,x),\ u) = -\delta\kappa_B(t,x)(a_P(t,x) - a_B(t,x))(u^1 + u^4) \leq 0. \tag{3.11}$$

where we denoted by $u = (u^1, \dots,\ u^4)^T$ the vector of the end densities and used condition 2.1.1 to obtain the sign. Likewise, we find

$$R(a_B(t,x),\ u) = -\delta\kappa_P(t,x)(a_B(t,x) - a_P(t,x))(u^2 + u^3) \geq 0. \tag{3.12}$$

Both of the last two inequalities are strict if the end densities are such that $u^1 + u^4 \neq 0$ and $u^2 + u^3 \neq 0$, respectively.

Furthermore, we can estimate the reaction term to be bounded by

$$\begin{aligned} |R(a,u)| &= \delta\left|\kappa_B(a_B - a)(u^1 + u^4) + \kappa_P(a_P - a)(u^2 + u^3)\right| \\ &\leq \delta \max\left\{\kappa_B(a - a_B)(u^1 + u^4),\ \kappa_P(a_P - a)(u^2 + u^3)\right\} \\ &\leq 2\delta \sup_{t,x} \kappa_B(\overline{a_P} - \underline{a_B}) \sup_{t,x} \max_{\alpha} |u^\alpha| \end{aligned} \tag{3.13}$$

whenever a is bounded between $\underline{a_B}$ and $\overline{a_P}$.

We readily obtain the following estimate for the monomer density a.

Lemma 3.3. *Assume, the parameters to satisfy*

$$\frac{v_R}{\delta} < \inf_{t,x} \kappa_B(t,x)(\overline{a_P} - \overline{a_B}) \tag{3.14}$$

$$\frac{v_R}{\delta} < \inf_{t,x} \kappa_P(t,x)(\underline{a_P} - \underline{a_B}). \tag{3.15}$$

Let $(u,\ a)$ be a smooth, physical solution to (2.14), (2.15) with initial conditions satisfying

$$\underline{a_B} = \inf_{t,x} a_B(t,x) \ \leq\ a(0,x)\ \leq \sup_{t,x} a_P(t,x) = \overline{a_P} \tag{3.16}$$

and moving boundary conditions as specified in section 2.2. Then a satisfies

$$\underline{a_B} \ \leq\ a(t,x)\ \leq\ \overline{a_P} \qquad \text{for each } (t,x) \in \overline{Q_T}. \tag{3.17}$$

Proof. (I) As the solution is considered to be continuous it suffices to show that a cannot grow if it equals $\overline{a_P}$ or shrink if it is $\underline{a_B}$. Assume first, a takes the value $\overline{a_P}$ in some point $(\bar{t}, \bar{x})$ inside $Q_T \cup \Omega_0$ where $\bar{t}$ is such that there is no smaller time t at which a attains this value. Then by continuity we infer that $a(\bar{t}, x) \leq \overline{a_P}$ for each $x \in \Omega_t$ and it follows $\partial_{xx} a(\bar{t}, \bar{x}) \leq 0$. Then, by equation (2.15) we calculate

$$\partial_t a(\bar{t}, \bar{x}) = D\partial_{xx} a(\bar{t}, \bar{x}) + R(\overline{a_P},\ u(\bar{t}, \bar{x})) \leq 0. \tag{3.18}$$

The value of a can thus not increase any further. By continuity again, we also obtain that $a \leq \overline{a_P}$ on Ω_T.

A completely analogous calculation shows the lower bound for a where we note that $\partial_{xx} a \geq 0$ at local minima.

(II) Consider now the case that a takes the value $\overline{a_P}$ on the lateral boundary of the domain Q_T. Then, the sign of the second spatial derivative is not known but we still can employ the boundary conditions and use our knowledge about the speed of the boundary. If the point in question belongs to the left boundary, say $a(\bar{t}, l(\bar{t})) = \overline{a_P}$, we calculate the possible characteristic speeds as

$$\begin{aligned} \lambda^1(\bar{t}, l(\bar{t})) &= v_R - \delta \kappa_B(\bar{t}, l(\bar{t}))(\overline{a_P} - a_B(\bar{t}, l(\bar{t}))) \\ &\leq v_R - \inf_{t,x} \kappa_B(t,x)(\overline{a_P} - \overline{a_B}) \end{aligned}$$

and

$$\begin{aligned} \lambda^2(\bar{t}, l(\bar{t})) &= -v_R - \delta \kappa_P(\bar{t}, l(\bar{t}))(\overline{a_P} - a_P(\bar{t}, l(\bar{t}))) \\ &\leq -v_R. \end{aligned}$$

Note that only these characteristic velocities are of interest as we are dealing with physical solutions. The first of those is negative by the hypothesis on the parameters, the second is negative anyway. From the boundary conditions (2.32) we thus derive

$$\partial_x a(\bar{t}, l(\bar{t})) > 0$$

which implies a to be larger than $a(\bar{t}, l(\bar{t})) = \overline{a_P}$ in some spatial neighborhood of $(\bar{t}, l(\bar{t}))$. That contradicts part (I) of the proof.

Similarly, assume the point where $\overline{a_P}$ is attained to belong to the right boundary, say $(\bar{t}, r(\bar{t}))$. There, the boundary velocity is given by

$$\begin{aligned} \lambda^4(\bar{t}, r(\bar{t})) &= -v_R + \delta \kappa_B(\bar{t}, r(\bar{t}))(\overline{a_P} - a_B(\bar{t}, r(\bar{t}))) \\ &\geq -v_R + \inf_{t,x} \kappa_B(t,x)(\overline{a_P} - \overline{a_B}) \end{aligned}$$

or

$$\begin{aligned} \lambda^3(\bar{t}, r(\bar{t})) &= v_R + \delta \kappa_P(\bar{t}, r(\bar{t}))(\overline{a_P} - a_P(\bar{t}, r(\bar{t}))) \\ &\geq v_R. \end{aligned}$$

Now both of them are positive and thus by (2.32) the derivative $\partial_x a(\bar{t}, r(\bar{t}))$ is negative which again yields a contradiction to (I).

If a takes the value $\underline{a_B}$ at the point $(\bar{t}, l(\bar{t}))$ on the left lateral boundary, then we compute the possible velocities as

$$\begin{aligned} \lambda^1(\bar{t}, l(\bar{t})) &= v_R - \delta \kappa_B(\bar{t}, l(\bar{t}))(\underline{a_B} - a_B(\bar{t}, l(\bar{t}))) \\ &\geq v_R, \end{aligned}$$

$$\begin{aligned}\lambda^2(\bar{t}, l(\bar{t})) &= -v_R - \delta\kappa_P(\bar{t}, l(\bar{t}))(\underline{a_B} - a_P(\bar{t}, l(\bar{t}))) \\ &\geq -v_R + \delta \inf_{t,x} \kappa_P(t,x)(\underline{a_P} - \underline{a_B}).\end{aligned}$$

These are both positive and the boundary conditions imply negativity of the derivative $\partial_x a(\bar{t}, l(\bar{t}))$. This in turn implies that a has to take smaller values than $\underline{a_B}$ in the vicinity of the boundary which again contradicts (I).

Finally, the case where a attains the value $\underline{a_B}$ on the right lateral boundary is treated analogously.

□

Remark 3.4. *It is obvious from the proof of the lemma that the assertion remains valid if the conditions (3.14) and (3.15) are only assumed to hold pointwise. So we can weaken them to*

$$\forall (t,x) \in \overline{Q_T}: \quad \begin{cases} \frac{v_R}{\delta} & < \quad \kappa_B(t,x)(\overline{a_P} - a_B(t,x)) \\ \frac{v_R}{\delta} & < \quad \kappa_P(t,x)(a_P(t,x) - \underline{a_B}). \end{cases} \tag{3.19}$$

Plugging the bounds on the monomer density into the reaction term R we readily find the following bound on the reaction term which has already been computed under the assumption of a being bounded between $\underline{a_B}$ and $\overline{a_P}$.

Corollary 3.5. *Under the hypotheses of lemma 3.3, the reaction term $R(a,\ u)$ in the monomer equation (2.15) satisfies the following uniform estimate:*

$$-2\delta\|\kappa_B\|_{C^0}\left(\overline{a_P} - \underline{a_B}\right)\|u\|_{C^0} \leq R(a(t,x),\ u(t,x)) \leq 2\delta\|\kappa_P\|_{C^0}\left(\overline{a_P} - \underline{a_B}\right)\|u\|_{C^0}. \tag{3.20}$$

Here, the C^0-norm of the end density vector u is defined relative to the maximum norm on $\mathbb{R}^4$:

$$\|u\|_{C^0} := \sup_{t,x} \max_{\alpha=1,\ldots,4} |u^\alpha(t,x)|. \tag{3.21}$$

We can furthermore give a gradient estimate for the monomer density a at the boundary.

Corollary 3.6. *Let (u,a) be a smooth, physical solution of the free boundary problem (2.14), (2.15), (2.22), (2.23), and (2.32) with compatible initial conditions. Then, for each $(t,x) \in \mathcal{L}Q_T$, the spatial derivative of the monomer density a satisfies:*

$$|\partial_x a(t,x)| \leq \frac{v_{max}\ \overline{a_P}}{D}. \tag{3.22}$$

Proof. This follows directly from the bound $|a| \leq \overline{a_P}$ from lemma 3.3 and the boundary conditions. □

Chapter 4

Existence and Uniqueness of Solutions

4.1 The strictly hyperbolic case with constant coefficients

Let us first assume that the reaction parameters are constant throughout the whole space-time domain and satisfy:

$$0 < a_B < a_P \tag{4.1}$$

$$0 < \kappa_P < \kappa_B, \tag{4.2}$$

$$\frac{v_R}{\delta} < \kappa_P(a_P - a_B), \tag{4.3}$$

and

$$a_P \geq a_B + 2\frac{v_R}{\delta}. \tag{4.4}$$

We recall that the first two of these conditions reflect the biophysical reality by stating that

1. at barbed ends, monomers are polymerized at much lower surrounding concentrations than at pointed ends and

2. the reaction kinetics at barbed ends are way faster than at pointed ends.

The third condition (4.3) ensures that the characteristic velocity of the pointed ends can take positive values. This is needed to allow for the pointed end velocity to vanish for some $a_P^0 \in (a_B, a_P)$. Finally, the last condition (4.4) guarantees the existence of some $a^{BP} \in (a_B, a_P)$ such that for larger monomer concentrations the barbed ends move faster than the pointed ends ($|v_B| > |v_P|$) (cf. figure 3.1, right). All of these conditions are satisfied under typical physiological conditions.

We wish to start with the strictly hyperbolic case indicated in figure 2.3 where the characteristic velocities satisfy

$$\lambda^1 < \lambda^2 < 0 < \lambda^3 < \lambda^4 \tag{4.5}$$

throughout the whole domain. By conditions (4.1)-(4.4) this will be the case for all monomer densities $a > a_{min}$ where

$$a_{min} := \max\{a_P^0, a_B^0, a^{BP}\} \tag{4.6}$$

lies between a_B and a_P.

We now equip system (2.13), (2.15) with initial data $u(0,\cdot)$ satisfying condition 2.3.1 and $a(0,\cdot)$ satisfying condition 2.3.2. In addition, we assume the following natural conditions which will in particular ensure strict hyperbolicity of the hyperbolic part at the boundary.

Condition 4.1.1. *1. There exists $\varepsilon_0 > 0$ such that*

$$u^3(0,x) = u^4(0,x) = 0 \qquad \text{on } (0,\varepsilon_0)$$

and

$$u^1(0,x) = u^2(0,x) = 0 \qquad \text{on } (L-\varepsilon_0, L).$$

These conditions tell us that initially, the left boundary is only supported by B_l or P_r and the right boundary only by B_r or P_l which ensures that the initial data are physical in the sense of remark 3.1.

2. There exists $\varepsilon_1 > 0$ such that

$$|a(0,0) - a^{BP}| > \varepsilon_1 \quad \text{and} \quad |a(0,L) - a^{BP}| > \varepsilon_1.$$

This condition assures that initially, the velocities of the ends directly at the boundary are different.

We start with some results stating existence and uniqueness for the single components $a,\ u,\ r$, and l of the solution supposed the others are given.

4.1.1 Existence and uniqueness for the parabolic equation

Assuming the boundary curves

$$l, r : [0,T] \to \mathbb{R}$$

and the end densities

$$u^1, \dots, u^4 : \overline{Q_T} \to [0,\infty)$$

are given, the monomer equation reduces to a linear equation

$$\partial_t a(t,x) - D\partial_{xx} a(t,x) - \varphi(t,x)a(t,x) = f(t,x) \tag{4.7}$$

with coefficient function

$$\varphi(t,x) = \delta(\kappa_B, \kappa_P, \kappa_P, \kappa_B) \begin{pmatrix} u^1 \\ u^2 \\ u^3 \\ u^4 \end{pmatrix} \geq 0$$

and right hand side

$$f(t,x) = \delta(\kappa_B a_B, \kappa_P a_P, \kappa_P a_P, \kappa_B a_B) \begin{pmatrix} u^1 \\ u^2 \\ u^3 \\ u^4 \end{pmatrix} \geq 0.$$

This problem is given on

$$Q_T = \{(t,x) \mid 0 < t < T,\ l(t) < x < r(t)\}$$

and equipped with boundary conditions

$$D\partial_x a(t,l(t)) + \dot{l}(t)a(t,l(t)) = 0 \tag{4.8}$$
$$D\partial_x a(t,r(t)) + \dot{r}(t)a(t,r(t)) = 0 \tag{4.9}$$

and initial conditions

$$a(0,\cdot) =: a_0 : [0,L] \to [0,\infty). \tag{4.10}$$

We will now derive a priori estimates for the solution a of the parabolic equation (4.7) in the closure of the space-time domain Q_T. In chapter 3 we already showed in lemma 3.3 the boundedness of the solution a by

$$a_B \leq a(t,x) \leq a_p. \tag{4.11}$$

Using the notation introduced in appendix A.1 we can cite theorem 4.31 from [19].

Proposition 4.1. *Let $\beta \in (0,1)$ and $l, r : [0,T] \to \mathbb{R}$ of class $C^{1+\frac{1+\beta}{2}}$ be given such that $l(t) < r(t)$ for each $t \in [0,T]$. Assume*

$$D + \max\left\{ \|\dot{l}\|_{C^{\frac{1+\beta}{2}}}, \|\dot{r}\|_{C^{\frac{1+\beta}{2}}} \right\} \leq DB_1, \tag{4.12}$$

for some constant B_1 and

$$\varphi,\ f \in C^{0+\beta,P}(\overline{Q_T}).$$

Then, there exists a constant C, depending only on

$$D, B_1, \|\varphi\|_{C^{0+\beta,P}}, \beta,\ \text{and } Q_T = \{(t,x) \mid 0 < t < T, l(t) < x < r(t)\}$$

such that for each solution $a \in C^{2+\beta,P}(\overline{Q_T})$ of (4.7), (4.8), (4.9) on Q_T with initial conditions

$$a_0 \in C^{2+\beta}([0,L];[0,\infty))$$

satisfying the compatibility conditions 2.3.2 we have:

$$\|a\|_{C^{2+\beta,P}} \leq C\left(\|a\|_{C^0} + \|f\|_{C^{0+\beta,P}} + \|a_0\|_{C^{2+\beta}}\right). \tag{4.13}$$

Proof. We slightly adapt the proof from [19] by making some notes on the changed hypotheses.

(I) We have to note that the coefficients $\dot{l}$ and $\dot{r}$ in the boundary conditions (4.8) and (4.9), respectively, are given on the respective boundary and may be extended to all of $[0,T]\times\mathbb{R}$ by just letting them be independent of x and find that for these extended velocities v_l, v_r we have:

$$\|v_l\|_{C^{1+\beta,P}} = \sup_{0\le t\le T}|\dot{l}(t)| + H\ddot{o}l_{\frac{1+\beta}{2}}(\dot{l}) \tag{4.14}$$

$$\|v_r\|_{C^{1+\beta,P}} = \sup_{0\le t\le T}|\dot{r}(t)| + H\ddot{o}l_{\frac{1+\beta}{2}}(\dot{r}). \tag{4.15}$$

(II) We note that our domain is not degenerate since in fact, $r(t)-l(t)$ remains bounded away from zero by continuity.

The parabolic boundary of our domain is not differentiable at the corner points $(0,0)$ and $(0,L)$. This is repaired by the compatibility conditions for the initial and boundary condtitions at these points (cf. theorem 5.3 in chapter IV of [16]).

In [19], it is required that the parabolic boundary is of class $C^{2+\beta}$ which in our case translates into $\mathcal{B}Q_T$ belonging to some hyperplane $\{(t,x)\mid t=t_0\}$ and $\mathcal{L}Q_T$ being locally the graph of some function of class $C^{2+\beta,P}$ so that Q_T locally lies on one side of that graph. The former condition is clearly true as $\mathcal{B}Q_T=\{0\}\times(0,L)$.

The latter reduces in one space dimension into the lateral boundary curves r and l being continuously differentiable with derivatives $\dot{r}$ and $\dot{l}$ being HÖLDER continuous with exponent $\frac{\beta}{2}$. Here, we recall that $\|\cdot\|_{C^{2+\beta,P}}$ is defined by (A.16), and in our one dimensional case only the temporal derivatives matter. Using now

$$H\ddot{o}l_{P,\beta}(f)=\sup_{t,s}\frac{|f(t)-f(s)|}{\sqrt{|t-s|}^{\beta}}$$

for functions only depending on time, we arrive at the exponent $\frac{\beta}{2}$. This regularity is encoded in the hypothesis $l,r\in C^{1+\frac{1+\beta}{2}}\subset C^{1+\frac{\beta}{2}}$.

(III) The conditions on the coefficient function φ and the right hand side f are explicitely stated, and the leading order coefficient is just the constant diffusion coefficient D.

(IV) The transversality assumption on the boundary condition in our one dimensional case reduces to the simple condition $D>0$ together with the lateral boundary curves being nowhere horizontal which is granted by the boundedness of the boundary velocities (cf. point (II)).

□

Remark 4.2. *(i) The requirement of the boundary velocities $\dot{r}$ and $\dot{l}$ being continuous cannot be relaxed if we wish the monomer density to be continuously differentiable up to the boundary. To see that, assume that, say, $\dot{r}$ jumps at $t=t_0$ from v_r^- to v_r^+. Then, the boundary curve r is still* LIPSCHITZ *at this point but a continuously differentiable solution a had to satisfy*

$$(D\partial_x+v_r^-)a(t_0,r(t_0)) = \lim_{t\nearrow t_0}\lim_{\Sigma_t\ni x\to r(t)}(D\partial_x+\dot{r}(t))a(t,x)=\dots$$

$$\dots=\lim_{t\searrow t_0}\lim_{\Sigma_t\ni x\to r(t)}(D\partial_x+\dot{r}(t))a(t,x) = (D\partial_x+v_r^+)a(t_0,r(t_0))$$

which contradicts the jump $v_r^- \neq v_r^+$. Thus, the above reasoning does not work in case of a switch of the boundary velocity.

(ii) The compatibility conditions for the initial and boundary conditions are particularly simple since the right hand side of the boundary conditions vanishes.

For completeness, we give a second theorem, corresponding to theorem 4.30 in [19], that states a similar estimate for $C^{1+\beta,P}$-solutions under weaker conditions on the boundary curves.

Proposition 4.3. *Let $\beta \in (0,1)$ and $l, r : [0,T] \to \mathbb{R}$ of class $C^{1+\frac{\beta}{2}}$ be given such that $l(t) < r(t)$ for each $t \in [0,T]$. Assume $\varphi, f \in M_{1,2+\beta}$ with*

$$\|\varphi\|_{M_{1,2+\beta}} \leq C_1.$$

Assume further

$$D + \max\left\{ \|\dot{l}\|_{C^{0+\frac{\beta}{2}}},\ \|\dot{l}\|_{C^{0+\frac{\beta}{2}}} \right\} \leq DB_1 \tag{4.16}$$

for some $B_1 > 0$. Then, there exists a constant C, depending only on

$$D, B_1, C_1, \beta, \text{ and } Q_T = \{(t,x) \mid 0 < t < T, l(t) < x < r(t)\}$$

such that for each solution $a \in C^{1+\beta,P}\left(\overline{Q_T}\right)$ of (4.7), (4.8), (4.9) on Q_T with initial conditions

$$a_0 : [0,L] \to [0,\infty)$$

satisfying the compatibility conditions 2.3.2 we have:

$$\|a\|_{C^{1+\beta,P}} \leq C\left(\|a\|_{C^0} + \|\varphi\|_{M^{1,2+\beta}} + \|a_0\|_{C^{1+\beta}}\right). \tag{4.17}$$

Note that in the previous proposition, the norm $\|a\|_{C^0}$ is bounded from above by a_P for our particular problem. In particular, the right hand side of the given estimate does not contain any dependence on the solution a at all.

Finally, we use adapted versions of theorems 5.18 and 5.19 from [19] to deduce existence and uniqueness of solutions to the parabolic problem under different assumptions on the coefficient functions, the right hand side, and the boundary velocities.

Theorem 4.4. *(cf. thm. 5.19 in [19]) Let $\beta, \gamma \in (0,1)$, let*

$$l, r \in C^{1+\frac{\beta}{2}}([0,T])$$

be given, assume $l(t) < r(t)$ for each $t \in [0,T]$, set

$$Q_T = \{(t,x) \mid 0 < t < T, l(t) < x < r(t)\}.$$

Assume

$$\varphi \in C^{0+\gamma,P}\left(\overline{Q_T}\right) \qquad \text{and} \qquad f \in C^{0+\gamma,P}_{(1-\beta)}(Q_T),$$

and let finally the initial conditions

$$a_0 \in C^{1+\beta}([0,L])$$

satisfy the compatibility conditions 2.3.2.

Then, the problem

$$\begin{aligned}
(\partial_t - D\partial_{xx} - \varphi(t,x))a(t,x) &= f(t,x) && \text{in } Q_T,\\
(D\partial_x + \dot{l}(t))a(t,l(t)) &= 0 && \text{for } 0<t<T,\\
(D\partial_x + \dot{r}(t))a(t,r(t)) &= 0 && \text{for } 0<t<T,\\
a(0,x) &= a_0(x) && \text{for } 0<x<L
\end{aligned}$$

has a unique solution a, this solution belongs to $C^{2+\gamma}_{(-1-\beta)}(Q_T)$ *and satisfies*

$$|a|^{(-1-\beta)}_{2+\gamma} \leq C\ \left(|f|^{(1-\beta)}_{0+\gamma} + \|a_0\|_{C^{1+\beta}}\right) \tag{4.18}$$

where C is a constant depending only on

$$D,\ \max\left\{\|l\|_{C^{1+\frac{\beta}{2}}},\ \|r\|_{C^{1+\frac{\beta}{2}}}\right\},\ \gamma,\ \beta,\ \text{and } T.$$

Proof. We only have to explain why the hypotheses of theorem 5.19 in [19] are satisfied.

(I) The assumption on $\mathcal{P}Q_T$ relies on the boundary curves being of class $C^{1+\frac{\beta}{2}}$ which is stronger than $C^{0+\frac{1+\beta}{2}}$. The uniform transversality of the boundary gradient operator $D\partial_x$ to the lateral boundary $\mathcal{L}Q_T$ follows as well, since the boundary velocities are necessarily bounded. More precisely, the transversality in one space dimension simply reduces to the condition that

$$D^2 + \left(\dot{l}(t)\right)^2 \qquad \left(\text{resp. } D^2 + \left(\dot{r}(t)\right)^2\right)$$

is bounded away from zero and bounded from above. This boundedness and the HÖLDER continuity of the boundary velocities also lead to the estimate for the coefficients of the boundary operator from above.

(II) The conditions on the coefficient functions and the right hand side of the parabolic equation are explicitely stated. The same is true for the initial conditions and in particular for the compatibility conditions at the corner points.

□

For better readability we explicitely write out the relevant norms in the hypothesis and the assertion of the theorem and make some remarks on the requirements that arise for the solution u of the hyperbolic part.

The boundary velocities shall be HÖLDER continuous of exponent $\frac{\beta}{2}$. We note that at least the boundedness of these velocities which is crucial for the behavior of the boundary operator

$$D\partial_x + v\cdot$$

has already been established in section 3.1. There we found that the velocities are bounded by v_{max} which only depends on the reaction parameters and the retrograde flow velocity v_R.

For the coefficient function $\varphi = cu$ we only require uniform parabolic HÖLDER continuity of exponent γ which is readily implied by LIPSCHITZ continuity of u.

The right hand side $f = \tilde{c}u$ is assumed to belong to the weighted HÖLDER space $C^{0+\gamma}_{(1-\beta)}(Q_T)$. Noting that

$$1 - \beta + \gamma > 0$$

we can in fact also assume the right hand side to belong to the smaller space $C^{0+\gamma}(\overline{Q_T})$. Again, the LIPSCHITZ continuity of the end densities u is sufficient to guarantee the global HÖLDER continuity of f to any exponent.

The assertion that the solution a belongs to $C^{2+\gamma}_{(-1-\beta)}$ implies the estimate

$$\|\partial_x a\|_{C^0} \leq (\operatorname{diam} Q_T)^\gamma C \left(|f|^{(1-\beta)}_{0+\gamma} + \|a_0\|_{C^{1+\beta}} \right). \tag{4.19}$$

The previous theorem requires quite mild assumptions on the functions involved. However, the assertion is not sufficient to expect sufficiently smooth boundary velocities since the Hölder continuity of $\partial_t a$ and $\partial_x a$ at the boundary is only granted up to rescaling the space-time by the parabolic distance to the boundary. This drawback is overcome by the following theorem that in turn requires stronger assumptions on the boundary curves and the coefficient functions.

Theorem 4.5. *(cf. thm. 5.18 in [19]) Let $\beta \in (0,1)$ and*

$$r, l \in C^{1+\frac{1+\beta}{2}}([0,T])$$

be given such that $l(t) < r(t)$ for each $t \in [0,T]$. Let furthermore

$$\varphi,\ f \in C^{0+\beta,P}\left(\overline{Q_T}\right),$$

and let the initial data

$$a_0 \in C^{2+\beta}([0,L])$$

satisfy the compatibility conditions 2.3.2.

Then, there exists a unique solution $a \in C^{2+\beta,P}\left(\overline{Q_T}\right)$ to the problem

$$\begin{aligned}
(\partial_t - D\partial_{xx} - \varphi(t,x))a(t,x) &= f(t,x) && \text{in } Q_T, \\
(D\partial_x + \dot{l}(t))a(t,l(t)) &= 0 && \text{for } 0 < t < T, \\
(D\partial_x + \dot{r}(t))a(t,r(t)) &= 0 && \text{for } 0 < t < T, \\
a(0,x) &= a_0(x) && \text{for } 0 < x < L,
\end{aligned}$$

and there exists a constant $C > 0$ depending only on

$$l,\ r,\ D,\ \beta,\ \text{and } \|\varphi\|_{0+\beta,P}$$

such that

$$\|a\|_{C^{2+\beta,P}} \leq C\left(\|f\|_{C^{0+\beta,P}} + \|a_0\|_{C^{2+\beta}}\right). \tag{4.20}$$

Proof. Again, most of the hypotheses of theorem 5.18 in [19] are trivially fulfilled. The interesting ones are again those on the (lateral) boundary and the boundary conditions. These follow again as in the proof of proposition 4.1. □

4.1.2 Existence and uniqueness of the boundary curves

We now turn our attention to the regularity of the boundary velocities once the solution a to the monomer equation is assumed to be given and of certain regularity. To this end, we note that the end velocities are affine functions of the monomer density.

For the following calculations we will still use constant coefficients but not without noting that sufficiently small and smooth variations only change the constants in the results. We also still assume to be in the strictly hyperbolic case so that the boundary curves are given by

$$l : [0,T] \to \mathbb{R}, \qquad \dot{l}(t) = \lambda^1(a(t,l(t))) \quad \text{for } t \in (0,T), \qquad l(0) = 0 \tag{4.21}$$

$$r : [0,T] \to \mathbb{R}, \qquad \dot{r}(t) = \lambda^4(a(t,r(t))) \quad \text{for } t \in (0,T), \qquad r(0) = L. \tag{4.22}$$

Assuming the monomer density a to be prescribed we can prove the following basic lemma.

Lemma 4.6. *Assume the monomer density a to be given on all of*

$$\overline{E_T^+} := [0,T] \times \mathbb{R}$$

and of class $C^{2+\beta,P}$. Then, any function $g : [0,T] \to \mathbb{R}$ given by

$$\begin{aligned} \dot{g}(t) &= c_1 a(t, g(t)) + c_2 \\ g(0) &= x_0 \end{aligned}$$

is of class $C^{2+\frac{\beta}{2}}([0,T])$.

Proof. Let us denote by A the parabolic HÖLDER norm of the given monomer density a:

$$A := \|a\|_{C^{2+\beta,P}}.$$

Let us further denote by M the following upper bound for the absolute velocity:

$$M := |c_1| \|a\|_{C^0} + |c_2|.$$

Clearly, $\dot{g}$ is continuous since a is differentiable with bounded derivatives and therefore globally LIPSCHITZ continuous. As a preliminary estimate we readily deduce

$$\begin{aligned} |g(t) - g(s)| &\leq \|\dot{g}\|_{C^0} |t - s| \\ &\leq M|t - s|. \end{aligned}$$

Moreover,

$$\ddot{g} = c_1(\partial_t a + \dot{g}\partial_x a) = c_1(\partial_t a + (c_1 a + c_2)\partial_x a)$$

is continuous as well and moreover satisfies the following estimate for any $t, s \in [0,T]$:

$$\begin{aligned} \frac{|\ddot{g}(t) - \ddot{g}(s)|}{|c_1|} \leq\ & |\partial_t a(t, g(t)) - \partial_t a(s, g(s))| + M|\partial_x a(t, g(t)) - \partial_x a(s, g(s))| \\ & + |c_1| \|\partial_x\|_{C^0} |a(t, g(t)) - a(s, g(s))| \end{aligned}$$

$$
\begin{aligned}
&\leq H\ddot{o}l_{P,\beta}(\partial_t a)|(t,g(t))-(s,g(s))|_P^\beta \\
&\quad +M\left(\|\partial_{xx}a\|_{C^0}|g(t)-g(s)|+H\ddot{o}l_{t,\frac{1+\beta}{2}}(\partial_x a)|t-s|^{\frac{1+\beta}{2}}\right) \\
&\quad +|c_1|A\left(\|\partial_t a\|_{C^0}|t-s|+\|\partial_x a\|_{C^0}|g(t)-g(s)|\right) \\
&\leq A\max\left\{|t-s|^{\frac{\beta}{2}},M|t-s|\right\}+A\ M\left(M|t-s|+|t-s|^{\frac{1+\beta}{2}}\right) \\
&\quad +|c_1|A^2\left(|t-s|+M|t-s|\right) \\
&\leq C\left(|t-s|+|t-s|^{\frac{1+\beta}{2}}+|t-s|^{\frac{\beta}{2}}\right).
\end{aligned}
$$

Since we deal with a bounded time interval $[0,T]$ we can by appropriately adjusting the constant C conclude the HÖLDER continuity of $\ddot{g}$ to the exponent $\frac{\beta}{2}$:

$$
|\ddot{g}(t)-\ddot{g}(s)|\leq C|t-s|^{\frac{\beta}{2}} \qquad \text{for any } t,s\in[0,T] \tag{4.23}
$$

which is the asserted regularity. □

If we assume weaker regularity for the monomer density, we still find sufficiently strong regularity for the boundary curves as is shown in the following corollary.

Corollary 4.7. *Given bounded*

$$
a\in C^1\left(\overline{E_T^+}\right)
$$

with bounded derivatives, any curve g being defined as in lemma 4.6 is continuously differentiable with LIPSCHITZ *continuous first derivative and thus belongs to $C^{1+1}([0,T])$.*

Proof. The proof relies on a short version of the calculations in the proof of lemma 4.6. Using now

$$
A:=\|a\|_{C^1} \qquad \text{and} \qquad M:=|c_1|\|a\|_{C^0}+|c_2|
$$

we calculate for the derivative $\dot{g}$:

$$
\begin{aligned}
\frac{|\dot{g}(t)-\dot{g}(s)|}{|c_1|} &\leq \|\partial_t a\|_{C^0}|t-s|+\|\partial_x a\|_{C^0}|g(t)-g(s)| \\
&\leq A(1+M)|t-s|
\end{aligned}
$$

and the LIPSCHITZ constant for $\dot{g}$ is therefore bounded from above by, say $M(1+M)$. □

4.1.3 Existence and uniqueness for the hyperbolic part

We assume now to be given a sufficiently smooth monomer density A and want to consider the problem

$$
\partial_t u+\partial_x\left(\Lambda(A)u\right)=0 \tag{4.24}
$$

where according to the notation introduced in chapter 2, $u=(u^1,\ldots,u^4)^T$ is the vector of end densities and Λ is the diagonal velocity matrix. The velocities now only depend on t and x indirectly via the given monomer density A since we deal with the constant coefficient case.

We observe that system (4.24) consists of four mutually decoupled, linear hyperbolic equations, and we thus can treat each of the equations separately. The velocities λ^α depend affinely on the given function A and therefore inherit its regularity.

The boundary conditions pose no problems at all. In fact, we have to distinguish two cases for the α^{th} equation at any given boundary point (t, x):

1. The velocity of the right (respectively left) boundary is larger (respectively smaller) than the characteristic velocity $\lambda^\alpha(t, x)$. In that case the characteristic curves enter the domain and the boundary values are put to zero.
2. The boundary velocity equals the characteristic velocity. Then we deal with a characteristic boundary and as we assume the initial conditions to be zero at the initial boundary points the value of the solution at such a point will be zero as well.

We can thus simply consider the CAUCHY problem in

$$E_T^+ := (0, T) \times \mathbb{R}$$

for each of the hyperbolic equations where we just extend the initial conditions by zero and the coefficient functions λ^α by smooth continuation in space. The precise form of this continuation does not matter as the solution u^α vanishes throughout $E_T^+ \backslash \overline{Q_T}$. In particular, for any continuously differentiable extension $\bar{A}$ of the monomer density A we can calculate as spatial derivatives from inside Q_T:

$$\begin{aligned}\lim_{Q_T \ni (t,x) \to (t_0,x_0) \in \mathcal{L}Q_T} \partial_x (u(t,x)\bar{A}(t,x)) &= \lim_{Q_T \ni (t,x) \to (t_0,x_0) \in \mathcal{L}Q_T} A(t,x)\partial_x u(x) \\ &\quad + \lim_{Q_T \ni (t,x) \to (t_0,x_0) \in \mathcal{L}Q_T} \partial_x A(t,x) u(t,x) \\ &= A(t_0,x_0)0 + 0\partial_x A(t_0,x_0) = 0,\end{aligned}$$

where we used the assumption

$$A \in C^{1_x,0_t}(\overline{Q_T}).$$

Coming from outside the domain Q_T, the product $\bar{A}u$ vanishes identically and thus the spatial derivative of $\bar{A}u$ is continuous across $\mathcal{L}Q_T$.

In the following discussion we will often follow the ideas from [18] where hyperbolic systems are considered. Here, due to the decoupling of our system we can deal with scalar equations. We thus introduce the following transport form of our equations:

$$\partial_t u^\alpha(t,x) + \lambda^\alpha(t,x)\partial_x u^\alpha(t,x) = -\partial_x \lambda^\alpha(t,x) u^\alpha(t,x) =: \mu^\alpha\left(t, x, u^\alpha(t,x)\right) \tag{4.25}$$

which will be equipped with initial conditions

$$u^\alpha(0,x) = u_0^\alpha(x) \tag{4.26}$$

with $u_0^\alpha \in C^1(\mathbb{R})$ having support in $[0, L]$. Let us define

$$M_0^\alpha := \|u_0^\alpha\|_{C^0(\mathbb{R})} \equiv \sup_{x \in \mathbb{R}} |u_0^\alpha(x)| \tag{4.27}$$

$$M_1^\alpha := \left\| \frac{d}{dx} u_0^\alpha \right\|_{C^0(\mathbb{R})}. \tag{4.28}$$

We recall the equation for the characteristic curve $(t, y^\alpha(t;\xi))$ emerging from the point $(0,\xi)$ to be

$$\frac{d}{dt}y^\alpha(t;\xi) = \lambda^\alpha(t, y^\alpha(t;\xi)). \tag{4.29}$$

Assuming the coefficient function λ^α to be continuously differentiable with respect to the space variable with

$$\|\lambda^\alpha\|_{C^{1_x,0_t}(\overline{Q_T})} \equiv \sup_{(t,x)\in\overline{Q_T}} (|\lambda^\alpha(t,x)| + |\partial_x\lambda^\alpha(t,x)|) = M_2^\alpha < \infty \tag{4.30}$$

we conclude that the characteristic curve passing through any point $(t,x) \in Q_T$ is a uniquely determined differentiable curve and thus to each point (t,x) we find a unique point $\xi^\alpha(t,x)$ such that

$$y^\alpha(t;\xi^\alpha(t,x)) = x.$$

More pictorally, $(0,\xi^\alpha(t,x))$ is the point on the x-axis from which the α^{th} characteristic curve passing through (t,x) emerges.

Proposition 4.8. *Assume*

$$A \in C^{2_x,1_t}([0,\infty)\times\mathbb{R})$$

to be bounded with bounded derivative $\partial_x A$.

Then the CAUCHY *problem for equation (4.24) with compactly supported continuously differentiable initial data has a unique solution which is continuously differentiable in all of $[0,\infty)\times\mathbb{R}$. The components u^α of this solution can be explicitely written as*

$$u^\alpha(t,x) = u^\alpha(0,\xi^\alpha(t,x)) \exp\left[-\int_0^t \partial_x\lambda^\alpha\left(\tau, y^\alpha(\tau;\xi^\alpha(t,x))\right)d\tau\right] =: (S^\alpha u^\alpha)(t,x). \tag{4.31}$$

Proof. The elementary proof of this proposition can be found in various standard textbooks. We refer to [23] where this particular form can be found as theorem 6.3. We only note that the velocity matrix is diagonal and has the same regularity and boundedness properties as A. In particular, the crucial LIPSCHITZ continuity with respect to the spatial variable follows directly from the boundedness of the first spatial derivative. □

Note that from the representation formula (4.31) in proposition 4.8 we immediately deduce that the solution remains non-negative whenever the initial data are, which we clearly assume since we deal with physical densities.

4.1.4 A priori estimates for the hyperbolic equations

Let us now derive some a priori estimates for the solutions u^α to the equations (4.25). We start with an estimate for the characteristic curves. Given any two points (t,x) and (t,y) in E_∞^+ with the same time we find for the distance of the points where the characteristic curves through these points emerge:

$$|\xi^\alpha(t,x) - \xi^\alpha(t,y)| \le |x-y| \exp\left[\|\partial_x\lambda^\alpha\|_{C^0\left(\overline{E_t^+}\right)} t\right] \tag{4.32}$$

which follows by applying GRÖNWALL's inequality to the evolution of the characteristic curves emerging in neighboring points. More precisely, let

$$d(\tau) := y^\alpha(\tau; \xi^\alpha(t,x)) - y^\alpha(\tau; \xi^\alpha(t,y))$$

denote the distance between the characteristics passing through (t,x) and (t,y) measured at time τ. Then, the evolution of this distance is given by

$$\dot{d}(\tau) = \lambda^\alpha(\tau, y^\alpha(\tau; \xi^\alpha(t,x))) - \lambda^\alpha(y^\alpha(\tau; \xi^\alpha(t,y))),$$

and this derivative is bounded by

$$|\dot{d}(\tau)| \;\leq\; \|\partial_x \lambda^\alpha\|_{C^0\left(\overline{E_t^+}\right)} \; |y^\alpha(\tau; \xi^\alpha(t,x)) - y^\alpha(\tau; \xi^\alpha(t,y))| \;\leq\; \|\partial_x \lambda^\alpha\|_{C^0\left(\overline{E_t^+}\right)} \; |d(\tau)|.$$

This is now the equation to which GRÖNWALL'S inequality in differential form can be applied with integration backward in time from t to 0.

We use this result to estimate the spatial LIPSCHITZ constant for the solution u^α at time t and thus an upper bound for the spatial derivative of the C^1-function u^α. Before deriving this bound we first calculate the supremum norm of u^α over temporally bounded strips E_T^+. This is achieved by estimating the representation (4.31) for the solution of (4.25):

$$\begin{aligned} u^\alpha(t,x) &= u_0^\alpha(\xi^\alpha(t,x)) \exp\left[-\int_0^t \partial_x \lambda^\alpha\left(\tau, y^\alpha(\tau; \xi^\alpha(t,x))\right) d\tau\right] \\ &\leq \|u_0^\alpha\|_{C^0} \exp\left[t \sup_{(\tau,z)\in E_t^+} |\partial_x \lambda^\alpha(\tau, z)|\right]. \end{aligned}$$

We thus find:

$$\|u^\alpha\|_{C^0(\overline{E_T^+})} \leq \exp\left[T \|\partial_x \lambda^\alpha\|_{C^0(\overline{E_T^+})}\right] M_0^\alpha. \tag{4.33}$$

In order to estimate the spatial derivative we calculate for any $t \in (0,T]$ and $x,\ y \in \mathbb{R}$:

$$\begin{aligned} |u^\alpha(t,x) - u^\alpha(t,y)| &= \Bigg| u_0^\alpha(\xi^\alpha(t,x)) \exp\left[-\int_0^t \partial_x \lambda^\alpha\left(\tau, y^\alpha(\tau; \xi^\alpha(t,x))\right) d\tau\right] \\ &\qquad - u_0^\alpha(\xi^\alpha(t,y)) \exp\left[-\int_0^t \partial_x \lambda^\alpha\left(\tau, y^\alpha(\tau; \xi^\alpha(t,y))\right) d\tau\right]\Bigg| \\ &\leq |u_0^\alpha(\xi^\alpha(t,x)) - u_0^\alpha(\xi^\alpha(t,y))| \exp\left[t \sup_{(\tau,z)\in E_t^+} |\partial_x \lambda^\alpha(\tau, z)|\right] \\ &\quad + |u_0^\alpha(\xi^\alpha(t,y))| \Bigg| \exp\left[-\int_0^t \partial_x \lambda^\alpha\left(\tau, y^\alpha(\tau; \xi^\alpha(t,x))\right) d\tau\right] \\ &\qquad - \exp\left[-\int_0^t \partial_x \lambda^\alpha\left(\tau, y^\alpha(\tau; \xi^\alpha(t,y))\right) d\tau\right]\Bigg|. \end{aligned}$$

For the last term we use the basic inequality

$$|\mathrm{e}^r - \mathrm{e}^s| \leq \mathrm{e}^r |\mathrm{e}^0 - \mathrm{e}^{s-r}| \leq \mathrm{e}^r \mathrm{e}^{|r-s|} |r-s|$$

which is true for arbitrary real numbers r and s and find

$$\begin{aligned}|u^\alpha(t,x)-u^\alpha(t,y)| \quad \leq \quad & \mathrm{Lip}[u_0^\alpha]\ |x-y| \exp\left[2t\|\partial_x\lambda^\alpha\|_{C^0}|\right] \\ & + \|u_0^\alpha\|_{C^0} \exp\left[3t\|\partial_x\lambda^\alpha\|_{C^0}|\right] \times \\ & \times \int_0^t |\partial_x\lambda^\alpha\left(\tau, y^\alpha(\tau;\xi^\alpha(t,x))\right) - \partial_x\lambda^\alpha\left(\tau, y^\alpha(\tau;\xi^\alpha(t,y))\right)|d\tau.\end{aligned}$$

The integral in the last line is bounded by

$$\int_0^t \|\partial_{xx}\lambda^\alpha\|_{C^0}|x-y| \exp\left[\|\partial_x\lambda^\alpha\|_{C^0}\tau\right]d\tau \ \leq \|\partial_{xx}\lambda^\alpha\|_{C^0}|x-y|t\exp\left[t\|\partial_x\lambda^\alpha\|_{C^0}\right] \quad (4.34)$$

We note that the norm $\|\partial_x\lambda^\alpha\|_{C^0}$ may be assumed to be positive since otherwise all the integrals would vanish and the whole equation for u^α would degenerate to a transport equation with constant velocity field.

Putting the estimates together we obtain

$$\begin{aligned}&|u^\alpha(t,x)-u^\alpha(t,y)| \\ \leq\ & \left(\mathrm{Lip}[u_0^\alpha] + \|u_0^\alpha\|_{C^0}\|\partial_{xx}\lambda^\alpha\|_{C^0}\exp[2t\|\partial_x\lambda^\alpha\|_{C^0}]t\right)\ \exp\left[2t\|\partial_x\lambda^\alpha\|_{C^0}\right]\ |x-y|.\end{aligned}$$

We thus find as an upper bound for the spatial LIPSCHITZ constant and thus the partial derivative of u^α in E_T^+ with respect to space:

$$|\partial_x u^\alpha(t,x)| \leq \left(M_1^\alpha + M_0^\alpha\|\partial_{xx}\lambda^\alpha\|_{C^0}\exp[2T\|\partial_x\lambda^\alpha\|_{C^0}]T\right)\ \exp\left[2T\|\partial_x\lambda^\alpha\|_{C^0}\right]. \quad (4.35)$$

Let us now deduce a bound for the partial derivative u^α with respect to time. This will be used to write down a simple form for the C^1-norm of u^α. To obtain the LIPSCHITZ bound with respect to time we consider two points (t,x) and (s,x) and estimate the difference

$$|u(t,x)-u(s,x)|.$$

For notational convenience, we assume without loss of generality $s<t$. From the point (s,x) we follow the α^{th} characteristic curve until time t where we end up at some point (t,y), and in general y will be different from x. However, we know that x and y are close by one another if s and t are close enough:

$$|x-y| \leq \|\lambda^\alpha\|_{C^0\left(\overline{E_t^+}\right)}(t-s).$$

Then, we use the triangle inequality to compute

$$\begin{aligned}|u^\alpha(t,x)-u^\alpha(s,x)| \ &\leq\ |u^\alpha(t,x)-u^\alpha(t,y)| + |u^\alpha(t,y)-u^\alpha(s,x)| \\ &\leq\ \left(\mathrm{Lip}[u_0^\alpha] + \|u_0^\alpha\|_{C^0}\|\partial_{xx}\lambda^\alpha\|_{C^0}\exp[2t\|\partial_x\lambda^\alpha\|_{C^0}]t\right)\exp\left[2t\|\partial_x\lambda^\alpha\|_{C^0}\right]\ |x-y| \\ &\quad + u^\alpha(s,x)\left|\exp\left[-\int_s^t \partial_x\lambda^\alpha(\tau, y^\alpha\left(\tau;\xi^\alpha(s,x)\right))d\tau\right] - 1\right|.\end{aligned}$$

In order to estimate the second term on the right hand side we note that for $\zeta\in\mathbb{R}$ the exponential satisfies

$$|\mathrm{e}^\zeta - 1| = |\zeta|e^{\theta\zeta} \leq |\zeta|e^{|\zeta|}$$

for some $\theta \in [0,1]$ which in our case implies

$$\left|\exp\left[-\int_s^t \partial_x\lambda^\alpha(\tau, y^\alpha(\tau;\xi^\alpha(s,x)))d\tau\right]-1\right| \leq (t-s)\|\partial_x\lambda^\alpha\|_{C^0}\exp\left[(t-s)\|\partial_x\lambda^\alpha\|_{C^0}\right]. \tag{4.36}$$

We obtain

$$\begin{aligned}
&|u^\alpha(t,x)-u^\alpha(s,x)| \\
&\leq \left((\mathrm{Lip}[u_0^\alpha]+\|u_0^\alpha\|_{C^0}\|\partial_{xx}\lambda^\alpha\|_{C^0}\exp[2t\|\partial_x\lambda^\alpha\|_{C^0}]t)\exp\left[t\|\partial_x\lambda^\alpha\|_{C^0}\right]\|\lambda^\alpha\|_{C^0}\right. \\
&\quad \left.+\|u_0^\alpha\|_{C^0}\|\partial_x\lambda^\alpha\|_{C^0}\right)\ \exp\left[t\|\partial_x\lambda^\alpha\|_{C^0}\right]\ (t-s).
\end{aligned}$$

For arbitrary $0 \leq s,t \leq T$ we finally find

$$\begin{aligned}
&|u^\alpha(t,x)-u^\alpha(s,x)| \\
&\leq \left(\mathrm{Lip}[u_0^\alpha]\|\lambda^\alpha\|_{C^0}+\|u_0^\alpha\|_{C^0}\left(\|\partial_{xx}\lambda^\alpha\|_{C^0}\exp[2T\|\partial_x\lambda^\alpha\|_{C^0}]T\|\lambda^\alpha\|_{C^0}+\|\partial_x\lambda^\alpha\|_{C^0}\right)\right)\times \\
&\quad \times\exp[2T\|\partial_x\lambda^\alpha\|_{C^0}]\ |t-s|.
\end{aligned}$$

Using again the continuous differentiability we thus find as upper bound for the time derivative of the solution u^α in E_T^+:

$$|\partial_t u^\alpha| \leq \left(M_1^\alpha\|\lambda^\alpha\|+M_0^\alpha\left(\|\partial_{xx}\lambda^\alpha\|\|\lambda^\alpha\|\exp[2T\|\partial_x\lambda^\alpha\|]T+\|\partial_x\lambda^\alpha\|\right)\right)\ \exp[2T\|\partial_x\lambda^\alpha\|] \tag{4.37}$$

with $\|\cdot\|$ standing for $\|\cdot\|_{C^0}$.

Adding up the estimates (4.33), (4.35), and (4.37) we find a bound for the C^1-norm of the solution u^α to the CAUCHY problem for equation (4.25) for times $t \in [0,T]$:

$$\begin{aligned}
\|u^\alpha\|_{C^1\left(\overline{E_T^+}\right)} &\leq \exp\left[2T\|\partial_x\lambda^\alpha\|\right]\times \\
&\quad \times\left(M_0^\alpha(1+\|\partial_x\lambda^\alpha\|)+(M_1^\alpha+M_0^\alpha\|\partial_{xx}\lambda^\alpha\|\exp[2T\|\partial_x\lambda^\alpha\|]T)(1+\|\lambda^\alpha\|)\right)
\end{aligned} \tag{4.38}$$

with $\|\cdot\|$ denoting the $C^0(\overline{E_T^+})$-norm.

Returning to the specific equations, we can now as well estimate the norms of the velocity λ and the growth term $\partial_x\lambda$ in terms of the given monomer concentration A and its spatial derivative. We recall that we are in the case of constant reaction coefficients and thus need not consider their derivatives. Assuming the given density A to satisfy $a_B \leq A \leq a_P$ we can estimate (cf. remark 3.2):

$$\max_{\alpha=1,\ldots,4}\|\lambda^\alpha\|_{C^0\left(\overline{E_T^+}\right)} \leq \max\left\{v_R, \delta\kappa_B\left(a_P-a_B\right)-v_R\right\} =: v_{max} \tag{4.39}$$

and likewise

$$\begin{aligned}
\max_{\alpha=1,\ldots,4}\|\partial_x\lambda^\alpha\|_{C^0\left(\overline{E_T^+}\right)} &\leq \delta\kappa_B\|\partial_x A\|_{C^0\left(\overline{E_T^+}\right)}\ , \\
\max_{\alpha=1,\ldots,4}\|\partial_{xx}\lambda^\alpha\|_{C^0\left(\overline{E_T^+}\right)} &\leq \delta\kappa_B\|\partial_{xx}A\|_{C^0\left(\overline{E_T^+}\right)}
\end{aligned}$$

and note that the first of these bounds (4.39) is completely independent of the function A and only depends on the parameter values.

Introducing furthermore the abbreviation

$$\mathcal{E}_0(t) := \exp[\delta\kappa_B t \|\partial_x A\|_{C^0}]$$

the resulting estimates for the solution u and its derivatives now read:

$$\|u\|_{C^0} \leq \mathcal{E}_0(T)M_0 \tag{4.40}$$

$$\|\partial_x u\|_{C^0} \leq \mathcal{E}_0(2T)(M_1 + M_0\delta\kappa_B\|\partial_{xx}A\|\mathcal{E}_0(2T)T) \tag{4.41}$$

$$\|\partial_t u\|_{C^0} \leq \mathcal{E}_0(2T)\left(M_1 v_{max} + \delta\kappa_B M_0\left(T\|\partial_{xx}A\|\mathcal{E}_0(2T)v_{max} + \|\partial_x A\|\right)\right) \tag{4.42}$$

and finally for the full C^1-norm:

$$\|u\|_{C^1} \leq \left(M_0(1+\delta\kappa_B\|\partial_x A\|) + (M_1 + M_0\delta\kappa_B\|\partial_{xx}A\|T\mathcal{E}_0(2T))(1+v_{max})\right)\mathcal{E}_0(2T). \tag{4.43}$$

In all of the equations (4.40) - (4.43), the norm used on $\mathbb{R}^4$ can be taken to be the maximum norm

$$|u|_\infty = \max_{\alpha=1,\ldots,4} |u^\alpha|$$

(corresponding to the estimates on the single components u^α) or the sum norm

$$|u|_1 = |u^1| + \cdots + |u^4|.$$

The constants M_0 and M_1 are then taken to be

$$M_0 = \max_{\alpha=1,\ldots,4} M_0^\alpha, \qquad M_1 = \max_{\alpha=1,\ldots,4} M_1^\alpha$$

or

$$M_0 = \sum_{\alpha=1}^{4} M_0^\alpha, \qquad M_1 = \sum_{\alpha=1}^{4} M_1^\alpha,$$

respectively.

4.1.5 Existence and uniqueness for the parabolic free boundary problem

Trying to put pieces together we summarize the results obtained so far.

1. The monomer density a is bounded between a_B and a_P whenever it is of class $C^{2_x,1_t}$ and if its initial conditions respect this bound (cf. lemma 3.3).

2. The boundary velocities $\dot{l}$ and $\dot{r}$ are bounded between $-v_{max}$ and v_{max} whenever the monomer density obeys the bound from point 1 (cf. remark 3.2).

3. For $\beta \in (0,1)$, given boundary curves of class $C^{1+\frac{1+\beta}{2}}$, end densities U of class $C^{0+\beta,P}$ and initial conditions $a(0,\cdot) \in C^{2+\beta}$, we obtain a solution a for the parabolic boundary value problem which is of class $C^{2+\beta,P}$ (cf. theorem 4.5).

4. If the monomer density is of class C^1, then the resulting boundary curves are of class $C^{1+1}([0,T])$ (cf. corollary 4.7).

5. Given a prescribed monomer distribution A of class $C^{2_x,1_t}$ we obtain solutions u^α for the hyperbolic equations which are of class C^1 and obey certain LIPSCHITZ bounds on each bounded time interval $[0,T]$ (cf. proposition 4.8 and estimates thereafter).

We are going to use a standard fixed point argument relying on the compactness of the embeddings

$$\begin{aligned} C^{1+1} &\hookrightarrow\!\!\!\!\!\!\rightarrow C^{1+\frac{1+\beta}{2}} \\ C^{2+\beta,P} &\hookrightarrow\!\!\!\!\!\!\rightarrow C^{2_x,1_t} \hookrightarrow C^1 \\ C^{0+1} \cap C^1 &\hookrightarrow\!\!\!\!\!\!\rightarrow C^{0+\beta,P} \end{aligned}$$

for any $\beta \in (0,1)$ and particular bounds on the embedding constants.

The main difficulty to overcome is the matching of the boundary curves with the domain Q_T the functions have to be defined on. As already noted in subsection 4.1.4, the hyperbolic part causes no problem at all since we deal with trivial boundary conditions for those end densities with support being bounded away from the boundary and with characteristic boundary conditions for the end densities supporting the boundary. More precisely, the supporting end densities follow the boundary curves determined by the parabolic equation and do not interfere with the boundary conditions since their value at the boundary remains zero if it is supposed to be so initially.

To circumvene these troubles we use a front fixing method similar to chapter 5 in [4] and rather write the parabolic equation on a fixed domain $(\tau,\xi) \in (0,T) \times (0,L)$ by using the coordinate transformation

$$\tau = t, \qquad \xi = L\frac{x-l(t)}{r(t)-l(t)}. \tag{4.44}$$

The derivatives are then transformed into

$$\partial_x \;\to\; \frac{L}{r-l}\partial_\xi, \qquad \partial_{xx} \;\to\; \frac{L^2}{(r-l)^2}\partial_{\xi\xi}$$

$$\begin{aligned} \partial_t \;\to\; & \partial_\tau - \frac{L}{(r-l)^2}\left(\left(l+\frac{r-l}{L}\xi\right)(\dot r - \dot l) + r\dot l - l\dot r\right)\partial_\xi \\ &= \partial_\tau - \frac{L}{r-l}\left(\frac{\xi}{L}(\dot r - \dot l) + \dot l\right)\partial_\xi \end{aligned}$$

which gives rise to the following initial boundary value problem for the rescaled density

$$\tilde a(\tau,\xi) = a(\tau, x(\tau,\xi)) :$$

$$\partial_\tau \tilde a - \frac{L^2 D}{(r-l)^2}\partial_{\xi\xi}\tilde a - \frac{L}{r-l}\left(\frac{\xi}{L}(\dot r - \dot l) + \dot l\right)\partial_\xi \tilde a + \tilde\varphi \tilde a = \tilde f \tag{4.45}$$

in $(0,T)\times(0,L)$, equipped with initial conditions

$$\tilde a(0,\xi) = a_0(\xi) \qquad \text{on } [0,L] \tag{4.46}$$

and boundary conditions

$$DL\partial_\xi \tilde{a}(\tau,0) + \dot{l}(r-l)\tilde{a}(\tau,0) = 0 \qquad \text{for } \tau \in (0,T). \tag{4.47}$$

$$DL\partial_\xi \tilde{a}(\tau,L) + \dot{r}(r-l)\tilde{a}(\tau,L) = 0 \tag{4.48}$$

The henceforth only virtual boundary curves are again given by the usual initial value problems, namely

$$\dot{l}(\tau) = \lambda^1(\tilde{a}(\tau,0)), \qquad l(0) = 0 \tag{4.49}$$

$$\dot{\tilde{r}}(\tau) = \lambda^4(\tilde{a}(\tau,L)), \qquad \tilde{r}(0) = 0. \tag{4.50}$$

where we used the abbreviation $\tilde{r} := r(\cdot - L)$. The reason is that $\tilde{r}$ can be said to be small in $C^{1+\frac{1+\beta}{2}}$ if the curve r is close to its initial value L and if its velocity $\dot{r}$ together with the HÖLDER constant $H\ddot{o}l_{\frac{1+\beta}{2}}(\dot{r})$ are small. We will occasionally mix the notation for $\tilde{r}$ and r if only the velocity is concerned which should not cause any confusion since we always have $\dot{\tilde{r}} = \dot{r}$.

We can now proceed as before by assuming the boundary curves l and r, which now serve as variable coefficients in the equation and in the boundary conditions, to be given and sufficiently smooth. For those, we easily find a unique solution to the initial boundary value problem (4.45) - (4.48).

As we are now dealing with a true space-time cylinder $\tilde{Q}_T = (0,T) \times (0,L)$ we may adapt theorem 5.3 from chapter IV in Ladyženskaja's book [16]. Putting $l = \beta \in (0,1)$ therein and using the notation established in appendix A.1, we formulate the following theorem.

Theorem 4.9. *Let $\beta \in (0,1)$, let $l, r : [0,T] \to \mathbb{R}$ be given of class $C^{1+\frac{1+\beta}{2}}$ such that for some $d > 0$ it is*

$$r(t) - l(t) > d \qquad \text{for each } t \in [0,T].$$

Assume further that φ and f belong to $C^{0+\beta,P}\left(\overline{Q_T}\right)$ and that the initial condition $a_0 \in C^{2+\beta}([0,L])$ satisfies the compatibility condition 2.3.2.

Then, there exists a unique solution $\tilde{a}$ to problem (4.45) - (4.48), this solution belongs to $C^{2+\beta,P}\left(\overline{\tilde{Q}_T}\right)$, and there exists a constant $C > 0$, depending only on

$$T,\ \beta,\ \|r-L\|_{C^{1+\frac{1+\beta}{2}}},\ \|l\|_{C^{1+\frac{1+\beta}{2}}},\ \|\varphi\|_{C^{0+\beta,P}},\ L,\ \text{and}\ \ D$$

such that

$$\|\tilde{a}\|_{C^{2+\beta,P}} \leq C\left(\|f\|_{C^{0+\beta,P}} + \|a_0\|_{C^{2+\beta}}\right). \tag{4.51}$$

Proof. All the hypotheses of theorem 5.3, chapter IV in [16] are fulfilled if we are able to show that the rescaled coefficients have the required regularity. First, we note that the spaces $H^{k+\beta,\frac{k+\beta}{2}}$ introduced in [16] are the same as $C^{k+\beta,P}$ which we borrowed from [19] in appendix A.1 and that the respective norms are equivalent.

To see that, we observe that the respective norms differ from one another in only two points. The first one is the constriction in Ladyženskaja's definition of the HÖLDER constants to points that are no more than a fixed distance ϱ_0 apart but this is for

bounded domains easily repaired by scaling the norms with

$$\operatorname{diam} Q_T + \sqrt{T}.$$

The second difference in the definition of the Hölder constants is that Ladyženskaja separates the spatial from the temporal modulus of continuity for all relevant derivatives whereas Lieberman combines both of them in the constant $H\ddot{o}l_{P,\beta}$ for the highest derivatives. However, splitting up this constant into a spatial and a temporal contribution (with exponents β and $\frac{\beta}{2}$, respecitvely) is easily achieved by the triangle inequality and the resulting norms differ from one another at most by a factor of 2.

We start with checking the hypotheses on the coefficient functions and the right hand side in the equation itself.

- The leading order coefficient
$$\frac{L^2}{\left(r(\tau) - l(\tau)\right)^2}$$
is positive, bounded and bounded away from zero as long as $r - l$ remains bounded away from zero; and in that case, this coefficent has the same regularity as r and l with respect to time. Moreover, it is independent of the space variable ξ. We thus find it to be of higher regularity than $C^{2_x,1_t}$ which is more than sufficient.

- The second coefficient
$$\frac{L}{(r-l)^2}\left(\left(l + \frac{r-l}{L}\xi\right)(\dot{r} - \dot{l}) + r\dot{l} - l\dot{r}\right) = \frac{L}{r-l}\left(\frac{\xi}{L}(\dot{r} - \dot{l}) + \dot{l}\right)$$
contains algebraic combinations of $r, l, \dot{r}$, and $\dot{l}$ and therefore inherits their regularity with respect to time − again as long as the denominator $r - l$ remains bounded away from zero. The dependence on the space variable ξ is affine and therefore smooth. Combining these observations we obtain a regularity of class $C^{1+\beta,P}$.

- The coefficient function $\tilde{\varphi}$ and the right hand side $\tilde{f}$ are of equal regularity, we therefore treat them together. They are obtained from the original functions φ and f by composition with the coordinate transformation:
$$\tilde{\varphi}(\tau,\xi) = \varphi(t(\tau,\xi), x(\tau,\xi)) = \varphi\left(\tau, l(\tau) + \frac{r(\tau) - l(\tau)}{L}\xi\right)$$
and analogously for $\tilde{f}$.

  To match the assumptions in theorem 5.3, chapter IV in [16], we require the functions $\tilde{\varphi}$ and $\tilde{f}$ to belong to $C^{0+\beta,P}$. The uniform continuity is obvious and we therefore can concentrate on the Hölder continuity:
$$\begin{aligned}
|\tilde{\varphi}(\tau,\xi) - \tilde{\varphi}(\sigma,\eta)| &= \left|\varphi\left(\tau, l(\tau) - \frac{r(\tau) - l(\tau)}{L}\xi\right) - \varphi\left(\sigma, l(\sigma) - \frac{r(\sigma) - l(\sigma)}{L}\eta\right)\right| \\
&\leq 2H\ddot{o}l_{P,\beta}(\varphi)\left(|\tau - \sigma|^{\frac{\beta}{2}} + \left|l(\tau) - \frac{r(\tau) - l(\tau)}{L}\xi - l(\sigma) + \frac{r(\sigma) - l(\sigma)}{L}\eta\right|^{\beta}\right)
\end{aligned}$$
due to φ being of class $C^{0+\beta,P}$ by assumption. The second term can be estimated

as follows:

$$\begin{aligned}
&\left| l(\tau) - \frac{r(\tau)-l(\tau)}{L}\xi - l(\sigma) + \frac{r(\sigma)-l(\sigma)}{L}\eta \right| \\
\leq\ & |l(\tau)-l(\sigma)| + \frac{1}{L}|(r(\tau)-l(\tau))(\xi-\eta)| + \frac{|\eta|}{L}|(r(\tau)-l(\tau))-(r(\sigma)-l(\sigma))| \\
\\
\leq\ & \|\dot{l}\|_{C^0}|\tau-\sigma| + \frac{\|r-L\|_{C^0}+\|l\|_{C^0}+L}{L}|\xi-\eta| + \left(\|\dot{r}\|_{C^0}+\|\dot{l}\|_{C^0}\right)|\tau-\sigma| \\
\leq\ & 2\|\dot{l}\|_{C^0}|\tau-\sigma| + \|\dot{r}\|_{C^0}|\tau-\sigma| + \left(1+\frac{\|r-L\|_{C^0}+\|l\|_{C^0}}{L}\right)|\xi-\eta| \\
=\ & C_1\ |\tau-\sigma| + C_2\ |\xi-\eta|.
\end{aligned}$$

Since $\beta < 1$ and since we can restrict ourselves to $|\tau-\sigma| < 1$ and $|\xi-\eta| < 1$ (otherwise, the constants are multiplied by $\max\{\|l\|_{C^0}+\|r-L\|_{C^0}, T\}$), this leads to theestimate

$$\begin{aligned}
|\tilde{\varphi}(\tau,\xi)-\tilde{\varphi}(\sigma,\eta)| &\leq 2H\ddot{o}l_{P,\beta}(\varphi)\left((1+C_1^\beta)|\tau-\sigma|^{\frac{\beta}{2}} + (C_2|\xi-\eta|)^\beta\right) \\
&\leq C_3\left(|\tau-\sigma|^{\frac{\beta}{2}} + |\xi-\eta|^\beta\right) \\
&\leq C_3\ |(\tau,\xi)-(\sigma,\eta)|_P^\beta
\end{aligned}$$

which is precisely the required HÖLDER condition. The very same calculation clearly holds with f replacing φ.

For the initial conditions, there is nothing to do since the coordinate transformation is the identity at $t = \tau = 0$.

It remains to investigate the coefficients in the boundary conditions. The transversality condition is still valid since DL is constant and positive. The coefficients $\dot{l}(r-l)$ and $\dot{r}(r-l)$ of the zeroth order terms are constant in space, and with respect to time they have the same regularity as $\dot{r}$ which is assumed to belong to $C^{0+\frac{1+\beta}{2}}$. In terms of parabolic HÖLDER norms this again translates to $C^{1+\beta,P}$ as required. □

Remark 4.10. *We note that the assertion of the theorem remains valid if the boundary conditions (4.49) and (4.50) are changed to*

$$DL\partial_\xi\tilde{a}(\tau,0) + \dot{l}(r-l)\tilde{a}(\tau,0) = g(\tau,0) \qquad \text{for } \tau \in (0,T). \tag{4.52}$$

$$DL\partial_\xi\tilde{a}(\tau,L) + \dot{r}(r-l)\tilde{a}(\tau,L) = g(\tau,L) \tag{4.53}$$

with g being of class $C^{1+\beta,P}$. It is only necessary to adapt the compatibility conditions for the initial and boundary conditions at the corner points $(0,0)$ and $(0,L)$ (unless g vanishes there), and in the assertion of the theorem, estimate (4.51) has to be changed to

$$\|\tilde{a}\|_{C^{2+\beta,P}} \leq C\left(\|f\|_{C^{0+\beta,P}} + \|a_0\|_{C^{2+\beta}} + \|g\|_{C^{1+\beta,P}}\right). \tag{4.54}$$

This is immediately clear from the original formulation of theorem IV.(5.3) in [16].

We note that the hypotheses of theorem 4.9 are precisely the same as those of theorem 4.5. It may therefore be expected that the analogue of corollary 4.7 is also true, and indeed we find the following lemma.

Lemma 4.11. *Assume the transformed monomer concentration $\tilde{a}$ to be given and of class C^1 on $[0,T]\times[0,L]$. Then, the boundary curves l and r defined by (4.49) and (4.50), respectively, are of class $C^{1+1}([0,T])$.*

Proof. The proof is even more obvious as in the setting with moving boundary. The initial value problem (4.49) for l now directly shows the following LIPSCHITZ estimate for $\dot{l}$:

$$|\dot{l}(\tau)-\dot{l}(\sigma)| \leq \delta\kappa_B|\tilde{a}(\tau,0)-\tilde{a}(\sigma,0)| \leq \delta\kappa_B\|\partial_t a\|_{C^0}|\tau-\sigma| \tag{4.55}$$

and the very same estimate is true for $\dot{r}$. □

At this point we also give a particular a priori estimate for the boundary curves that will be useful in what follows.

Corollary 4.12. *Given $\tilde{a}\in C^1([0,T]\times[0,L])$ the boundary curves satisfy the following estimates:*

$$\begin{aligned}
\|l\|_{C^0} &\leq (\delta\kappa_B a_B + v_R + \delta\kappa_B\|\tilde{a}\|_{C^0})T && (4.56)\\
\|\dot{l}\|_{C^0} &\leq \delta\kappa_B a_B + v_R + \delta\kappa_B\|\tilde{a}\|_{C^0} && (4.57)\\
Lip(\dot{l}) &\leq \delta\kappa_B\|\partial_t\tilde{a}\|_{C^0}. && (4.58)
\end{aligned}$$

If, in addition, $\tilde{a}$ satisfies the standard estimate from lemma 3.3, then the constant

$$\delta\kappa_B a_B + v_R + \delta\kappa_B\|\tilde{a}\|_{C^0}$$

appearing in the first two equations can be replaced by v_{max} which is given by (4.39).

The same estimates also hold for $\tilde{r}=r-L$ where in (4.56), l has to be replaced by $r-L$.

A priori estimates for the monomer denstiy

We first note that the proof of lemma 3.3 remains valid for our rescaled equation if the coefficient function φ and the right hand side f are given in the form $\varphi = cU$ and $f=\tilde{c}U$ with c and $\tilde{c}$ being composed of the reaction parameters as in (2.16) and (2.17) and with the components of U being non-negative. Of course, we assume that the given end densities U are parabolically HÖLDER continuous as indicated in the hypotheses of theorem 4.9 and vanish on the lateral boundary.

The reason why the same proof for this estimate still works is that the first order term in (4.45) does not contribute to the calculations in the proof of lemma 3.3 since at local extrema the gradient necessarily vanishes.

For the bounds on $\tilde{a}$ at the boundary we need some additional assumptions on the boundary velocities. Let us recall that we deal with the strictly hyperbolic case where we assume the initial monomer density to be bounded from below by $a^{BP}+\varepsilon$ and therefore expect the boundary velocities to satisfy $\dot{l}<0$ and $\dot{r}>0$. Imposing this as assumption on l and r, the boundary part of the proof of lemma 3.3 still can be used without changes.

We will use the uniform bound

$$a_B \leq \tilde{a}(\tau, \xi) \leq a_P \qquad \text{for each } (\tau, \xi) \in [0, T] \times [0, L] \tag{4.59}$$

to derive further a priori estimates on the solution $\tilde{a}$ to problem (4.45) - (4.48).

The next point is the derivation of a bound for $|\partial_\xi \tilde{a}|$ that translates directly into a bound on $|\partial_x a|$ if the distance $r - l$ of the boundary curves remains bounded away from zero.

We start by noting that under the assumption of bounded boundary velocities $\dot{l}$ and $\dot{r}$, the spatial derivative at the lateral boundary obeys the uniform estimates

$$\begin{aligned} |\partial_\xi \tilde{a}(\tau, 0)| &\leq \frac{|\dot{l}|(r(\tau) - l(\tau))}{DL} |\tilde{a}| \\ &\leq \frac{\|\dot{l}\|_{C^0} \left(L + (\|\dot{l}\|_{C^0} + \|\dot{r}\|_{C^0}) T \right)}{DL} a_P \qquad (4.60) \\ |\partial_\xi \tilde{a}(\tau, L)| &\leq \frac{\|\dot{r}\|_{C^0} \left(L + (\|\dot{l}\|_{C^0} + \|\dot{r}\|_{C^0}) T \right)}{DL} a_P \qquad (4.61) \end{aligned}$$

where we already used the boundedness of $\tilde{a}$ and the assumption

$$r - l \geq d > 0.$$

To obtain a global bound for $\partial_\xi \tilde{a}$ we employ theorem 11.5 in [19].

Lemma 4.13. *Given a maximal boundary velocity V let*

$$T \leq \frac{L}{4V},$$

let boundary curves

$$l, r \in C^{1+\frac{1+\beta}{2}}([0, T])$$

and end densities $U \in C^{0+\beta, P}$ be given such that

$$\|\dot{l}\|_{C^0},\ \|\dot{r}\|_{C^0} \leq V \tag{4.62}$$

$$\dot{l}(\tau) \leq 0 \leq \dot{r}(\tau) \qquad \text{for each } \tau \in [0, T]. \tag{4.63}$$

Then, the solution

$$\tilde{a} \in C^{2+\beta, P}([0, T] \times [0, L])$$

of problem (4.45) - (4.48) satisfies

$$\|\partial_\xi \tilde{a}\|_{C^0} \leq C \left(\max \left\{ \sqrt{\frac{V}{LD}}, \frac{2V}{D} + \sqrt{\frac{A_1}{D}} \right\} + \frac{3V}{2D} a_P \right) \tag{4.64}$$

where A_1 is given by

$$A_1 = \delta \kappa_B (a_P - a_B) \max_{\alpha = 1, \ldots, 4} \|u^\alpha\|_{C^0} \tag{4.65}$$

and C only depends on $a_P - a_B$.

Proof. We have to check the hypotheses of theorem 11.5 in [19]. With the notation and

numbering therein we first note that by theorem 4.9, our solution $\tilde{a}$ is indeed of class $C^{2+\beta,P}$ up to boundary and therefore belongs to $C^{2_x,1_t}$ and in particular, $\partial_\xi \tilde{a}$ belongs to $C^0([0,T]\times[0,L])$.

We furthermore note that due to the sign of the boundary velocities on the one hand and by their boundedness and the bound on T on the other hand, we have

$$L \leq r - l \leq \frac{3}{2}L.$$

Moreover, the coefficient function $\tilde{\varphi}$ is always non-negative. Concerning the conditions [19].(11.25a-d) in [19] we put

$$\mu = \frac{9}{2} \qquad \text{and} \qquad \lambda_0 = \min\left\{\frac{4}{9}, \frac{1}{D}\right\}$$

to show the validity of the hypotheses.

1. Inequality [19].(11.25a) is void since our highest order coefficient

$$\frac{L^2}{(r-l)^2}D$$

is independent of $\xi, \tilde{a}$, and $\partial_\xi \tilde{a}$, and therefore the left hand side of this inequality vanishes. We also note that by our assumptions, the scaled diffusion coefficient satisfies

$$\frac{4D}{9} \leq \frac{L^2 D}{(r-l)^2} \leq D \tag{4.66}$$

which already shows that with the choice of λ_0 as above we can satisfy [19].(11.25d). (The lower bound in the previous equation is called λ in [19], the upper one Λ)

2. Inequality [19].(11.25b) is true for any

$$|p| \geq P_1 = \sqrt{\frac{V}{LD}}$$

which gives the first term on the right hand side of (4.64). To see this we calculate the left hand side of this inequality to be

$$-\tilde{\varphi} + \frac{\dot{r} - \dot{l}}{r - l} \leq \frac{2V}{L}. \tag{4.67}$$

The right hand side is for

$$|p| \geq P_1, \quad \mu = \frac{9}{2}, \quad \text{and } \lambda = \frac{4D}{9}$$

bounded from below by

$$2Dp^2 \geq 2D\frac{V}{LD} = \frac{2V}{L} \tag{4.68}$$

which shows the validity of [19].(11.25b).

3. For inequality [19].(11.25c) we calculate the left hand side to be

$$\begin{aligned}
& |p| \left| \frac{L}{(r-l)^2} \left(\left(l + \frac{r-l}{L}\xi \right) (\dot{r} - \dot{l}) + r\dot{l} - l\dot{r} \right) \right| \\
& + \left| \frac{L}{(r-l)^2} \left(\left(l + \frac{r-l}{L}\xi \right) (\dot{r} - \dot{l}) + r\dot{l} - l\dot{r} \right) p + \tilde{\varphi}\tilde{a} - \tilde{f} \right| \\
\leq \; & 2|p| \frac{L}{(r-l)^2} (r-l)|\dot{r} - \dot{l}| + \sup_{\tau,\xi} |\tilde{\varphi}\tilde{a} - \tilde{f}| \\
\leq \; & 4V|p| + 2M_1
\end{aligned}$$

where we used the bound (3.13) to estimate $\tilde{\varphi}\tilde{a} - \tilde{f}$ under the assumption of $\tilde{a}$ being bounded between a_B and a_P. The right hand side of [19].(11.25c) can for

$$|p| \geq P_2 = \frac{2V}{D} + \sqrt{\frac{M_1}{D}}$$

be estimated from below by

$$\begin{aligned}
\frac{9}{2} \, \frac{4D}{9} p^2 \quad \geq \quad 2D|p|P_2 \quad &= \quad 2D|p| \left(\frac{2V}{D} + \sqrt{\frac{M_1}{D}} \right) \\
\geq \quad 4V|p| + 2D \; P_2 \sqrt{\frac{M_1}{D}} \quad &\geq \quad 4V|p| + 2M_1
\end{aligned}$$

and the inequality is shown. Note that P_2 is the second term in the maximum in inequality (4.64).

Recalling now that the spatial derivative along the boundary is bounded by

$$\frac{V(L+2VT)}{2D} a_P = \frac{3V}{2D} a_P$$

and that the total oscillation $\operatorname{osc}\tilde{a}$ is simply given by at most $a_P - a_B$, we arrive at estimate (4.64) as an adapted form of inequality [19].(11.27). □

Remark 4.14. *The whole proof remains literally the same if the hypothesis*

$$T \leq \frac{L}{4V}$$

is dropped. The only difference is the upper bound on $r - l$ which is always given by $L + 2VT$. We therefore only would have to change some of the constants.

However, we included this hypothesis since it allows to apply the same proof with only minor changes to other initial conditions. Another possible strictly hyperbolic case is given by assuming the monomer density to be strictly smaller than a^{BP}. In that case, the boundary velocities would be given by $\lambda^2(\tilde{a})$ and $\lambda^3(\tilde{a})$, respectively, and these are now directed inwards. If we now assume these velocities to be absolutely bounded by some constant V, the condition $T \leq \frac{L}{4V}$ guarantees the value $r - l$ to be larger than $\frac{L}{2}$ and in particular bounded away from zero. This is not only required for the proof of lemma 4.13 to work but also for the validity of theorem 4.9 where the value $r - l$ occurs in the

denominators of the coefficients.

The final estimate we require is concerned with the temporal derivative of a along the lateral boundary. This in turn will allow us to find bounds on the variation of the boundary velocities.

Construction of a solution to the parabolic free boundary problem

We now want to continue with our fixed point argument. For $\beta \in (0,1)$, we introduce the following spaces.

$$X_T := C^{1+\frac{1+\beta}{2}}([0,T]) \times C^{1+\frac{1+\beta}{2}}([0,T]) \times C^{2_x,1_t}([0,T]\times[0,L]) \tag{4.69}$$

and

$$Y_T := C^{1+1}([0,T]) \times C^{1+1}([0,T]) \times C^{2+\beta,P}([0,T]\times[0,L]) \tag{4.70}$$

equipped with the following norms:

$$\|(l,\tilde{r},\tilde{a})\|_{X_T} := \|l\|_{C^{1+\frac{1+\beta}{2}}} + \|r(\cdot)-L\|_{C^{1+\frac{1+\beta}{2}}} + \|\tilde{a}\|_{C^1} \tag{4.71}$$

$$\|(l,\tilde{r},\tilde{a})\|_{Y_T} := \|l\|_{C^{1+1}} + \|r(\cdot)-L\|_{C^{1+1}} + \|\tilde{a}\|_{C^{2+\beta,P}} \tag{4.72}$$

with all the spaces on the right hand side having $[0,T]$ or $[0,T]\times[0,L]$ as domains.

The reason why we chose different HÖLDER exponents for the boundary curves in X_T and the monomer density in Y_T will become obvious during the estimates. Basically, the gap between β or $\frac{1}{2}(1+\beta)$ on the one hand and 1 on the other hand is required to derive a contraction principle.

We furthermore define the operator

$$A : X_T \ni (l,\tilde{r},\tilde{a}) \mapsto (l',\tilde{r'},\tilde{a'}) \in X_T \tag{4.73}$$

by saying that

1. l' and $\tilde{r'}$ are the solutions of (4.49) and (4.50), respectively, with $\tilde{a}$ plugged into the right hand sides, and

2. $\tilde{a'}$ is the solution of the initial boundary value problem (4.45) - (4.48) with l and $\tilde{r}$ as given boundary curves.

We are now going to show that for sufficiently well-behaved given initial conditions a_0, the operator $A : X_T \to X_T$ is a strict contraction on some closed bounded subset of X_T for sufficiently small T.

More precisely, let $a_0 \in C^{2+\beta}([0,L])$ satisfy the required compatibility conditions 2.3.2 which we rewrite in the following shape

$$D\frac{d}{dx}a_0(0) + \gamma_{l.1}\ a_0(0)^2 + \gamma_{l,2} = 0 \tag{4.74}$$

$$D\frac{d}{dx}a_0(L) + \gamma_{r,1}\ a_0(L)^2 + \gamma_{r,2} = 0 \tag{4.75}$$

where $\gamma_{r/l,i}$ are constants depending on the parameters $\delta, v_R, \kappa_{B/P}$, and $a_{B/P}$. We

observe that the boundary velocities by continuity now satisfy

$$v_{l0} := \dot{l}(0) \ = \gamma_{l,1} a_0(0) + \gamma_{l,2} \tag{4.76}$$

$$v_{r0} := \dot{r}(0) \ = \gamma_{r,1} a_0(L) + \gamma_{r,2}. \tag{4.77}$$

The bounded set we consider shall be given by

$$\begin{aligned} \mathcal{B}_T = \Big\{ (l, r, \tilde{a}) \in X_T \ \Big| \quad & \|r - L\|_{C^0} \le \varepsilon_1, \|\dot{r} - v_{r0}\|_{C^0} \le \varepsilon_2, H\ddot{o}l_{\frac{1+\beta}{2}}(\dot{r}) \le \Lambda_1, \\ & \|l\|_{C^0} \le \varepsilon_1, \|\dot{l} - v_{l0}\|_{C^0} \le \varepsilon_2, H\ddot{o}l_{\frac{1+\beta}{2}}(\dot{l}) \le \Lambda_1, \\ & a_B \le \tilde{a}(\tau, \xi) \le a_P, \|\tilde{a}\|_{C^{2_x, 1_t}} \le \Upsilon_1, \\ & l(0) = 0, \ r(0) = L, \ \dot{l}(0) = v_{l0}, \ \dot{r}(0) = v_{r0}, \ \tilde{a}(0, \cdot) = a_0 \Big\} \end{aligned} \tag{4.78}$$

for some $\varepsilon_1, \varepsilon_2, \Lambda_1, \Upsilon_1 > 0$ to be determined later. We first show that for appropriate parameters, the operator A maps $\mathcal{B}_T$ into itself.

Lemma 4.15. *Fix $\beta \in (0,1)$, let $a_0 \in C^{2+\beta}([0,L])$ be given with*

$$\|a_0\|_{C^{2+\beta}} =: M_2. \tag{4.79}$$

For given $\Lambda_1 > 0$ define T^* to be the positive solution of

$$\max\{|v_{r0}|, |v_{l0}|\} T^* + \Lambda_1 \ (T^*)^{1+\frac{1+\beta}{2}} = \frac{L}{4} \tag{4.80}$$

where v_{l0} and v_{r0} are given by (4.76) and (4.77), respectively.

For $T \in (0, T^*]$ put

$$\varepsilon_2(T) \ = \ \Lambda_1 \ T^{\frac{1+\beta}{2}} \tag{4.81}$$

$$\bar{V}(T) \ = \ \max\{|v_{r0}|, |v_{l0}|\} + \varepsilon_2(T) \tag{4.82}$$

$$\varepsilon_1(T) \ = \ \bar{V}(T) T. \tag{4.83}$$

Let furthermore

$$\tilde{\varphi}, \tilde{f} \in C^{0+\beta, P}([0, T^*] \times [0, L])$$

be given with norms

$$\|\tilde{\varphi}\|_{C^{0+\beta,P}([0,T^*]\times[0,L])} \ =: \ A_2 \tag{4.84}$$

$$\|\tilde{f}\|_{C^{0+\beta,P}([0,T^*]\times[0,L])} \ =: \ A_3 \tag{4.85}$$

Let $\hat{C}(T)$ be the constant C from equation (4.51) in theorem 4.9 with

$$\|l\|_{C^{1+\frac{1+\beta}{2}}} = \|r - L\|_{C^{1+\frac{1+\beta}{2}}} = \varepsilon_1(T^*) + \bar{V}(T^*) + \Lambda_1$$

and

$$\|\varphi\|_{C^{0+\beta,P}} = A_2.$$

Put

$$\Upsilon_1(T) := \hat{C}(T)\ (A_3 + M_2). \tag{4.86}$$

Now define $\mathcal{B}_T \subset X_T$ by (4.78) with $\varepsilon_{1/2}$ and Υ_1 replaced by $\varepsilon_{1/2}(T)$ and $\Upsilon_1(T)$, respectively.

Then, there exists $T_1 \in (0, T^*]$ such that for each $T \in (0, T_1]$, the operator A from (4.73) maps $\mathcal{B}_T$ into (a compact subset of) itself.

Proof. Assume we are given $(l, r, \tilde{a}) \in \mathcal{B}_T$. We will show that for sufficiently small T the image

$$(l', r', \tilde{a'}) = A(l, r, \tilde{a})$$

also belongs to $\mathcal{B}_T$. That is, we have to show that this solution satisfies

1. $(l', r', \tilde{a'}) \in X_T$. This is clear since A maps X_T into Y_T which compactly embeds into X_T. That is also the reason why A can be asserted to map $\mathcal{B}_T$ into a *compact* subset of itself.

2. the required conditions at $\tau = 0$. These are automatically fulfilled by continuity.

3. $\|l'\|_{C^0} \leq \varepsilon_1(T)$ and $\|r' - L\|_{C^0} \leq \varepsilon_1(T)$.

4. $\|\dot{l'} - v_{l0}\|_{C^0} \leq \varepsilon_2(T)$ and $\|\dot{r'} - v_{r0}\|_{C^0} \leq \varepsilon_2(T)$.

5. $H\ddot{o}l_{\frac{1+\beta}{2}}(\dot{l'}) \leq \Lambda_1$ and $H\ddot{o}l_{\frac{1+\beta}{2}}(\dot{r'}) \leq \Lambda_1$.

6. $\|\tilde{a'}\|_{C^{2_x,1_t}} \leq \Upsilon_1(T)$.

Before showing the claims 3-6, we note that $\hat{C}(T), \varepsilon_1(T), \varepsilon_2(T)$, and $\Upsilon(T)$ do not increase as T decreases, and are therefore bounded by

$$\begin{aligned}
\hat{C}(T) &\leq C^* = \hat{C}(T^*) \\
\varepsilon_1(T) &\leq \varepsilon_1^* = \varepsilon_1(T^*) \\
\varepsilon_2(T) &\leq \varepsilon_2^* = \varepsilon_2(T^*) \\
\Upsilon_1(T) &\leq \Upsilon_1^* = \Upsilon_1(T^*).
\end{aligned}$$

We furthermore note that the constant C obviously does not increase as

$$\|\varphi\|_{C^{0+\beta,P}}, \quad \|l\|_{C^{1+\frac{1+\beta}{2}}}, \quad \text{and } \|\tilde{r}\|_{C^{1+\frac{1+\beta}{2}}}$$

decrease and that for the restrictions of $\tilde{\varphi}$ and $\tilde{f}$ to $[0, T] \times [0, L]$ and the restrictions of r and l to $[0, T]$ with $T \leq T^*$, the relevant norms are not larger than those for the larger domains corresponding to T^*.

We show the claims 3, 4, and 5 only for l', the proves for r' are practically the same. We start with point 5 which will provide the basis for 3 and 4.

By corollary 4.7 we have

$$\begin{aligned}
Lip(\dot{l'}) &\leq \delta\kappa_B \|\partial_t \tilde{a}\|_{C^0} \leq \delta\kappa_B \|\tilde{a}\|_{C^{2_x,1_t}} \\
&\leq \delta\kappa_B \Upsilon^* \qquad\qquad\qquad (\text{for } T \leq T^*)
\end{aligned}$$

and therefore

$$H\ddot{o}l_{\frac{1+\beta}{2}}(\dot{l}') \quad \leq \quad Lip(\dot{l}')T^{\frac{1-\beta}{2}} \leq \delta\kappa_B\Upsilon^*T^{\frac{1-\beta}{2}}.$$

Choosing

$$T \leq T_1 = \min\left\{\left(\frac{\Lambda_1}{\delta\kappa_B\Upsilon^*}\right)^{\frac{2}{1-\beta}}, T^*\right\}$$

we obtain the desired bound on the HÖLDER constant of $\dot{l}'$.

We proceed with the bound on the velocity $\dot{l}'$ itself:

$$\begin{aligned} |\dot{l}' - v_{l0}| &\leq H\ddot{o}l_{\frac{1+\beta}{2}}(\dot{l}')T^{\frac{1+\beta}{2}} \\ &\leq \Lambda_1 T^{\frac{1+\beta}{2}} \qquad \text{if } T \leq T_1. \end{aligned}$$

With the same automatism we obtain for the supremum norm of l':

$$\begin{aligned} |l'| &\leq \|\dot{l}'\|_{C^0}T \\ &\leq \bar{V}(T)T = \varepsilon_1(T). \end{aligned}$$

We see that as soon as we found claim 5 to be valid, the claims 3 and 4 are satisfied just by the choice of ε_1 and ε_2.

Not too surprisingly, point 6 follows by the definition of $\Upsilon_1(T)$. By theorem 4.9 we have

$$\begin{aligned} \|\tilde{a'}\|_{C^{2_x,1_t}([0,T]\times[0,L])} &\leq \|\tilde{a'}\|_{C^{2+\beta,}([0,T]\times[0,L])} \\ &\leq C(T,\beta,\varepsilon_1(T) + \bar{V}(T) + \Lambda_1, A_2, L, D)\ (A_3 + A1) \\ &\leq \hat{C}(T)\ (A_3 + M_2) = \Upsilon_1(T). \end{aligned}$$

□

To establish a contraction principle, let now $(l_1, \tilde{r}_1, \tilde{a}_1) \in \mathcal{B}_T$ and $(l_2, \tilde{r}_2, \tilde{a}_2) \in \mathcal{B}_T$ be given and assume

$$\|(l_2 - l_1, r_2 - r_1, \tilde{a}_2 - \tilde{a}_1)\|_{X_T} \leq \omega.$$

This immediately implies

$$\begin{aligned} H\ddot{o}l_{\frac{1+\beta}{2}}(\dot{r}_2 - \dot{r}_1) + H\ddot{o}l_{\frac{1+\beta}{2}}(\dot{l}_2 - \dot{l}_1) &\leq \omega \\ \|\dot{r}_2 - \dot{r}_1\|_{C^0} + \|\dot{l}_2 - \dot{l}_1\|_{C^0} &\leq \omega T^{\frac{1+\beta}{2}} \\ \|r_2 - r_1\|_{C^0} + \|l_2 - l_1\|_{C^0} &\leq \omega T^{1+\frac{1+\beta}{2}}. \end{aligned}$$

We also deduce some further estimates that will become useful for later calculations. Introducing the notation $L_i(\tau) := r_i(\tau) - l_i(\tau)$ for $i = 1, 2$ and $\tau \in [0, T]$ we can compute

$$\begin{aligned} |(L_1(\tau) - L_2(\tau)) - (L_1(\sigma) - L_2(\sigma))| &\leq \omega T^{\frac{1+\beta}{2}}|\tau - \sigma| \\ |(\dot{L}_1(\tau) - \dot{L}_2(\tau)) - (\dot{L}_1(\sigma) - \dot{L}_2(\sigma))| &\leq \omega|\tau - \sigma|^{\frac{1+\beta}{2}} \\ |L_2(\tau)L_2(\sigma) - L_1(\tau)L_1(\sigma)| &\leq \omega T^{1+\frac{1+\beta}{2}}L_{max}(T) \end{aligned}$$

where

$$L_{max}(T) := \sup_{\tau\in[0,T]} r(\tau) - \inf_{\tau\in[0,T]} l(\tau) \leq L + 2\bar{V}(T)T$$

denotes the largest possible value for the virtual domain length.

Given such $(l_1, \tilde{r}_1, \tilde{a}_1)$ and $(l_2, \tilde{r}_2, \tilde{a}_2)$, the difference

$$(\lambda, \varrho, w) := A(l_2, \tilde{r}_2, \tilde{a}_2) - A(l_1, \tilde{r}_1, \tilde{a}_1)$$

satisfies the following problems

$$\dot{\lambda}(\tau) = \gamma_{l,1}\left(\tilde{a}_2(\tau, 0) - \tilde{a}_1(\tau, 0)\right), \qquad \lambda(0) = 0 \tag{4.87}$$

$$\dot{\varrho}(\tau) = \gamma_{r,1}\left(\tilde{a}_2(\tau.L) - \tilde{a}_1(\tau, L)\right), \qquad \varrho(0) = 0 \tag{4.88}$$

and

$$\begin{aligned}
\partial_\tau w &= \frac{L^2 D}{(r_2 - l_2)^2}\partial_{\xi\xi} w + \frac{L}{r_2 - l_2}\left(\frac{\xi}{L}(\dot{r}_2 - \dot{l}_2) + \dot{l}_2\right)\partial_\xi w - \tilde{\varphi} w \\
&\quad + \frac{L^2 D}{(r_2 - l_2)^2 (r_1 - l_1)^2}\left((r_1 - l_1)^2 - (r_2 - l_2)^2\right)\partial_{\xi\xi}\tilde{a'}_1 \\
&\quad + \left[\frac{L}{r_2 - l_2}\left(\frac{\xi}{L}(\dot{r}_2 - \dot{l}_2) + \dot{l}_2\right) - \frac{L}{r_1 - l_1}\left(\frac{\xi}{L}(\dot{r}_1 - \dot{l}_1) + \dot{l}_1\right)\right]\partial_\xi \tilde{a'}_1
\end{aligned} \tag{4.89}$$

Since we know about the existence and uniqueness of the solution $\tilde{a'}_1 \in C^{2+\beta,P}$ as part of $A(l_1, \tilde{r}_1, \tilde{a}_1)$, we can consider the terms containing $\partial_{\xi\xi}\tilde{a'}_1$ and $\partial_\xi \tilde{a'}_1$ as right hand side F and observe that

$$\begin{aligned}
F &= \frac{L^2 D}{(r_2 - l_2)^2 (r_1 - l_1)^2}\left((r_1 - l_1)^2 - (r_2 - l_2)^2\right)\partial_{\xi\xi}\tilde{a'}_1 \\
&\quad + \left[\frac{L}{r_2 - l_2}\left(\frac{\xi}{L}(\dot{r}_2 - \dot{l}_2) + \dot{l}_2\right) - \frac{L}{r_1 - l_1}\left(\frac{\xi}{L}(\dot{r}_1 - \dot{l}_1) + \dot{l}_1\right)\right]\partial_\xi \tilde{a'}_1 \\
&= L^2 D\Theta\partial_{\xi\xi}\tilde{a'}_1 + (\Sigma_2 - \Sigma_1)\partial_\xi \tilde{a'}_1
\end{aligned} \tag{4.90}$$

belongs to $C^{0+\beta,P}$, and we will show in an instance that it is bounded in this space. For better readability we introduced the notation

$$\begin{aligned}
\Theta(\tau) &:= \frac{(r_1(\tau) - l_1(\tau))^2 - (r_2(\tau) - l_2(\tau))^2}{(r_2(\tau) - l_2(\tau))^2 (r_1(\tau) - l_1(\tau))^2} \\
\Sigma_i(\tau) &:= \frac{L}{(r_i - l_i)^2}\left(\left(l_i + \frac{r_i - l_i}{L}\xi\right)(\dot{r}_i - \dot{l}_i) + r_i\dot{l}_i - l_i\dot{r}_i\right) \\
&= \frac{L}{r_i(\tau) - l_i(\tau)}\left(\frac{\xi}{L}(\dot{r}_i(\tau) - \dot{l}_i(\tau)) + \dot{l}_i(\tau)\right)
\end{aligned}$$

which will regularly be used in the following calculations.

Furthermore, w satisfies trivial initial conditions

$$w(0, \cdot) \equiv 0 \tag{4.91}$$

and the boundary conditions

$$DL\partial_\xi w(\tau,0) + \dot{l}_2(r_2-l_2)w(\tau,0) \;= \left[\dot{l}_2(r_2-l_2) - \dot{l}_1(r_1-l_1)\right]\tilde{a'}_1(\tau,0) =: g(\tau,0) \tag{4.92}$$

$$DL\partial_\xi w(\tau,L) + \dot{r}_2(r_2-l_2)w(\tau,L) \;= \left[\dot{r}_2(r_2-l_2) - \dot{r}_1(r_1-l_1)\right]\tilde{a'}_1(\tau,L) =: g(\tau,L). \tag{4.93}$$

Again, the solution $\tilde{a'}_1$ exists and is of class $C^{2+\beta,P}$, and we can therefore use it to define the inhomogeneity of the boundary conditions g in the sense of remark 4.10. We note that g is a priori only given on the boundary curves but we can easily choose to interpolate it linearly with respect to ξ in order to define it on all of $[0,T]\times\mathbb{R}$.

Estimates for the right hand sides F and g

We want to exploit the estimate (4.51) from theorem 4.9, or rather its version (4.54) from remark 4.10, together with the estimates in lemma 4.6 to obtain bounds for the $C^{0+\beta,P}$-norm of F and the $C^{1+\beta,P}$-norm of g.

The first thing to note is that the boundary curves l and r appearing in the definitions of F and g only depend on the time variable τ (which coincides with the true time variable t) and therefore do not contribute directly to variations in space. Let us start with estimating spatial changes in F.

$$\begin{aligned}
|F(\tau,\xi)-F(\tau,\eta)| \le\;& L^2 D\frac{\left|(r_1-l_1)^2-(r_2-l_2)^2\right|}{(r_2-l_2)^2(r_1-l_1)^2}|\partial_{\xi\xi}\tilde{a'}_1(\tau,\xi)-\partial_{\xi\xi}\tilde{a'}_1(\tau,\eta)| \\
&+ \left|\frac{L}{r_2-l_2}\left(\frac{\xi}{L}(\dot{r}_2-\dot{l}_2)+\dot{l}_2\right)-\frac{L}{r_1-l_1}\left(\frac{\xi}{L}(\dot{r}_1-\dot{l}_1)+\dot{l}_1\right)\right|\times \\
&\times \left|\partial_\xi\tilde{a'}_1(\tau,\xi)-\partial_\xi\tilde{a'}_1(\tau,\eta)\right| \\
&+ \left|\xi\frac{\dot{r}_2-\dot{l}_2}{r_2-l_2}-\xi\frac{\dot{r}_1-\dot{l}_1}{r_1-l_1}-\eta\frac{\dot{r}_2-\dot{l}_2}{r_2-l_2}+\eta\frac{\dot{r}_1-\dot{l}_1}{r_1-l_1}\right||\partial_\xi\tilde{a'}_1(\tau,\eta)| \\
=:\;& E_1+E_2+E_3
\end{aligned}$$

where at each appearance, r_1, r_2, l_1, l_2, and all their derivatives are to be evaluated at the argument τ.

We first estimate some quantities that appear regularly on the right hand side and in what follows. We may start with

$$\begin{aligned}
r_i(\tau)-l_j(\sigma) &\ge (L-\bar{V}(\tau)\tau)-\bar{V}(\sigma)\sigma \\
&\ge L-2\bar{V}(T)T \equiv d(T) \qquad (i,j=1,2;\ \tau,\sigma\le T)
\end{aligned}$$

where $\bar{V}(T)$ is given by (4.82). We note that

$$d(T)\ge\frac{L}{2}$$

whenever $T\le T^*$ with T^* as in lemma 4.15 which we will henceforth always assume

even if not explicitely stated at every occurence.

The next quantity to estimate is

$$\begin{aligned}
&|(r_2(\tau)-l_2(\tau))^2-(r_1(\sigma)-l_1(\sigma))^2| \\
&\leq |r_2^2(\tau)-r_1^2(\sigma)|+|l_2^2(\tau)-l_1^2(\sigma)|+2|l_1(\sigma)r_1(\sigma)-l_2(\tau)r_2(\tau)| \\
&\leq 2r_{max}(T)\|r_2-r_1\|_{C^0}+2\varepsilon_1(T)\|l_2-l_1\|_{C^0} \\
&\quad +2\left(\varepsilon_1(T)\|l_2-l_1\|_{C^0}+r_{max}(T)\|r_2-r_1\|_{C^0}\right) \\
&\leq 2(r_{max}(T)+\varepsilon_1(T))\omega T^{1+\frac{1+\beta}{2}} \qquad\qquad \text{if } \tau,\sigma\leq T.
\end{aligned}$$

Here we used $\varepsilon_1(T)$ as in lemma 4.15 and the largest possible value for the right boundary $r_{max}(T)$ being given by

$$r_{max}(T) := L+\bar{V}(T)T.$$

Combining the last two estimates we find

$$\begin{aligned}
|\Theta(\tau)| &\leq \frac{|(r_2(\tau)-l_2(\tau))^2-(r_1(\sigma)-l_1(\sigma))^2|}{(r_2(\tau)-l_2(\tau))^2(r_1(\tau)-l_1(\tau))^2} \\
&\leq \frac{2}{d(T)^4}(r_{max}(T)+\varepsilon_1(T))\omega T^{1+\frac{1+\beta}{2}}.
\end{aligned}$$

We now find E_1 to be bounded by

$$\begin{aligned}
E_1 &= L^2D|\Theta|\;|\partial_{\xi\xi}\tilde{a'}_1(\tau,\xi)-\partial_{\xi\xi}\tilde{a'}_1(\tau,\eta)| \\
&\leq 2\frac{L^2D}{d(T)^4}(r_{max}(T)+\varepsilon_1(T))H\ddot{o}l_{P,\beta}(\partial_{\xi\xi}\tilde{a'}_1)\omega T^{1+\frac{1+\beta}{2}}|\xi-\eta|^\beta. \qquad (4.94)
\end{aligned}$$

In the following estimate, we assume all quantities to be evaluated at τ but we will suppress the argument for better readability.

$$\begin{aligned}
&\left|\frac{\dot{r}_2-\dot{l}_2}{r_2-l_2}-\frac{\dot{r}_1-\dot{l}_1}{r_1-l_1}\right| \leq \frac{|(\dot{r}_2-\dot{l}_2)(r_1-l_1)-(\dot{r}_1-\dot{l}_1)(r_2-l_2)|}{(r_2-l_2)(r_1-l_1)} \\
&\leq \frac{|\dot{r}_2-\dot{l}_2-\dot{r}_1+\dot{l}_1||r_1-l_1|+|\dot{r}_1-\dot{l}_1||r_1-l_1-r_2+l_2|}{d(T_1)^2} \\
&\leq \frac{L_{max}(T)(\|\dot{r}_2-\dot{r}_1\|_{C^0}+\|\dot{l}_2-\dot{l}_1\|_{C^0})+2\bar{V}(T)(\|r_2-r_1\|_{C^0}+\|l_2-l_1\|_{C^0})}{} \\
&\leq \frac{1}{d(T)^2}(L_{max}(T)+2\bar{V}(T)T)\omega T^{\frac{1+\beta}{2}} \qquad\qquad \text{for } \tau\leq T. \qquad (4.95)
\end{aligned}$$

where we recall $L_{max}(T)$ to be the maximal spatial extension of the domain.

We are now ready to estimate E_3 by

$$\begin{aligned}
E_3 &\leq \left|\frac{\dot{r}_2-\dot{l}_2}{r_2-l_2}-\frac{\dot{r}_1-\dot{l}_1}{r_1-l_1}\right||\xi-\eta|\|\partial_\xi\tilde{a'}_1\|_{C^0} \\
&\leq \frac{1}{d(T)^2}(L_{max}(T)+2\bar{V}(T)T)\|\partial_\xi\tilde{a'}_1\|_{C^0}\omega T^{\frac{1+\beta}{2}}|\xi-\eta| \qquad (4.96)
\end{aligned}$$

whenever $\tau\leq T$.

To find a bound for E_2 we calculate

$$\begin{aligned}
&|\Sigma_2(\tau,\xi) - \Sigma_1(\tau,\xi)| \\
&= \left| \frac{L}{r_2 - l_2} \left(\frac{\xi}{L}(\dot{r}_2 - \dot{l}_2) + \dot{l}_2 \right) - \frac{L}{r_1 - l_1} \left(\frac{\xi}{L}(\dot{r}_1 - \dot{l}_1) + \dot{l}_1 \right) \right| \\
&\leq \xi \left| \frac{\dot{r}_2 - \dot{l}_2}{r_2 - l_2} - \frac{\dot{r}_1 - \dot{l}_1}{r_1 - l_1} \right| + L \left| \frac{\dot{l}_2}{r_2 - l_2} - \frac{\dot{l}_1}{r_1 - l_1} \right| \\
&= \frac{2L}{d(T)^2} \left(2\bar{V}(T)T + L_{max}(T) \right) \omega T^{\frac{1+\beta}{2}}. \qquad (4.97)
\end{aligned}$$

The resulting estimate for E_2 reads:

$$E_2 \leq \frac{2L}{d(T)^2} \left(L_{max}(T) + 2\bar{V}(T)T \right) \|\partial_{\xi\xi} \tilde{a'}_1\|_{C^0} \omega T^{\frac{1+\beta}{2}} |\xi - \eta|. \qquad (4.98)$$

We note that for $T \leq T^*$ as in lemma 4.15, we always have

$$\bar{V}(T)T \quad \leq \quad \frac{L}{4}$$

which implies

$$\begin{aligned}
L_{max}(T) = L + 2\bar{V}(T)T &\leq \frac{3}{2}L \\
r_{max}(T) = L + \bar{V}(T)T &\leq \frac{5}{4}L \\
d(T) = L - 2\bar{V}(T)T &\geq \frac{L}{2}.
\end{aligned}$$

Using this, we can sum up the inequalities (4.94), (4.96), and (4.98) to end up with

$$\begin{aligned}
&\frac{|F(\tau,\xi) - F(\tau,\eta)|}{|\xi - \eta|^\beta} \\
&\leq 2D \frac{16}{L^2} \left(L + \bar{V}(T)T + \varepsilon_1(T) \right) H\ddot{o}l_{P,\beta}(\partial_{\xi\xi} \tilde{a'}_1) \omega T^{1+\frac{1+\beta}{2}} \\
&\quad + \frac{2L}{d(T)^2} (L + 4\bar{V}(T)T) \|\partial_{\xi\xi} \tilde{a'}_1\|_{C^0} \omega T^{\frac{1+\beta}{2}} |\xi - \eta|^{1-\beta} \\
&\quad + \frac{1}{d(T)^2} (L + 4\bar{V}(T)T) \|\partial_{\xi} \tilde{a'}_1\|_{C^0} \omega T^{\frac{1+\beta}{2}} |\xi - \eta|^{1-\beta} \\
&\leq 8 \left(6\frac{DT}{L} H\ddot{o}l_{P,\beta}(\partial_{\xi\xi} \tilde{a'}_1) + 2L^{1-\beta} \|\partial_{\xi\xi} \tilde{a'}_1\|_{C^0} + \frac{\|\partial_{\xi} \tilde{a'}_1\|_{C^0}}{L^\beta} \right) \omega T^{\frac{1+\beta}{2}} \\
&\leq 8 \left(6\frac{DT}{L} + L^{-\beta} + 2L^{1-\beta} \right) \|\tilde{a'}_1\|_{C^{2+\beta,P}} \omega T^{\frac{1+\beta}{2}} = K_{F,x}(D, L, T^*) \|\tilde{a'}_1\|_{C^{2+\beta,P}} \omega
\end{aligned}$$

We thus found a spatial HÖLDER constant to the exponent β for F that becomes small as T is getting small.

The next step is to find a temporal HÖLDER constant to the exponent $\frac{\beta}{2}$. This is approached by estimating the difference of the values of F at different times:

$$
\begin{aligned}
|F(\tau,\xi)-F(\sigma,\xi)| \;\leq\; & L^2 D|\Theta(\tau)-\Theta(\sigma)|\|\partial_{\xi\xi}\tilde{a'}_1\|_{C^0} \\
& + L^2 D|\Theta(\sigma)|H\ddot{o}l_{P,\beta}(\partial_{\xi\xi}\tilde{a'}_1)|\tau-\sigma|^{\frac{\beta}{2}} \\
& + |\Sigma_2(\tau,\xi)-\Sigma_1(\tau,\xi)|\; H\ddot{o}l_{t,\frac{1+\beta}{2}}(\partial_\xi\tilde{a'}_1)\;|\tau-\sigma|^{\frac{1+\beta}{2}} \\
& + \left(|\Sigma_2(\tau,\xi)-\Sigma_1(\tau,\xi)-\Sigma_2(\sigma,\xi)-\Sigma_1(\sigma,\xi)|\right)\|\partial_\xi\tilde{a'}_1\|_{C^0}
\end{aligned}
$$

with Θ, Σ_1, and Σ_2 being defined as in (4.90). The terms

$$
|\Theta(\tau)| \qquad \text{and} \qquad |\Sigma_2(\tau,\xi)-\Sigma_1(\tau,\xi)|
$$

have already been treated in the estimate for E_1 and in (4.97), respectively. We therefore focus on

$$
|\Theta(\tau)-\Theta(\sigma)|
$$

and the last term.

We start with the first term, again assuming τ and σ to be not larger than T which is bounded from above by T^*. In that case, Θ is differentiable as algebraic combination of l and r with denominator bounded away from zero. We can therefore write

$$
|\Theta(\tau)-\Theta(\sigma)| \leq \|\dot{\Theta}\|_{C^0}|\tau-\sigma|
$$

and estimate $\dot{\Theta}$ by writing the coefficient Θ as

$$
\Theta(\tau) = \frac{1}{L_2(\tau)^2} - \frac{1}{L_1(\tau)^2}
$$

with the abbreviation

$$
L_i(\tau) := r_i(\tau) - l_i(\tau) \qquad\qquad (i=1,2).
$$

The derivative of L_i is clearly given by

$$
\dot{L}_i(\tau) = \dot{r}_i(\tau) - \dot{l}_i(\tau)
$$

and we calculate for $\dot{\Theta}$ under the assumption $\tau \leq T \leq T^*$:

$$
\begin{aligned}
|\dot{\Theta}| \;\leq\; & \left|\frac{-2\dot{L}_2}{L_2^3} + \frac{2\dot{L}_1}{L_1^3}\right| \\
= \; & \frac{2}{L_1^3 L_2^3}\left|-\dot{L}_2 L_1^3 + \dot{L}_1 L_2^3\right| \\
\leq \; & \frac{2}{d(T)^6}\left(|\dot{l}_2-\dot{r}_2|\;|L_1^3-L_2^3| + |\dot{l}_2-\dot{r}_2-\dot{l}_1+\dot{r}_1|L_2^3\right).
\end{aligned}
$$

The term $|L_1^3 - L_2^3|$ is bounded by

$$
\begin{aligned}
|L_1^3-L_2^3| \;=\; & |(L_1-L_2)^3 - L_1L_2(L_2-L_1)| \;=\; |L_1-L_2|\;|L_1^2+L_2^2-L_1L_2| \\
\leq \; & \omega T^{1+\frac{1+\beta}{2}}\left(L_{max}(T)^2 + L_{max}(T)^2 - d(T)^2\right)
\end{aligned}
$$

and we obtain

$$\begin{aligned}|\dot{\Theta}| &\leq \frac{2}{d(T)^6}\left(2\bar{V}(T)\omega T^{1+\frac{1+\beta}{2}}(2L_{max}(T)^2 - d(T)^2) + L_{max}(T)^3\omega T^{\frac{1+\beta}{2}}\right)\\ &\leq \frac{64}{L^6}\left(2\bar{V}(T)TL^2\left(\frac{9}{2}-\frac{1}{4}\right)+\frac{27}{8}L^3\right)\omega T^{\frac{1+\beta}{2}} = \frac{352}{L^3}\omega T^{\frac{1+\beta}{2}}\end{aligned}$$

and consequently

$$|\Theta(\tau)-\Theta(\sigma)| \leq \frac{352}{L^3}\omega T^{\frac{1+\beta}{2}}|\tau-\sigma|. \tag{4.99}$$

For the term

$$|\Sigma_2(\tau,\xi)-\Sigma_1(\tau,\xi)-\Sigma_2(\sigma,\xi)+\Sigma_1(\sigma,\xi)|$$

we write Σ_i in the more concise form

$$\Sigma_i(\tau,\xi) = \frac{\xi\dot{L}_i(\tau) - L\dot{l}_i(\tau)}{L_i(\tau)}$$

and can now calculate

$$\begin{aligned}&|\Sigma_2(\tau,\xi)-\Sigma_1(\tau,\xi)-\Sigma_2(\sigma,\xi)+\Sigma_1(\sigma,\xi)|\\ &\leq \frac{\xi}{d(T)^4}\Big|\dot{L}_2(\tau)L_1(\tau)L_2(\sigma)L_1(\sigma) - L_2(\tau)\dot{L}_2(\tau)L_2(\sigma)L_1(\sigma)\\ &\qquad -L_2(\tau)L_1(\tau)\dot{L}_2(\sigma)L_1(\sigma) + \dot{L}_2(\tau)L_1(\tau)L_2(\sigma)\dot{L}_1(\sigma)\Big|\\ &\quad + \frac{L}{d(T)^4}\Big|\dot{l}_2(\tau)L_1(\tau)L_2(\sigma)L_1(\sigma) - L_2(\tau)\dot{l}_2(\tau)L_2(\sigma)L_1(\sigma)\\ &\qquad -L_2(\tau)L_1(\tau)\dot{l}_2(\sigma)L_1(\sigma) + \dot{L}_2(\tau)L_1(\tau)L_2(\sigma)\dot{l}_1(\sigma)\Big|.\end{aligned}$$

The first term of this sum is estimated by splitting it up into two more terms as follows:

$$\begin{aligned}&\Big|L_1(\tau)L_1(\sigma)(\dot{L}_2(\tau)L_2(\sigma) - \dot{L}_2(\sigma)L_2(\tau)) - L_2(\sigma)L_2(\tau)(\dot{L}_1(\tau)L_1(\sigma) - \dot{L}_1(\sigma)L_1(\tau))\Big|\\ &\leq L_1(\sigma)L_2(\sigma)\Big(|L_1(\tau)-L_2(\tau)|\,|\dot{L}_2(\tau)-\dot{L}_2(\sigma)|\\ &\qquad +L_2(\tau)|\dot{L}_1(\tau)-\dot{L}_2(\tau)-\dot{L}_1(\sigma)+\dot{L}_2(\sigma)|\Big)\\ &\quad + \Big|L_1(\tau)L_1(\sigma)(L_2(\tau)-L_2(\sigma))\dot{L}_2(\sigma) - L_2(\tau)L_2(\sigma)(L_1(\tau)-L_1(\sigma))\dot{L}_1(\sigma)\Big|\\ &=: E_1 + E_2.\end{aligned}$$

The term E_1 can be estimated directly to be

$$E_1 \leq L_{max}(T)^2\left(2\omega T^{1+\frac{1+\beta}{2}}\Lambda_1|\tau-\sigma|^{\frac{1+\beta}{2}} + L_{max}(T)\omega|\tau-\sigma|^{\frac{1+\beta}{2}}\right).$$

The term E_2 is split up even further to

$$\begin{aligned} E_2 &\leq |L_2(\tau)-L_2(\sigma)|\,|L_1(\tau)L_1(\sigma)\dot{L}_2(\sigma)-L_2(\tau)L_2(\sigma)\dot{L}_1(\sigma)| \\ &\quad +|\dot{L}_1(\sigma)L_2(\tau)L_2(\sigma)|\,|L_2(\tau)-L_2(\sigma)-L_1(\tau)+L_1(\sigma)| \\ &\leq 2\bar{V}(T)|\tau-\sigma|\left(L_{max}(T)^2\omega T^{\frac{1+\beta}{2}}+2\bar{V}(T)L_{max}(T)\omega T^{1+\frac{1+\beta}{2}}\right) \\ &\quad +2\bar{V}(T)L_{max}(T)^2\omega T^{\frac{1+\beta}{2}}|\tau-\sigma|. \end{aligned}$$

Very similarly, we obtain for the second part with $\dot{l}_i$ in place of $\dot{L}_i$:

$$\begin{aligned} &\Big|\dot{l}_2(\tau)L_1(\tau)L_2(\sigma)L_1(\sigma)-L_2(\tau)\dot{l}_2(\tau)L_2(\sigma)L_1(\sigma) \\ &-L_2(\tau)L_1(\tau)\dot{l}_2(\sigma)L_1(\sigma)+\dot{L}_2(\tau)L_1(\tau)L_2(\sigma)\dot{l}_1(\sigma)\Big| \\ &\leq L_{max}(T)^2\left(\Lambda_1 T^{1+\frac{1+\beta}{2}}+L_{max}(T)\right)\omega|\tau-\sigma|^{\frac{1+\beta}{2}}+\bar{V}(T)L_{max}(T)^2T^{\frac{1+\beta}{2}}\omega|\tau-\sigma| \\ &+2\bar{V}(T)\left(L_{max}(T)^2+\bar{V}(T)L_{max}(T)T\right)T^{\frac{1+\beta}{2}}\omega|\tau-\sigma|. \end{aligned}$$

Besides some missing factors 2, this is precisely the same as the first part we estimated, and we therefore use the same bound for both terms:

$$\begin{aligned} &|\Sigma_2(\tau,\xi)-\Sigma_1(\tau,\xi)-\Sigma_2(\sigma,\xi)+\Sigma_1(\sigma,\xi)| \\ &\leq \frac{(\xi+L)L_{max}(T)^2}{d(T)^4}\omega|\tau-\sigma|^{\frac{1+\beta}{2}}\times \\ &\quad\times\left(L_{max}(T)+2\Lambda_1T^{1+\frac{1+\beta}{2}}+4\bar{V}(T)|\tau-\sigma|^{\frac{1-\beta}{2}}T^{\frac{1+\beta}{2}}\left(1+\frac{\bar{V}(T)T}{L_{max}(T)}\right)\right) \\ &\leq \frac{48}{L^2}\left(\frac{9}{4}L^2+\frac{3}{8}L^2+\frac{3}{2}L^2+\frac{L^2}{4}\right)T^{\frac{1}{2}}\omega|\tau-\sigma|^{\frac{\beta}{2}} \quad\leq\quad 210\;T^{\frac{1}{2}}\omega|\tau-\sigma|^{\frac{\beta}{2}}. \end{aligned}$$

The temporal Hölder constant for F is therefore given by

$$\begin{aligned} \frac{|F(\tau,\xi)-F(\sigma,\xi)|}{|\tau-\sigma|^{\frac{\beta}{2}}} &\leq \left(\frac{352\;DT}{L}\|\partial_{\xi\xi}\tilde{a'}_1\|_{C^0}T^{\frac{1-\beta}{2}}+\frac{48\;DT}{L}H\ddot{o}l_{P,\beta}(\partial_{\xi\xi}\tilde{a'}_1)\right. \\ &\quad \left.+8H\ddot{o}l_{t,\frac{1+\beta}{2}}(\partial_{xi}\tilde{a'}_1)T+210\|\partial_\xi\tilde{a'}_1\|_{C^0}T^{\frac{1-\beta}{2}}\right)\omega \\ &\leq K_{F,t}(D,L,T^*)\|\tilde{a'}_1\|_{C^{2+\beta,P}}\omega. \end{aligned} \tag{4.100}$$

We finally estimate the maximum of F by

$$\begin{aligned} |F(\tau,\xi)| &\leq L^2D\;|\Theta(\tau)|\;\|\partial_{\xi\xi}\tilde{a'}_1\|_{C^0}+|\Sigma_2(\tau,\xi)-\Sigma_1(\tau,\xi)|\;\|\partial_\xi\tilde{a'}_1\|_{C^0} \\ &\leq \frac{48\;D}{L}T^{1+\frac{1+2\beta}{2}}\omega\|\partial_{\xi\xi}\tilde{a'}_1\|_{C^0}+8T^{\frac{1+2\beta}{2}}\omega\|\partial_\xi\tilde{a'}_1\|_{C^0} \\ &\leq K_{F,0}(D,L,T^*)\|\tilde{a'}_1\|_{C^{2+\beta,P}}\omega. \end{aligned} \tag{4.101}$$

Together we find as a very crude estimate for the right hand side F:

$$\|F\|_{C^{0+\beta,P}}\leq K_F(D,L,T^*)\|\tilde{a'}_1\|_{C^{2+\beta,P}}\;\omega \tag{4.102}$$

where K_F is just the sum of the previously introduced constants from the estimates of the maximum value and the spatial and temporal HÖLDER constants of F:

$$K_F = K_{F,0} + K_{F,x} + K_{F,t}.$$

Very similar calculations lead to estimates for the inhomogeneity g in the boundary conditions. We already noted that we are going to interpolate g linearly in space between the points $(\tau, 0)$ and (τ, L) which reads

$$\begin{aligned} g(\tau,\xi) &= g(\tau,0)\left(1-\frac{\xi}{L}\right) + g(\tau,L)\frac{\xi}{L} \\ &= \left[\dot{l}_2(\tau)(r_2(\tau)-l_2(\tau)) - \dot{l}_1(\tau)(r_1(\tau)-l_1(\tau))\right]\tilde{a'}_1(\tau,0)\left(1-\frac{\xi}{L}\right) \\ &\quad + \left[\dot{r}_2(\tau)(r_2(\tau)-l_2(\tau)) - \dot{r}_1(\tau)(r_1(\tau)-l_1(\tau))\right]\tilde{a'}_1(\tau,L)\frac{\xi}{L} \\ &=: \Xi_l(\tau)\tilde{a'}_1(\tau,0)\left(1-\frac{\xi}{L}\right) + \Xi_r(\tau)\tilde{a'}_1(\tau,L)\frac{\xi}{L}. \end{aligned} \tag{4.103}$$

For the maximum of g we readily obtain

$$|g(\tau,\xi)| \leq |\Xi_l(\tau)|\ \|\tilde{a'}_1\|_{C^0} + |\Xi_r(\tau)|\ \|\tilde{a'}_1\|_{C^0} \tag{4.104}$$

and further, again assuming $\tau \leq T \leq T^*$,

$$\begin{aligned} |\Xi_r(\tau)| &\leq |\dot{r}_2(\tau) - \dot{r}_1(\tau)|\ |r_2(\tau) - l_2(\tau)| + |\dot{r}_1(\tau)|\ |r_2(\tau) - r_1(\tau) - l_2(\tau) + l_1(\tau)| \\ &\leq T^{\frac{1+\beta}{2}}\omega L_{max}(T) + \bar{V}(T)\omega T^{1+\frac{1+\beta}{2}} \leq \frac{7}{4}LT^{\frac{1+\beta}{2}}\omega. \end{aligned}$$

and likewise for $\Xi_l(\tau)$ which then leads to

$$\|g\|_{C^0} \leq \frac{7}{2}L\|\tilde{a'}_1\|_{C^0}T^{\frac{1+\beta}{2}}\omega. \tag{4.105}$$

The estimate for the spatial derivative of g is particularly simple since we chose it to be linear in space:

$$\partial_\xi g(\tau,\xi) \equiv \frac{g(\tau,L) - g(\tau,0)}{L}$$

and we immediately have as a bound on this derivative the following:

$$|\partial_\xi g(\tau,\xi)| \leq \frac{1}{L}(|g(\tau,L)| + |g(\tau,0)|) \leq 7\|\tilde{a'}_1\|_{C^0}T^{\frac{1+\beta}{2}}\omega. \tag{4.106}$$

Moreover, we find the spatial variation of the derivative to vanish identically by construction

$$|\partial_\xi g(\tau,\xi) - \partial_\xi g(\tau,\eta)| \equiv 0. \tag{4.107}$$

It remains to calculate the temporal variation of g and its spatial derivative. We

start with

$$\begin{aligned}|g(\tau,\xi)-g(\sigma,\xi)| &\leq \left(1-\frac{\xi}{L}\right)|\Xi_l(\tau)\tilde{a'}_1(\tau,0)-\Xi_l(\sigma)\tilde{a'}_1(\sigma,0)| \\ &\quad +\frac{\xi}{L}|\Xi_r(\tau)\tilde{a'}_1(\tau,L)-\Xi_r(\sigma)\tilde{a'}_1(\sigma,L)| \\ &\leq |\Xi_l(\tau)-\Xi_l(\sigma)|\|\tilde{a'}_1\|_{C^0}+|\Xi_l(\sigma)|\|\partial_t\tilde{a'}_1\|_{C^0}|\tau-\sigma| \\ &\quad +|\Xi_r(\tau)-\Xi_r(\sigma)|\|\tilde{a'}_1\|_{C^0}+|\Xi_r(\sigma)|\|\partial_t\tilde{a'}_1\|_{C^0}|\tau-\sigma|.\end{aligned}$$

For the first terms in each of the last two lines we derive the following estimate

$$\begin{aligned}&|\Xi_l(\tau)-\Xi_l(\sigma)| \\ &= \left|\dot{l}_2(\tau)L_2(\tau)-\dot{l}_1(\tau)L_1(\tau)-\dot{l}_2(\sigma)L_2(\sigma)+\dot{l}_1(\sigma)L_1(\sigma)\right| \\ &\leq \left|(\dot{l}_2(\tau)-\dot{l}_2(\sigma))(L_2(\tau)-L_1(\tau)) \;+\; L_1(\tau)(\dot{l}_2(\tau)-\dot{l}_2(\sigma)-\dot{l}_1(\tau)+\dot{l}_1(\sigma))\right| \\ &\quad + \left|(\dot{l}_2(\sigma)-\dot{l}_1(\sigma))(L_2(\tau)-L_2(\sigma)) \;+\; \dot{l}_1(\sigma)(L_2(\tau)-L_2(\sigma)-L_1(\tau)+L_1(\sigma))\right| \\ &\leq \Lambda_1|\tau-\sigma|^{\frac{1+\beta}{2}}\omega T^{1+\frac{1+\beta}{2}} \;+\; \omega|\tau-\sigma|^{\frac{1+\beta}{2}}+(2+1)\left(\omega T^{\frac{1+\beta}{2}}\bar{V}(T)|\tau-\sigma|\right).\end{aligned}$$

The same formula is true with r replacing l, and we obtain for the temporal HÖLDER constant of g:

$$\begin{aligned}H\ddot{o}l_{t,\frac{1+\beta}{2}}(g) &= \sup_{0\leq\sigma<\tau\leq T,\xi\in[0,L]}\frac{|g(\xi,\tau)-g(\xi,\sigma)|}{|\tau-\sigma|^{\frac{1+\beta}{2}}} \\ &\leq 2\left[\|\tilde{a'}_1\|_{C^0}\left(\Lambda_1 T^{\frac{3+2\beta}{2}}+1+3\bar{V}(T)T^{\frac{2-\beta}{2}}\right)+\frac{7}{4}\|\partial_t\tilde{a'}_1\|_{C^0}LT^{\frac{2-\beta}{2}}\right]\omega \\ &\leq K_{g,t}(L,T^*)\|\tilde{a'}_1\|_{C^{2+\beta,P}}\omega\end{aligned}$$

whenever we make the usual assumption $T\leq T^*$. The only point to note is that the term

$$\bar{V}(T)T^{\frac{2-\beta}{2}}$$

does not decrease as T increases. This is obvious by the definition of $\bar{V}(T)$:

$$\bar{V}(T)T^{\frac{2-\beta}{2}}=\max\{|v_{r0}|,|v_{l0}|\}T^{\frac{2-\beta}{2}}+\Lambda_1 T^{\frac{3}{2}}$$

wherein both terms decrease as T does.

Similarly, we proceed for the temporal contribution to the parabolic HÖLDER constant of $\partial_x g$. We find

$$\begin{aligned}|\partial_\xi g(\tau,\xi)-\partial_\xi g(\sigma,\xi)| &\leq \frac{1}{L}|g(\tau,L)-g(\tau,0)-g(\sigma,L)+g(\sigma,0)| \\ &\leq \sup_{\xi\in[0,L]}\frac{2}{L}|g(\tau,\xi)-g(\sigma,\xi)|\end{aligned}$$

where the first step again reflects the linear interpolation of g with respect to space.

Using now the results just obtained, we arrive at

$$\begin{aligned} H\ddot{o}l_{P,\beta}(\partial_\xi g) = & \sup_{0\le\sigma<\tau\le T} \frac{|\partial_\xi g(\tau,L)-\partial_\xi g(\sigma,L)-\partial_\xi g(\tau,0)+\partial_\xi g(\sigma,0)|}{|\tau-\sigma|^{\frac{\beta}{2}}} \\ \le & \frac{4}{L}\left[\|\tilde{a'}_1\|_{C^0}\left(\Lambda_1 T^{\frac{4+2\beta}{2}}+T^{\frac{1}{2}}+3\bar{V}(T)T^{\frac{3-\beta}{2}}\right)+\frac{7}{4}\|\partial_t\tilde{a'}_1\|_{C^0}LT^{\frac{3-\beta}{2}}\right]\omega \\ \le & K_{g,P}(L,T^*)\|\tilde{a'}_1\|_{C^{2+\beta,P}}\omega. \end{aligned}$$

Putting the single estimates together, we find the following parabolic HÖLDER norm for g:

$$\|g\|_{C^{1+\beta,P}} \le K_g(L,T^*)\|\tilde{a'}_1\|_{C^{2+\beta,P}}\omega \tag{4.108}$$

where

$$K_g = \frac{7}{2}L\ T^{*\ \frac{1+\beta}{2}} + K_{g,P} + K_{g,t}. \tag{4.109}$$

Having bounds on the inhomogeneities F and g and recalling that w satisfies zero initial conditions, we will now deduce estimates for w from theorem 4.9, or rather from remark 4.10 thereafter.

Estimates for w

As w is identically zero at $\tau = 0$ and belongs to $C^{2+\beta,P}$, we can estimate

$$\begin{aligned} |w(\tau,\xi)| \le & \quad \|\partial_\tau w\|_{C^0}\tau \le & \|w\|_{C^{2+\beta,P}}\ \tau \\ |\partial_\xi w(\tau,\xi)| \le & \quad H\ddot{o}l_{t,\frac{1+\beta}{2}}(\partial_\xi w)\tau^{\frac{1+\beta}{2}} \le & \|w\|_{C^{2+\beta,P}}\ \tau^{\frac{1+\beta}{2}} \\ |\partial_{\xi\xi} w(\tau,\xi)| \le & \quad H\ddot{o}l_{P,\beta}(\partial_{\xi\xi} w)\tau^{\frac{\beta}{2}} \le & \|w\|_{C^{2+\beta,P}}\ \tau^{\frac{\beta}{2}} \\ |\partial_\tau w(\tau,\xi)| \le & \ |\partial_\tau w(0,\xi)| + H\ddot{o}l_{P,\beta}(\partial_\tau w)\tau^{\frac{\beta}{2}} \le & \|w\|_{C^{2+\beta,P}}\ \tau^{\frac{\beta}{2}} \end{aligned}$$

where we already used that by continuity of the derivatives, w satisfies its governing equation also at $\tau = 0$, and therefore $\partial_\tau w(0,\xi) = 0$ since the right hand side vanishes at $\tau = 0$. This is immediately seen by noting that all the terms including w vanish due to the initial conditions and since $F(0,\xi)$ satisfies:

$$F(0,\xi) \ = \ L^2 D\Theta(0)\partial_{\xi\xi}\tilde{a'}_1 + (\Sigma_2(0,\xi)-\Sigma_1(0,\xi))\partial_\xi\tilde{a'}_1 \ = \ 0$$

where Θ and $\Sigma_2-\Sigma_1$ vanish at $\tau = 0$ since the boundary curves l_1 and l_2 (respectively r_1 and r_2) start at the same value 0 (respectively L) with the same velocity v_{l0} (respectively v_{r0}).

As an immediate consequence we conclude that the $C^{2_x,1_t}$-norm of w can be made small for small times whenever its parabolic HÖLDER norm is small:

$$\|w\|_{C^{2_x,1_t}} \le T^{*\ \frac{2+\beta}{2}}\ T^{\frac{\beta}{2}}\|w\|_{C^{2+\beta,P}}.$$

By the estimate from remark 4.10 we know the boundedness of the latter norm by

$$\|w\|_{C^{2+\beta,P}} \le \hat{C}(T)\left(\|F\|_{C^{0+\beta,P}} + \|g\|_{C^{1+\beta,P}}\right)$$

where $\hat{C}(T)$ is the constant defined in lemma 4.15 and besides T only depends on L,

D, Λ_1, β, and the relevant HÖLDER norms of the initial conditions (which in this case vanish) and the coefficient function φ. Moreover, it decreases with increasing T.

For the norms in the parentheses on the right hand sides we just derived the estimates (4.102) and (4.108) where we found them to be bounded by some multiple of

$$\omega \|\tilde{a'}_1\|_{C^{2+\beta}}$$

with factors only depending on the above mentioned parameters and moreover non-decreasing in T. If we now choose T to be not greater than T_1 which is defined in the proof of lemma 4.15 (and by construction is at most T^*) we can in addition assert that this norm is bounded by Υ_1.

Replacing the assumption $T \leq T^*$ by $T \leq T_1$ in the estimates for F and g, we conclude:

$$\|w\|_{C^{2_x,1_t}} \leq \hat{C}(T_1) T_1^{\frac{2+\beta}{2}} (K_F(T_1) + K_g(T_1)) \Upsilon_1 \omega T^{\frac{\beta}{2}}. \tag{4.110}$$

Choosing T to be not bigger than T_2 which shall be the minimum of T_1 and

$$\tilde{T}_2 = \left(\frac{1}{4} \hat{C}(T_1) T_1^{\frac{2+\beta}{2}} (K_F(T_1) + K_g(T_1)) \Upsilon_1 \right)^{-\frac{2}{\beta}} \tag{4.111}$$

we find the desired contraction property for w:

$$\|w\|_{C^{2_x,1_t}} \leq \frac{\omega}{4}. \tag{4.112}$$

Estimates for λ *and* ϱ

We recall that the differences

$$\lambda = l_2 - l_1 \qquad \text{and} \qquad \varrho = r_2 - r_1$$

satisfy the initial value problems (4.87) and (4.88), respectively. By the calculations in the proof of corollary 4.7 we readily find

$$Lip(\dot{\lambda}) \leq \delta \kappa_B \|\tilde{a}_2 - \tilde{a}_1\|_{C^{2_x,1_t}} \leq \delta \kappa_B \omega \tag{4.113}$$

and literally the same estimate is obtained for $Lip(\dot{\varrho})$. Direct computations show

$$\begin{aligned} H\ddot{o}l_{\frac{1+\beta}{2}}(\dot{\lambda}) &\leq \delta \kappa_B \omega T^{\frac{1-\beta}{2}} \\ \|\dot{\lambda}\|_{C^0} &\leq 0 + Lip(\dot{\lambda}) T \leq \delta \kappa_B \omega T^{1+\frac{1-\beta}{2}} \\ &\leq \delta \kappa_B T \omega T^{\frac{1-\beta}{2}} \\ \|\lambda\|_{C^0} &\leq 0 + \|\dot{\lambda}\|_{C^0} T \leq \delta \kappa_B T^2 \omega T^{\frac{1-\beta}{2}}. \end{aligned}$$

and consequently

$$\|\lambda\|_{C^{1+\frac{1+\beta}{2}}} \leq \delta \kappa_B \left(1 + T + T^2\right) \omega T^{\frac{1-\beta}{2}} \tag{4.114}$$

The very same estimates hold for ϱ as well. It should be noted that we used the initial conditions $\lambda(0) = 0$ and $\dot{\lambda}(0) = v_{l0} - v_{l0} = 0$.

We now assume again T to be not greater than T_2 and define

$$\tilde{T}_3 = \left(\frac{1}{4} \delta \kappa_B \left(1 + T_2 + T_2^2 \right) \right)^{-\frac{2}{1-\beta}}. \tag{4.115}$$

Then, for

$$T \leq T_3 = \min\{T_2, \tilde{T}_3\},$$

we conclude

$$\|\lambda\|_{C^{1+\frac{1+\beta}{2}}} \leq \frac{\omega}{4} \tag{4.116}$$

$$\|\varrho\|_{C^{1+\frac{1+\beta}{2}}} \leq \frac{\omega}{4}. \tag{4.117}$$

The crucial point is that the time T_3 does not depend on the particular pair $(l_1, r_1, \tilde{a}_1)$, $(l_2, r_2, \tilde{a}_2)$ but only on the bounds on $\mathcal{B}_T$ and the given parameters and initial conditions.

Together we find that for each $T \leq T_3$,

$$\|(\lambda, \varrho, w)\|_{X_T} \leq \frac{3}{4} \|(l_2, r_2, \tilde{a}_2) - (l_1, r_1, \tilde{a}_1)\|_{X_T} \tag{4.118}$$

and therefore the operator A is a $\frac{3}{4}$-contraction in $\mathcal{B}_T$ for any $T \leq T_3$ and thus, by the contraction mapping theorem, possesses a unique fixed point

$$(l_*, \tilde{r}_*, \tilde{a}_*) \in \mathcal{B}_T.$$

We summarize our conclusion in the following theorem.

Theorem 4.16. *Let $\beta \in (0,1)$ be given. Assume the given initial conditions $a_0 \in C^{2+\beta}([0,L])$ to satisfy the compatibility condition 2.3.2. Assume furthermore a_0 to satisfy*

$$a^{BP} < a_0(x) < a_P$$

for each $x \in [0,L]$. Let finally

$$\varphi, f \in C^{0+\beta, P}$$

be given.

Then, there exists a constant $\Lambda_1 > 0$ and a time $T_3 > 0$ such that for any $T \in (0, T_3]$, the problem (4.45) - (4.48), (4.49), (4.50) has a unique solution $(l_*, \tilde{r}_*, \tilde{a}_*)$ belonging to $\mathcal{B}_T$ as defined in (4.78).

Moreover, this solution in fact belongs to $Y_T \cap \mathcal{B}_T$.

Corollary 4.17. *By transforming everything back to physical coordinates (t,x), under the hypotheses of theorem 4.16, we obtain for T_3 as therein and any $T \in (0, T_3]$ the existence and uniqueness of a space-time domain Q_T with lateral boundary of class $C^{1+\frac{1+\beta}{2}}$, and on that domain a unique solution a_* of the problem (4.7) - (4.9) with initial conditions a_0. Together, this space-time domain and the solution a_* comprise a unique solution to the parabolic free boundary problem.*

Remark 4.18. *We note that the time T_3 strongly depends on the choice of β. One might try to find an optimal $\beta \in (0,1)$ where optimal means that the corresponding time T_3 is as large as possible. However, this shall not be our aim at this point.*

4.1.6 Construction of a solution to the full problem

In the previous subsection we found a unique solution to the parabolic free boundary problem describing

a) the space-time domain Q_T and thereby the spatial extension of the cell in dependence on time, and

b) the monomer density a in that space-time domain.

Furthermore, we showed some a priori estimates for the boundary velocities and the monomer density.

Moreover, in subsection 4.1.3, we proved the existence and uniqueness of a solution to the hyperbolic characteristic initial boundary value problem under the assumption of a given solution to the parabolic free boundary problem. The corresponding estimates are given in subsection 4.1.4.

To obtain a solution to the full problem we are going to exploit once more the contraction mapping principle, now in a space describing all quantities we are interested in.

Following the lines of the previous subsection we consider again the transformed system in the fixed space-time domain $[0,T] \times [0,L]$. On that domain we define the spaces

$$V_T := X_T \times \left(C_b^{0+\beta,P}([0,T] \times \mathbb{R}) \right)^4 \tag{4.119}$$

and

$$W_T := Y_T \times \left(C_b^1([0,T] \times \mathbb{R}) \right)^4 \tag{4.120}$$

where the subscript b means that the end densities u are required to be bounded together with their HÖLDER constant, or respectively their first derivatives.

We could also have chosen the transformed end densities to be only given on the domain $\overline{Q_T}$. In that case we would have asked for these densities to vanish on the lateral boundaries. Instead we chose them to be defined in all of $[0,T] \times \mathbb{R}$ by extending them by zero outside the domain. This conveniently reflects the desired regularity at the boundary. The major advantage of this setting is that our operator to be defined below may now generically take values in W_T for which the support of the end densities does not coincide with the domain prescribed by the (virtual) boundary curves. The fixed point we are going to find will however satisfy these conditions.

The spaces V_T and W_T shall be equipped with the norms

$$\|(l,r,\tilde{a},\tilde{u})\|_{V_T} := \|(l,r,\tilde{a})\|_{X_T} + \max_{\alpha=1,\dots,4} \|\tilde{u}^\alpha\|_{C^{0+\beta,P}} \tag{4.121}$$

and

$$\|(l,r,\tilde{a},\tilde{u})\|_{W_T} := \|(l,r,\tilde{a})\|_{Y_T} + \max_{\alpha=1,\dots,4} \|\tilde{u}^\alpha\|_{C^1}, \tag{4.122}$$

respectively.

As before, we assume to be given initial conditions

$$a_0 \in C^{2+\beta}([0,L])$$

satisfying the compatibility conditions 2.3.2. In addition, we assume to have initial conditions

$$u_0 \in C^1([0,L])$$

for the end densities which shall satisfy the conditions 2.3.1. For these, we are trying to find a solution (l_*, r_*, a_*, u_*).

As we plan to use a contraction principle, we require a closed bounded subset of V_T on which we can define an operator having a fixed point. For sufficiently small $T > 0$ to be determined later, this subset will be given by

$$\begin{aligned}
\mathcal{C}_T \quad = \quad & \Big\{ (l,\tilde r,\tilde a,u) \in \mathcal{B}_T \times \Big(C_b^{0+\beta,P}([0,T]\times\mathbb{R}) \Big)^4 \;\Big|\; a^{BP} \le \tilde a \le a_P, \|\partial_\xi \tilde a\|_{C^0} \le \Upsilon_0 \\
& \dot l(\tau) = c_1^1 \tilde a(\tau,0) + c_2^1,\ \dot r(\tau) = c_1^4 \tilde a(\tau,L) + c_2^4 \quad \text{for } \tau \in [0,T], \qquad (4.123) \\
& \max_{\alpha=1,\dots,4} \|u^\alpha\|_{C^{0+\beta,P}} \le \Upsilon_2, \\
& \operatorname{supp} u \subset [0,T] \times \left[-\frac{L}{4}, \frac{5}{4} L \right],\ u(0,\cdot) = u_0,\ a(0,\cdot) = a_0 \Big\}
\end{aligned}$$

On this set we want to define a contraction A by stating that

$$(l', \tilde{r'}, \tilde{a'}, u') := A(l, \tilde r, \tilde a, u) \qquad (4.124)$$

is composed of the solution $(l', \tilde{r'}, \tilde{a'})$ of the parabolic free boundary problem with initial data a_0 for the monomer density and initial values for the boundary velocities being compatible to those where in (4.45) the coefficient functions $\tilde\varphi$ and $\tilde f$ are the transforms of cu and $\tilde c u$, respectively. The function u' in turn shall be the restriction to Q_T of the solution to the CAUCHY problem (4.24) with the velocity matrix determined by the transform a of $\tilde a$. In this case, Q_T shall denote the space-time domain with lateral boundaries given by l and $r = \tilde r + L$.

The first thing to check is that this operator maps $\mathcal{C}_T$ into itself if only the parameters Λ_1, $\varepsilon_{1/2}$, and $\Upsilon_{0/1/2}$ are chosen appropriately and if T is sufficiently small.

Lemma 4.19. *Fix $\beta \in (0,1)$, let*

$$a_0 \in C^{2+\beta}([0,L]) \qquad \text{and} \qquad u_0 \in \left(C_0^2([0,L])\right)^4$$

be given such that

a) a_0 satisfies the compatibility condition 2.3.2 and

$$a^{BP} < a_0(x) \le a_P \qquad \text{for each } x \in [0,L].$$

b) u_0 satisfies the compatibility conditions 2.3.1 with u^1 being positive in some interval $(0,x_1)$ and u^4 being positive in some interval (x_2,L).

Define

$$M_0 := \|u_0\|_{C^0}, \qquad M_1 := \left\| \frac{d}{dx} u_0 \right\|_{C^0}, \qquad M_2 := \|a_0\|_{C^{2+\beta}}, \qquad M_3 := \left\| \frac{d^2}{dx^2} u_0 \right\|_{C^0}.$$

Given Λ_1, let $\varepsilon_1(T)$, $\varepsilon_2(T)$, $\bar V(T)$, and T^* be defined as in lemma 4.15. Choose some

arbitrary, small number $\varepsilon_3 > 0$ *and define* v_{max} *by (4.39) with* a_P *being replaced by* $(1+\varepsilon_3)a_P$*, put*

$$\Upsilon_2 = 3\left(M_0 + \left(\frac{3}{2}L\right)^{1-\beta} M_1\right).$$

Choose moreover Υ_1 *to be*

$$\Upsilon_1 = \hat{C}(T^*)(M_2 + \tilde{K}_2\Upsilon_2)$$

where $\hat{C}(T)$ *is defined as in lemma 4.15 but with* $K_2\Upsilon_2$ *replacing* $\|\tilde{\varphi}\|_{C^{0+\beta}}$ *(The constants* K_2 *and* $\tilde{K}_2$ *will be specified in the proof). Put finally*

$$\Upsilon_0 = 2\check{C}(\bar{V}(T^*), D, L, \delta\kappa_B(a_P - a^{BP}), a_P, \Upsilon_2)$$

where $\check{C}$ *shall denote the right hand side of estimate (4.64) in lemma 4.13 with* Υ_2 *plugged in as upper bound for* $\|u\|_{C^0}$ *and with* a^{BP} *replacing* a_B *as lower bound on the monomer density.*

Then, there exists $T_1 \in (0, T^*]$ *such that for each* $T \in (0, T_1]$*, the operator* A *from (4.124) maps* $\mathcal{C}_T$ *into (a compact subset of) itself.*

Proof. By theorem 4.16, we find some time $T_3 \in (0, T^*]$ and for each $T \in (0, T_3]$ a solution $(l', \tilde{r'}, \tilde{a'})$ to the parabolic free boundary problem that in fact belongs to Y_T, and we already know some properties of this solution:

- $l', \tilde{r'} \in C^{1+1}([0,T])$
- $\tilde{a} \in C^{2+\beta,P}(\overline{Q_T})$ where Q_T is defined by its lateral boundary being given by l' and $\tilde{r'}$
- The boundary curve solutions satisfy the estimates (cf. lemma 4.15)

$$\begin{aligned} H\ddot{o}l_{\frac{1+\beta}{2}}(\dot{l'}) &\leq \Lambda_1 \\ \|\dot{l'} - v_{l0}\|_{C^0} &\leq \varepsilon_2(T) = \Lambda_1 T^{\frac{1+\beta}{2}} \\ \|l'\|_{C^0} &\leq \varepsilon_1(T) = (\max\{v_{r0}, v_{l0}\} + \varepsilon_2(T)). \end{aligned}$$

  At this point it is only crucial to choose T_3 sufficiently small such that

$$\delta\kappa_B\Upsilon_1 T_3^{\frac{1-\beta}{2}} \leq \Lambda_1$$

  which is true for T_3 as in theorem 4.16 once we are given Υ_1.

- The boundary velocities automatically satisfy

$$\dot{l'}(\tau) = c_1^1\tilde{a'}(\tau, 0) + c_2^1 \qquad \text{and} \qquad \dot{r'}(\tau) = c_1^4\tilde{a'}(\tau, L) + c_2^4.$$

We are now going to check the bounds on the monomer density $\tilde{a'}$. First, the $C^{2,1}$-norm of $\tilde{a}$ is bounded by its $C^{2+\beta,P}$-norm for which theorem 4.9 yields the estimate

$$\begin{aligned} \|\tilde{a'}\|_{C^{2_x,1_t}} &\leq \|\tilde{a'}\|_{C^{2+\beta,P}} \\ &\leq \hat{C}(T)(M_2 + \|\tilde{f}\|_{C^{0+\beta,P}}). \end{aligned}$$

The only things to calculate are the $C^{0+\beta,P}$-norms of $\tilde{\varphi}$ (which enters $\hat{C}$) and of $\tilde{f}$. This is easily achieved since both depend on the $C^{0+\beta,P}$-norm of the given end density u. We already calculated in the proof of theorem 4.9 how the HÖLDER constants are affected by the transformation:

$$\begin{aligned} H\ddot{o}l_{P,\beta}(\tilde{\varphi}) &\leq 2H\ddot{o}l_{P,\beta}(cu)\left((1+(3\varepsilon_2(T))^{\beta}+\left(1+\frac{2\varepsilon_1(T)}{L}\right)^{\beta}\right) \\ &\leq 2H\ddot{o}l_{P,\beta}(cu)\left((1+(3\varepsilon_2^*)^{\beta}+\left(1+\frac{2\varepsilon_2^*}{L}\right)^{\beta}\right) \qquad =: K_2H\ddot{o}l_{P,\beta}(u) \end{aligned}$$

where c is the coefficient vector defined in (2.16). Since we know in addition that the maximum norm remains unaffected by the transformation, we can state

$$\|\tilde{\varphi}\|_{C^{0+\beta,P}} \leq K_2\|u\|_{C^{0+\beta,P}} \leq K_2\Upsilon_2.$$

Completely analogously, we obtain

$$\|\tilde{f}\|_{C^{0+\beta,P}} \leq \tilde{K}_2\|u\|_{C^{0+\beta,P}} \leq \tilde{K}_2\Upsilon_2.$$

where $\tilde{K}_2$ differs from K_2 only in the coefficient vector c being replaced by $\tilde{c}$ which is given by (2.17). We note again, that by decreasing T, the constants and the norms of the restriction of u can only become smaller.

Together with the estimate from theorem 4.9 and our particular choice of Υ_1, we immediately deduce

$$\|\tilde{a'}\|_{C^{2_x,1_t}} \leq \Upsilon_1,$$

and we conclude that $(l', \tilde{r'}, \tilde{a'})$ belongs to $\mathcal{B}_T$ for each $T \leq T_3$.

We note that for sufficiently small T – say $T \leq T_4$ – we can employ the continuity of $\tilde{a'}$ and the boundedness of its temporal derivative to conclude that $\tilde{a'}$ is bounded from below by a^{BP} if the initial conditions a_0 are bounded away from a^{BP}.

Finally, the spatial derivative of $\tilde{a'}$ is bounded by the estimate (4.64) in lemma 4.13, and by the construction of $\check{C}$ and the definition of Υ_0 is automatically bounded by

$$\|\partial_\xi\tilde{a'}\|_{C^0} \leq \Upsilon_0$$

whenever $T \leq T^*$.

We therefore found $T_4 > 0$ such that for $T \in (0, T_4]$ the components l', $\tilde{r'}$, and $\tilde{a'}$ satisfy the conditions of $\mathcal{C}_T$.

On the other hand, proposition 4.8 guarantees a C^1-solution to the hyperbolic problems (4.25) ($\alpha = 1, \ldots, 4$)) with a suitable extension of the back transform of $\tilde{a}$ plugged in for the given monomer density. For this solution we found the estimates (4.40) - (4.42). Noting now that for the back transform we have

$$\|\partial_x a\|_{C^0} \leq \frac{L}{d(T)}\|\partial_{xi}\tilde{a}\|_{C^0} \leq 2\Upsilon_0$$

and

$$\|\partial_{xx} a\|_{C^0} \leq \frac{L^2}{d(T)^2}\|\partial_{\xi\xi}\tilde{a}\|_{C^0} \leq 4\Upsilon_1$$

and that, for the arbitrarily chosen $\varepsilon_3 > 0$, the extension A can be forced to satisfy

$$\begin{aligned} a^{BP} - \varepsilon_3 &= \inf_{(\tau,\xi)\in[0,T]\times[0,L]} \tilde{a} - \varepsilon_3 \leq A \leq \sup_{(\tau,\xi)\in[0,T]\times[0,L]} \tilde{a} + \varepsilon_3 \quad = a_P + \varepsilon_3, \\ \|\partial_x A\|_{C^0} &\leq 2(1+\varepsilon_3)\|\partial_\xi \tilde{a}\|_{C^0} \leq 2(1+\varepsilon_3)\Upsilon_0, \\ \|\partial_{xx} A\|_{C^0} &\leq 4(1+\varepsilon_3)\Upsilon_1 \end{aligned}$$

we can achieve the following estimates for u':

$$\begin{aligned} \|u'\|_{C^0} &\leq M_0 \mathcal{E}(T) \leq M_0 \mathcal{E}(2T), \\ H\ddot{o}l_{x,\beta}(u') &\leq \|\partial_x u_0\|_{C^0} L_{max}^{1-\beta} \\ &\leq \mathcal{E}(2T)\left(M_1 + M_0 \delta \kappa_B \|\partial_{xx} A\|_{C^0} \mathcal{E}(2T) T\right) L_{max}^{1-\beta}, \end{aligned}$$

and

$$\begin{aligned} H\ddot{o}l_{t,\frac{\beta}{2}}(u') &\leq \|\partial_t u_0\|_{C^0} T^{1-\frac{\beta}{2}} \\ &\leq T^{1-\frac{\beta}{2}} \mathcal{E}(2T)(M_1 v_{max} + \delta \kappa_B M_0 (T\|\partial_{xx} A\| \mathcal{E}(2T) v_{max} + \|\partial_x A\|_{C^0})) \end{aligned}$$

where we introduced the notation

$$\mathcal{E}(T) = \exp\left[2\delta\kappa_B(1+\varepsilon_3)\Upsilon_0 T\right].$$

We now choose $T_5 > 0$ sufficiently small to guarantee

$$\begin{aligned} \exp\left[2\delta\kappa_B(1+\varepsilon_3)\Upsilon_0 T_5\right] &\leq 2, \\ 2 v_{max} T_5^{1-\frac{\beta}{2}} &\leq \left(\frac{3}{2}L\right)^{1-\beta}, \end{aligned}$$

and

$$4\delta\kappa_B(1+\varepsilon_3)\left(4\Upsilon_1\left(\left(\frac{3}{2}L\right)^{1-\beta} T_5 + T_5^{\frac{\beta}{2}} v_{max}\right) + \Upsilon_0\right) T_5^{1-\frac{\beta}{2}} \leq 1.$$

This leads to the norm of u' to be bounded by

$$\|u'\|_{C^{0+\beta,P}} \leq 3M_0 + 3\left(\frac{3}{2}L\right)^{1-\beta} M_1 = \Upsilon_2.$$

The compactness assertion for the u component readily follows from the compactness of the embedding

$$C^1 \hookrightarrow C^{0+\beta,P}.$$

The last thing to be noted is that the support of u is determined by the support $[0, L]$ of the initial conditions and the outer characteristic curves whose velocity is bounded by v_{max}. In particular,

$$\operatorname{supp} u' \subset [0,T] \times \left[-\frac{L}{4}, \frac{5}{4}L\right],$$

whenever $4v_{max}T \leq L$ which can be assumed to be true for T_5 by making it sufficiently

small.

Thus, for

$$T \leq \min\{T_4, T_5\},$$

the map A indeed maps $\mathcal{C}_T$ into a compact subset of itself. This maximal time shall again be denoted by T_5. □

The next step is the establishment of a contraction principle. We therefore assume all initial conditions and parameters to be given as in 4.19 and choose arbitrary

$$(l_i, \tilde{r}_i, \tilde{a}_i, u_i) \in \mathcal{C}_T \qquad (i = 1, 2)$$

satisfying

$$\|(l_2, \tilde{r}_2, \tilde{a}_2, u_2) - (l_1, \tilde{r}_1, \tilde{a}_1, u_1)\|_{V_T} \leq \omega. \tag{4.125}$$

The difference of the images under the map A shall be denoted by

$$(\lambda, \varrho, w, \upsilon) := A(l_2, \tilde{r}_2, \tilde{a}_2, u_2) - A(l_1, \tilde{r}_1, \tilde{a}_1, u_1) \equiv (l_2', \tilde{r'}_2, \tilde{a'}_2, u_2') - (l_1', \tilde{r'}_1, \tilde{a'}_1, u_1').$$

The differences of the boundary curves again satisfy the equations (4.87) and (4.88) and we readily obtain some time T_6 such that for each $T \in (0, T_6]$ estimates in analogy to (4.116) and (4.117) hold with $\frac{\omega}{4}$ replaced by $\frac{\omega}{5}$.

The difference of the monomer densities is governed by

$$\begin{aligned} \partial_\tau w \;=\; & \frac{L^2 D}{(r_2 - r_1)^2} \partial_{\xi\xi} w + \frac{L}{r_2 - l_2} \left(\frac{\xi}{L} (\dot{r_2} - \dot{l_2}) + \dot{l_2} \right) \partial_\xi w - \tilde{\varphi}_2 w \\ & + \Theta \partial_{\xi\xi} \tilde{a'}_1 + (\Xi_2 - \Xi_1) \partial_\xi \tilde{a'}_1 - (\tilde{\varphi}_2 - \tilde{\varphi}_1) \tilde{a'}_1 + (\tilde{f}_2 - \tilde{f}_1) \end{aligned} \tag{4.126}$$

where Θ and the Ξ_i are the same as in (4.90).

This equation only differs from (4.89) by the right hand side F containing the additional terms

$$(\tilde{\varphi}_2 - \tilde{\varphi}_1) \tilde{a'}_1 \qquad \text{and} \qquad (\tilde{f}_2 - \tilde{f}_1)$$

and thus being given by

$$F = \Theta \partial_{\xi\xi} \tilde{a'}_1 + (\Xi_2 - \Xi_1) \partial_\xi \tilde{a'}_1 - (\tilde{\varphi}_2 - \tilde{\varphi}_1) \tilde{a'}_1 + (\tilde{f}_2 - \tilde{f}_1).$$

The initial conditions are of course again trivial, and the boundary conditions remain the same as (4.92) and (4.93).

The existence of a unique solution w of class $C^{2+\beta, P}$ again follows from theorem 4.9 by noting that the new right hand side F is of class $C^{0+\beta, P}$. The only term to check is

$$(\tilde{\varphi}_2 - \tilde{\varphi}_1) \tilde{a'}_1$$

but since $\tilde{a'}_1$ is even of class $C^{2+\beta, P}$, this is clearly of the required regularity.

To obtain a contraction estimate similar to (4.112) we only need to find an estimate for F analogously to (4.102). We thus require estimates for the new terms

$$(\tilde{\varphi}_2 - \tilde{\varphi}_1) \tilde{a'}_1 \qquad \text{and} \qquad (\tilde{f}_2 - \tilde{f}_1).$$

But these are particularly simple, since by assumption we have

$$\begin{aligned}\|(\tilde{\varphi}_2 - \tilde{\varphi}_1)\tilde{a'}_1\|_{C^{0+\beta,P}} &\leq \|\tilde{a'}_1\|_{C^{0+\beta,P}}\|\tilde{\varphi}_2 - \tilde{\varphi}_1\|_{C^{0+\beta,P}} \leq K_2\|\tilde{a'}_1\|_{C^{2+\beta,P}}\omega \\ \|\tilde{f}_2 - \tilde{f}_1\|_{C^{0+\beta,P}} &\leq \tilde{K}_2\omega\end{aligned}$$

with K_2 and $\tilde{K}_2$ as in the proof of lemma 4.19. The other terms included different versions of

$$\|\tilde{\varphi}\|_{C^{0+\beta,P}} \qquad \text{and} \qquad \|\tilde{f}\|_{C^{0+\beta,P}}$$

as well but these can be uniformly bounded by $K_2\Upsilon_2$ and $\tilde{K}_2\Upsilon_2$, respectively.

Now we can choose some $T_7 > 0$ which will in general be smaller than T_3 but independent of the precise value of

$$\|u\|_{C^{0+\beta,P}}$$

. With that T_7 we can guarantee

$$\|w\|_{C^{2_x,1_t}} \leq \frac{\omega}{5} \tag{4.127}$$

whenever $T \leq T_7$.

We can now turn our attention to the difference υ of the end densities. For these, we have the explicite representation (4.31) which allows us to write the α^{th} component of the difference as

$$\begin{aligned}\upsilon^\alpha(t,x) &= {u'_2}^\alpha(t,x) - {u'_1}^\alpha(t,x) \\ &= u_0^\alpha(\xi_2^\alpha(t,x)) \exp\left[-\int_0^t \partial_x\lambda_2^\alpha\left(\tau, y_2^\alpha(\tau;\xi_2^\alpha(t,x))\right)d\tau\right] \\ &- u_0^\alpha(\xi_1^\alpha(t,x)) \exp\left[-\int_0^t \partial_x\lambda_1^\alpha\left(\tau, y_1^\alpha(\tau;\xi_1^\alpha(t,x))\right)d\tau\right].\end{aligned}$$

Here, the subscripts 1 and 2 refer to the characteristic curves and velocities according to the monomer densities $\tilde{a}_1$ and $\tilde{a}_2$, respectively. We will frequently use some estimates on the difference of these characteristics. We start with calculating an upper bound for

$$d(t) := |y_2^\alpha(t;\xi_2^\alpha(t_0,x_0)) - y_1^\alpha(t;\xi_1^\alpha(t_0,x_0))|.$$

We note that the derivative of d is bounded by

$$\begin{aligned}|\dot{d}(t)| &= |\lambda_2^\alpha(t, y_2^\alpha(t;\xi_2^\alpha(t_0,x_0))) - \lambda_1^\alpha(t, y_1^\alpha(t;\xi_1^\alpha(t_0,x_0)))| \\ &\leq |\lambda_2^\alpha(t, y_2^\alpha(t;\xi_2^\alpha(t_0,x_0))) - \lambda_1^\alpha(t, y_2^\alpha(t;\xi_2^\alpha(t_0,x_0)))| + \|\partial_x\lambda_1\|_{C^0}d(t) \\ &\leq 2\delta\kappa_B(\omega + \Upsilon_0 d(t)),\end{aligned}$$

and d satisfies the initial condition $d(t_0) = 0$.

It follows that

$$\begin{aligned}d(t) &\leq \frac{\omega}{\Upsilon_0}\left(\exp[2\delta\kappa_B\Upsilon_0|t-t_0|] - 1\right) \\ &\leq 2\delta\kappa_B|t-t_0|\exp[2\delta\kappa_B\Upsilon_0|t-t_0|]\omega \leq 2\delta\kappa_B T\mathcal{E}(T)\omega,\end{aligned}$$

and for the particular value $t = 0$ this turns into:

$$|\xi_2^\alpha(t,x) - \xi_1^\alpha(t,x)| \quad \leq \quad 2\delta\kappa_B T\mathcal{E}(T)\omega.$$

For the quantities

$$d_i(t) := |y_i^\alpha(t;\xi_i^\alpha(t_0,x_0)) - y_i^\alpha(t;\xi_i^\alpha(t_0,y_0))|$$

we calculate

$$\begin{aligned} d_i(t) \ &\leq |x_0 - y_0| + \int_{t_0}^t |\lambda_i^\alpha(\tau, y_i^\alpha(\tau;\xi_i^\alpha(t_0,x_0))) - \lambda_i^\alpha(\tau, y_i^\alpha(\tau;\xi_i^\alpha(t_0,y_0)))|d\tau \\ &\leq |x_0 - y_0| + \int_{t_0}^t \|\partial_x\lambda_i^\alpha\|_{C^0} d_i(\tau)d\tau. \end{aligned}$$

By Grönwall's inequality we deduce

$$d_i(t) \ \leq \exp\left[\|\partial_x\lambda_i\|_{C^0}|t-t_0|\right] \ |x_0 - y_0| \ \leq \ \mathcal{E}(T)|x_0 - y_0|.$$

Similarly, we find an upper bound for the quantity

$$d(t) := |y_2^\alpha(t;\xi_2^\alpha(t_0,x_0)) - y_1^\alpha(t;\xi_1^\alpha(t_0,x_0)) - y_2^\alpha(t;\xi_2^\alpha(t_0,y_0)) + y_1^\alpha(t;\xi_1^\alpha(t_0,y_0))|$$

by the following considerations.

In the following calculations we will occasionally suppress the upper index α, always keeping in mind that the basic shape of the characteristic velocities is the same for all end densities. We would like to estimate d by regarding each characteristic curve as a function of the starting point

$$y_i(t;\xi_i(t_0,x_0)) =: \mathsf{y}_i(t,x_0)$$

for a moment and calculate

$$d(t) \leq \sup_x \left|\frac{d}{dx}(\mathsf{y}_2(t,x) - \mathsf{y}_1(t,x))\right| |x_0 - y_0|.$$

The time t is regarded as a parameter and the common initial time t_0 is suppressed to avoid an overloaded notation.

To calculate the derivative of $\mathsf{y}_2 - \mathsf{y}_1$ we use the integral representation

$$\mathsf{y}_i(t,x_0) = x_0 + \int_{t_0}^t \lambda_i(\tau, \mathsf{y}_i(\tau,x_0))d\tau$$

and write the derivative of the difference as

$$\begin{aligned} &\frac{d}{dx}(\mathsf{y}_2 - \mathsf{y}_1)\rfloor_{(t,x_0)} \\ &= \lim_{h\to 0}\frac{1}{h}\int_{t_0}^t (\lambda_2(\tau,\mathsf{y}_2(\tau,x_0+h)) - \lambda_2(\tau,\mathsf{y}_2(\tau,x_0)) \\ &\qquad -\lambda_1(\tau,\mathsf{y}_1(\tau,x_0+h)) + \lambda_1(\tau,\mathsf{y}_1(\tau,x_0)))\,d\tau \end{aligned}$$

$$= \lim_{h\to 0} \frac{1}{h} \int_{t_0}^{t} \big(\partial_x \lambda_2\rfloor_{(\tau,\mathsf{y}_2(x_0))} \ (\mathsf{y}_2(\tau, x_0+h) - \mathsf{y}_2(,\tau,x_0)) + \mathcal{O}(|h|) \\ -\partial_x \lambda_1\rfloor_{(\tau,\mathsf{y}_1(x_0))} \ (\mathsf{y}_1(\tau, x_0+h) - \mathsf{y}_1(,\tau,x_0)) + \mathcal{O}(|h|)\big)\, d\tau.$$

Here, we already used that

$$|\mathsf{y}_i(\tau, x_0+h) - \mathsf{y}_i(,\tau,x_0)|$$

grows like $|h|$ for small h and that λ_i is twice continuously differentiable with respect to its second argument. We note that the integrand tends to zero as $h \to 0$ and does so uniformly in $\tau \in [0,T]$ by our previous estimates.

We interchange integration and limit to obtain

$$\frac{d}{dx}(\mathsf{y}_2 - \mathsf{y}_1)\rfloor_{(t,x_0)} \\ = \int_{t_0}^{t} \left(\partial_x \lambda_2\rfloor_{(\tau,\mathsf{y}_2(x_0))} \ \frac{d}{dx}\mathsf{y}_2(\tau,x_0) - \partial_x \lambda_1\rfloor_{(\tau,\mathsf{y}_1(x_0))} \ \frac{d}{dx}\mathsf{y}_1(\tau,x_0) \right) d\tau$$

and estimate

$$\left| \frac{d}{dx}(\mathsf{y}_2 - \mathsf{y}_1)\rfloor_{(t,x_0)} \right| \\ \leq \int_{t_0}^{t} \Bigg(\left(|\partial_x \lambda_2\rfloor_{(\tau,\mathsf{y}_2)} - \partial_x \lambda_2\rfloor_{(\tau,\mathsf{y}_1)}| + |\partial_x \lambda_2\rfloor_{(\tau,\mathsf{y}_1)} - \partial_x \lambda_1\rfloor_{(\tau,\mathsf{y}_1)}| \right) \frac{d}{dx}\mathsf{y}_2(t,x_0) \\ + \left|\partial_x \lambda_1\rfloor_{(\tau,\mathsf{y}_1)}\right| \ \left| \frac{d}{dx}\mathsf{y}_2(\tau,x_0) - \frac{d}{dx}\mathsf{y}_1(\tau,x_0) \right| \Bigg) d\tau \\ \leq |t-t_0| \left(\|\partial_{xx}\lambda_2\|_{C^0} \cdot 2\delta\kappa_B \mathcal{E}(|t-t_0|) + 1 \right) \omega + \|\partial_x \lambda_1\|_{C^0} \int_{t_0}^{t} \left| \frac{d}{dx}(\mathsf{y}_2 - \mathsf{y}_1)\rfloor_{(\tau,x_0)} \right| d\tau$$

Using again Grönwall's inequality, we find

$$\left| \frac{d}{dx}(\mathsf{y}_2 - \mathsf{y}_1)\rfloor_{(t,x_0)} \right| \leq \left(8\delta^2 \kappa_B^2 \mathcal{E}(T) \Upsilon_1 + 1 \right) \mathcal{E}(T) |t-t_0| \omega$$

and consequently

$$|y_2^\alpha(t;\xi_2^\alpha(t_0,x_0)) - y_1^\alpha(t;\xi_1^\alpha(t_0,x_0)) - y_2^\alpha(t;\xi_2^\alpha(t_0,y_0)) + y_1^\alpha(t;\xi_1^\alpha(t_0,y_0))| \\ \leq \left(8\delta^2 \kappa_B^2 \mathcal{E}(T) \Upsilon_1 + 1 \right) \mathcal{E}(T) |t-t_0| |x_0 - y_0| \omega$$

We note that particularly for $t = 0$ we obtain

$$|\xi_2^\alpha(t_0,x_0) - \xi_1^\alpha(t_0,x_0) - \xi_2^\alpha(t_0,y_0) + \xi_1^\alpha(t_0,y_0)| \\ \leq \left(8\delta^2 \kappa_B^2 \mathcal{E}(T) \Upsilon_1 + 1 \right) \mathcal{E}(T) t_0 |x_0 - y_0| \omega$$

with the ξ^α denoting the points in space where the respective characteristic curves originate.

The absolute value of υ is bounded by

$$\begin{aligned}
|\upsilon(t,x)| \;&\leq |u_0(\xi_2(t,x)) - u_0(\xi_1(t,x))| \exp\left[T\|\partial_x\lambda_2\|_{C^0}\right] \\
&\quad + |u_0(\xi_1(t,x))| \left| \exp\left[-\int_0^t \partial_x\lambda_2\left(\tau, y_2(\tau;\xi_2(t,x))\right) d\tau \right] \right. \\
&\qquad \left. - \exp\left[-\int_0^t \partial_x\lambda_1\left(\tau, y_1(\tau;\xi_1(t,x))\right) d\tau \right] \right| \\
&\leq \; M_1 \; \|\lambda_2 - \lambda_1\|_{C^0} T \exp[T\|\partial_x\lambda_2\|_{C^0}] \\
&+ M_0 \; \exp[T\|\partial_x\lambda_2\|_{C^0}] \int_0^t |\partial_x\lambda_2\left(\tau, y_2(\tau;\xi_2(t,x))\right) - \partial_x\lambda_1\left(\tau, y_1(\tau;\xi_1(t,x))\right)| \, d\tau \times \\
&\qquad \times \exp\left[\int_0^t |\partial_x\lambda_2\left(\tau, y_2(\tau;\xi_2(t,x))\right) - \partial_x\lambda_1\left(\tau, y_1(\tau;\xi_1(t,x))\right)| \, d\tau \right]
\end{aligned}$$

where we again suppressed the index α.

The integral in the last term is bounded by

$$\begin{aligned}
&\int_0^t |\partial_x\lambda_2\left(\tau, y_2(\tau;\xi_2(t,x))\right) - \partial_x\lambda_1\left(\tau, y_1(\tau;\xi_1(t,x))\right)| \, d\tau \\
&\leq T\left(\|\partial_{xx}\lambda_2\|_{C^0} 2\delta\kappa_B T \exp[2\delta\kappa_B \Upsilon_0 T]\omega + \|\partial_x\lambda_2 - \partial_x\lambda_1\|_{C^0} \right) \\
&\leq 2\delta\kappa_B \left(2\delta\kappa_B \Upsilon_1 T\mathcal{E}(T) + 1\right) \omega T.
\end{aligned}$$

The resulting bound on υ is:

$$|\upsilon(t,x)| \leq K_{\upsilon,0}(T)\omega T \tag{4.128}$$

where the constant $K_{\upsilon,0}$ is given by

$$K_{\upsilon,0}(T) \;=\; 2\delta\kappa_B \mathcal{E}(T) \left(M_1 + M_0 \tilde{K}_0(T) \exp[2\delta\kappa_B \tilde{K}_0(T)\omega T] \right)$$

with

$$\tilde{K}_0(T) = \left(2\delta\kappa_B \Upsilon_1 T\mathcal{E}_0(T) + 1\right).$$

We note that $K_{\upsilon,0}(T)$ increases in T and can therefore be bounded from above by the fixed constant $K_{\upsilon,0}(T_7)$ where T_7 is the maximal time we allowed for the bound on w.

In order to find an estimate for the spatial HÖLDER constant of υ we introduce the following notation

$$\begin{aligned}
U_i(z) \;&:=\; u_0(\xi_i(t,z)) \\
I_i(z) \;&:=\; \exp\left[-\int_0^t \partial_x\lambda_i(\tau, y_i(\tau;\xi_i(t,z)))d\tau \right]
\end{aligned}$$

for $i = 1, 2$ and $z = x, y$.

The spatial variation of υ can now be written as

$$\begin{aligned}
|\upsilon(t,x) - \upsilon(t,y)| \;\leq\; &|U_2(x)(I_2(x) - I_1(x)) + (U_2(x) - U_1(x))I_1(x) \\
&- U_2(y)(I_2(y) - I_1(y)) + (U_2(y) - U_1(y))I_1(y)|
\end{aligned}$$

$$
\begin{aligned}
&\le |U_2(x)-U_2(y)||I_2(x)-I_1(x)| + |U_2(x)-U_1(x)||I_1(x)-I_1(y)| \\
&\quad + |U_2(y)||I_2(x)-I_1(x)-I_2(y)+I_1(y)| + |U_2(x)-U_1(x)-U_2(y)+U_1(y)||I_1(y)| \\
&=: E_1+E_2+E_3+E_4.
\end{aligned}
$$

We start with the term E_1 and compute for

$$
d_i(\tau) := |y_i(\tau;\xi_i(t,x)) - y_i(\tau;\xi_i(t,y))|
$$

the bound

$$
|\dot{d}_i| \le \delta\kappa_B \Upsilon_0 d_i
$$

and then, by GRÖNWALL's inequality and the initial conditions $d_i(t) = |x-y|$,

$$
d_i(\tau) \le |x-y| \exp[2\delta\kappa_B\Upsilon_0|\tau-t|] \equiv |x-y|\mathcal{E}(|\tau-t|).
$$

It follows:

$$
|U_2(x)-U_2(y)| \le M_1|x-y|\mathcal{E}(T).
$$

The second factor of E_1 has already been estimated during the derivation of (4.128), and we obtain

$$
E_1 \le 2\delta\kappa_B\tilde{K}_0(T)\exp[2\delta\kappa_B\tilde{K}_0(T)\omega T]\mathcal{E}(2T)M_1|x-y|\omega T = \tilde{K}_{E_1}(T)|x-y|\omega T.
$$

Concerning E_2 we already found a bound for the first factor, and for the second factor we calculate

$$
\begin{aligned}
&|I_1(x)-I_1(y)| \\
&\le \mathcal{E}(T)\exp\left[T\|\partial_{xx}\lambda_1\|_{C^0}\sup_\tau d_1(\tau)\right] T\|\partial_{xx}\lambda_1\|_{C^0}\sup_\tau d_1(\tau) \\
&\le \mathcal{E}(T)\exp[2\delta\kappa_B T\Upsilon_1|x-y|\mathcal{E}(T)]\ 2\delta\kappa_B T\Upsilon_1|x-y|\mathcal{E}(T) \\
&\le \tilde{K}_I(T)T|x-y|
\end{aligned}
$$

with $\tilde{K}_I(T)$ being decreasing in T. We note that the term $|x-y|$ in the exponent is bounded from above by

$$
L_{max} = \frac{3}{2}L
$$

for $T \le T^*$. As an upper bound for E_2 we therefore find

$$
\begin{aligned}
E_2 &\le (2\delta\kappa_B)^2\mathcal{E}(3T)M_1\Upsilon_1\exp\left[2\delta\kappa_B\Upsilon_1\mathcal{E}(T)|x-y|T\right]|x-y|\omega T^2 \\
&= \tilde{K}_{E_2}(T)|x-y|\omega T.
\end{aligned}
$$

We now turn to E_3 which we estimate in the following shape

$$
\begin{aligned}
|I_2(x)-I_1(x)-I_2(y)+I_1(y)| &= \left|\mathrm{e}^{a_2}-\mathrm{e}^{a_1}-\mathrm{e}^{b_2}+\mathrm{e}^{b_1}\right| \\
&= \left|\left(\mathrm{e}^{a_2}-\mathrm{e}^{b_2}\right)\left(1-\mathrm{e}^{a1-b_1}\right)-\mathrm{e}^{b_2}\left(\mathrm{e}^{a_1-a_2}-\mathrm{e}^{b_1-b2}\right)\right| \\
&\le \left|\mathrm{e}^{a_2}-\mathrm{e}^{b_2}\right|\mathrm{e}^{|a_1-a_2|}|a_1-a_2| \\
&\quad + \mathrm{e}^{|b_2(a_1-a_2)|}\mathrm{e}^{|b_1-b_2-a_1+a_2|}|b_1-b_2-a_1+a_2|.
\end{aligned}
$$

where we used the abbreviations

$$\begin{aligned} a_i &:= \int_0^t \partial_x \lambda_i(\tau, y_i(\tau; \xi_i(t,x)))d\tau \qquad (i=1,2) \\ b_i &:= \int_0^t \partial_x \lambda_i(\tau, y_i(\tau; \xi_i(t,y)))d\tau \qquad (i=1,2). \end{aligned}$$

The only part we have not yet estimated is the term

$$\begin{aligned} |b_1 - b_2 - a_1 + a_2| \;\leq \int_0^t & |\partial_x \lambda_1(\tau, y_1(\tau;\xi_1(t,y))) - \partial_x \lambda_2(\tau, y_2(\tau;\xi_2(t,y))) \\ & -\partial_x \lambda_1(\tau, y_1(\tau;\xi_1(t,x))) + \partial_x \lambda_2(\tau, y_2(\tau;\xi_2(t,x)))|\, d\tau \end{aligned}$$

$$\begin{aligned} &\leq T\|\partial_{xx}\lambda_2 - \partial_{xx}\lambda_1\|_{C^0} |y_2(\tau;\xi_2(t,x)) - y_1(\tau;\xi_1(t,x)) \\ &\qquad\qquad - y_2(\tau;\xi_2(t,y)) + y_1(\tau;\xi_1(t,y))| \\ &\leq 4\delta\kappa_B T \|\tilde{a}_2 - \tilde{a}_1\|_{C^{2_x,1_t}} \left(|y_2(\tau;\xi_2(t,x)) - y_2(\tau;\xi_2(t,y))|\right. \\ &\qquad\qquad \left. + |y_1(\tau;\xi_1(t,x)) - y_1(\tau;\xi_1(t,y))|\right) \\ &\leq 4\delta\kappa_B T\omega \cdot 2\mathcal{E}(T)|x-y|. \end{aligned}$$

Together with the estimates found before we calculate

$$\begin{aligned} E_3 \;&\leq M_0 \left(\tilde{K}_I(T)|x-y|\; T \exp\left[\tilde{K}_\lambda(T)\omega T\right] \tilde{K}_\lambda(T)\omega T \right. \\ &\quad \left. + \exp\left[2\delta\kappa_B\left(\Upsilon_1 T\tilde{K}_\lambda(T) + 4\mathcal{E}_0(T)|x-y|\right)\omega T\right] \cdot 8\delta\kappa_B\mathcal{E}(T)|x-y|\omega T \right) \\ &\leq \tilde{K}_{E_3}(T)|x-y|\omega T \end{aligned}$$

with

$$\tilde{K}_\lambda(T) := 2\delta\kappa_B(2\delta\kappa_B\Upsilon_1\mathcal{E}(T)T + 1).$$

For the term E_4 we only need to compute

$$\begin{aligned} &|u_0(\xi_2(t,x)) - u_0(\xi_1(t,x)) - (u_0(\xi_2(t,y)) - u_0(\xi_1(t,y)))| \\ &= \left|\frac{d}{dx}u_0(x_0)(\xi_2(t,x) - \xi_1(t,x)) - \frac{d}{dx}u_0(y_0)(\xi_2(t,y) - \xi_1(t,y))\right| \\ &\leq \left|\frac{d}{dx}u_0(x_0) - \frac{d}{dx}u_0(y_0)\right| |\xi_2(t,x) - \xi_1(t,x)| \\ &\quad + \left|\frac{d}{dx}u_0(y_0)\right| |\xi_2(t,x) - \xi_1(t,x) - \xi_2(t,y) + \xi_1(t,y)| \\ &\leq M_3|x-y|2\delta\kappa_B\mathcal{E}(T)\omega T + M_1\left(8\delta^2\kappa_B^2\mathcal{E}(T)\Upsilon_1 + 1\right)\mathcal{E}(T)T|x-y|\omega \\ &\leq 2\delta\kappa_B\mathcal{E}(T)\left(M_3 + (4\delta\kappa_B\Upsilon_1 + 1)M_1\right)T|x-y|\omega, \end{aligned}$$

and we finally find

$$\begin{aligned} E_4 \;&\leq 2\delta\kappa_B\mathcal{E}(2T)\left(M_3 + (4\delta\kappa_B\Upsilon_1 + 1)M_1\right)T|x-y|\omega \\ &= \tilde{K}_{E_4}(T)|x-y|\omega T. \end{aligned}$$

The spatial HÖLDER constant for υ is therefore bounded by

$$\begin{aligned}\frac{|\upsilon(t,x)-\upsilon(t,y)|}{|x-y|^\beta} &\leq \left(\tilde{K}_{E_1}(T)+\tilde{K}_{E_2}(T)+\tilde{K}_{E_3}(T)+\tilde{K}_{E_4}(T)\right) L_{max}(T)^{1-\beta}\omega T \\ &\leq K_{\upsilon,x}(T)\omega T \end{aligned} \tag{4.129}$$

where $K_{\theta,x}(T)$ is bounded from above by, say

$$\left(\tilde{K}_{E_1}(T_7)+\tilde{K}_{E_2}(T_7)+\tilde{K}_{E_3}(T_7)+\tilde{K}_{E_4}(T_7)\right)\left(\frac{3}{2}L\right)^{1-\beta}$$

whenever $T \leq T_7$.

It remains to find a bound on the temporal HÖLDER constant of θ. We therefore estimate

$$|\upsilon(t,x)-\upsilon(s,x)| = |u_2'(t,x)-u_1'(t,x)-u_2'(s,x)+u_1'(s,x)|.$$

We split this quantity up into one part where we go along the characteristic curves from (t,x) to $(s,y_i(s;\xi_i(t,x))) =: (s,\mathsf{y}_i(s))$ and a second part where we pass from these points to (s,x). This expands the term to estimate into

$$\begin{aligned}|\upsilon(t,x)-\upsilon(s,x)| &\leq \left|u_2'(t,x)\int_t^s \partial_x\lambda_2(\tau,\mathsf{y}_2(\tau))d\tau - u_1'(t,x)\int_t^s \partial_x\lambda_1(\tau,\mathsf{y}_1(\tau))\right| \\ &\quad + |\upsilon(s,\mathsf{y}_2(s))-\upsilon(s,x)| + |u_1'(s,\mathsf{y}_2(s))-u_1'(s,\mathsf{y}_1(s))|.\end{aligned}$$

The latter two terms we already estimated in similar form:

$$\begin{aligned}|\upsilon(s,\mathsf{y}_2(s))-\upsilon(s,x)| &\leq \left(\tilde{K}_{E_1}(T)+\tilde{K}_{E_2}(T)+\tilde{K}_{E_3}(T)+\tilde{K}_{E_4}(T)\right)\omega T|\mathsf{y}_2(s)-x| \\ &\leq \left(\tilde{K}_{E_1}(T)+\tilde{K}_{E_2}(T)+\tilde{K}_{E_3}(T)+\tilde{K}_{E_4}(T)\right)\omega T v_{max}|t-s| \\ &=: \tilde{K}_{\upsilon,t,1}(T)\omega|t-s|\end{aligned}$$

$$\begin{aligned}|u_1'(s,\mathsf{y}_2(s))-u_1'(s,\mathsf{y}_1(s))| &\leq \|\partial_x u_1'\|_{C^0}|\mathsf{y}_2(s)-\mathsf{y}_1(s)| \\ &\leq \mathcal{E}(2T)\left(M_1+4\delta\kappa_B\Upsilon_1\mathcal{E}(2T)M_0T\right)\ 2\delta\kappa_B\mathcal{E}(|t-s|)|t-s|\omega \\ &\leq 2\delta\kappa_B\mathcal{E}(3T)\left(M_1+4\delta\kappa_B\Upsilon_1\mathcal{E}(2T)M_0T\right)\ \omega|t-s| \\ &=: \tilde{K}_{\upsilon,t,2}(T)\omega|t-s|.\end{aligned}$$

The remaining term is bounded by

$$\begin{aligned}&\left|u_2'(t,x)\int_t^s \partial_x\lambda_2(\tau,\mathsf{y}_2(\tau))d\tau - u_1'(t,x)\int_t^s \partial_x\lambda_1(\tau,\mathsf{y}_1(\tau))\right| \\ &\leq \left|\int_s^t \partial_x\lambda_2(\tau,\mathsf{y}_2(\tau))-\partial_x\lambda_2(\tau,\mathsf{y}_1(\tau))+\partial_x\lambda_2(\tau,\mathsf{y}_1(\tau))-\partial_x\lambda_1(\tau,\mathsf{y}_1(\tau))d\tau\right||u_2'(t,x)| \\ &\quad + |t-s|\|\partial_x\lambda_1\|_{C^0}|\upsilon(t,x)| \\ &\leq |t-s|(\|\partial_{xx}\lambda_1\|_{C^0}\sup_\tau|\mathsf{y}_2(\tau)-\mathsf{y}_1(\tau)|+\omega)M_0\mathcal{E}(T)+2\delta\kappa_B\Upsilon_0|t-s|K_{\upsilon,0}(T)\omega T \\ &\leq \left((8\delta^2\kappa_B^2\Upsilon_1 T\mathcal{E}(T)+1)M_0\mathcal{E}(T)+2\delta\kappa_B\Upsilon_0K_{\upsilon,0}(T)T\right)\omega|t-s| =: \tilde{K}_{\upsilon,t,3}(T)|t-s|\omega.\end{aligned}$$

Adding the three terms up, we arrive at the following bound on the temporal HÖLDER constant of υ

$$\frac{|\upsilon(t,x)-\upsilon(s,x)|}{|t-s|^{\frac{\beta}{2}}} \leq K_{\upsilon,t}(T)\omega T^{1-\frac{\beta}{2}}$$

with

$$K_{\upsilon,t}(T) = \tilde{K}_{\upsilon,t,1}(T) + \tilde{K}_{\upsilon,t,2}(T) + \tilde{K}_{\upsilon,t,3}(T)$$

being non-decreasing in T.

The parabolic HÖLDER norm of υ can now be estimated by

$$\begin{aligned} \|\upsilon\|_{C^{0+\beta,P}} &\leq \|\upsilon\|_{C^0} + H\ddot{o}l_{x,\beta}(\upsilon) + H\ddot{o}l_{t,\frac{\beta}{2}}(\upsilon) \\ &\leq \left(K_{\upsilon,0}(T)T^{\frac{\beta}{2}} + K_{\upsilon,x}(T)T^{\frac{\beta}{2}} + K_{\upsilon,t}(T)\right)\omega T^{1-\frac{\beta}{2}} \leq K_\upsilon(T_7)\omega T^{1-\frac{\beta}{2}}. \end{aligned} \tag{4.130}$$

At this point we could plug T_7 as upper bound on the time into the constant since all the constants

$$K_{\upsilon,0}T^{\frac{\beta}{2}}, \quad K_{\upsilon,x}T^{\frac{\beta}{2}}, \text{ and } \quad K_{\upsilon,t}$$

are increasing in T.

It is now easy to find some time $T_8 \in (0, T_7]$ such that for each $T \leq T_8$, the parabolic HÖLDER norm of the component υ^α satisfies

$$\|\upsilon^\alpha\|_{C^{0+\beta,P}} \leq \frac{\omega}{5}.$$

For such times we therefore have

$$\|(\lambda, \varrho, w, \upsilon)\|_{V_T} \leq \frac{4}{5}\omega \tag{4.131}$$

and our operator is indeed a contraction.

Remark 4.20. *The above estimate works if the norm of υ is assumed to be the maximum of the norms of the components υ^α. If we instead used the sum norm, the time T_8 would have to be chosen such that*

$$\|\upsilon^\alpha\|_{C^{0+\beta,P}} \leq \frac{\omega}{20}.$$

On the other hand, the constants $\tilde{K}_2$ and K_2 in lemma 4.19 would be smaller by a factor of 2 in case of the sum norm as compared to the case with the maximum norm.

We can now formulate the main theorem of this part.

Theorem 4.21. *Given $\beta \in (0,1)$ and initial data*

$$u_0 \in C^2([0,L]) \qquad \text{and} \qquad a_0 \in C^{2+\beta}([0,L])$$

satisfying the compatibility conditions and the bounds of lemma 4.19, let all quantities be defined as in lemma 4.19 and its proof.
Then, there exists some time $T_8 > 0$ being smaller than T_3 from theorem 4.16 and depending only on

$$\beta,\ L,\ D,\ M_0, \dots\ M_3,\ v_R,\ \delta,\ \kappa_{B/P},\ a_{B/P}, \quad \text{and } \min_{x\in[0,L]}\left(a_0(x) - a^{BP}\right)$$

such that for each $T \in (0, T_8]$, the operator A defined by (4.124) is a $\frac{4}{5}$-contraction on V_T. In particular, the full problem (4.45), (4.47), (4.48), (2.13), (4.49), (4.50) has a unique solution $(l_*, \tilde{r}_*, \tilde{a}_*, u_*)$ in V_T that actually belongs to W_T.

Corollary 4.22. *The solution $(l_*, \tilde{r}_*, \tilde{a}_*, u_*)$ found in theorem 4.21 corresponds to a unique solution (l_*, r_*, a_*, u_*) to the full problem (2.15), (2.32), (2.13), (2.22), (2.23) equipped with the initial conditions u_0, a_0. This solution exists for the same time T_8 and satisfies similar estimates.*

4.2 Notes on the strictly hyperbolic case with variable coefficients

It should not be too surprising that the results from the previous section remain valid if the reaction rates $\kappa_{B/P}$ and the critical concentrations $a_{B/P}$ are allowed to vary in space and time. These variations of the reaction parameters may be modulated by additional regulatory proteins and may serve as the manifestation of the external stimulus leading the cell to polarization and driving it into motion. How these proteins can be distributed asymmetrically throughout the cell and thereby lead to spatially and temporally variable reaction parameters has been investigated for instance in [22].

Of course, we will have to require certain regularity assumptions. The reaction parameters enter the following coefficient functions of the equations.

- the velocities λ^α of the hyperbolic part. In particular, the derivatives of the velocities change their shape and also depend on lower derivatives of the monomer density a. For the velocity of right oriented barbed ends we obtain

$$\begin{aligned}
\partial_x \lambda^4(t,x) &= \delta \left(\partial_x \kappa_B(t,x)\ a(t,x) + \kappa_B(t,x) \partial_x a(t,x) - \partial_x(\kappa_B(t,x) a_B(t,x)) \right) \\
\partial_{xx} \lambda^4 &= \delta \left(\partial_{xx} \kappa_B\ a + 2 \partial_x \kappa_B \partial_x a + \kappa_B \partial_{xx} a - \partial_{xx}(\kappa_B a_B) \right) \\
\partial_t \lambda^4 &= \delta \left(\partial_t \kappa_B\ a + \kappa_B \partial_t a - \partial_t(\kappa_B a_B) \right).
\end{aligned}$$

  If we deal with (small) differences of velocities for different prescribed monomer densities we have to take care of the more complicated behavior:

$$\begin{aligned}
|\partial_x \lambda_2 - \partial_x \lambda_1| &\leq \delta \max_{m=B,P} \left(\|\partial_x \kappa_m\|_{C^0} \|a_2 - a_1\|_{C^0} + \|\kappa_m\|_{C^0} \|\partial_x a_2 - \partial_x a_1\|_{C^0} \right) \\
&\leq \delta \max_{m=B,P} \|\kappa_m\|_{C^{2_x,1_t}}\ \|a_2 - a_1\|_{C^{2_x,1_t}}
\end{aligned}$$

$$\begin{aligned}
|\partial_{xx} \lambda_2 - \partial_{xx} \lambda_1| &\leq \delta \max_{m=B,P} \big(\|\partial_{xx} \kappa_m\|_{C^0} \|a_2 - a_1\|_{C^0} \\
&\quad + \|\partial_x \kappa_m\|_{C^0} \|\partial_x a_2 - \partial_x a_1\|_{C^0} + \|\kappa_m\|_{C^0} \|\partial_{xx} a_2 - \partial_{xx} a_1\|_{C^0} \big) \\
&\leq \delta \max_{m=B,P} \|\kappa_m\|_{C^{2_x,1_t}}\ \|a_2 - a_1\|_{C^{2_x,1_t}}
\end{aligned}$$

and

$$\begin{aligned}|\partial_t\lambda_2 - \partial_t\lambda_1| &\leq \delta \max_{m=B,P} (\|\partial_t\kappa_m\|_{C^0}\|a_2 - a_1\|_{C^0} + \|\kappa_m\|_{C^0}\|\partial_t a_2 - \partial_t a_1\|_{C^0}) \\ &\leq \delta \max_{m=B,P} \|\kappa_m\|_{C^{2_x,1_t}} \ \|a_2 - a_1\|_{C^{2_x,1_t}}\end{aligned}$$

- the zeroth order coefficient $\varphi = cu$ in the monomer equation. Its parabolic HÖLDER constant in terms of the end densities u now depends on the variations of the coefficients encoded in c as well and is changed to

$$\begin{aligned}H\ddot{o}l_{\beta,P}(cu) &= \sup_{(t,x)\neq(s,y)} \frac{|(c(t,x) - c(s,y))u(t,x) + c(s,y)(u(t,x) - u(s,y))|}{|(t,x) - (s,y)|_P^\beta} \\ &\leq H\ddot{o}l_{\beta,P}(c)\|u\|_{C^0} + \|c\|_{C^0} H\ddot{o}l_{\beta,P}(u).\end{aligned}$$

- the right hand side $f = \tilde{c}u$ in the monomer equation. We find the same estimate as for φ and only note that $\tilde{c}$ is composed of products $\kappa_B a_B$ and $\kappa_P a_P$ rather than κ_B and κ_P alone as in c.

- in the equations for the boundary velocities. The respective estimates take the form

$$\begin{aligned}|\dot{l}(t) - \dot{l}(s)| &= \delta \left|\kappa_B(a - a_B)\rfloor_{(t,l(t))} - \kappa_B(a - a_B)\rfloor_{(s,l(s))}\right| \\ &\leq \delta v_{max}(\|\kappa_B\|_{C^0}\|a\|_{C^1} + \|\kappa_B\|_{C^1}\|a\|_{C^0} + \|\kappa_B a_B\|_{C^1})|t - s|.\end{aligned}$$

The variations in the coefficients thus only affect the constants in the estimates from the previous section. Since the most regular function we used in the definition of the spaces X_T and V_T, respectively, is the monomer density which is required to be of class $C^{2_x,1_t}$ we shall assume the coefficients $\kappa_{B/P}$ and $a_{B/P}$ to belong to $C_b^{2_x,1_t}(E_\infty^*)$.

As we deal with the strictly hyperbolic case, we also have to take care of variations in the quantity a^{BP} which we recall to be given by (3.7):

$$a^{BP}(t,x) = \frac{2\frac{v_R}{\delta} + \kappa_B(t,x)a_B(t,x) - \kappa_P(t,x)a_P(t,x)}{\kappa_B(t,x) - \kappa_P(t,x)}.$$

If we want a to lie between a^{BP} and a_P we shall assume $a_P - a^{BP}$ to be bounded away from zero. This is granted if we require

$$2\delta\kappa_B(t,x)(a_P(t,x) - a_B(t,x)) - 2v_R \geq A_0 > 0.$$

By continuity of both, the monomer density a and the reaction parameters, we can now assert that if a is initially bounded away from a^{BP} this will also be true for sufficiently small positive time.

We finally recall that the general bounds on the monomer density, the velocities, and the reaction term in chapter 3 have been derived for variable reaction coefficients satisfying certain assumptions.

Without carrying out the precise calculations corresponding to those from the previous section, we can state the following corollary of theorem 4.21.

Corollary 4.23. *Assume to be given $\beta \in (0,1)$, coefficient functions $\kappa_B, \kappa_P, a_B, a_P \in C_b^{2_x,1_t}(E_\infty^+)$, and initial conditions*

$$u_0 \in C^2([0,L]) \qquad \text{and} \qquad a_0 \in C^{2+\beta}([0,L])$$

satisfying the compatibility conditions 2.3.1, condition b) in lemma 4.19, 2.3.2, and the following general conditions

a)

$$\inf_{t>0, x\in\mathbb{R}} (\kappa_B(t,x) - \kappa_P(t,x)) > 0,$$

b)

$$2\delta \inf_{t>0, x\in\mathbb{R}} \kappa_B(t,x)(a_P(t,x) - a_B(t,x)) - 2v_R > 0,$$

c)

$$a_0(x) \leq a_P(0,x) \qquad \text{for each } x \in [0,L],$$

d)

$$\min_{x\in[0,L]} (a_0(t,x) - a^{BP}(0,x)) > 0.$$

Then, there exists some time $T_9 > 0$ such that for each $T \in (0, T_9]$, the problem (2.15), (2.32), (2.13), (2.22), (2.23) equipped with the initial conditions u_0, a_0 possesses a unique solution (l_*, r_*, a_*, u_*) belonging to

$$C^{1+1}([0,T]) \times C^{1+1}([0,T]) \times C^{2+\beta,P}(\overline{Q_T}) \times \left(C^1(\overline{Q_T})\right)^4$$

where Q_T is given by (2.21). The time T_9 only depends on β, D, L, v_R, δ, the relevant norms of the reaction parameters and the initial conditions, and on the bounds from the hypotheses a), c), and d). The norms of l_*, r_*, a_*, and u_* in the respective spaces only depend on the same quantities and in addition on the choice of $T \in (0, T_9]$.

4.3 The loss of strict hyperbolicity

For the strictly hyperbolic case we required the monomer density to be bounded between the values a^{BP} and a_P. This is a very strong condition and can only be assured for small times. It would therefore be useful to relax this assumption by allowing the crossing of characteristic curves.

In the interior of the domain the loss of strict hyperbolicity does not change the situation at all since there are no interactions of the end densities among each other and we do not have to consider any transition conditions where the characteristic curves intersect. In particular, proposition 4.8 does not require any hypotheses on the strict hyperbolicity.

We therefore have to consider the case of crossing characteristics on the boundary. In general, if the leading characteristic curve switches we obtain a jump in the boundary velocity. The boundary curves can thus only be expected to be LIPSCHITZ continuous.

Let us concentrate on the left boundary as the case of the right boundary is just the mirror image. Let us furthermore only deal with physical solutions, meaning that in

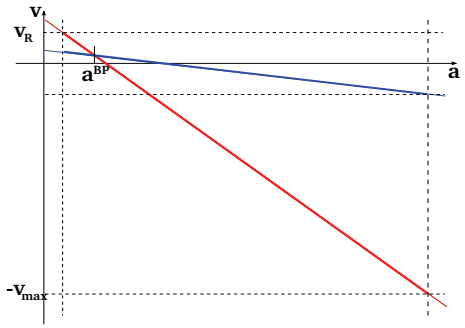

Figure 4.1: Possible boundary velocities for the left boundary depending on the monomer concentration. *Red*: $-v_B(a)$, *blue*: $v_P(a)$. It should be noted that the slopes and the position of the endpoints on the abscissa may vary if the coefficients are variable.

some neighborhood of the left boundary the densities of right oriented barbed and left oriented pointed ends vanish. That means, we only have to consider the end densities u^1 and u^2 with the characteristic velocities being $\lambda^1 = -v_B$ and $\lambda^2 = v_P$, respectively.

The particular monomer concentration to take care of is the value a^{BP} given by (3.7). At this particular value, both end velocities of interest coincide, at lower values of a, λ^2 is smaller than λ^1 and therefore takes the lead, and at higher concentrations, the leading characteristic velocity is λ^1. We refer to figure 4.1 for a sketch of the dependence of the relevant velocities on the monomer density.

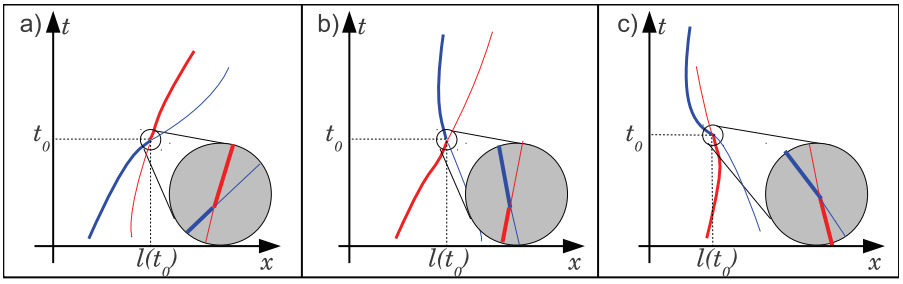

Figure 4.2: Possible behavior of the left boundary curve (thick line) around a point $(t_0, l(t_0))$ where the outer characteristics of u^1 and u^2 cross. Different colors stand for different characteristic families, *blue*: $l^1(t)$, *red*: $l^2(t)$. Inside the grey circles, a zoom into the vicinity of the crossing points is shown. Picture (a) corresponds to case 1. Note that case 2.a) has a similar shape with colors being exchanged. Pictures (b) and (c) sketch the situation of cases 2.b) and 2.c), respectively.

Recalling that we assumed the parameters to satisfy

$$\delta\kappa_P(a_P - a_B) > v_R$$

in order to allow for a positive pointed end velocity v_P, we conclude that the value a^{BP} is such that

$$\lambda^1(a^{BP}) = \lambda^2(a^{BP}) > 0.$$

A jump in the boundary velocity may occur in the following ways which are sketched in figure 4.2.

1. The leading characteristic curve is the one corresponding to $B_l = u^1$ and at $t = t_0$

the outer characteristic curve corresponding to $P_r = u^2$ takes over the lead. Then, necessarily $\lambda^2 < \lambda^1$ − or equivalently $a \leq a^{BP}$ − in some parabolic cylinder

$$\mathrm{Cyl}_r(t_0, l(t_0)) \cap Q_T$$

below $(t_0, l(t_0))$. Since both characteristic velocities are positive for such values of a, we have the following situation.

The membrane is supported by the leading left oriented barbed ends which retract at velocity $\lambda^1 > 0$. Behind that, the leading right oriented pointed ends retract at lower velocity λ^2 and are caught up by the membrane at time $t = t_0$. We may without loss of generality assume that

$$\lim_{t \nearrow t_0} a(t, l(t)) \lneq a^{BP}(t_0, l(t_0))$$

since otherwise the characteristic velocities would coincide and there was no jump to be expected.

2. The leading characteristic curve is the one corresponding to $P_r = u^2$ and at $t = t_0$ is replaced by the outer characteristic curve corresponding to $B_l = u^1$. In any case we can state that $a(t, x) \geq a^{BP}$ in some cylinder below $(t_0, l(t_0))$ but we cannot assert anything about the signs of the characteristic velocities. In fact, we have to consider three generic cases:

   a) Both types of ends shrink:

   $$0 < \lim_{t \nearrow t_0} \lambda^1(a(t, l(t))) < \lim_{t \nearrow t_0} \lambda^2(a(t, l(t))).$$

   b) The barbed ends grow whereas the pointed ends shrink:

   $$\lim_{t \nearrow t_0} \lambda^1(a(t, l(t))) < 0 < \lim_{t \nearrow t_0} \lambda^2(a(t, l(t))),$$

   c) Both characteristic curves grow outwards:

   $$\lim_{t \nearrow t_0} \lambda^1(a(t, l(t))) < \lim_{t \nearrow t_0} \lambda^2(a(t, l(t))) < 0,$$

   Of course, equality of one of the velocities to zero cannot be excluded.

If we assume that the solution to our full problem exists up to time $t = t_0$ and possesses the regularity asserted in the previous section, we may consider the problem we are dealing with as a free boundary problem with initial conditions at $t = t_0$. However we are now in the situation that the compatibility conditions 2.3.2 will be violated at the point (t_0, l_1).

We recall that our boundary conditions were derived by stating that there shall be no flux of monomers across the boundary. This is also recovered from the weak formulation of the initial boundary value problem for (4.45) on the fixed saptial domain $(0, L)$.

To define the appropriate initial conditions at $t = t_0$ we put

$$a_1(\xi) := \lim_{\tau \nearrow t_0} \tilde{a}(\tau, \xi)$$

and observe that by construction a_1 belongs to $C^{2+\beta}([0,L])$.

For the fixed domain problem with initial conditions a_1 at $\tau = t_0 < T$ we classically have the weak formulation

$$\begin{aligned} 0 = & \int_{t_0}^{T}\int_0^L -\partial_\tau\psi\ \tilde{a} + \frac{DL^2}{(r-l)^2}\partial_\xi\psi\partial_\xi\tilde{a} - \psi\ \Xi(\tau,\xi)\partial_\xi\tilde{a} + \psi(\tilde{\varphi}\tilde{a} - \tilde{f})d\xi d\tau \\ & + \int_0^L \psi(t_0,\xi)a_1(\xi)d\xi + \int_{t_0}^{T}\frac{L}{r-l}\left[\psi(\tau,L)\dot{r}(\tau)\tilde{a}(\tau,L) - \psi(\tau,0)\dot{l}(\tau)\tilde{a}(\tau,0)\right]d\tau \end{aligned}$$

for each $\psi \in C^\infty([t_1,T]\times[0,L])$ which vanishes on $\{T\}\times[0,L]$. We can now formally integrate the term

$$\psi\Xi(\tau,\xi)\partial_\xi\tilde{a}$$

once by parts with respect to ξ:

$$\begin{aligned} & \int_{t_0}^{T}\int_0^L -\psi\Xi\partial_\xi\tilde{a}d\xi d\tau \\ = & \int_{t_0}^{T}\int_0^L \partial_\xi(\psi\Xi)\tilde{a}d\xi d\tau - \int_{t_0}^{T}\psi(\tau,L)\Xi(\tau,L)\tilde{a}(\tau,L) - \psi(\tau,0)\Xi(\tau,0)\tilde{a}(\tau,0)d\tau. \end{aligned}$$

Recalling the particular shape of Ξ we obtain

$$\begin{aligned} \Xi(\tau,0) = \frac{L}{r(\tau)-l(\tau)}\left(\frac{0}{L}(\dot{r}(\tau)-\dot{l}(\tau)) + \dot{l}(\tau)\right) &= \frac{L}{r(\tau)-l(\tau)}\dot{l}(\tau) \\ \Xi(\tau,L) = \frac{L}{r(\tau)-l(\tau)}\left(\frac{L}{L}(\dot{r}(\tau)-\dot{l}(\tau)) + \dot{l}(\tau)\right) &= \frac{L}{r(\tau)-l(\tau)}\dot{r}(\tau) \\ \partial_\xi\Xi(\tau,\xi) &\equiv \frac{\dot{r}(\tau)-\dot{l}(\tau)}{r(\tau)-l(\tau)}, \end{aligned}$$

and see that in particular, the boundary terms in the weak formulation are canceled.

We end up with the following shape

$$\begin{aligned} 0 = & \int_{t_0}^{T}\int_0^L -\partial_\tau\psi\ \tilde{a} + \partial_\xi\psi\left(\frac{DL^2}{(r-l)^2}\partial_\xi\tilde{a} + \Xi\tilde{a}\right) + \psi\left(\left(\tilde{\varphi} + \frac{\dot{r}-\dot{l}}{r-l}\right)\tilde{a} - \tilde{f}\right)d\xi d\tau \\ & + \int_0^L \psi(t_0,\xi)a_1(\xi)d\xi. \end{aligned} \tag{4.132}$$

This in turn is just the weak formulation of the homogeneous NEUMANN boundary problem for the equation

$$\partial_\tau\tilde{a} - \frac{L}{r-l}\partial_\xi\left(\frac{DL}{r-l}\partial_\xi\tilde{a} + \left(\frac{\xi}{L}(\dot{r}-\dot{l}) + \dot{l}\right)\tilde{a}\right) + \left(\tilde{\varphi} + \frac{\dot{r}-\dot{l}}{r-l}\right)\tilde{a} - \tilde{f} = 0. \tag{4.133}$$

which in fact is the same as (4.45).

To understand the effect of the incompatibility of the boundary and initial conditions, it is therefore sufficient to consider the heat equation with homogeneous NEUMANN boundary conditions and initial data having non-zero spatial derivatives at the corner.

More precisely, in our original problem (4.7), (4.8), (4.9), we could have neglected

the terms φa and f since both are assumed to be uniformly HÖLDER continuous and φ is moreover non-negative. These terms only affect the regularity of the solution in the way that it is only of class $C^{2+\beta,P}$ rather than C^∞ as we have seen in subsection 4.1.1.

The first order term

$$\Xi(\tau,\xi)\partial_\xi \tilde{a}$$

is just the one emerging from the moving boundary and has been seen to have no effect of reducing the regularity of the solution to less than $C^{2+\beta,P}$. This remains true since the boundary velocities $\dot{l}$ and $\dot{r}$ are still uniformly HÖLDER continuous up to the kinks in the boundary which are our new corner points of the domain.

The only remaining source of irregularity for the solution is therefore indeed the violation of the compatibility conditions on the initial and boundary values at the corners.

Let us therefore consider the auxiliary problem

$$\partial_t a(t,x) - D\partial_{xx} a(t,x) = 0 \tag{4.134}$$

in $(0,T)\times(0,L)$ with homogeneous NEUMANN boundary conditions and initial conditions

$$a(0,x) = a_1(x) \qquad \text{in } [0,L]$$

with $a_1 \in C^{2+\beta}([0,L])$.

The unique bounded, continuous solution to this problem is given by

$$a(t,x) = \frac{b_0}{2} + \sum_{n=1}^{\infty} b_n \exp\left[-\frac{n^2\pi^2}{L^2}Dt\right]\cos\left[\frac{n\pi}{L}x\right] \tag{4.135}$$

with

$$b_n = \frac{2}{L}\int_0^L a_1(x)\cos\left[\frac{n\pi}{L}x\right]dx\ , \qquad n = 0,1,2,\ldots$$

being the cosine - FOURIER coefficients of a_1.

Now we observe that a defined in that way is uniformly continuous and bounded on $[0,T]\times[0,L]$ and that also its spatial derivative $\partial_x a$ is bounded although not continuous on the corner points. Moreover, the solution is smooth in $(0,T]\times[0,L]$ with integrable derivatives $\partial_t a$ and $\partial_{xx} a$ satisfying

$$\sup_x(|\partial_t a(t,x)|, |\partial_{xx} a(t,x)|) \sim \frac{1}{\sqrt{t}}$$

as $t \searrow 0$ with proportionality factor depending on D, L, and the initial conditions a_1, in particular on their behavior at the boundary points 0 and L. The strength of the incompatibility − that is, the deviation of the initial spatial derivative from that required by the boundary condition − is bounded by

$$\left|\frac{d}{dx}a_1(t_0,l_1) - \partial_x a\rfloor_{BC}\right| \le \frac{1}{D}|v_B(a(t_0,l_1)) - v_P(a(t_0,l_1))|. \tag{4.136}$$

What is most important is the observation that both, $\partial_t a$ and $\partial_{xx} a$ belong to $L_p(0,T;\ L_\infty(0,L))$ for any $p \in [1,2)$.

For the behavior in the interior we can employ the original equation (4.7) to conclude

that $a \in C^{2+\beta}(\overline{Q'})$ for any Q' being compactly included in Q_T.

If we therefore assume to be given HÖLDER continuous (exponent β) end densities and HÖLDER continuous (exponent $\frac{1+\beta}{2}$) boundary curves, we conlcude that we find a uniformly continuous monomer density with bounded first spatial derivative and integrable (weak) first temporal and second spatial derivatives.

Moreover, if the boundary curves have derivatives which are piecewise $C^{\frac{1+\beta}{2}}$, this monomer density will in fact be of class $C^{2+\beta,P}$ over the whole domain except possibly at times t_* where the boundary velocities are discontinuous. One might call this property *piecewise (in time) smoothness* and write for a suitable extension $\bar{a}(t,\cdot)$ of $a(t,\cdot)$ to all of $\mathbb{R}$ as discussed in subsection 4.1.6

$$\bar{a} \in C^0([0,T]\times\mathbb{R}) \cap C^1((0,T)\backslash\mathcal{N}; C^2(\mathbb{R}))$$

where $\mathcal{N}$ is the collection of discontinuity points of the boundary curves which is assumed to be finite and in particular of Lebesgue measure zero. We note that even if this assumption is dropped we can still assert

$$\bar{a} \in C^0([0,T]\times\mathbb{R}) \cap L_\infty(0,T; C^{0+1}(\mathbb{R})).$$

Turning our attention to the boundary curves we find initial value problems of the form

$$\dot{l}(t) = c_{l,1}(t)a(t,l(t)) + c_{l,2}(t) =: v_l(t,l(t)) \quad \text{for } t\in[0,T), \qquad l(0)=0 \tag{4.137}$$

$$\dot{r}(t) = c_{r,1}(t)a(t,l(t)) + c_{r,2}(t) =: v_r(t,r(t)) \quad \text{for } t\in[0,T), \qquad r(0)=L. \tag{4.138}$$

These can be solved in the sense of CARATHÉODORY since the vector fields $v = v_l, v_r$ satisfy

1. For each $t\in[0,T]$, the function $v(t,\cdot)$ is globally LIPSCHITZ continuous on $\mathbb{R}$ with uniform (in t) LIPSCHITZ constant.

2. v is globally bounded: $v \in L_\infty((0,T))$.

These properties in particular imply that the velocities are CARATHÉODORY functions which assures the existence of absolutely continuous solutions. Their uniqueness is granted due to the uniform LIPSCHITZ bound on the velocities with respect to x. Moreover, since the velocities are globally uniformly bounded, the solutions are not only absolutely continuous but even globally LIPSCHITZ continuous with LIPSCHITZ constant bounded by $\|v_{r/l}\|_{L_\infty}$ which we already know to be at most v_{max}. Apart from the discontinuity points of the coefficient functions $c_{l,i}$ and $c_{r,i}$ $(i=1,2)$ the boundary curves are moreover differentiable with continuous derivatives since a has been found to be continuous.

We finally ask for the end densities and again consider the CAUCHY problem upon if necessary extending the given monomer density to all of $[0,T]\times\mathbb{R}$. By the theory of DiPerna and Lions (cf. [5]) these CAUCHY problems for $u^1,\dots,u^4$ have unique solutions in the space of RADON measures for velocity fields λ^α belonging to $L_1(0,T;W_\infty^{1,loc}(\mathbb{R}))$.

Since our velocity fields are globally bounded, uniformly continuous and even have globally bounded classical spatial derivatives, these measure valued solutions μ_t^α are for each $t\in[0,T]$ absolutely continuous with respect to the Lebesgue measure on $\mathbb{R}$ and

we can even calculate their (RADON-NIKODYM-) density by (4.31) which we necessarily find to be continuous.

Moreover, we can employ the estimates from subsection 4.1.4 with one minor adaptation. Namely, if we only assume the given velocity field λ to belong to

$$L_\infty(0,T;W^1_\infty(\mathbb{R})) \cap L_p(0,T;W^2_\infty(\mathbb{R}))$$

we have a different estimate for the integral

$$\int_s^t \partial_x\lambda(\tau,y_1(\tau) - \partial_x\lambda(\tau,y_2(\tau)dx.$$

Instead of (4.34) we now use the following estimate:

$$\begin{aligned}
&\int_s^t |\partial_x\lambda(\tau,y^\alpha(\tau;\xi^\alpha(t,y)) - \partial_x\lambda(\tau,y^\alpha(\tau;\xi^\alpha(t,x)))|d\tau \\
&\leq \int_s^t \|\partial_{xx}\lambda(\tau,\cdot)\|_{L_\infty}|x-y|\exp[\|\partial_x\lambda\|_{L_\infty}(t-\tau)]d\tau \\
&\leq C|x-y||t-s|^q\exp[|t-s|\|\partial_x\lambda\|_{L_\infty}] \qquad \text{for any } q \in \left(0,1-\frac{1}{p}\right)
\end{aligned}$$

with the constant C only depending on

$$p, \quad \|\partial_{xx}\lambda\|_{L_p(0,T;L_\infty)}, \quad \text{and} \quad q.$$

We therefore in fact obtain estimates very similar to (4.40), (4.41), (4.42), namely

$$\|u\|_{L_\infty} \leq \mathcal{E}_0(T)M_0 \tag{4.139}$$

$$\|\partial_x u\|_{L_\infty} \leq \mathcal{E}_0(2T)(M_1 + M_0C_1\mathcal{E}_0(2T)T^q) \tag{4.140}$$

$$\|\partial_t u\|_{L_\infty} \leq \mathcal{E}_0(2T)\left(M_1v_{max} + \delta\kappa_B M_0\left(C_2T^q\mathcal{E}_0(2T)v_{max} + \|\partial_x A\|_{L_\infty}\right)\right) \tag{4.141}$$

with q as indicated above and $C_1,\ C_2$ only depending on

$$p, \quad \|\partial_{xx}\lambda\|_{L_p(0,T;L_\infty)}, \quad \text{and} \quad q.$$

In particular, the solution u is differentiable in both, space and time, with bounded derivatives and thus LIPSCHITZ continuous. Moreover, the precise values of the constants $C_1,\ C_2$ do not pose a problem since they are multiplied by terms T^q which can be made small by choosing T appropriately small. We therefore can find an upper bound on the derivatives of u which is independent of the particular values for p, q, and the L_p-norm of $\partial_{xx}\lambda$.

We remark that if we assume the monomer density (that is, the velocity fields) to have continuous spatial derivatives with discontinuities only along isolated LIPSCHITZ continuous, piecewise continuously diffentiable curves Γ, we can even employ the weak formulation of the conservation laws to deduce explicite regularity assertions on the end densities.

Let us more precisely assume the velocity field λ to be of class $C^{1+1_x,0+1_t}$ in $(0,T)\times\mathbb{R}^n$ except for some isolated curves as indicated above. We choose one of them, call

it Γ and write it as disjoint union of two pieces Γ_1 and Γ_2 which may without loss of generality be assumed to be connected such that Γ_1 is the graph of a curve which is nowhere tangent to a line $\{t = const\}$ and Γ_2 is nowhere tangent to a line $\{x = const\}$.

Now we choose some test function

$$\phi \in C_c^\infty((0,T) \times \mathbb{R})$$

with support D containing some part $\Gamma^{(D)}$ of Γ and such that D is bounded away from all other curves where λ is of lower regularity. We partition the support of ϕ into

$$D = D_1 \cup D_2 \cup \Gamma^{(D)}$$

where D_1 and D_2 are the connected components of $D \backslash \Gamma$ as indicated in figure 4.3.

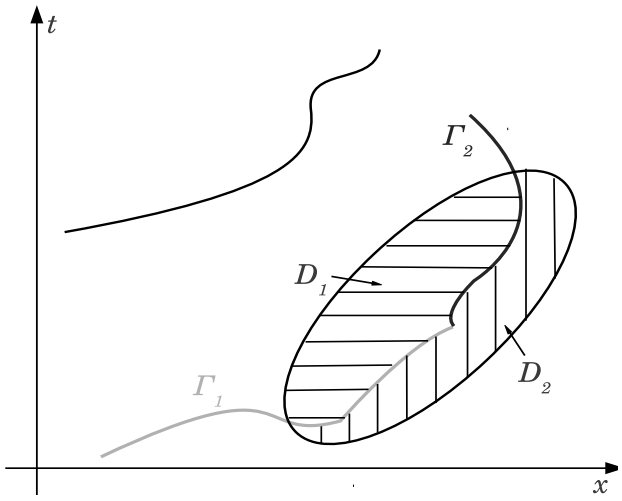

Figure 4.3: Domain of integration around a curve $\Gamma = \Gamma_1 \cup \Gamma_2$ and partition of D into D_1 and D_2.

Formally differentiating the equation with respect to x and interchanging the differentiations in the first term reads

$$\partial_t(\partial_x u) + \partial_x(\partial_x(\lambda u)) = 0 \tag{4.142}$$

and in weak form tested against ϕ (whose support should be assumed to contain no points $(0, x)$):

$$\begin{aligned} 0 &= \int_D (\partial_x u \partial_t \phi + \partial_x(\lambda u)\partial_x \phi) dx dt \\ &= \int_{D_1} (\partial_x u \partial_t \phi + \partial_x(\lambda u)\partial_x \phi) dx dt + \int_{D_2} (\partial_x u \partial_t \phi + \partial_x(\lambda u)\partial_x \phi) dx dt. \end{aligned}$$

We note that the integral makes sense since both, λ and u, are known to be continuous with first spatial derivatives belonging to L_∞. Now, we assumed that in the interiors of D_1 and D_2, both have even LIPSCHITZ continuous spatial derivatives and are LIPSCHITZ continuous with respect to time. Inside D_1 and D_2, equation (4.142) is assumed to be

satisfied almost everywhere and we conclude:

$$\begin{aligned} 0 &= \int_{D_1} (\partial_t(\partial_x u\ \phi) + \partial_x(\partial_x(\lambda u)\phi) - \phi(\partial_{tx}u + \partial_{xx}(\lambda u))dxdt \\ &\quad + \int_{D_2} (\partial_t(\partial_x u\ \phi) + \partial_x(\partial_x(\lambda u)\phi) - \phi(\partial_{tx}u + \partial_{xx}(\lambda u))dxdt \\ &= \int_{D_1} \operatorname{div} \begin{pmatrix} \partial_x(\lambda u)\phi \\ \partial_x u\ \phi \end{pmatrix} dxdt + \int_{D_2} \operatorname{div} \begin{pmatrix} \partial_x(\lambda u)\phi \\ \partial_x u\ \phi \end{pmatrix} dxdt. \end{aligned}$$

We can now apply the divergence theorem and recall that ϕ vanishes on ∂D together with all its derivatives. Moreover, we denote by λ_i, u_i the values of λ, u, respectively, in D_i $(i = 1, 2)$. Then, we calculate

$$0 = \int_\Gamma ((\partial_x(\lambda_2 u_2) - \partial_x(\lambda_1 u_1))\phi dt - (\partial_x u_2 - \partial_x u_1)\ \phi dx)\,.$$

Now we split this integral up into integrals over Γ_1 and Γ_2 and denote by $[f] := f_2 - f_1$ the jump of the function f across Γ. We pointed out that Γ_1 is (locally) the graph of a LIPSCHITZ continuous, piecewise differentiable function $t = t(x)$, and we denote the derivative by

$$\frac{dt}{dx} =: \mu.$$

Analogously, Γ_2 can be written as a function $x(t)$ whose derivative shall be denoted by

$$\frac{dx}{dt} =: \nu.$$

Using these notations we calculate

$$0 = \int_{\Gamma_1} (\mu[\partial_x(\lambda u)] - [\partial_x u])\,\phi\ dx + \int_{\Gamma_2} ([\partial_x(\lambda u)] - \nu[\partial_x u])\,\phi\ dt$$

Since ϕ was arbitrary and we can in particular choose it in a way such that $D \cap \Gamma_j = \emptyset$ for either $j = 1, 2$, we conclude

$$(\nu - \lambda)[\partial_x u] = u[\partial_x \lambda] \qquad \text{along } \Gamma_2 \tag{4.143}$$

$$(1 - \mu\lambda)[\partial_x u] = \mu u[\partial_x \lambda] \qquad \text{along } \Gamma_1. \tag{4.144}$$

We should note that the partition of Γ into Γ_1 and Γ_2 does not lack some ambiguity. The only restriction on the choice of Γ_1 and Γ_2 is that Γ_1 should nowhere be parallel to the t-axis and Γ_2 should not contain parts parallel to the x-axis. However, at all other parts of Γ a switch from the notation of Γ_1 to that of Γ_2 yields

$$\nu = \frac{1}{\mu}$$

(both being neither zero nor infinite). Under this equality, we easily see that (4.144) turns into (4.143).

If we assume the possible lines of discontinuities of $\partial_x \lambda$ to be of the type $\{t = const\}$ we observe that (4.144) with $\mu = 0$ yields in fact continuity of $\partial_x u$ across these lines.

To solve the initial value problem starting at a time t_0 where the outer characteristic curves cross we therefore may use similar arguments as in subsection 4.1.6. Here, the spaces V_T and W_T have to be replaced by $\tilde{V}_{t_0,T}$ and $\tilde{W}_{t_0,T}$ which are given by the following definitions.

The given boundary curves are assumed to belong to the space

$$C^{1+\beta_0}([t_0,T])$$

with $\beta_0 \in \left(\frac{1}{2},1\right)$ being some given number.

The given monomer density − or rather its spatial extension to $[0,T]\times[l_{min},r_{max}]$ − belongs to

$$C^0([t_0,T]\times[l_{min},r_{max}])\cap L_\infty(0,T;W^1_\infty(l_{min},r_{max}))\cap L_{p_0}(0,T;W^2_\infty(l_{min},r_{max}))$$

where $p_0 \in [1,2)$.

For the given end densities we merely assume as before regularity according to

$$C^{0+\beta_0,P}(\overline{Q_{t_0,T}}).$$

The image space $\tilde{W}_{t_0,T}$ shall be composed of the following spaces. The boundary curves belong to

$$C^{1+\beta_1}([t_0,T])$$

with β_1 satisfying $\beta_1 p_0 < 1$ and $\beta_1 > \beta_0$. The former condition assures boundedness of the norm in the image space and the second one guarantees that, for small $T-t_0$, the distance of two curves from the image space is small in the preimage space by the Hölder scale from remark A.1.

The (extension of the) monomer density lies in

$$C^0(\overline{Q_{t_0,T}})\cap L_\infty(t_0,T;W^1_\infty(l_{min},r_{max}))\cap L_{p_1}(t_0,T;W^2_\infty(l_{min},r_{max}))$$

where the exponent p_1 is required to satisfy $p_0 < p_1 < 2$. As the solution is bounded in

$$L_{p_1}(t_0,T;W^2_\infty(l_{min},r_{max})) \qquad \text{for any } p_1<2,$$

the Lebesgue scale guarantees that the distance of two appropriate solutions is small in

$$L_{p_0}\left(t_0,T;W^2_\infty(l_{min},r_{max})\right)$$

by calculating

$$\left\| t\mapsto \|a_1(t,\cdot)-a_2(t,\cdot)\|_{W^2_\infty}\right\|_{L_{p_0}} \le (T-t_0)^{\frac{p_1-p_0}{p_0p_1}}\left\| t\mapsto \|a_1(t,\cdot)-a_2(t,\cdot)\|_{W^2_\infty}\right\|_{L_{p_1}}.$$

Finally, for the end densities we obtain solutions in the space

$$W^1_\infty([t_0,T]\times[l_{min},r_{max}]).$$

Again, the Hölder scale between β_0 and 1 allows for smallness of differences of solutions in the pre-image space for small differences of the given data and small $T-t_0$.

We therefore find again a contraction for sufficiently small $T-t_0$ where a lower bound of T depends on the parameters $\beta_{0/1}$, and $p_{0/1}$, in particular on

$$1-\left(\frac{1}{p_0}-\beta_1\right) \qquad \text{and} \qquad \frac{p_1-p_0}{p_1 p_0}.$$

Of course, it is possible to find parameters $\beta_{0/1}$ and $p_{0/1}$ satisfying all the conditions above. A possible choice would be

$$\begin{aligned} \beta_0 &= \frac{5}{8} & \beta_1 &= \frac{2}{3} \\ p_0 &= \frac{5}{4} & p_1 &= \frac{15}{8}. \end{aligned}$$

Chapter 5

Interior Gradient Blow Up and Shock Formation

We are now going to investigate the possibility of singularities forming in the interior of the domain by

a) blow-up of the spatial derivative $\partial_x a$ of the monomer density, or

b) mass concentration of filament ends in DIRAC measures.

The latter type of discontinuity already showed up in the discussion of interior steady states in section 2.4 where we also indicated the possibility of states with jumps in the monomer density.

Besides being useful for the investigation of the well posedness of our model for long times we recall these solutions to be of biological relevance as well. The accumulation of filament tips in a very narrow region in space and their eventual collapse into an concentrated measure describes nothing else than the emergence of a sharp front of polymerizing filaments. It is therefore only natural to ask for the occurance of such solutions.

We start with the investigation of two limiting cases.

5.1 The limiting case of rapid diffusion

Let us first consider the case of rapid diffusion so that any inhomogeneities in the monomer distribution equilibrate instantaneously. This formally corresponds to setting the diffusion coefficient D in the eqution for the monomers to ∞. This equation consequently reduces to

$$\partial_{xx} a(t,x) = 0. \tag{5.1}$$

5.1.1 Rapid diffusion in a fixed domain

Let us start with a toy model where we assume the cell to occupy a fixed domain with filament ends being located away from the boundary.

Using the equation $\partial_{xx} a = 0$ together with the no-flux conditions on the boundary we conclude a homogeneous distribution of monomers at any instant of time, and we call

this value $A(t)$. The total amount of G-actin in the cell is now simply given by $A(t)L$. This entity is governed by an ordinary differential equation capturing the polymerization kinetics at all filament ends throughout the domain:

$$L\frac{d}{dt}A = \delta \int_0^L \tilde{c}(t,x)u(t,x) - c(t,x)u(t,x)A(t)dx. \tag{5.2}$$

Note that the right hand side is nothing else than the spatial integral over the reaction term

$$R(A(t), u(t,x)).$$

In the case of constant reaction parameters c and $\tilde{c}$, this reduces to a simple linear equation with constant coefficients:

$$\frac{d}{dt}A = -\frac{\delta}{L}CA(t) + \frac{\delta}{L}\tilde{C} \tag{5.3}$$

where

$$C := c\int_0^L u(t,x)dx \qquad \text{and} \qquad \tilde{C} := \tilde{c}\int_0^L u(t,x)dx$$

are indeed constants since the integrals are nothing else than the conserved L_1-norm of the end densities.

The equation for A is solved by

$$\begin{aligned} A(t) &= \left(K_0 + \frac{\tilde{C}}{C}\exp\left[\frac{\delta C}{L}t\right]\right)\exp\left[-\frac{\delta C}{L}t\right] \\ &= \left(A(0) - \frac{\tilde{C}}{C}\right)\exp\left[-\frac{\delta C}{L}t\right] + \frac{\tilde{C}}{C}. \end{aligned} \tag{5.4}$$

We see the (uniform) monomer concentration approaching some equilibrium value $\tilde{C}/C$ at an exponential rate. If in addition, the reaction parameters are assumed to satisfy 2.1.1 and the compatibility condition from remark 2.1, and if we assume an initially symmetric cell satisfying

$$\int_0^L u^1(0,x)dx = \int_0^L u^2(0,x)dx = \int_0^L u^3(0,x)dx = \int_0^L u^4(0,x)dx \tag{5.5}$$

then the constant $\tilde{C}/C$ is just the steady state monomer concentration a^{ss}. In that case, the monomer concentration approaches its steady state value which implies asymptotically vanishing velocities of the filament tips. Without the compatibility condition the end velocities may be different from zero at the asymptotically reached monomer concentration.

Let us also note that for this limiting case we do not require the pointwise condition on the end densities

$$B_r + B_l = P_r + P_l$$

known from the discussion of strong steady states in section 2.4 to sustain a homogeneous monomer density.

5.1.2 Rapid diffusion for the free boundary problem

If the boundary curves evolve according to (2.22) and (2.23) we also have to consider the nontrivial no-flux conditions given by (2.32). However, setting D to infinity, we obtain homogeneous NEUMANN boundary conditions as well.

Now, in case of a moving boundary, the total monomer concentration is given by

$$(r(t) - l(t))\, A(t)$$

and evolves according to

$$\frac{d}{dt}\left((r(t) - l(t))A(t)\right) + CA(t) = \tilde{C}.$$

with C and $\tilde{C}$ being the integrals defined above. For these we should note that the conservation of the number of filament tips of either type does not rely on the domain having a fixed estension but is also granted for the free boundary case.

Since we know the evolution of the boundary curves r and l in terms of A to be given by

$$\begin{aligned} \dot{l}(t) &= \kappa_l(t)A(t) + k_l(t) \\ \dot{r}(t) &= \kappa_r(t)A(t) + k_r(t) \end{aligned}$$

we obtain an integro-differential equation for the global monomer density A:

$$\left(L + \int_0^T \kappa(\tau)A(\tau) + k(\tau)d\tau\right)\dot{A}(t) + (C + k(t))A(t) + \kappa(t)A(t)^2 = \tilde{C} \tag{5.6}$$

where the coefficient functions

$$\kappa(t) := \kappa_r(t) - \kappa_l(t) \qquad \text{and} \qquad k(t) := k_r(t) - k_l(t)$$

are determined by the end densities evolving according to the linear transport equation

$$\partial_t u + \Lambda(A(t))\partial_x u = 0. \tag{5.7}$$

We therefore find smooth solutions as long as the factor

$$L + \int_0^T \kappa(\tau)A(\tau) + k(\tau)d\tau = r - l$$

does not vanish. These solutions are in particular characterized by end densities of constant shape as the velocity fields in their governing equations are independent of the spatial variable.

5.2 The limiting case of vanishing diffusion

If the monomers are assumed not to diffuse their density is again governed by ordinary differential equations but now there is one for each space point. We arrive at the

pointwise equation

$$\frac{d}{dt}a(t,x) = -c(t,x)u(t,x)a(t,x) + \tilde{c}(t,x)u(t,x) \tag{5.8}$$

which can be solved to

$$\begin{aligned} a(t,x) = \exp\left[-\int_0^t c(\tau,x)u(\tau,x)d\tau\right] \times \\ \times \left(a(0,x) + \int_0^t \exp\left[-\int_0^\tau c(\sigma,x)u(\sigma,x)d\sigma\right]\tilde{c}(\tau,x)u(\tau,x)d\tau\right). \end{aligned} \tag{5.9}$$

Assuming the kinetic coefficients encoded in c and $\tilde{c}$ to be independent of time and introducing the notation

$$\mathcal{U}(t,x) := \int_0^t u(\tau,x)d\tau,$$

this solution can be rewritten to

$$a(t,x) = \exp\left[-c(x)\mathcal{U}(t,x)\right]\left(a(0,x) + \tilde{c}(x)\int_0^t \exp\left[-c(x)\mathcal{U}(\tau,x)\right]u(\tau,x)d\tau\right). \tag{5.10}$$

This can be directly plugged into the hyperbolic part of the system where it makes the indirect coupling between the single hyperbolic equations clearly visible:

$$\begin{aligned} \partial_t u^\alpha(t,x) &= -\partial_x\left(\lambda^\alpha(t,x,a(t,x))u^\alpha(t,x)\right) \\ &= -\exp\left[-c\,\mathcal{U}(t,x)\right]\left(a(0,x) + \tilde{c}\int_0^t \exp\left[-c\,\mathcal{U}(\tau,x)\right]u(\tau,x)d\tau\right)\partial_x u^\alpha \\ &\quad - \delta\partial_x k^\alpha u^\alpha \\ &\quad - \delta\partial_x\kappa^\alpha \exp\left[-c\,\mathcal{U}(t,x)\right]\left(a(0,x) + \tilde{c}\int_0^t \exp\left[-c\,\mathcal{U}(\tau,x)\right]u(\tau,x)d\tau\right)u^\alpha \\ &\quad - \delta\kappa^\alpha\partial_x\left(\exp\left[-c\,\mathcal{U}(t,x)\right]\left(a(0,x) + \tilde{c}\int_0^t \exp\left[-c\,\mathcal{U}(\tau,x)\right]u(\tau,x)d\tau\right)\right)u^\alpha. \end{aligned} \tag{5.11}$$

Here the reaction parameters have been written in the following abbreviated form:

$$k := \left(\kappa_B a_B, \kappa_P a_P, -\kappa_P a_P, -\kappa_B a_B\right)^T$$

and

$$\kappa := \left(-\kappa_B, -\kappa_P, \kappa_P, \kappa_B\right)^T.$$

Alternatively, we may write the system

$$\partial_t u + \Lambda(a)\partial_x u = -\partial_x\Lambda(a)u \tag{5.12}$$

$$\frac{d}{dt}a = R(a,u) \tag{5.13}$$

as completely hyperbolic one. We note that the velocities λ^α have the shape

$$\pm v_R + \delta\kappa^\alpha a + \delta k^\alpha$$

with possibly variable coefficients κ and k. We thus calculate

$$\partial_x \lambda^\alpha(a) = \delta \kappa^\alpha \partial_x a + \delta \partial_x \kappa^\alpha a.$$

The system can therefore be rewritten to

$$\partial_t \begin{pmatrix} u^1 \\ u^2 \\ u^3 \\ u^4 \\ a \end{pmatrix} + \begin{pmatrix} \lambda^1(a) & 0 & 0 & 0 & -\delta\kappa^1 u^1 \\ 0 & \lambda^2(a) & 0 & 0 & -\delta\kappa^2 u^2 \\ 0 & 0 & \lambda^3(a) & 0 & -\delta\kappa^3 u^3 \\ 0 & 0 & 0 & \lambda^4(a) & -\delta\kappa^4 u^4 \\ 0 & 0 & 0 & 0 & 0 \end{pmatrix} \partial_x \begin{pmatrix} u^1 \\ u^2 \\ u^3 \\ u^4 \\ a \end{pmatrix} + \begin{pmatrix} \delta\partial_x\kappa^1 a u^1 \\ \delta\partial_x\kappa^2 a u^2 \\ \delta\partial_x\kappa^3 a u^3 \\ \delta\partial_x\kappa^4 a u^4 \\ R(a,u) \end{pmatrix} = 0$$

The eigenvalues of the coefficient matrix are clearly given by

$$\lambda^1(t,x,a),\ \lambda^2(t,x,a),\ \lambda^3(t,x,a),\ \lambda^4(t,x,a),\ \text{and } 0,$$

and the corresponding eigenvectors can be chosen to be the usual unit vectors.

The system can now be written in standard form by adding to each equation for $u^1, \ldots, u^4$ a multiple of the last equation:

$$\begin{pmatrix} 1 & 0 & 0 & 0 & \frac{m^1}{\lambda^1} \\ 0 & 1 & 0 & 0 & \frac{m^2}{\lambda^2} \\ 0 & 0 & 1 & 0 & \frac{m^3}{\lambda^3} \\ 0 & 0 & 0 & 1 & \frac{m^4}{\lambda^4} \\ 0 & 0 & 0 & 0 & 1 \end{pmatrix} \partial_t U + \begin{pmatrix} \lambda^1 & 0 & 0 & 0 & m^1 \\ 0 & \lambda^2 & 0 & 0 & m^2 \\ 0 & 0 & \lambda^3 & 0 & m^3 \\ 0 & 0 & 0 & \lambda^4 & m^4 \\ 0 & 0 & 0 & 0 & 0 \end{pmatrix} \partial_x U = \begin{pmatrix} r^1 \\ r^2 \\ r^3 \\ r^4 \\ r^5 \end{pmatrix} \tag{5.14}$$

where we used the following abbreviated notation

$$\begin{aligned} m^\alpha &= \delta \kappa^\alpha u^\alpha \quad , && \alpha = 1, \ldots, 4 \\ r^\alpha &= -\delta \partial_x \kappa^\alpha a u^\alpha + \frac{m^\alpha}{\lambda^\alpha} R(a,u) \quad , && \alpha = 1, \ldots, 4 \\ r^5 &= R(a,u). \end{aligned}$$

We note that this is only valid if neither of the characteristic velocities $\lambda^1, \ldots, \lambda^4$ vanishes at any point which for example of the special parameter values satisfying (3.8) is true if the system for the end densities $u^1, \ldots, u^4$ is strictly hyperbolic.

Using the notation of [18] we can check the hypotheses of theorem 4.1. in chapter 1 therein. Noting that the bound

$$\underline{a_B} \leq a(t,x) \leq \overline{a_P}$$

remains valid due to the sign of the reaction term R, we conclude that also the velocity bounds

$$-v_{max} \leq \lambda^\alpha \leq v_{max}, \qquad \alpha = 1, \ldots, 4$$

are still true. If we therefore prescribe $C^1([0,L])$-data at time $t = 0$, we find a strongly determinate domain to be given by

$$\overline{Q_{min,T}} = \{(t,x) \mid 0 \leq t \leq T,\ v_{max} t \leq x \leq L - v_{max} t\} \tag{5.15}$$

whenever $2v_{max}T \leq L$.

If the initial data satisfy

$$\|u^\alpha\|_{C^0([0,L])} \leq M_0$$

then an appropriate extended domain in the sense of theorem 4.1 in [18] is

$$E_T = \left\{ (t,x,\xi) \mid (t,x) \in \overline{Q_{min,T}},\ \max_{i=1,\ldots,5} |\xi^i| \leq \max\{M_0, a_P\} \right\}.$$

We now check the hypotheses:

1) The coefficient matrix

$$\begin{pmatrix} 1 & 0 & 0 & 0 & \frac{m^1(t,x,u)}{\lambda^1(t,x,a)} \\ 0 & 1 & 0 & 0 & \frac{m^2(t,x,u)}{\lambda^2(t,x,a)} \\ 0 & 0 & 1 & 0 & \frac{m^3(t,x,u)}{\lambda^3(t,x,a)} \\ 0 & 0 & 0 & 1 & \frac{m^4(t,x,u)}{\lambda^4(t,x,a)} \\ 0 & 0 & 0 & 0 & 1 \end{pmatrix}$$

is clearly nonsingular and depends smoothly on t, x, u, and a as long as the velocities λ^α do not vanish which can only be guaranteed for certain values of a. This can be circumvened by replacing a by the new variable $\tilde{a} = a - \bar{a}$ where $\bar{a}$ is some monomer concentration for which there exists $\varepsilon > 0$ such that

$$\lambda^\alpha(t,x,a) \neq 0 \qquad \text{for each } \alpha = 1,\ldots,4,\ (t,x) \in Q_{min,T},\ \text{and } \bar{a} - \varepsilon \leq a \leq \bar{a} + \varepsilon.$$

Then we may choose initial conditions for $\tilde{a}$ in

$$\left[\bar{a} - \frac{\varepsilon}{2}, \bar{a} + \frac{\varepsilon}{2}\right]$$

and conclude that as long as the monomer density changes continuously in time, the nonsingularity of the coefficient matrix is granted for sufficiently small times.

2) The λ^l in the theorem are just the characteristic velocities which are in our case

$$\lambda^1(t,x,a), \ldots,\ \lambda^4(t,x,a), \quad \text{and } 0.$$

These are clearly smooth in t and x if the coefficients $\kappa_{B/P}$ and $a_{B/P}$ are which we always assume to be the case. The same is true for their partial derivatives with respect to $u^1, \ldots, u^4$ (which vanish identically as the equations themselves are semilinear) and the one with respect to a which is simply given by $\delta\kappa^\alpha$.

The right hand sides $r^1, \ldots, r^5$ consist of terms $\delta\partial_x\kappa^\alpha a u^\alpha$ which are well behaved if $\kappa_{B/P}$ are smooth, and the terms

$$\frac{\delta\kappa^\alpha u^\alpha}{\lambda^\alpha}$$

which satisfy all the conditions whenever we are away from zeros of the velocities $\lambda^1, \ldots, \lambda^4$. The right hand side of the last equation is just $R(t,x,a,u)$ which is smooth in all of its arguments.

3) The initial conditions can be chosen to be continuously differentiable on $[0, L]$.

We conclude that we find a C^1 solution of the problem in $\overline{Q_{min,T}}$ for sufficiently small T. Translated into the terms of the boundary value problem this means that there are no discontinuities of either the densities or their derivatives emerging instantaneously in the interior of the domain.

For larger times we expect the emergence of shocks whose shape we will investigate in the following.

To do so we will deal with the corresponding RIEMANN problem, that is, we consider data

$$(u_r^1, u_r^2, u_r^3, u_r^4, a_r)^T \text{ on } (0,\infty) \qquad \text{and} \qquad (u_l^1, u_l^2, u_l^3, u_l^4, a_l)^T \text{ on } (-\infty, 0) \tag{5.16}$$

for the problem in its original form

$$\partial_t \begin{pmatrix} u^1 \\ u^2 \\ u^3 \\ u^4 \\ a \end{pmatrix} + \partial_x \left(\begin{pmatrix} \lambda^1(a) & 0 & 0 & 0 & 0 \\ 0 & \lambda^2(a) & 0 & 0 & 0 \\ 0 & 0 & \lambda^3(a) & 0 & 0 \\ 0 & 0 & 0 & \lambda^4(a) & 0 \\ 0 & 0 & 0 & 0 & 0 \end{pmatrix} \begin{pmatrix} u^1 \\ u^2 \\ u^3 \\ u^4 \\ a \end{pmatrix} \right) = \begin{pmatrix} 0 \\ 0 \\ 0 \\ 0 \\ R(a, u^1, u^2, u^3, u^4) \end{pmatrix} \tag{5.17}$$

and ask for shocks emerging from $x = 0$ at time $t = 0$.

In particular, the data on either side have to be homogeneous solutions of the system, that is

$$R(a_l, u_l^1, u_l^2, u_l^3, u_l^4) = 0 = R(a_r, u_r^1, u_r^2, u_r^3, u_r^4). \tag{5.18}$$

For $\alpha = 1, \ldots, 4$ let us denote by $\lambda_{l/r}^\alpha$ the values $\lambda^\alpha(a_{l/r})$ of the characteristic velocities on the left and right side of the expected shock curve, respectively.

It should be noted that these considerations are only concerned with the possible existence of this type of solutions. We do not show whether they also evovle from smooth data. In particular, recalling that the DIRAC measures for the end densities are to be interpreted as polymerization fronts, we do not assert here that these fronts develop from generic initial states of the resting cell. Moreover, recall that we are here in the fully hyperbolic setting without monomer diffusion.

The question of the actual emergence of polymerization fronts from smooth initial conditions in the original hyperbolic parabolic setting will be addressed by numerical simulations in chapter 7.

5.2.1 Shocks for two end species

Let us start with a specific example. We assume that $u^1 = u^2 \equiv 0$, that is, we only have right oriented barbed and left oriented pointed ends. This may be justified by assuming that the corresponding right oriented pointed and left oriented barbed ends are located far to the left of the shock curve under consideration. If we now ask for a shock we have to assume $a_l > a_r$ since then the characteristic velocities on the right side are smaller than those on the left side. This is necessary for the characteristics to run into the shock curve which in that case will have an intermediate speed.

The conditions for the reaction term to vanish on both sides of the shock now read

$$\kappa_B(a_l - a_B)u_l^4 = \kappa_P(a_P - a_l)u_l^3 \tag{5.19}$$
$$\kappa_B(a_r - a_B)u_r^4 = \kappa_P(a_P - a_r)u_r^3 \tag{5.20}$$

Extreme monomer densities

The easiest possible situation emerges if we assume $a_l = a_P$ and $a_r = a_B$. Then, (5.19) and (5.20) yield $u_r^3 = u_l^4 = 0$ whereas u_r^4 and u_l^3 are some positive constants which have to be determined. Let the shock curve be given by $x = S(t)$, and let us denote its speed by $s(t) = \dot{S}(t)$. We furthermore deduce that the characteristic velocities are given by:

$$\lambda_l^3 = v_R \qquad \lambda_r^3 = v_R - \delta\kappa_P(a_P - a_B)$$
$$\lambda_l^4 = -v_R + \delta\kappa_B(a_P - a_B) = v_{max} \qquad \lambda_r^4 = -v_R.$$

In particular, both velocities are positive in the left half space and negative in the right one so that we can find shock speeds s for which all characteristic curves corresponding to the end densities run into the shock.

We have now to determine what is going on there. Since there are constantly filament ends entering the shock from both sides which do not leave again, there will be an accumulation of finitely many filament ends at the shock position. The number of tips being found there depends on the shock velocity and the densities $u_l^3,\ u_r^4$:

$$\begin{aligned} u^3(t,x) &= u_l^3\chi_{\{x<S(t)\}} + u_l^3\int_0^t \big(\lambda_l^3 - s(\tau)\big)d\tau\ \delta_{S(t)} \\ &= u_l^3\chi_{\{x<S(t)\}} + u_l^3\left(v_R t - S(t)\right)\ \delta_{S(t)} \\ u^4(t,x) &= u_r^4\chi_{\{x>S(t)\}} + u_r^4\int_0^t \big(s(\tau) - \lambda_r^4\big)d\tau\ \delta_{S(t)} \\ &= u_r^4\chi_{\{x>S(t)\}} + u_r^4\left(v_R t + S(t)\right)\ \delta_{S(t)} \end{aligned}$$

where $\delta_{S(t)}$ denotes the DIRAC measure with respect to the spatial variable x with mass concentrated at the shock position at time t. We note that this type of shocks with DIRAC measures at the shock position are also referred to as δ-shocks and have recently been studied for certain nonlinear systems of conservation laws. For instance, in [28] the emergence of such solutions is investigated via viscosity methods. Here we will most often simply refer to these solutions as shocks since we do not have classical shocks and therefore shall not expect any confusion to be generated.

These ends are constantly producing or consuming monomers and the rate of production or consumption has to be balanced by the flux of monomers into or out of the shock. The latter is given by

$$-s(t)(a_l - a_r) = -s(t)(a_P - a_B)$$

where a positive sign corresponds to monomers being taken up by the shock. The production rate due to pointed ends in the shock depends on the shock velocity which is the velocity the filament tips in the shock are moving at. This velocity corresponds

to some hypothetical monomer concentration $a^s(t)$ at $S(t)$ given by

$$s(t) = \lambda^3(a^s(t)) = v_R - \delta\kappa_P(a_P - a^s(t)) \tag{5.21}$$

or equivalently

$$a^s(t) = \frac{s(t) - v_R + \delta\kappa_P a_P}{\delta\kappa_P}. \tag{5.22}$$

Similarly, we find a hypothetical monomer concentration $a_s(t)$ corresponding to the barbed ends in the shock and given by

$$a_s(t) = \frac{s(t) + v_R + \delta\kappa_B a_B}{\delta\kappa_B}. \tag{5.23}$$

This allows us to write the corresponding parts of the reaction terms and thus the monomer production rate due to pointed ends and the consumption rate due to barbed ends as

$$\delta\left(v_R - s(t)\right)\left(v_R t - S(t)\right) u_l^3 \tag{5.24}$$

and

$$-\,\delta\left(v_R + s(t)\right)\left(v_R t + S(t)\right) u_r^4, \tag{5.25}$$

respectively. As creation or destruction of mass is impossible, the fluxes have to balance each other which leads to

$$0 = \left(v_R - s(t)\right)\left(v_R t - S(t)\right) u_l^3 - \left(v_R + s(t)\right)\left(v_R t + S(t)\right) u_r^4 - s(t)(a_P - a_B).$$

Recalling that $s(t)$ is just the speed of the shock curve $x = S(t)$ we write $\dot{S}$ rather than s and obtain an ordinary differential equation for the shock position S:

$$0 = \left(dS - v_R\Sigma t\right)\dot{S} - (a_P - a_B)\dot{S} - v_R\Sigma S + dv_R^2 t \tag{5.26}$$

with abbreviated notations

$$d := u_l^3 - u_r^4 \qquad \text{and} \qquad \Sigma := u_l^3 + u_r^4.$$

This equation is equipped with the initial condition $S(0) = 0$ which we chose to be the point where the discontinuity is located in the data.

In case $u_l^3 = u_r^4$ we immediately obtain the trivial solution $S(t) \equiv 0$ corresponding to a standing shock. By the Picard-Lindelöf theorem this solution is unique and independent of the precise value of $u_l^3 = u_r^4$.

The fronts we are interested in are moving ones corresponding to the actin fronts already discussed in subsection 2.4.2 and being observed as lamellipodium-lamella interface in [26].

Since these moving fronts cannot be observed for equal densities of barbed and pointed ends we therefore consider the case $u_l^3 \neq u_r^4$ and rewrite the ODE (5.26) for the shock curve to

$$\dot{S}(t) = v_R \frac{dv_R t - \Sigma S(t)}{a_P - a_B + v_R\Sigma t - dS(t)} =: F(t, S(t)), \tag{5.27}$$

recall that $S(0) = 0$ and require $|\dot{S}(t)| < v_R$ since the shock cannot move faster than the free velocities of the ends on either side.

Given this condition and using the trivial observation $\Sigma - d > 0$, we see that the denominator of F will always be bounded from below by $a_P - a_B > 0$. In particular, the right hand side satisfies on the cone

$$\mathcal{C} := \{(t, S) \mid t \geq 0, |S| \leq v_R t\}$$

the following estimate

$$\begin{aligned}
&F(t,x) - F(t,y) \\
&= v_R \frac{(dv_R t - \Sigma x)(a_P - a_B + \Sigma v_R t - dy) - (dv_R t - \Sigma y)(a_P - a_B + \Sigma v_R t - dx)}{(a_P - a_B + \Sigma v_R t - dx)(a_P - a_B + \Sigma v_R t - dy)} \\
&= v_R \frac{(a_P - a_B)\Sigma + (\Sigma^2 - d^2) v_R t}{(a_P - a_B + \Sigma v_R t - dx)(a_P - a_B + \Sigma v_R t - dy)} (y - x) \qquad \forall\ (t,x), (t,y) \in \mathcal{C}
\end{aligned}$$

We know the denominator to be larger than $(a_P - a_B)^2$ on $\mathcal{C}$ and see the numerator to be positive and bounded for bounded t. We thus deduce the Lipschitz continuity of F with respect to its second argument and therefore the local existence of a unique solution.

Let us next investigate the behavior of the flux F on the boundaries of the cone $\mathcal{C}$:

$$\begin{aligned}
F(t, v_R t) &= v_R \frac{(d - \Sigma) v_R t}{a_P - a_B + (\Sigma - d) v_R t} &< 0 \quad \text{for } t > 0 \\
F(t, -v_R t) &= v_R \frac{(d + \Sigma) v_R t}{a_P - a_B + (\Sigma + d) v_R t} &> 0 \quad \text{for } t > 0.
\end{aligned}$$

Moreover, we find the nullcline of F to lie in the interior of this cone

$$F(t, S) = 0 \quad \Longleftrightarrow \quad S = \frac{d}{\Sigma} v_R t < v_R t$$

and observe that

1. for fixed $t > 0$, $F(t, \cdot)$ is a decreasing function on $(-v_R t, v_R t)$ since

$$\frac{d}{dS} F(t, S) = \frac{-\Sigma(a_P - a_B) + (d^2 - \Sigma^2) v_R t}{(a_P - a_B + v_R \Sigma t - dS)^2}$$

   is strictly negative, and

2. F is bounded between $-v_R$ and v_R on the cone $\mathcal{C}$. More precisely, for any $t > 0$, we have

$$\max_{-v_R t \leq S \leq v_R} F(t, S) = F(t, -v_R t) < v_R$$

   and

$$\min_{-v_R t \leq S \leq v_R} F(t, S) = F(t, v_R t) > -v_R,$$

   and as t grows to infinity, the maximum approaches v_R from below whereas the minimum approaches $-v_R$ from above.

We conclude that once a solution curve $(t, S(t))$ has a point $(t_0, S(t_0))$ in the interior of the cone $\mathcal{C}$, it cannot leave this cone anymore. If in addition, we are in the smaller cone

$$\left\{0 \leq S \leq \frac{d}{\Sigma} v_R t\right\},$$

we will remain there since $F(t, 0) \geq 0$ and $F(t, \frac{d}{\Sigma} v_R t) = 0$. Moreover, this region is also an attractor with its basin of attraction containing the sector

$$\{(t, S) \mid t > 0, S \leq v_R t\}.$$

This follows from the flux $F(t, S)$ being bounded from below by some positive number for $S < 0$ so that the system is always driven towards positive S. From the other side, F is negative for

$$\frac{d}{\Sigma} v_R t < S < v_R t$$

and therefore, the system will be caught up by the line

$$x = \frac{d}{\Sigma} v_R t.$$

To assert the existence of a unique shock curve S, we only have to check that the system initially does not start with a velocity larger than v_R. To do so, we linearize the system around $t = S = 0$ and find the following approximate equation for small times:

$$\dot{S}(t) = \frac{v_R}{a_P - a_B}(d v_R t - \Sigma S(t)) + \mathcal{O}(t^2, S^2).$$

Neglecting the higher order terms, this can now be explicitely solved with the initial condition $S(0) = 0$, and the solution is given by

$$\begin{aligned} S(t) &= \frac{d(a_P - a_B)}{\delta \Sigma^2} \left(\frac{v_R \Sigma}{aP - a_B} t + \exp\left[-\frac{v_R \Sigma}{a_P - a_B} t \right] - 1 \right) \\ &= \frac{d v_R^2}{a_P - a_B} \frac{t^2}{2} + \mathcal{O}(t^3). \end{aligned} \tag{5.28}$$

We can also calculate the derivative of this approximate solution to be

$$\dot{S}(t) = v_R \frac{d}{\Sigma} \left(1 - \exp\left[-\frac{v_R \Sigma}{a_P - a_B} t \right] \right).$$

This clearly lies between

$$-\frac{d}{\Sigma} v_R \quad \text{and} \quad \frac{d}{\Sigma} v_R,$$

and therefore, the solution starts off into the cone $\mathcal{C}$. We therefore find a unique shock curve $x = S(t)$.

Now we ask for the asymptotic shock velocity. Suspecting the shock speed $\dot{S}$ to converge to some constant value s for large times − which is supported by the numerical solution to the initial value problem for S − we make the ansatz $S(t) \sim st$ for large t. Since we know that this asymptotic velocity cannot be larger than v_R we can then neglect the constant term $a_P - a_B$ in the denominator of the right hand side for large t

to compute

$$s \leftarrow \dot{S}(t) \sim v_R \frac{dv_R t - \Sigma st}{v_R \Sigma t - dst}$$

which has the roots

$$s = \left(\frac{\Sigma}{d} \pm \sqrt{\frac{\Sigma^2}{d^2} - 1} \right) v_R$$

and again by noting that the velocity cannot be larger than v_R, we conclude that the relevant root is the one with the negative sign. The asymptotic velocities computed in that way also coincide perfectly with the ones found by numerical solutions of the initial value problem for S for large times. Having found an asymptotically constant shock speed is also an a posteriori justification of the ansatz $S(t) \sim st$.

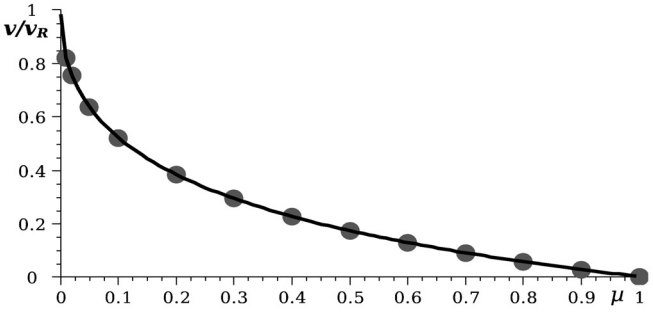

Figure 5.1: Asymptotic shock speed in units of v_R, depending on the ratio $\mu = u_r^4/u_l^3$. *line*: calculated by (5.29), *bullets*: obtained from simulations of the ordinary differential equation (5.27).

Note, that the asymptotic velocity only depends on the ratio of u_l^3 and u_r^4 rather than on the ablosute values. More precisely, writing $u_r^4 := \mu u_l^3$ with $\mu \in (0, 1)$, we find

$$s = \left(\frac{1+\mu}{1-\mu} \pm \sqrt{\frac{(1+\mu)^2}{(1-\mu)^2} - 1} \right) v_R. \tag{5.29}$$

This relation is sketched in figure 5.1.

We furthermore find that the time which is needed to reach the asymptotic velocity strongly depends on both, μ and the absolute value values of u_l^3 and u_r^4. The latter connection becomes immediately clear from (5.27) by recalling that the asymptotic velocity is approximately reached when the term

$$v_R \Sigma t - dS(t)$$

dominates the zero order term $a_P - a_B$. We are therefore not surprised that for large values of both end densities, the asymptotic velocity is approached faster than for small ones.

The former dependence of the transient time on μ may not be as obvious but if we recall that μ being close to 1 leads to small asymptotic velocities we observe that the term

$$v_R \Sigma t - dS(t)$$

also becomes large as Σ and d are of comparable size and $S(t)$ is much smaller than $v_R t$. In figure 5.2 we provide an impression of both effects.

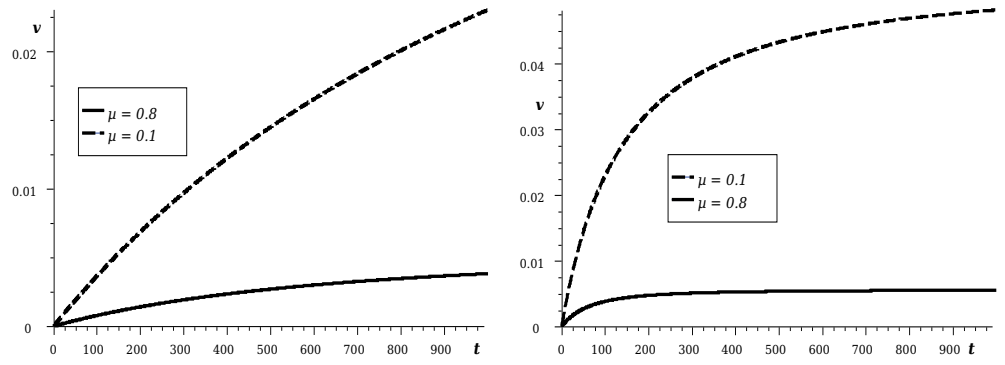

Figure 5.2: Shock velocity over time for different end densities. *Left*: $u_l^3 = 10000\ \mu m^{-2}$, $u_r^4 = 1000\ \mu m^{-2}$ (*dashed*), $u_r^4 = 8000\ \mu m^{-2}$ (*solid*); *right*: $u_l^3 = 10^5\ \mu m^{-2}$, $u_r^4 = 10000\ \mu m^{-2}$ (*dashed*), $u_r^4 = 80000\ \mu m^{-2}$ (*solid*).

Noncritical monomer densities

Let us now consider a slightly more general situation by assuming the monomer density on one side of the shock to be different from the critical concentrations, say $a_B < a_r < a_l = a_P$. We still have $u_l^4 = 0$ but no longer $u_l^3 = 0$. However, this value is coupled to u_r^4 by (5.20). We now have as characteristic velocities:

$$\begin{aligned} \lambda_l^3 &= v_R & \lambda_r^3 &= v_R - \delta\kappa_P(a_P - a_r) \\ \lambda_l^4 &= -v_R + \delta\kappa_B(a_p - a_B) & \lambda_r^4 &= -v_R + \delta\kappa_B(a_r - a_B). \end{aligned}$$

For the number of filament tips being captured by the shock we consequently find:

$$\begin{aligned} u^3(t,x) &= u_l^3\chi_{\{x<S(t)\}} + u_r^3\chi_{\{x>S(t)\}} + \left(u_l^3\left(v_R t - S(t)\right) + u_r^3\left(S(t) - \lambda_r^3 t\right)\right)\ \delta_{S(t)} \\ u^4(t,x) &= u_r^4\chi_{\{x>S(t)\}} + u_r^4\left(S(t) - \lambda_r^4 t\right)\ \delta_{S(t)}. \end{aligned}$$

Note that in case $\lambda_l^3 < \dot{S}(t)$, there is no gain of pointed ends in the shock from the left side but rather a loss as pointed ends leave the shock at rate $(\lambda_r^3 - \dot{S}(t))u_l^3$. This loss has now to be balanced by the inflow from the right or can for some time be fed from the pointed ends being already accumulated in the shock. For constant shock velocities we thus obtain some Rankine-Hugoniot conditions for the shock speed and the end densities on the left and right side, respectively.

This allows us to compute the rates of production and consumption of monomers by the filament tips in the shock to be

$$\delta(v_R - s(t))\left(u_l^3\left(v_R t - S(t)\right) + u_r^3\left(S(t) - \lambda_r^3 t\right)\right) \tag{5.30}$$

and

$$-\delta(s(t) + v_R)(S(t) - \lambda_r^4 t)u_r^4, \tag{5.31}$$

respectively.

The ordinary differential equation describing the evolution of the shock curve S is

now given by

$$\begin{aligned} 0 &= \left(u_l^3 - u_r^3 - u_r^4\right)\dot{S}S + \left(\lambda_r^3 u_r^3 - v_R u_l^3 + \lambda_r^4 u_r^4\right) t\dot{S} \\ &\quad -(a_l - a_r)\dot{S} + \left(u_r^3 - u_l^3 - u_r^4\right) v_R S + \left(v_R u_l^3 - \lambda_r^3 u_r^3 + \lambda_r^4 u_r^4\right) v_R t \end{aligned} \tag{5.32}$$

We find the trivial solution $S(t) \equiv 0$ to exist if the last term vanishes independently of t, that is, if

$$\begin{aligned} 0 &= v_R u_l^3 - \lambda_r^3 u_r^3 + \lambda_r^4 u_r^4 \\ &= v_R u_l^3 + \left(2\delta\kappa_P(a_P - a_r) - v_R\left(1 + \tfrac{\kappa_P(a_P - a_r)}{\kappa_B(a_r - a_B)}\right)\right) u_r^3. \end{aligned} \tag{5.33}$$

Since both densities $u_{r/l}^3$ have to be positive, we require the following relation to be satisfied by a_r:

$$M := v_R\left(1 + \frac{\kappa_P(a_P - a_r)}{\kappa_B(a_r - a_B)}\right) - 2\delta\kappa_P(a_P - a_r) > 0. \tag{5.34}$$

This is not a too strong restriction as we see from the following reformulation of the same quantity:

$$M = v_R + \kappa_P(a_P - a_r)\left(\frac{v_R}{\kappa_B(a_r - a_B)} - 2\delta\right). \tag{5.35}$$

If a_r is sufficiently close to a_B this is clearly true. However, given some value of u_l^3, as a_r approaches a_B from above, the corresponding value for u_r^3 approaches zero which is consistent with the observations for the case $a_r = a_B$.

We conclude that there exists some $a_0 > a_B$ such that for each $a_r \in (a_B, \min\{a_P, a_0\})$ a standing shock is possible. For any such a_r there is one degree of freedom left which can be used to choose either of the values $u_l^3,\ u_r^3$, or u_r^4, and the remaining two values are then computed by (5.20) and (5.33).

Let us now check for possible shocks of constant but nonzero speed. Let us denote this speed by

$$s = \dot{S}(t) \equiv const.$$

and rewrite the ODE for the shock curve as:

$$0 = \left([\lambda^3 u^3 + \lambda^4 u^4] + [u^3 - u^4]v_R\right) st - [u^3 + u^4]s^2 t + ([\lambda^4 u^4 - \lambda^3 u^3])v_R t - (a_P - a_r)s \tag{5.36}$$

where $[f] = f_r - f_l$ denotes the jump of f across the shock. This can only be satisfied for arbitrary $t > 0$ if either $a_r = a_P$ (which can be excluded) or $s = 0$, and it follows that no shocks of constant, nonzero velocity exist in that setting.

Let us finally consider the generic situation $a_B < a_r < a_l < a_P$. The conditions (5.19) and (5.20) now require one of the following nontrivial cases:

1. $u_l^3 = u_l^4 = 0$ and $u_r^3, u_r^4 > 0$

2. $u_l^3, u_l^4 > 0$ and $u_r^3 = u_r^4 = 0$

3. $u_l^3, u_l^4 > 0$ and $u_r^3, u_r^4 > 0$.

The characteristic velocities are generalized to:

$$\begin{aligned} \lambda_l^3 &= v_R - \delta\kappa_P(a_P - a_l) & \lambda_r^3 &= v_R - \delta\kappa_P(a_P - a_r) \\ \lambda_l^4 &= -v_R + \delta\kappa_B(a_l - a_B) & \lambda_r^4 &= -v_R + \delta\kappa_B(a_r - a_B). \end{aligned}$$

We continue with case 1 according to the already known procedure. The densities of pointed and barbed ends are now

$$\begin{aligned} u^3(t,x) &= u_r^3\chi_{\{x>S(t)\}} + u_r^3\left(S(t) - \lambda_r^3 t\right)\ \delta_{S(t)} \\ \text{and} & \\ u^4(t,x) &= u_r^4\chi_{\{x>S(t)\}} + u_r^4\left(S(t) - \lambda_r^4 t\right)\ \delta_{S(t)}, \end{aligned}$$

respectively.

The actin balance across the shock yields the following equation for the shock curve:

$$\begin{aligned} 0 \;=\; & -\left(u_r^3 + u_r^4\right)\dot{S}S + \left(\lambda_r^3 u_r^3 + \lambda_r^4 u_r^4\right)t\dot{S} \\ & -(a_l - a_r)\dot{S} + \left(u_r^3 - u_r^4\right)v_R S - \left(\lambda_r^3 u_r^3 - \lambda_r^4 u_r^4\right)v_R t, \end{aligned} \tag{5.37}$$

and we find as condition for a standing shock $S \equiv 0$:

$$\lambda_r^3 u_r^3 = \lambda_r^4 u_r^4 \tag{5.38}$$

which together with the expressions for the characteristic velocities and (5.20) formally yield:

$$\begin{aligned} a_r^{\pm} \;=\; & \frac{a_B + a_P}{2} + \frac{v_R}{2\delta}\frac{\kappa_P - \kappa_B}{\kappa_B\kappa_P} \\ & \pm\sqrt{\left(\frac{v_R}{2\delta}\frac{\kappa_P - \kappa_B}{\kappa_B\kappa_P}\right)^2 + \left(\frac{a_B + a_P}{2}\right)^2 + \frac{v_R}{2\delta}\frac{\kappa_B a_P - \kappa_P a_B}{\kappa_B\kappa_P}} \end{aligned} \tag{5.39}$$

as possible values of the monomer density. We easily see that all the terms under the square root are positive and thus the solutions are real. It can be furthermore shown that both roots lie between a_B and a_P if in addition to standard assumptions on the parameters the following are true:

1. In case
$$\kappa_B \leq (3 + 2\sqrt{2})\kappa_P \tag{5.40}$$
the parameters satisfy:
$$\kappa_B\kappa_P(a_P - a_B) > \frac{v_R}{\delta}\left(\frac{\kappa_B + \kappa_P}{2} + \sqrt{\kappa_B\kappa_P}\right). \tag{5.41}$$

2. In case
$$\kappa_B > (3 + 2\sqrt{2})\kappa_P \tag{5.42}$$
it is sufficient to require
$$\delta\kappa_P(a_P - a_B) > v_R \tag{5.43}$$
which is precisely the condition that λ^3 can take negative as well as positive values.

We remark that the second case is the physiological one being discussed in [10] but that the first case cannot be excluded. In fact, in vitro measurements indicate a ratio of $\kappa_B \approx 25\kappa_P$ as measured in [25] but in vivo this situation can be changed dramatically, for example, by depolymerizing agents like ADF/cofilin (cf. [1]).

Given one of the values for a_r from (5.39) and any (freely chosen) positive value for u_r^3, the corresponding value for u_r^4 can be computed to be

$$u_r^4 = \frac{\kappa_P(a_P - a_r)}{\kappa_B(a_r - a_B)} u_r^3. \tag{5.44}$$

A very similar discussion applies to the second case where the end densities on the right vanish whereas those on the left are positive. As this situation is just symmetric to case 1 we do not carry out the detailed calculations here.

Let us now consider the case of non-vanishing end densities on either side of the shock (case 3 above). The ODE for the shock curve now becomes

$$\begin{aligned} 0 \quad = \quad & -\left[u^3 + u^4\right] \dot{S}S + \left[\lambda^3 u^3 + \lambda^4 u^4\right] t\dot{S} \\ & +[a]\dot{S} + \left[u^3 - u^4\right] v_R S - \left[\lambda^3 u^3 - \lambda^4 u^4\right] v_R t \end{aligned}$$

with the brackets again denoting the jump across the shock. This can be rewritten in the familiar form

$$\dot{S} = v_R \frac{[\lambda^3 u^3 - \lambda^4 u^4]t - [u^3 - u^4]S}{[a] + [\lambda^3 u^3 + \lambda^4 u^4]t - [u^3 + u^4]S}. \tag{5.45}$$

The condition for a standing shock now reads:

$$\lambda_r^3 u_r^3 - \lambda_r^4 u_r^4 = \lambda_l^3 u_l^3 - \lambda_l^4 u_l^4 \tag{5.46}$$

which is accompanied by (5.19), (5.20) and the usual conditions on the parameters.

Assuming we prescribe the value of u_r^3, say, we have now five unknowns

$$a_l,\ a_r,\ u_l^3,\ u_l^4, \quad \text{and } u_r^4$$

and only three equations and several inequalities to determine them. Let us start with determining three of the end densities from a given one, regardless of what the monomer densities a_r and a_l are. Given u_r^3 we can always calculate from equation (5.20):

$$u_r^4 = \frac{\pi_r}{\beta_r} u_r^3 \tag{5.47}$$

where we already used some of the following abbreviations:

$$\pi_{r/l} := \kappa_P(a_P - a_{r/l}) \qquad \text{and} \qquad \beta_{r/l} := \kappa_B(a_{r/l} - a_B).$$

Now we can use (5.47) and (5.19) in the form

$$u_l^3 = \frac{\beta_l}{\pi_l} u_l^4 \tag{5.48}$$

and plug this into (5.46) to obtain

$$u_l^4 \;=\; \frac{\lambda_r^3 - \frac{\pi_r}{\beta_r}\lambda_r^4}{\frac{\beta_l}{\pi_l}\lambda_l^3 - \lambda_l^4} u_r^3 \;=\; \frac{v_R\left(1+\frac{\pi_r}{\beta_r}\right) - 2\delta\pi_r}{v_R\left(1+\frac{\beta_l}{\pi_l}\right) - 2\delta\beta_l} u_r^3.$$

Using this together with (5.19) we finally compute

$$u_l^3 \;=\; \frac{\beta_l}{\pi_l} u_l^4 \;=\; \frac{v_R\left(1+\frac{\pi_r}{\beta_r}\right) - 2\delta\pi_r}{v_R\left(1+\frac{\pi_l}{\beta_l}\right) - 2\delta\pi_l} u_r^3.$$

These computations were formally and only yield finite and non-vanishing end densities if all coefficients are nonzero. From (5.47) we readily conclude the requirements

$$a_B < a_{r/l} < a_P. \tag{5.49}$$

The positivity of the other coefficients is equivalent to

$$\left(v_R\left(1+\frac{\pi_r}{\beta_r}\right) - 2\delta\pi_r\right)\left(v_R\left(1+\frac{\beta_l}{\pi_l}\right) - 2\delta\beta_l\right) \;>\; 0$$

and

$$\left(v_R\left(1+\frac{\pi_r}{\beta_r}\right) - 2\delta\pi_r\right)\left(v_R\left(1+\frac{\pi_l}{\beta_l}\right) - 2\delta\pi_l\right) \;>\; 0$$

which can be rewritten as two sets of inequalities.

More precisely, these conditions are fulfilled if either

1. both

$$2\delta\kappa_P\kappa_B(a_P - a_r)(a_r - a_B) \;>\; v_R\,(\,\kappa_B(a_r - a_B) + \kappa_P(a_P - a_r)\,)$$

and

$$2\delta\kappa_P\kappa_B(a_P - a_l)(a_l - a_B) \;>\; v_R\,(\,\kappa_B(a_l - a_B) + \kappa_P(a_P - a_l)\,)$$

hold, or

2. both

$$2\delta\kappa_P\kappa_B(a_P - a_r)(a_r - a_B) \;<\; v_R\,(\,\kappa_B(a_r - a_B) + \kappa_P(a_P - a_r)\,)$$

and

$$2\delta\kappa_P\kappa_B(a_P - a_l)(a_l - a_B) \;<\; v_R\,(\,\kappa_B(a_l - a_B) + \kappa_P(a_P - a_l)\,)$$

hold.

We would like to understand what these conditions mean for the parameters. The

second case is the easier one to evaluate as can be seen by rewriting the equations to

$$\frac{2\delta}{v_R} < \frac{1}{\kappa_P(a_P - a_r)} + \frac{1}{\kappa_B(a_r - a_B)} \tag{5.50}$$

$$\frac{2\delta}{v_R} < \frac{1}{\kappa_P(a_P - a_l)} + \frac{1}{\kappa_B(a_r - a_B)}. \tag{5.51}$$

Both of these inequalities are satisfied if at least one of the terms on the right hand side is sufficiently large. They can thus be made valid by choosing the monomer densities a_r and a_l sufficiently close to either a_B or a_P. However, the inequalities from the second case might be violated for certain values of a_r and a_l. In that case, there exist values $a \in (a_B, a_P)$ such that

$$\varphi(a) := 2\delta\kappa_P\kappa_B(a_P - a)(a - a_B) - v_R\,(\,\kappa_B(a - a_B) + \kappa_P(a_P - a)\,) \tag{5.52}$$

is positive.

We already know, that in some neighborhoods of a_P and a_B the expression is negative:

$$\begin{aligned} \varphi(a_B) &= -v_R\kappa_P(a_P - a_B) < 0, \\ \varphi(a_P) &= -v_R\kappa_B(a_P - a_B) < 0. \end{aligned} \tag{5.53}$$

We can therefore compute

$$\varphi'(a) = 2\delta\kappa_B\kappa_P(a_P + a_B - 2a) - v_R(\kappa_B + \kappa_P) \tag{5.54}$$

which is linear in a and thus has precisely one zero. This is given by

$$a^* = \frac{1}{2}\left(a_P + a_B - \frac{v_R}{2\delta}\frac{\kappa_B - \kappa_P}{\kappa_B\kappa_P}\right), \tag{5.55}$$

and we will show that this a^* lies between a_B and a_P and that φ has a maximum there and attains a positive value.

Since

$$\varphi''(a) \equiv -4\delta\kappa_B\kappa_P < 0 \tag{5.56}$$

we conclude that φ has a maximum at a^*. Furthermore, we find a^* to lie between a_B and a_P:

$$a^* - a_B = \frac{1}{2}\left(a_P - a_B - \frac{v_R}{2\delta}\frac{\kappa_B - \kappa_P}{\kappa_B\kappa_P}\right) \tag{5.57}$$

$$a_P - a^* = \frac{1}{2}\left(a_P - a_B + \frac{v_R}{2\delta}\frac{\kappa_B - \kappa_P}{\kappa_B\kappa_P}\right). \tag{5.58}$$

The second value is clearly positive as both of its terms are, whereas the first value is positive if and only if

$$2(a_P - a_B)\frac{\kappa_B\kappa_P}{\kappa_B - \kappa_P} > \frac{v_R}{\delta}, \tag{5.59}$$

and we can estimate:

$$\frac{v_R}{\delta} < \kappa_P(a_P - a_B) = \frac{\kappa_B\kappa_P}{\kappa_B}(a_P - a_B) < \frac{\kappa_B\kappa_P}{\kappa_B - \kappa_P}(a_P - a_B) \tag{5.60}$$

and thus $a_B < a^*$.

We now ask whether $\varphi(a^*)$ is positive. Plugging the value of a^* found in 5.55 into φ we obtain:

$$\begin{aligned}
\varphi(a^*) &= \frac{1}{2}\delta\kappa_B\kappa_P\left((a_B - a_P)^2 - \frac{v_R}{2\delta}\frac{\kappa_B - \kappa_P}{\kappa_B\kappa_P} - \frac{1}{2}(a_B + a_P)^2\right) \\
&+ \frac{1}{2}\delta\kappa_B\kappa_P\left(\frac{v_R}{2\delta}\frac{(\kappa_B - \kappa_P)^2}{2\kappa_B^2\kappa_P^2} - \frac{v_R^2}{2\delta^2}\frac{(\kappa_B - \kappa_P)^2}{2\kappa_B^2\kappa_P^2}\right) \\
&- v_R\left(\frac{\kappa_B - \kappa_P}{2}(a_P + a_B) - \frac{v_R}{2\delta}\frac{\kappa_B - \kappa_P}{2\kappa_P} - \kappa_B a_B + \kappa_P a_P + \frac{v_R}{2\delta}\frac{\kappa_B - \kappa_P}{2\kappa_B}\right) \\
&= \frac{\delta}{4}\kappa_B\kappa_P(a_P + a_B)^2 + \frac{v_R}{2}(\kappa_B + \kappa_P)(a_P - a_B) - \frac{v_R}{4\delta^2}\frac{(\kappa_B - \kappa_P)^2}{4\kappa_B\kappa_P}.
\end{aligned}$$

Being now concerned with the question whether this is positive, we equivalently ask for

$$\left(\frac{a_P + a_B}{2}\right)^2 + V(\kappa_B + \kappa_P)(a_P - a_B) - V^2\left(\frac{\kappa_B - \kappa_P}{2\kappa_B\kappa_P}\right)^2 \tag{5.61}$$

to be positive. For fixed reaction parameters, this may be viewed as quadratic function of the scaled retrograde flow velocity

$$V := \frac{v_R}{2\delta}$$

and rewritten to

$$\begin{aligned}
&-V^2 - 2\kappa_B\kappa_P\frac{\kappa_B + \kappa_P}{(\kappa_B - \kappa_P)^2}(a_P - a_B) + \left(\frac{\kappa_B\kappa_P}{\kappa_B - \kappa_P}\right)^2(a_P - a_B)^2 \\
= \; &-(V^2 + pV + q)
\end{aligned}$$

which is negative for large values of $|V|$. It vanishes for

$$V_\pm = -\frac{p}{2} \pm \sqrt{\frac{p^2}{4} - q} \tag{5.62}$$

and is positive for $V \in (V_-, V_+)$.

Observing that p as well as q are negative, the root with the plus sign is positive and in particular larger than $-\frac{p}{2}$. We calculate:

$$\begin{aligned}
V_+ > -\frac{p}{2} &= \frac{\kappa_B\kappa_P(\kappa_B + \kappa_P)}{(\kappa_B - \kappa_P)^2} = \frac{\kappa_B}{\kappa_B - \kappa_P}\frac{\kappa_B + \kappa_P}{\kappa_B - \kappa_P}\kappa_P(a_P - a_B) \\
&> \kappa_P(a_P - a_B) > \frac{v_R}{\delta},
\end{aligned}$$

the last inequality being one of our standard assumptions.

Recalling that V coded for $\frac{v_R}{2\delta}$ we conclude that for all admissable parameter settings

V lies between zero and V_+ from which we conclude that $\varphi(a^*)$ is always positive.

As a consequence we can assert the existence of values $a_\pm$ for the monomer density satisfying

$$a_B < a_- < a_+ < a_P \tag{5.63}$$

such that $\varphi(a)$ is positive if and only if a lies between a_- and a_+.

We now recall that we are looking for shocks rather than rarefaction waves which in our case requires more ends to be transported into the initial discontinuity than leaving it:

$$\lambda_l^3 u_l^3 + \lambda_r^3 u_r^3 \ > \ 0 \qquad \text{and} \qquad \lambda_l^4 u_l^4 + \lambda_r^4 u_r^4 \ > \ 0$$

or in more detail:

$$\begin{aligned} (v_R - \delta\kappa_P a_P)(u_l^3 + u_r^3) + \delta\kappa_P(a_l u_l^3 + a_r u_r^3) \ &> \ 0 \qquad (5.64)\\ (v_R + \delta\kappa_B a_B)(u_l^4 + u_r^4) - \delta\kappa_B(a_l u_l^4 + a_r u_r^4) \ &> \ 0. \qquad (5.65) \end{aligned}$$

Summarizing the previous computations we find the following essences:

1. There exist standing shocks with positive end densities $u_{r/l}^{3/4}$ if and only if either

   - $a_r \in (a_-, a_+)$ and $a_l \in (a_-, a_+)$
     or
   - $a_r \in (a_B, a_-) \cup (a_+, a_P)$ and $a_l \in (a_B, a_-) \cup (a_+, a_P)$

   where $a_\pm \in (a_B, a_P)$ are the roots of

   $$2\delta\kappa_P\kappa_B(a_P - a)(a - a_B) - v_R\,(\ \kappa_B(a - a_B) + \kappa_P(a_P - a)\ ) = 0 \tag{5.66}$$

   viewed as equation for a. In particular, these roots $a_\pm$ are real, lie between a_B and a_P, and they are different.

2. Given monomer densities a_r and a_l satisfying the above and given any positive value of u_r^3, the other end densities are computed by:

$$\begin{aligned} u_r^4 \ &= \ \frac{\kappa_P(a_P - a_r)}{\kappa_B(a_r - a_B)} u_r^3 \qquad (5.67)\\ u_l^4 \ &= \ \frac{v_R\left(1 + \frac{\kappa_P(a_P - a_r)}{\kappa_B(a_r - a_B)}\right) - 2\delta\kappa_P(a_P - a_r)}{v_R\left(1 + \frac{\kappa_B(a_l - a_B)}{\kappa_P(a_P - a_l)}\right) - 2\delta\kappa_B(a_l - a_B)} u_r^3 \qquad (5.68)\\ u_l^3 \ &= \ \frac{v_R\left(1 + \frac{\kappa_P(a_P - a_r)}{\kappa_B(a_r - a_B)}\right) - 2\delta\kappa_P(a_P - a_r)}{v_R\left(1 + \frac{\kappa_P(a_P - a_l)}{\kappa_B(a_l - a_B)}\right) - 2\delta\kappa_P(a_P - a_l)} u_r^3. \qquad (5.69) \end{aligned}$$

5.2.2 Shocks without singular measures

Another issue to be addressed is the existence of shocks without singularities in the end densities which will be the case if as many ends of either type are transported into the shock from one side as are leaving it to the other side. In that case we have to ask for

a (necessarily constant) shock velocity s such that $(s-\lambda_r^3)$ and $(s-\lambda_l^3)$ have the same sign and such that $(s-\lambda_r^4)$ and $(s-\lambda_l^4)$ also have the same sign.

More precisely, we require

$$\begin{aligned}(v_R-\delta\kappa_P(a_P-a_l)-s)u_l^3 &= (v_R-\delta\kappa_P(a_P-a_r)-s)u_r^3 &(5.70)\\ (-v_R+\delta\kappa_B(a_l-a_B)-s)u_l^4 &= (-v_R+\delta\kappa_B(a_r-a_B)-s)u_r^4. &(5.71)\end{aligned}$$

In particular, we deal with non classical shocks for which the Lax entropy conditions are not satisfied.

Of course, we still require (5.19) and (5.20) for the reaction terms to vanish on either side. This yields four equations which are linear in $u_{r/l}^{3/4}$ and can be written in concise notation as

$$\begin{pmatrix} v_R-\delta\pi_r-s & -v_R+\delta\pi_l+s & 0 & 0\\ 0 & 0 & -v_R+\delta\beta_r-s & v_R-\delta\beta_l+s\\ 0 & \pi_l & 0 & -\beta_l\\ \pi_r & 0 & -\beta_r & 0\end{pmatrix}\begin{pmatrix}u_r^3\\u_l^3\\u_r^4\\u_l^4\end{pmatrix}=0. \quad (5.72)$$

This problem has a nontrivial solution if and only if the coefficient matrix is singular, and we therefore compute:

$$\begin{aligned}0 &\overset{!}{=} \det\begin{pmatrix} v_R-\delta\pi_r-s & -v_R+\delta\pi_l+s & 0 & 0\\ 0 & 0 & -v_R+\delta\beta_r-s & v_R-\delta\beta_l+s\\ 0 & \pi_l & 0 & -\beta_l\\ \pi_r & 0 & -\beta_r & 0\end{pmatrix}\\ &= -\pi_r\det\begin{pmatrix} -v_R+\delta\pi_l+s & 0 & 0\\ 0 & -v_R+\delta\beta_r-s & v_R-\delta\beta_l+s\\ \pi_l & 0 & -\beta_l\end{pmatrix}\\ &+ \beta_r\det\begin{pmatrix} v_R-\delta\pi_r-s & -v_R+\delta\pi_l+s & 0\\ 0 & 0 & v_R-\delta\beta_l+s\\ 0 & \pi_l & -\beta_l\end{pmatrix}\\ &= \pi_r(v_R-\delta\pi_l-s)(v_R-\delta\beta_r+s)\beta_l-\beta_r(v_R-\delta\pi_r-s)(v_R-\delta\beta_l+s)\pi_l.\end{aligned}$$

This equation reduces to $a_r=a_l$ – which we exclude since we are looking for a discontinuity in a – or:

$$(\pi_r\beta_l-\beta_r\pi_l)(v_R^2-s^2)=\delta\left(\pi_r\pi_l(\beta_l-\beta_r)(v_R+s)+\beta_l\beta_r(\pi_r-\pi_l)(v_R-s)\right)$$

or equivalently:

$$0=s^2-ps+q \quad (5.73)$$

with

$$\begin{aligned}p &= \frac{\delta\left(\kappa_B(a_r-a_B)(a_l-a_B)-\kappa_P(a_P-a_r)(a_P-a_l)\right)}{a_P-a_B}\\ q &= \frac{\delta v_R\left(\kappa_B(a_r-a_B)(a_l-a_B)+\kappa_P(a_P-a_r)(a_P-a_l)\right)}{a_P-a_B}-v_R^2.\end{aligned}$$

Equation (5.73) has real roots

$$s_\pm = \frac{1}{2}\left(p \pm \sqrt{(p^2 - 4q)}\right)$$

if and only if

$$p^2 - 4q > 0,$$

and these have different signs if $q < 0$ which is the case if

$$\frac{v_R}{\delta} > \kappa_B(a_r - a_B)(a_l - a_B) + \kappa_P(a_P - a_r)(a_P - a_l). \tag{5.74}$$

This in turn can always be achieved by choosing a_r close to a_B and a_l close to a_P or vice versa.

In addition, we have to require that for each characteristic family $\alpha = 3, 4$, the shock velocity is either larger or smaller than the characteristic velocities on both sides of the shock − at least if we want the end densities to be positive.

Given suitable a_r and a_l and one of the densities $u_{r/l}^{3/4}$, (5.72) allows us compute the other end densities whereas from (5.73) we can calculate the shock speed.

In any case, it remains to check that for at least one root of (5.73), the other end densities are positive.

To put everything to figures we will conclude with two numerical examples.

Example 1. Given the standard reaction parameters

$$\begin{aligned}
\kappa_B &= \frac{5}{12\delta} 10^{-4}\ \mu m\ s^{-1} \\
\kappa_P &= \frac{5}{24\delta} 10^{-5}\ \mu m\ s^{-1} = \frac{\kappa_B}{20} \\
a_B &= a_B^0 \quad = \quad 9600\ \mu m^{-1} \\
a_P &= a_P^0 \quad = \quad 60000\ \mu m^{-1},
\end{aligned}$$

let us choose the following values of the monomer density on the left and the right:

$$\begin{aligned}
a_l &= 50000\ \mu m^{-1} \\
a_r &= 10200\ \mu m^{-1}
\end{aligned}$$

and a density of left oriented pointed ends to the left of the shock of

$$u_r^3 = 10000\ \mu m^{-2}.$$

Then, we readily compute as solutions of (5.73)

$$s \approx \begin{cases} 0.0467\ \mu m\ s^1 \\ -0.0520\ \mu m\ s^{-1} \end{cases} \tag{5.75}$$

and for the characteristic velocities outside the shock:

$$\begin{aligned}
\lambda_l^3 &\approx 0.0583\ \mu m\ s^1 & \lambda_r^3 &\approx -0.0021\ \mu m\ s^1 \\
\lambda_l^4 &\approx 1.167\ \mu m\ s^1 & \lambda_r^4 &\approx -0.0417\ \mu m\ s^1.
\end{aligned}$$

In figure 5.3 we sketch the shock curve and the characteristics for both end densities.

Since the shock speed cannot lie between the characteristic velocities of one family, we conclude that the negative speed is to be taken. With that we can compute the other end densities to be

$$\begin{aligned} u_r^4 = \frac{\pi_r}{\beta_r} u_r^3 &= 17500\ \mu m^{-2} \\ u_l^3 = \frac{\lambda^3(a_r) - s}{\lambda^3(a_l) - s} u_r^3 &\approx 4526\ \mu m^{-2} \\ u_l^4 = \frac{\pi_l}{\beta_l} u_l^3 &\approx 149\ \mu m^{-2}. \end{aligned}$$

The last quantity could also have been calculated by

$$u_l^4 = \frac{\lambda^4(a_r) - s}{\lambda^4(a_l) - s} u_r^4$$

which is easily checked to yield the same result.

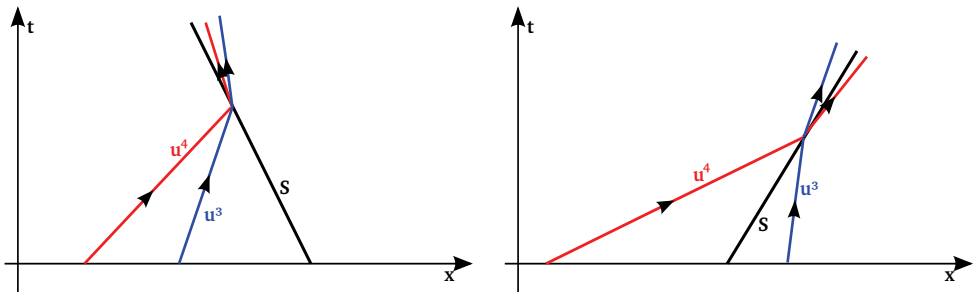

Figure 5.3: Sketch of the characteristics running through the shock curve S (*black*) for examples 1 (*left*) and 2 (*right*). Note that the characteristics of both families indeed run *through* the shock and are merely deflected there.

Example 2. Using for a second example slightly increased reactivity and correspondingly a slightly faster retrograde flow velocity, say

$$\begin{aligned} \kappa_B &= 2\kappa_B^0 &&= \frac{5}{6\delta} 10^{-4}\ \mu m\ s^{-1} \\ \kappa_P &= 4\kappa_P^0 &&= \frac{5}{6\delta} 10^{-5}\ \mu m\ s^{-1} = \frac{\kappa_B}{10} \\ a_B &= 0.5 a_B^0 &&= 4800\ \mu m^{-1} \\ a_P &= a_P^0 &&= 60000\ \mu m^{-1} \end{aligned}$$

and

$$v_R = 0.4\ \mu m\ s^{-1},$$

let us choose the following values of the monomer density on the left and the right

$$\begin{aligned} a_l &= 55000\ \mu m^{-1} &&= \frac{11}{12} a_P, \\ a_r &= 20000\ \mu m^{-1} &&= \frac{1}{3} a_P, \end{aligned}$$

and a density of left oriented pointed ends to the left of the shock of

$$u_r^3 = 10000\ \mu m^{-2}.$$

Now, (5.73) yields as possible shock speeds

$$s = \begin{cases} 0.6024\ m\ s^1 \\ 0.5193\ m\ s^{-1} \end{cases} \tag{5.76}$$

whereas the characteristic velocities are given by

$$\begin{aligned} \lambda_l^3 &\approx 0.3583\ \mu m\ s^1 & \lambda_r^3 &\approx 0.2333\ \mu m\ s^1 \\ \lambda_l^4 &\approx 3.783\ \mu m\ s^1 & \lambda_r^4 &\approx 0.8667\ \mu m\ s^1. \end{aligned}$$

Therefore, both shock speeds are compatible, and the situation sketched on the right of figure 5.3 basically captures both cases if we do not request it to be to scale.

Using $s = 0.6024\ m\ s^1$ we obtain for the other end densities

$$\begin{aligned} u_r^4 = &\approx 2632\ \mu m^{-2} \\ u_l^3 &\approx 21950\ \mu m^{-2} \\ u_l^4 &\approx 219\ \mu m^{-2}, \end{aligned}$$

whereas for $s = 0.5193\ m\ s^{-1}$ the latter two densities are given by

$$\begin{aligned} u_l^3 &\approx 28115\ \mu m^{-2} \\ u_l^4 &\approx 280\ \mu m^{-2}. \end{aligned}$$

5.3 The effect of finite diffusion

Asking for blow-up phenomena in the full model we first have to check which type of shocks discussed in the previous section can persist in the presence of diffusion in the monomer equation.

We recall that for end densities exhibiting DIRAC measure valued solutions we can think of the monomer equation to be satisfied to both sides of the shock whereas at the shock itself we have to consider certain flux conditions. Whenever the shock speed is different from zero we would expect that the flux into or out of the shock may not only be driven by the movement but also by a diffusive flux corresponding to non constant monomer densities. In that case, the characteristic velocities of the filament ends become variable near the shock and we might expect the latter to degenerate to a traveling wave rather than a true shock.

This expectation is also supported by the simulations in chapter 7.

Chapter 6

Alternative Boundary Conditions

Besides the free boundary problem which assumes a freely growing cytoskeleton without resistance by the cell membrane we may also consider a variety of other boundary conditions. Another particularly simple but still biophysically meaningful setting is comprised of a fixed cell wall − described by a non-moving domain − where filament tips may be adsorbed. This setting may reflect an in vitro experiment where the cell is indeed confined to a box of limited size.

6.1 Adhesion at a fixed cell wall

We now consider system (2.4a) - (2.4e) on a fixed domain $(0, L)\times(0, T)$ and prescribe the following boundary conditions. The monomers are still reflected at the boundary, and their flux has to balanced by the polymerization flux through the barbed and pointed ends located at the boundary.

Filament tips approaching the membrane stop extending and accumulate as point masses at the boundary. We thus have to couple the flux of filament ends with a partial differential equation for the number of membrane attached tips. It should be noted that the word *attachment* does not necessarily mean a chemical bond between the filament and the membrane in this context. It only accounts for the filament tip being located directly at the membrane. A distinction between free and membrane bound barbed ends will be discussed later.

For obvious physical reasons we only specify these conditions for

$$\begin{aligned} & B_l,\ P_r \quad \text{at} \quad x = 0 \\ \text{and} \\ & B_r,\ P_l \quad \text{at} \quad x = L. \end{aligned}$$

6.1.1 Definition and evolution of the boundary densities

As soon as a filament end reaches the boundary it is assumed to leave the domain $(0, L)$ and is counted as a filament tip of size 0 and being located at the membrane. Any further polymerization to that filament is not accounted for by a displacement of the tip but rather by a size change. If the filament velocity has the opposite sign then the

filament tips at the membrane decrease in size, and as soon as their size reaches zero they are released and reenter the domain $(0, L)$.

We thus have to couple the partial differential equations (2.4a) - (2.4d) from within the domain to respective size structured equations for the densities at the boundary points. With the notation from chapter 2, the flux of filament tips to or from the boundary is given by $\pm\lambda^\alpha u^\alpha$. If the velocity is directed towards the boundary, this produces new membrane attached tips of size zero. For velocities pointing into the cell, the number of attached ends shrinking to size zero give the boundary values for this type of filament ends.

In order to precisely formulate the boundary conditions we first have to write down the evolution equations for the end densities at the boundaries. We will in general distinguish between up to three types of filament tips at the membrane:

1. $B^f_{r/l}$: free barbed ends of right/left orientation. These are barbed ends being located at the membrane without having any chemical bonds to it.

2. $B^b_{r/l}$: bound barbed ends of right/left orientation. These are chemically attached to the membrane which either prevents them from further polymerization or even enhances the polymerization activity. Both effects may be mediated by different members of a family of processive actin polymerizing motors called formins. These can enhance the polymerization rate by approximately one order of magnitude if the actin binding protein profilin is present. On the other hand, some formins are reported to completely block actin dynamics at bound barbed ends in the absence of profilin (see [27]). For obvious reasons we only consider left oriented barbed ends at the left boundary and right oriented barbed ends at the right boundary.

3. $P_{r/l}$: (free) pointed ends of right/left orientation. Of course, the former are located only at the left boundary, the latter ones at the right boundary.

We exemplarily discuss the case of barbed ends of right oriented filaments located at the right boundary. Their position is clearly fixed at $x = L$, and we assign to them a size z the meaning of which has to be thought of as follows. A filament tip at the membrane may further polymerize which causes a length change of the filament. Since the position of the tip is fixed we may assume the filament to buckle due to the length change. We define the size of the membrane attached end to be the length by which the filament would reach beyond the cell membrane if it was not stuck there. Since the expected buckling of the filament presses the tip against the membrane this affects the polymerization velocity.

On the other hand, a barbed end being bound to a polymerization motor in the membrane may also be polymerized faster than a free one resulting in a fast change of size. The appropriate equations to describe such a growth process are:

$$\partial_t B^f_r(t,z) + \partial_z \left(v^{L,f}_B(t,z) B^f_r(t,z) \right) = -\beta^L_+ B^f_r(t,z) f^L(t) + \beta^L_- B^b_r(t,z) \quad (6.1)$$

$$\partial_t B^b_r(t,z) + \partial_z \left(v^{L,b}_B(t,z) B^b_r(t,z) \right) = \beta^L_+ B^f_r(t,z) f^L(t) - \beta^L_- B^b_r(t,z) \quad (6.2)$$

with a growth velocity depending explicitely on the size z and implicitely on time via

- the monomer concentration $a(t, L)$ at the boundary

- the possible time dependence of the reaction parameters κ_B and a_B
- in the case of bound barbed ends possibly on the polymerizing activity of the membrane protein being attached to the filament end.

The right hand sides of (6.1) and (6.2) describe the binding and unbinding of the filament tips from the membrane protein. The number of free binding sites is denoted by f^L, and $\beta^L_\pm$ are the binding and unbinding rates, respectively. For left oriented pointed ends at $x = L$ we analogously find

$$\partial_t P^L_l(t,z) + \partial_z \left(v^L_P(t,z) P^L_l(t,z) \right) = 0. \tag{6.3}$$

The F-actin binding protein at the boundary obeys the ordinary differential equation

$$\frac{d}{dt} f^L(t) = -\beta^L_+ f^L(t) \int_0^\infty B^f_r(t,z)dz + \beta^L_- \int_0^\infty B^b_r(t,z)dz. \tag{6.4}$$

Let us note that the case $\beta^L_+ = 0$ represents the situation where no bonds between filament tips and membrane proteins are formed. As a consequence, equation (6.1) then becomes the only one of interest and its right hand side becomes identically zero.

6.1.2 Formulation of the flux condition at the boundary

With these evolution equations we can now write down the boundary conditions for the filament tips at the right boundary as a continuity condition at $x = L$ for B_r and P_l and at $z = 0$ for $B^{b/f}_r$ and P^L_l, respectively. We just require the flux from/to the cell interior to balance the influx/efflux to/from the membrane at $z = 0$. For the pointed ends we write this as

$$-\, v_P(t, x = L)\ P_l(t, x = L) = v^L_P(t, z = 0)\ P^L_l(t, z = 0). \tag{6.5}$$

Here we assume that the boundary velocities have the same sign for the same values of a, κ_P, and a_P. In that case, equation (6.5) is an active boundary condition

- for P_l at $x = L$ if the velocity of left oriented pointed ends at the right boundary points into the cell as well as
- for P^L_l at $z = 0$ if the growth velocity of left oriented pointed ends at the right membrane is positive for ends of zero size.

In particular, the condition is compatible with the characteristic directions of the respective partial differential equations.

If chemical bonds of barbed ends to the membrane are ignored, the same procedure works for them as well and we obtain the boundary condition

$$v_B(t, x = L) B_r(t, x = L) = v^{L,f}_B(t, z = 0) B^f_r(t, z = 0). \tag{6.6}$$

More care has to be taken if we have a true distinction between bound and free barbed ends at the membrane. We now have to address the question what happens to bound barbed ends of size zero if the barbed end velocity at the boundary is negative.

One may assume that they immediately detach without the chemical bonds holding them back which leads to the condition

$$v_B(t,x=L)B_r(t,x=L) = v_B^{L,f}(t,z=0)B_r^f(t,z=0)+v_B^{L,b}(t,z=0)B_r^b(t,z=0). \quad (6.7)$$

This is obviously underdetermined if $v_B(t,x=L) > 0$, that is, if barbed ends grow into the membrane. In that case we have to provide a rule by which the ratio between new free and new bound barbed ends at the membrane can be determined. A plausible choice would be that all barbed ends hitting the membrane are initially free in which case (6.7) reduces to (6.6). Note that this choice will typically produce discontinuities in B_r^f and B_r^b with respect to z upon any change of $v_B(t,x=L)$ from negative to positive sign.

Another possible choice would be a continuity condition for B_r^f and B_r^b. We then write for positive $v_B(t,L=0)$

$$\begin{aligned} v_B^{L,f}(t,z=0)\ B_r^f(t,z=0) &= \rho^L(t)v_B(t,x=L)\ B_r(t,x=L) && (6.8)\\ v_B^{L,b}(t,z=0)\ B_r^b(t,z=0) &= (1-\rho^L(t))\ v_B(t,x=L)\ B_r(t,x=L) && (6.9)\end{aligned}$$

where ρ^L is the ratio

$$\rho^L(t) = \lim_{z\searrow 0}\frac{B_r^f(t,z)}{B_r^b(t,z)+B_r^f(t,z)} \quad (6.10)$$

with the convention $\frac{0}{0} := 0$ ensuring consistency. Adding up these equations leads again to the combined equation (6.7) which still is valid for negative $v_B(t,x=L)$.

In order to preserve the number of F-actin binding proteins in the membrane the binding site being occupied by new bound barbed ends and those becoming vacant by detachment of bound ends have to be accounted for as source terms in the equation for f^L. This results in

$$\begin{aligned}\frac{d}{dt}f^L(t) &= -\beta_+^L f^L(t)\int_0^\infty B_r^f(t,z)dz + \beta_-^L\int_0^\infty B_r^b(t,z)dz\\ &\quad -(1-\rho^L(t))\ v_B(t,x=L)\ B_r(t,x=L).\end{aligned} \quad (6.11)$$

For the sake of completeness we also write down the equations for the densities of left oriented barbed ends and right oriented pointed ends at the left boundary $x=0$. We start with the evolution equations for free (B_l^f) and bound (B_l^b) left oriented barbed ends and right oriented pointed pointed (P_r^0) ends of size z:

$$\begin{aligned}\partial_t B_l^f(t,z)+\partial_z\left(v_B^{L,f}(t,z)B_l^f(t,z)\right) &= -\beta_+^0 B_l^f(t,z)f^0(t)+\beta_-^0 B_l^b(t,z) && (6.12)\\ \partial_t B_l^b(t,z)+\partial_z\left(v_B^{L,b}(t,z)B_l^b(t,z)\right) &= \beta_+^0 B_l^f(t,z)f^0(t)-\beta_-^0 B_l^b(t,z) && (6.13)\\ \partial_t P_r^0(t,z)+\partial_z\left(v_P^0(t,z)P_r^0(t,z)\right) &= 0 && (6.14)\end{aligned}$$

where it should be kept in mind that negative end velocities $v_B,\ v_P$ correspond to a motion of filament tips to the left which is compatible with negative growth velocities $v_B^{0,f/b},\ v_P^0$.

For the number of binding sites at this end of the domain we write analogously to equation (6.4)

$$\frac{d}{dt}f^0(t) = -\beta_+^0 f^0(t)\int_0^\infty B_l^f(t,z)dz + \beta_-^0\int_0^\infty B_l^b(t,z)dz. \tag{6.15}$$

The flux condition for the pointed ends reads

$$-v_P(t,x=0)P_r(t,x=0) = v_P^0(t,z=0)P_r^0(t,z=0), \tag{6.16}$$

and for the barbed ends we write

$$v_B(t,x=0)\ B_l(t,x=0) = v_B^{0,f}(t,z=0)\ B_l^f(t,z=0) + v_B^{0,b}(t,z=0)\ B_l^b(t,z=0) \tag{6.17}$$

or, split up into the conditions for free and bound barbed ends in case of the velocity pointing to the outside of the cell:

$$\begin{aligned} v_B^{0,f}(t,z=0)\ B_l^f(t,z=0) &= \rho^0(t)v_B(t,x=0)\ B_l(t,x=0) &(6.18)\\ v_B^{0,b}(t,z=0)\ B_l^b(t,z=0) &= (1-\rho^0(t))v_B(t,x=0)\ B_l(t,x=0) &(6.19)\end{aligned}$$

with

$$\rho^0(t) = \lim_{z\searrow 0}\frac{B_l^f(t,z)}{B_l^b(t,z)+B_l^f(t,z)}. \tag{6.20}$$

To account for the reaction of binding sites with barbed ends of zero size we again extend the equation for f^0 to

$$\begin{aligned}\tfrac{d}{dt}f^0(t) &= -\beta_+^0 f^0(t)\textstyle\int_0^\infty B_l^f(t,z)dz + \beta_-^0\int_0^\infty B_l^b(t,z)dz\\ &\quad -(1-\rho^0(t))v_B(t,x=0)B_r(t,x=0).\end{aligned} \tag{6.21}$$

6.1.3 Growth velocities of boundary attached filaments

We have so far not yet given formulas for the growth velocities of the filament tips at the membrane. As these are crucial model ingredients we will work them out now.

We start with the pointed ends and note that we only consider steric interactions of those with the membrane. The pointed end growth velocity will thus be at most as large as their free velocity (viewed in the direction to the outside of the cell) and decreases further as z increases. One would expect that filaments cannot grow to infinite length even if supplied with sufficiently many monomers to be polymerized. To fix notation let us consider pointed ends of left oriented filaments at the right boundary. Their free velocity is given by

$$-v_P(t,L) = v_R + \delta\kappa_P\left(a(t,L) - a_P\right). \tag{6.22}$$

If this velocity is positive then the filament tips tend to grow into the membrane, and we assume that this growth is slowed down as the size z increases. This is considered to be caused by slower polymerization at the filament tip being pressed against the membrane. The effector should thus be the polymerization term $\kappa_P a$ whereas the depolymerization term $k_P := \kappa_P a_P$ may be assumed to be independent of z. The retrograde flow velocity will not depend on z anyway.

To put the z dependence of the polymerization into figures one may assume either

of the following shapes:

- a sharp cut off at some finite size z_0:

$$v_P^L(t,z) = v_R - \delta k_P + \delta\kappa_P a(t,L)\left(1 - \frac{z}{z_0}\right)\chi_{\{z<z_0\}} \tag{6.23}$$

  or

- a decay to zero as z goes to infinity, say exponentially with characteristic length z_0:

$$v_P^L(t,z) = v_R - \delta k_P + \delta\kappa_P a(t,L)\exp\left[-\frac{z}{z_0}\right]. \tag{6.24}$$

We remark that in both cases z_0 is the crucial parameter entering the model due to these boundary conditions.

Similarly, we can write down the growth velocity for right oriented pointed ends at the left boundary based on the free velocity

$$-v_P(t,0) = v_R + \delta\kappa_P\left(a(t,0) - a_P\right) \tag{6.25}$$

where the negative sign in that case has been introduced since the velocity towards the outside of the cell has to be considered. Depending on the choice of the z dependence of the polymerization term we obtain as growth velocity

$$v_P^0(t,z) = v_R - \delta k_P + \delta\kappa_P a(t,0)\left(1 - \frac{z}{z_0}\right)\chi_{\{z<z_0\}} \tag{6.26}$$

or

$$v_P^0(t,z) = v_R - \delta k_P + \delta\kappa_P a(t,0)\exp\left[-\frac{z}{z_0}\right]. \tag{6.27}$$

The free barbed ends behave similarly, and with the notation $k_B := \kappa_B a_B$ we obtain for right oriented free barbed ends at the right boundary the growth velocities

$$v_B^{L,f}(t,z) = -v_R - \delta k_B + \delta\kappa_B a(t,L)\left(1 - \frac{z}{z_0}\right)\chi_{\{z<z_0\}} \tag{6.28}$$

or

$$v_B^{L,f}(t,z) = -v_R - \delta k_B + \delta\kappa_B a(t,L)\exp\left[-\frac{z}{z_0}\right], \tag{6.29}$$

and for left oriented barbed ends at the left boundary

$$v_B^{0,f}(t,z) = -v_R - \delta k_B + \delta\kappa_B a(t,0)\left(1 - \frac{z}{z_0}\right)\chi_{\{z<z_0\}} \tag{6.30}$$

or

$$v_B^{0,f}(t,z) = -v_R - \delta k_B + \delta\kappa_B a(t,0)\exp\left[-\frac{z}{z_0}\right]. \tag{6.31}$$

The situation with the bound barbed ends may be somewhat trickier. Recall that we distinguish two basic cases:

1. Barbed ends are simply attached to some membrane fixed proteins which prevent any polymerization or depolymerization. Then the growth velocities at both

boundaries are simply given by $-v_R$.

2. Processive polymerization motors in the membrane enhance polymerization and block depolymerization of monomers from the barbed ends. In that case the grwoth velocity is larger than the free velocity − at least for small z. We assume for simplicity that the polymerization is simply enhanced by some factor $\zeta^{0/L} > 1$ and that the polymerization rate again decreases with increasing size z. The corresponding growth velocities are given by

$$v_B^{L,b}(t,z) = -v_R + \delta\zeta^L \kappa_B a(t,L)\left(1 - \frac{z}{z_0}\right)\chi_{\{z<z_0\}} \tag{6.32}$$

or

$$v_B^{L,b}(t,z) = -v_R + \delta\zeta^L \kappa_B a(t,L)\exp\left[-\frac{z}{z_0}\right] \tag{6.33}$$

for right oriented barbed ends at the right boundary, and by

$$v_B^{0,b}(t,z) = -v_R + \delta\zeta^0 \kappa_B a(t,0)\left(1 - \frac{z}{z_0}\right)\chi_{\{z<z_0\}} \tag{6.34}$$

or

$$v_B^{0,b}(t,z) = -v_R + \delta\zeta^0 \kappa_B a(t,0)\exp\left[-\frac{z}{z_0}\right] \tag{6.35}$$

for left oriented barbed ends at the left boundary.

6.1.4 Boundary conditions for actin monomers

The zero flux conditions for the monomer density a have to be adjusted to the new situation as well. The polymerization flux of the filament tips at the membrane corresponds to the flux of monomers from or to the cell. The resulting equations are

$$D\partial_x a(t,0) = \int_0^\infty v_{B,pol}^{0,f}(t,z)B_l^f(t,z) + v_{B,pol}^{0,b}(t,z)B_l^b(t,z) + v_{P,pol}^0 P_r^0(t,z)dz \tag{6.36}$$

for the left boundary and

$$-D\partial_x a(t,L) = \int_0^\infty v_{B,pol}^{L,f}(t,z)B_r^f(t,z) + v_{B,pol}^{L,b}(t,z)B_r^b(t,z) + v_{P,pol}^L P_r^0(t,z)dz \tag{6.37}$$

for the right one. Here, the polymerization velocities are just the growth velocities without the retrograde flow term v_R − similar to the reaction term in the reaction diffusion equation. In particular, the right hand sides of (6.36) and (6.37) are affine in $a(t,0)$ and $a(t,L)$, respectively. Using the expressions for the velocities from the last subsection we can write down explicite formulas for the polymerization fluxes.

We start by noting that bound barded ends do not contribute to the monomer turnover if we assume the first case of binding protein which prevents polymerization. We will therefore only give the formulas for the case with polymerization enhancing proteins since otherwise the terms including $B_{l/r}^b$ simply vanish. The flux condition

(6.36) thus can be stated more precisely as:

$$\begin{aligned} -\frac{D}{\delta}\partial_x a(t,0) &= -\int_0^\infty k_B B_l^f(t,z) + k_P P_r^0(t,z)dz \\ &+ a(t,0)\int_0^\infty \left(\kappa_B\left(B_l^f(t,z)+\zeta^0 B_l^b(t,z)\right)+\kappa_P P_r^0(t,z)\right)\exp\left[-\frac{z}{z_0}\right]dz. \end{aligned}$$

The term $\exp[-z/z_0]$ may as well be replaced by $1 - z/z_0$, and in that case the integration only runs from 0 to z_0. For the right boundary we find correspondingly

$$\begin{aligned} \frac{D}{\delta}\partial_x a(t,L) &= -\int_0^\infty k_B B_r^f(t,z) + k_P P_l^L(t,z)dz \\ &+ a(t,L)\int_0^\infty \left(\kappa_B\left(B_r^f(t,z)+\zeta^L B_r^b(t,z)\right)+\kappa_P P_l^L(t,z)\right)\exp\left[-\frac{z}{z_0}\right]dz. \end{aligned}$$

Chapter 7

Numerical Simulations for the Full Problem

In this chapter we shall introduce different numerical schemes for the full model. To start with, we are going to focus on the question of interior blow-up and therefore do not implement the free boundary in the first point. The basic goal of these investigations is to get a glimpse of the formation of fronts of polymerization fronts of actin filament tips in the interior of the cell. We shall also show that these fronts may indeed exist as interior steady states of moving and non-moving types as predicted in section 2.4.

7.1 Idea of the discretization and different schemes

The general idea we rely on is that the dynamics of the monomers is faster than that of the filament tips and we can therefore decouple the parabolic and hyperbolic parts from each other in every time step.

More precisely, we always solve the reaction diffusion equation for a by an implicite EULER scheme with central differences in space using the old values for the end densities to determine the reaction term. Then, the new end densities are computed by an explicite scheme with the velocities calculated from the new monomer density or an interpolation between the new and old monomer concentration.

7.1.1 Initial and boundary conditions

As initial data for the filament tips we consider two distinct cases. The first one corresponds to the case of confined collections of end densities of different types and will be implemented by initial data with support being bounded away from the fixed domain boundary. This will assure the filament tips to stay away from the boundary which is in that case to be understood as some interface within the cell. It should be recalled that we focus on the behavior in the interior and therefore zoom into some small portion of the cell body.

The second type of initial conditions is given by plateaus of the different end densities which extend up to the boundary of the domain at which the boundary conditions are fixed according to that plateau value. Somewhere inside the domain the end densities

smoothly change to a different plateau value which will most often be zero and equals the boundary value at the other end of the fixed simulation domain. This situation corresponds to some interior distribution of filament ends, and we now have zoomed into some portion of the cell on whose boundaries there are still filament ends but we do not have any changes in the end density transported into that region from the rest of the cell.

In both cases, the initial monomer density is given as some smooth function being approximatly constant in some neighborhood of the boundary and is forced to satisfy homogeneous NEUMANN boundary conditions. We may interpret this as being sufficiently far away from any sources of strong variations in the monomer density.

7.1.2 Different integration schemes for the hyperbolic part

In [9] we used a modified LAX-WENDROFF scheme to compute the evolution of the end densities. Since this type of discretizations tends to produce artificial oscillations at the trailing edges of moving humps they are not suitable for investigating blow-up events. We therefore use two other schemes with complementary behavior.

On the one hand we apply a LAX-FRIEDRICHS like scheme that smoothes every type of shock which might possibly emerge, and on the other hand we employ a finite volume method with upwind flux which is able to capture shocks without introducing artificial extrema to the solution.

A scheme with artificial diffusion in the hyperbolic part

It is obvious that all densities − monomers and filament tips − together with their spatial derivatives will remain bounded if we introduce some artificial diffusion in the hyperbolic equations. This is automatically done by using a LAX-FRIEDRICHS scheme for the discretization of the transport part of the hyperbolic equations. From the step sizes Δt and Δx in time and space direction, respectively, we can even calculate the precise value of the artificial diffusion coefficient to be

$$D_{num} = \frac{\Delta x^2}{2\Delta t}.$$

Using this discretization we therefore rather than the original problem solve the regularized problem

$$\begin{aligned} \partial_t u + \partial_x(\Lambda u) &= D_{num}\partial_{xx} u \\ \partial_t a - D\partial_{xx} a &= R(a,u). \end{aligned} \tag{7.1}$$

Since the numerical diffusion coefficient tends to zero as the spatial step size does we can invesitgate numerically the behavior of the solutions to the regularized problem as the artificial diffusion decreases. As the COURANT-FRIEDRICHS-LEVY condition

$$v_{max}\Delta t < \frac{1}{2}\Delta x$$

has to be satisfied we fix the ratio $\nu = \Delta x/\Delta t$ and obtain a numerical diffusion coefficient

$$D_{num} = \frac{\nu}{2}\Delta x$$

decreasing linearly in the step size Δx.

A finite volume scheme with upwind flux

As an alternative discretization with minimal artificial diffusion we use an upwind scheme for the different tips. It is in general not entirely free of diffusive effects but minimizes them to a level that is sufficient to prevent spurious numerical blow-up effects.

Contrary to the usual notation we denote the average value of u at time t^k in the grid cell (x_i, x_{i+1}) by u_i^k rather than $u_{i+\frac{1}{2}}^k$. The cell average u_i^{k+1} is then computed according to

$$u_i^{k+1} = u_i^k - \frac{\Delta t}{\Delta x}\left(F_{i+1}^k - F_i^k\right) \tag{7.2}$$

where F_i^k denotes the numerical flux through the left face x_i of the i^{th} cell . We choose the classical upwind flux and use the mean of the already updated and the current monomer density:

$$F_i^k = \begin{cases} \lambda_i^{k+\frac{1}{2}} u_i^k & \text{if } \lambda_i^{k+\frac{1}{2}} \leq 0 \\ \lambda_i^{k+\frac{1}{2}} u_{i-1}^k & \text{if } \lambda_i^{k+\frac{1}{2}} > 0 \end{cases} \tag{7.3}$$

with velocity

$$\lambda_i^{k+\frac{1}{2}} = \frac{\lambda(a_i^{k+1}) + \lambda(a_i^k)}{2}.$$

If in particular, the difference of the monomer density on both ends of the interval is large then we may have characteristics of opposite orientation on both faces. This allows for shock cells into which characteristics enter from both sides

As usual for explicite schemes, the consistency of the scheme requires the CFL condition

$$v_{max}\Delta t < \frac{1}{2}\Delta x \tag{7.4}$$

to be satisfied. Since the maximal velocity can be estimated from the parameters, the step sizes in space and time can be chosen accordingly.

7.2 Numerical blow-up results

We separately discuss the results for both types of initial conditions (compactly supported end distributions in isolated peaks versus extended plateaus of filament ends) and the different discretization schemes (Lax-Friedrichs versus upwind).

7.2.1 Isolated peaks with Lax-Friedrichs scheme

Let us start with the case of end densities being initially confined to some small region in space which is bounded away from the boundary of the simulation domain. The type of

discontinuities we may expect to develop from appropriate smooth data are comparable to the interior steady states discussed in subsection 2.4.2.

The particular setting we use consists of bell shaped initial conditions for both, right oriented barbed and left oriented pointed ends where the peaks are allowed to overlap but the pointed ends should not be too far to the right compared to the barbed ends. As initial monomer concentration we use a smooth distribution with high values in the left part of the domain and low values on the right.

To put figures to it we use sine shaped humps of the type

$$B_r(0,x) = B_0 \left(1 - \cos\left[2\pi \frac{x - l_B}{r_B - l_B}\right] \chi_{[l_B, r_B]}\right) \tag{7.5}$$

$$P_r(0,x) = P_0 \left(1 - \cos\left[2\pi \frac{x - l_P}{r_P - l_P}\right] \chi_{[l_P, r_P]}\right) \tag{7.6}$$

where

- $l_{B/P}$ are sufficiently far away from the left boundary, $r_{B/P}$ are sufficiently far away from the right boundary.
- $r_{B/P} - l_{B/P}$ are not too large in order to have concentrated initial conditions.
- $B_0(r_B - l_B) \approx P_0(r_P - l_P)$ with precise equality if we try to find interior steady states as in subsection 2.4.2.

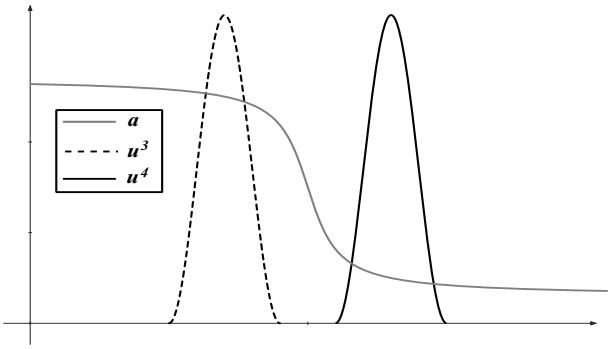

Figure 7.1: An example for concentrated peaks of end densities as initial conditions with different numbers of barbed and pointed ends. *solid, black*: B_r, *dashed*: P_l, *solid, gray*: a. Note that the units of the ordinate are arbitrary.

Moreover, we choose the initial condition for the monomer density to be of the shape

$$a(0,x) = a_r + (a_r - a_l)\left(\frac{1}{2} - \frac{1}{\pi}\arctan\left[\frac{x - \frac{1}{2}(r_a - l_a)}{w}\right]\right) \tag{7.7}$$

where $[l_a, r_a]$ is the spatial domain under consideration and w determines the width of the profile. In figure 7.1, a prototypical example of such initial data is shown.

With this type of initial conditions, the simulations using a Lax-Friedrichs scheme for the end densities show an evolution to smooth peaks of filament ends whose sharpness for given initial conditions increases as the spatial step size Δx is decreased. Two typical results for a small diffusion coefficient ($D = 1\ \mu m^2 s^{-1}$) with different step sizes Δx are shown in figure 7.2.

As expected, the center of the pointed end peak is located left, the one for the barbed ends on the right. Both peaks overlap and develop rather long tails towards the left and

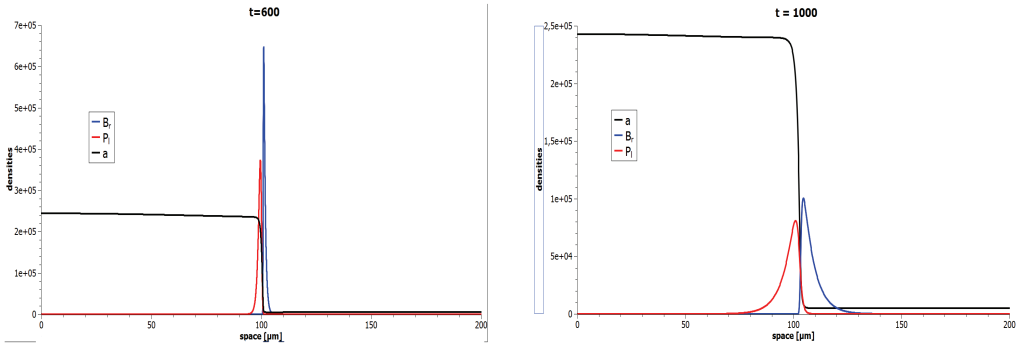

Figure 7.2: Steady state distributions of monomers (*black*), right oriented barbed ends (*blue*), and left oriented pointed ends (*red*) evolving from initial conditions as in figure 7.1 according to a Lax-Friedrichs finite difference scheme with different spatial step sizes (*left*: $\Delta x = 0.02\ \mu m$, *right*: $\Delta x = 0.15\ \mu m$). The diffusion coefficient is given by $D = 1\ \mu m^2 s^{-1}$. Note the different scales of the ordinate axes!

right boundary, respectively. Moreover, their distance decreases with the step size and approaches some finite value l_0 as Δx tends to zero. Both, the peak heights and the distance l in dependence on the mesh size Δx are displayed in figure 7.3.

This value l_0 corresponds to that found in subsection 2.4.2 if the mass b_0 is replaced by its smoothed version

$$\int_{l_B}^{r_B} B_r dx$$

since the end densities are smoothed by the artificial diffusion. More precisely, we have control over all quantities in (2.47) except l_0. In the case of the simulations whose results are shown in figure 7.3 we used the following set of parameters:

$$\begin{aligned} a_P &= 240000\ \mu m^{-1} & a_B &= 4800\ \mu m^{-1} \\ v_R &= 0.3\ \mu m\ s^{-1} & \delta &= 0.0022\ \mu m \\ \kappa_B &= \frac{5}{6\delta} 0.0001\ \mu m\ s^{-1} & \kappa_P &= 0.1\kappa_B. \end{aligned}$$

Moreover, the initial conditions are given by (7.5), and the total number of barbed ends (scaled by δ) is therefore given by

$$b_0 = B_0 \int_{l_B}^{r_B} 1 dx = B_0(r_B - l_B).$$

In our particular situation we chose the following initial conditions for the simulations:

$$\begin{aligned} D &= 1\ \mu m^2 s^{-1}, & B_0 &= 85000\ \mu m^{-2}, & r_B - l_B &= 8\ \mu m \\ D &= 3\ \mu m^2 s^{-1}, & B_0 &= 100000\ \mu m^{-2}, & r_B - l_B &= 4\ \mu m \\ D &= 10\ \mu m^2 s^{-1}, & B_0 &= 100000\ \mu m^{-2}, & r_B - l_B &= 2\ \mu m \end{aligned}$$

Plugging these values into (2.47), we obtain the following predicted distances between the ends:

$$\begin{aligned} l_0 &\approx 1\ \mu m && \text{for } D = 1\ \mu m^2 s^{-1} \\ l_0 &\approx 5\ \mu m && \text{for } D = 3\ \mu m^2 s^{-1} \\ l_0 &\approx 8\ \mu m && \text{for } D = 10\ \mu m^2 s^{-1}. \end{aligned}$$

Comparing this to the results of the simulations we observe that the distances measured with the Lax-Friedrichs scheme nicely converge to these values l_0 as the step size tends to zero.

The maximal peak heights of the barbed and pointed end distributions depend on the artificial diffusion coefficient as well. More precisely, the peak heights increase with decreasing spatial step size Δx and we observe a divergent behavior which is consistent with the expectation of a point measure in the limit.

Here, we observe another difference to the precise states found in 2.4.2. The peak for the barbed ends is always slightly higher and narrower than that for the pointed ends. This can be understood if one recalls the reaction kinetics to be faster at the barbed ends while the artificial diffusion does not distinguish between different types of ends.

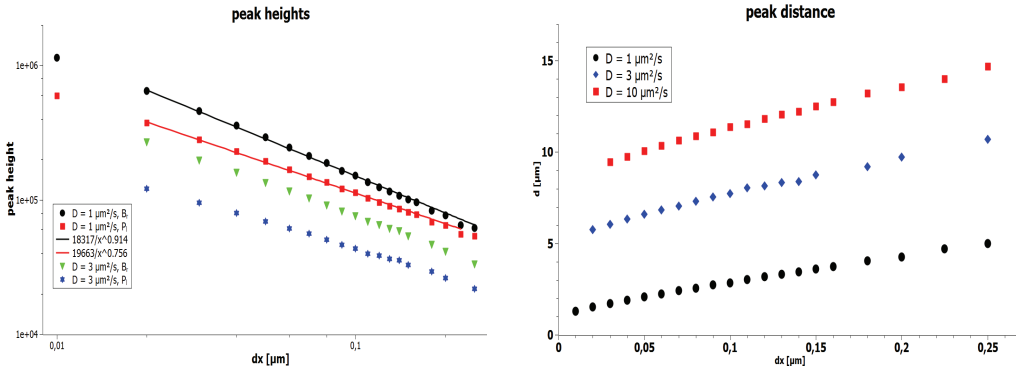

Figure 7.3: Peak heights (*left*) and distance between peaks (*right*) of right oriented barbed ends and left oriented pointed ends for different diffusion coefficients in dependence on the spatial step size Δx.

What should also be noted is that those peaks very slowly decay as time proceeds further which is due to a diffusive loss of filament ends through the boundary of the spatial domain.

The monomer density keeps its monotonicity – at least if the initial values a_r and a_l are appropriately chosen – and attains a profile which can be interpreted as a smoothed version of the continuous, piecewise linear shape introduced in subsection 2.4.2.

7.2.2 Isolated peaks with upwind scheme

If we use precisely the same type of initial conditions as in the previous subsection and let the end densities evolve by the finite volume algorithm described above we observe a behavior that may be viewed as limiting case of the Lax-Friedrichs variant as the

artificial diffusion approaches zero. More precisely, the end densities finally concentrate in sharp peaks which are located in a well defined distance from one another.

For the precise simulations we chose the same parameters and initial conditions as for the LAX-FRIEDRICHS case. In figure 7.4, the resulting profile for the case with diffusion coefficient $D = 10\ \mu m^2 s^{-1}$ is shown.

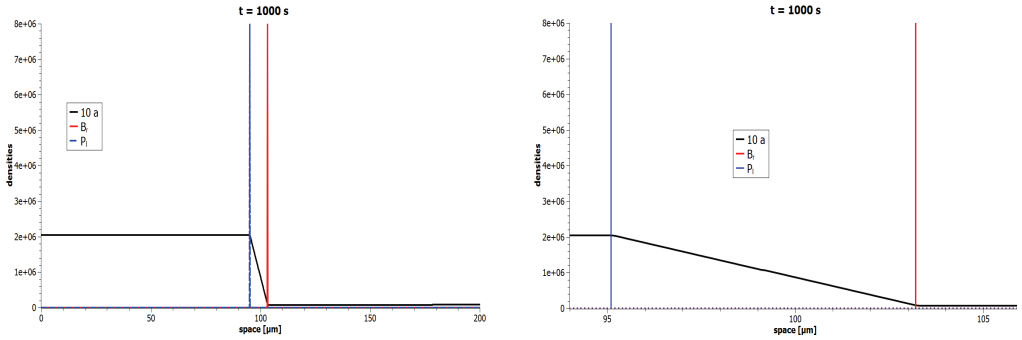

Figure 7.4: Asymptotic profile of right oriented barbed end density (*red*), pointed end density (*blue*), and ten fold monomer concentration (*black*) with diffusion coefficient $D = 10\ \mu m^2 s^{-1}$. On the *left*, the whole domain is shown, the *right* diagraph is a zoom to the center of the domain. The theoretical distance of the peaks is $l_0 \approx 8\ \mu m$ which perfectly fits to the profile.

To complete the picture concerning these types of steady states we also show the results for a profile corresponding to a moving interior steady state which has also been introduced in subsection 2.4.2. We chose initial conditions according to a speed of $v_0 = 0.8 v_R$ and parameters as in the previous subsection. According to the calculations in 2.4.2, this leads to asymptotic monomer concentrations of

$$\begin{aligned} a_l &= a_P - 0.2\frac{v_R}{\delta\kappa_P} \approx 232800\ \mu m^{-1} \\ a_r &= a_B + 1.8\frac{v_R}{\delta\kappa_B} \approx 11280\ \mu m^{-1}, \end{aligned}$$

and given $b_0 = 400000\ \mu m^{-1}$ barbed ends we obtain

$$p_0 = \frac{1}{0.2}\left(0.8(a_l - a_r) + 1.8 b_0\right) \approx 4.486 \times 10^6\ \mu m^{-1}.$$

This is large as compared to the total number of barbed ends which reflects the relatively large velocity of $0.8 v_R$.

The corresponding predicted distance between the peaks can be found to be

$$l_0 = \frac{D}{0.8 v_R} \log\left[1 + \frac{a_l - a_r}{b_0}\frac{0.8}{1.8}\right] \approx 9.17\ \mu m.$$

This is rather small, and we expect an approximately linear profile for the monomer density given by (2.53). This is in fact the kind of solution we obtain by the simulations whose results are depicted in figure 7.5. We note that according to the simulations the peaks are not of point measure type.

Recalling the notes on the dimension free version of the model in subsection 2.4.3

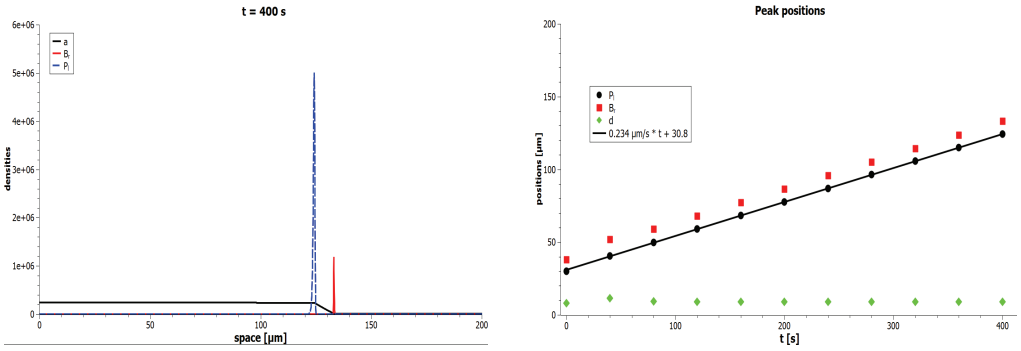

Figure 7.5: Moving profile with large end densities and correspondingly small distance of the peaks. *Left*: the steady profile moving at a measured velocity $v_{0,meas} \approx 0.235\ \mu m\ s^{-1}$. Note that the peaks are not as sharp as predicted! *Right*: To understand the motion of the profile, the positions of the peaks and the distance between them is plotted against time. We note that the distance is constant from $t = 120\ s$ on, and attains a value of $8.9\ \mu m$. The black line is a linear fit to the motion of the pointed end peak.

this approximately linear shape of the monomer density should not come as a surprise as large end densities have been seen to have the same effect as small diffusion coefficients. We therefore might already have expected an approximately linear profile.

To see that the monomer profile is indeed exponential between the two peaks we perform the same simulation with the very same parameters but a given number $b_0 = 10000\ \mu m^{-1}$ of barbed ends for which the number of pointed ends is

$$p_0 \approx 976080\ \mu m^{-1}.$$

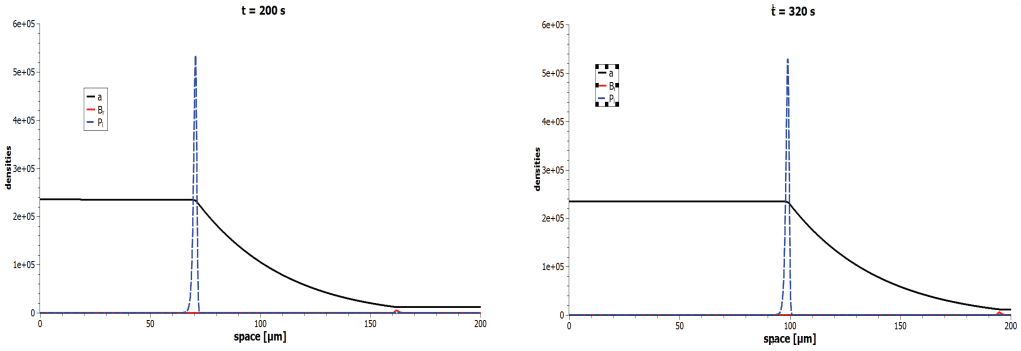

Figure 7.6: Moving profile with small end densities and correspondingly large distance of the peaks at different instances of time (*left*: 200 s, *right*: 320 s). Note the exponential monomer profile between the peaks!

Now, we find the expected distance between the peaks to be larger, namely

$$l_0 \approx 99.3\ \mu m$$

and we may expect a wider and more convex profile which is in fact observed in figure 7.6. The exponential profile for the monomer concentration we found by direct caluclation in subsection 2.4.2 and depicted in figure 2.8 is perfectly recovered by the simulations. However, the peaks in the end densities are not as pronounced as one might expect. They rather attain a certain shape which is maintained and travels through space at a measured velocity of

$$v_{0,meas} \approx 0.235\ \mu m\ s^{-1}$$

as can be seen from figure 7.7.

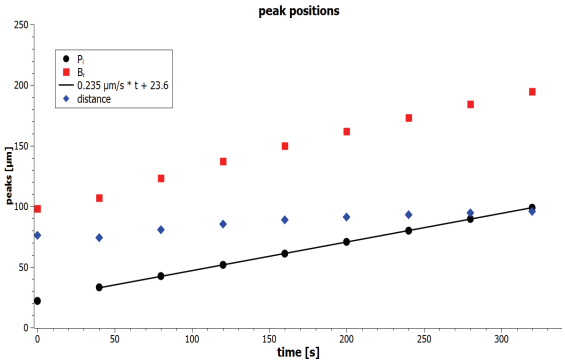

Figure 7.7: Peak positions and distance between the peaks over time for small end densities and correspondingly large distance. Again, the black line provides a linear fit of the position of the pointed end peak which yields a velocity that nicely fits the expected one of $v_0 = 0.24\ \mu m\ s^{-1}$. Note moreover, that the distance between the peaks equilibrates at approximately 99 μm!

7.2.3 Plateau shaped data with Lax-Friedrichs scheme

We now consider the second type of initial conditions indicated above. These consist of a monomer distribution which is very similar to the previous one (and may in fact be chosen as precisely the same).

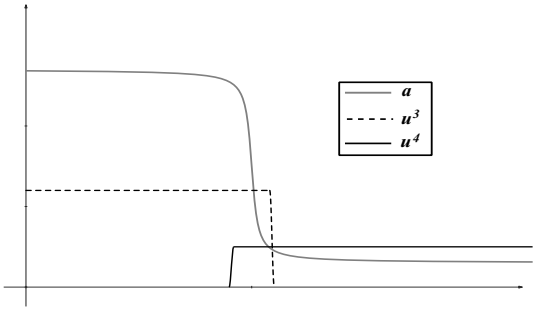

Figure 7.8: An example for plateaus of end densities as initial conditions with different plateau heights of barbed and pointed ends. *red*: B_r, *blue*: P_l, *black*: a. Note that the units of the ordinate are arbitrary.

A very different situation now applies to the end densities which are assumed to be plateau shaped. More precisely, the density of left oriented pointed ends shall be constant from the left boundary of the computational domain and then smoothly drop to zero somewhere in the center of the domain. This drop may again be accomplished by means of a sine shaped shoulder.

Similarly, the right oriented barbed end density is assumed to be constant from the right boundary to the center of the domain and drops to zero there as well. Here, the supports of the initial end densities may or may not overlap. The former case is sketched in figure 7.8.

So, how does the evolution of such initial conditions look like?

As to be expected, the monomer concentration tends to a_P in the left part of the domain and approaches a_B in the right part. This in particular yields both end plateaus moving towards the center of the domain and the filament ends accumulating there. The result are growing peaks of barbed and pointed ends, the former having its maximum to the right of the latter one. Both peaks typically overlap.

Again, the peaks become higher and narrower as the step size and thus the numerical diffusion in the hyperbolic part is decreased.

The drop of the monomer density from a_P to a_B in the center of the domain now becomes significantly steeper as the artificial diffusion in the end equations is reduced. Four typical patterns evolving from the initial conditions of the type shown in 7.8 are sketched in figure 7.9. In this figure, it should be paid attention to the peak heights of the end densities. As comparison the monomer density on the left of the shock may be used.

The peak heights obviously depend much more on the spatial step size − and thus on the (artificial) diffusion of filament ends − than on the actual diffusion coefficient for the monomers. In fact, they diverge as Δx tends to zero which is depicted in figure 7.10.

The positions where the peaks first occur clearly depends on the initial conditions, but we observe that their distance quickly decreases in the beginning of the simulation. As the mass concentrated in the peaks grows, for the case without natural and artificial diffusion, we would expect this distance to decrease toward zero and possibly even reaching this value. This situation would correspond to a shock with discontinuity in the monomer density as predicted for the system without diffusion in subsection 5.2.1.

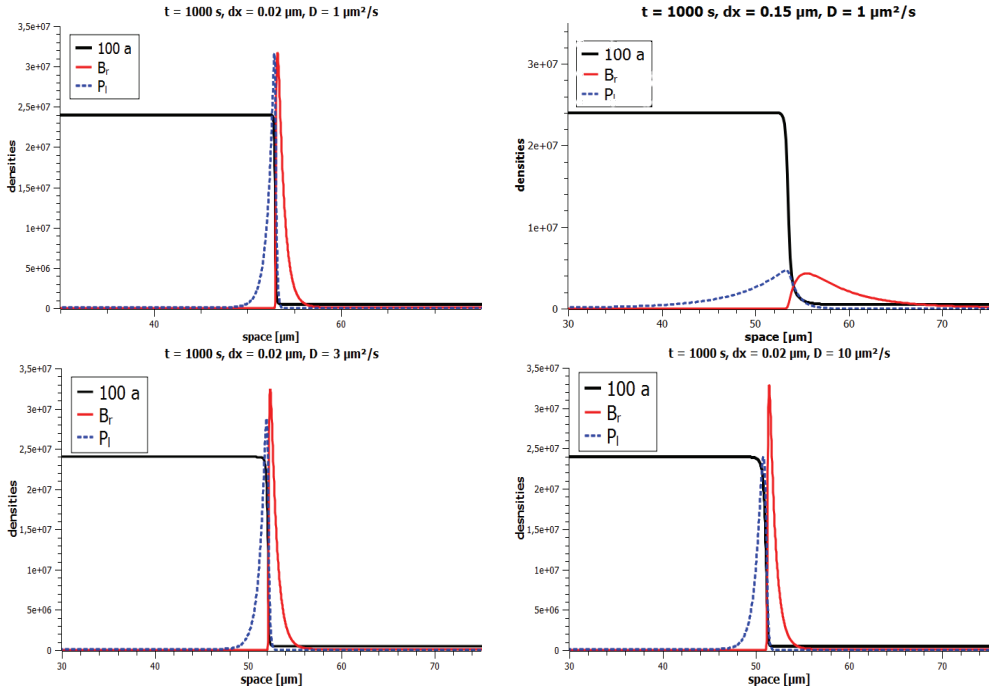

Figure 7.9: Shape of the monomer distribution (*black*, 100-fold increased for better visibility), and right oriented barbed (*red*) and left oriented pointed (*blue*) end densities after a simulation time of 1000 s for different diffusion coefficients using a Lax-Friedrichs scheme for the end densities. The spatial step size was chosen as $\Delta x = 0.02\ \mu m$. *Top, left*: $D = 1\ \mu m^2\ s^{-1}$, *top, right*: $D = 1\ \mu m^2\ s^{-1}$ with $\Delta x = 0.15\ \mu m$ as comparison, *bottom, left*: $D = 3\ \mu m^2\ s^{-1}$, *bottom, right*: $D = 10\ \mu m^2\ s^{-1}$.

In our situation with artificial diffusion, the simulations show the peak distance to equilibrate at some finite value for large times. This value depends on both, the diffusion coefficient in the monomer equation and the spatial steps size of the numerical scheme which codes for the artificial diffusion in the end equation.

Having a closer look at figure 7.11 we still observe a linear decrease as the spatial step size Δx tends to zero. As this distance is a measure for the width of the smoothed shock we would expect it to be zero in the absence of artificial diffusion of filament ends if we dealt with a real jump in the monomer density. Strikingly, as in the case of isolated peaks, the extrapolated distance for $\Delta x \to 0$ is not zero but rather a finite value that increases with the diffusion coefficient D in the monomer equation.

A linear extrapolation of the distances between the maxima after a simulation time of $1000s$ to vanishing step size yields the following values:

$$d_0 = (0.032 \pm 0.006)\ \mu m \qquad \text{for } D = 1\ \mu m^2 s^{-1}$$
$$d_0 = (0.096 \pm 0.007)\ \mu m \qquad \text{for } D = 3\ \mu m^2 s^{-1}$$
$$d_0 = (0.321 \pm 0.007)\ \mu m \qquad \text{for } D = 10\ \mu m^2 s^{-1}.$$

These numbers indicate that the distances not only decrease linearly with respect

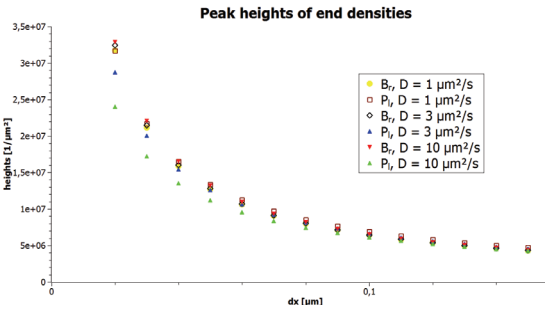

Figure 7.10: Peak heights of the end distributions after $t = 1000\ s$ for different diffusion coefficients D depending on the spatial step size of the simulation. Note that the height seems to diverge as Δx tends to zero.

to the artificial diffusion of filament tips but as well with respect to the diffusion coefficient D of the monomers. This gives rise to the conjecture that the gradient of the monomer density remains bounded (although becoming very large) as soon as diffusion is present. We recall that in the previous subsection we observed a similar linear relationship between the peak distance for the isolated peaks on the diffusion coefficient. This behavior was in good agreement with the dimensional analysis in subsection 2.4.3. For the plateau shaped data considered here we were not able to make any predictions on the peak distance.

We might therefore not talk about shocks in the classical sense but rather consider these solutions as some kind of smoothed shock profiles as indicated in section 5.3.

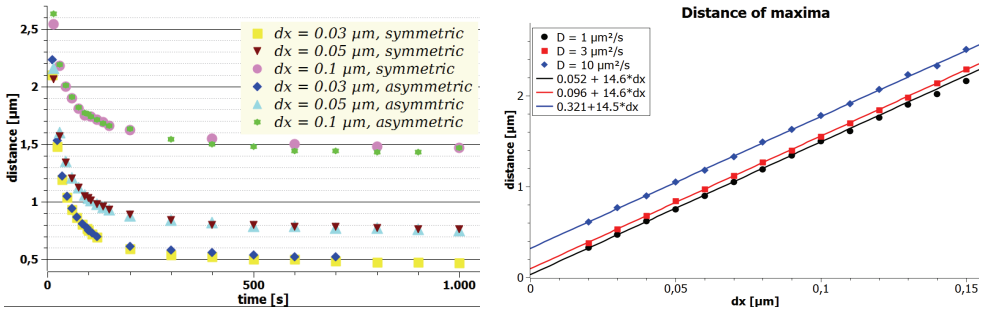

Figure 7.11: Distance between the maxima of barbed and pointed end distributions evolving in time for fixed $D = 1\ \mu m^2\ s^{-1}$ and three values of Δx (*left*) and for different diffusion coefficients and step sizes after $t = 1000\ s$ (*right*). On the left, the term *symmetric* refers to equal plateau values for B_r and P_l whereas *asymmetric* means a fivefold higher plateau value for P_l than for B_r.

Besides the distances between the peaks which are a measure for the damping effect of the diffusion we may also ask for the positions of the peaks in space. In subsection 5.2.1, we deduced that in case the plateau values of P_l and B_r are different, we would have to expect moving shocks. For equal plateau heights, in contrast, we were led to expect a standing shock.

In fact, if the plateau height for B_r and P_l coincide, we observe very slowly moving profiles. It should be noted that the velocity is not actually zero which should be an effect of the articficial diffusion in the end equations introduced by the numerical scheme. In fact, this nonzero velocity may be viewed as wave speed of something similar to a traveling wave. It should though be noted that the actual situation does not precisely

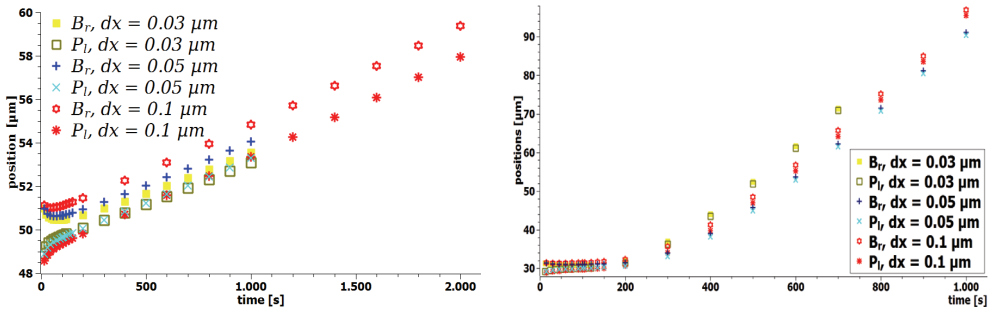

Figure 7.12: Movement of the peaks for plateau shaped data with equal (*left*) and different plateau heights (*right*) with diffusion coefficient $D = 1\ \mu m^2 s^{-1}$, retrograde flow velocity $v_R = 0.3\ \mu m\ s^{-1}$ and reaction rates slightly increased compared to the standard case. The plateau value for P_l is in both cases $10^5\ \mu m^{-2}$, that for B_r is the same on the left and 20000 μm^{-2} on the right. Note the different scales of the ordinates!

fit into the framework of traveling waves since the end density peaks are permanently growing rather than being constant in shape and height.

Taking initial conditions with a ratio μ of the plateau values close to zero, the velocity of the peaks is much larger. From figure 7.12, we can estimate the velocity for the case $\mu = 0.2$ a velocity of $v \approx 0.045\ \mu m\ s^{-1}$ whereas the measured velocity for $\mu = 1$ can be calculated to be approximately $0.0045\ \mu m\ s^{-1}$. We will find more precise figures for the velocities from the simulations using the upwind scheme in the following subsection.

A final interesting observation is that the distance between the barbed and the pointed end peak do not seem to be significantly affected by the asymmetry in the plateau heights as becomes clear from figure 7.11.

7.2.4 Plateau shaped data with upwind scheme

We finally discuss the evolution of plateau shaped initial conditions as introduced in the previous subsection if we use the upwind finite volume scheme.

As in the Lax-Friedrichs case, the monomer concentration tends to a_B and a_P in the right and left part of the domain, respectively. In between we observe a very sharp drop in the monomer density.

The end densities develop sharp, delta like peaks at the interface between the plateaus whose permanent growth is fed by the filament ends being transported towards the center with retrograde flow velocity v_R. As the peaks grow, the distance between the barbed and pointed end peaks initially decreases and thereby, the gradient of the monomer density strongly increases.

Two particular examples of such a solution are shown in figure 7.13. Obviously, the profiles are sharper for the smaller diffusion coefficient $D = 1\ \mu m^2 s^{-1}$ than for the larger value of $D = 10\ \mu m^2 s^{-1}$ (note the different scales for the space variable).

However, we do not find a particular dependence of the peak distance on the diffusion coefficient on the diffusion coefficient in case of these standing shocks. On the contrary, the peaks of the very sharp end density profiles are located in the same grid cell. More precisely, we performed simulations for diffusion coefficients ranging from 0.1 $\mu m^2 s^{-1}$

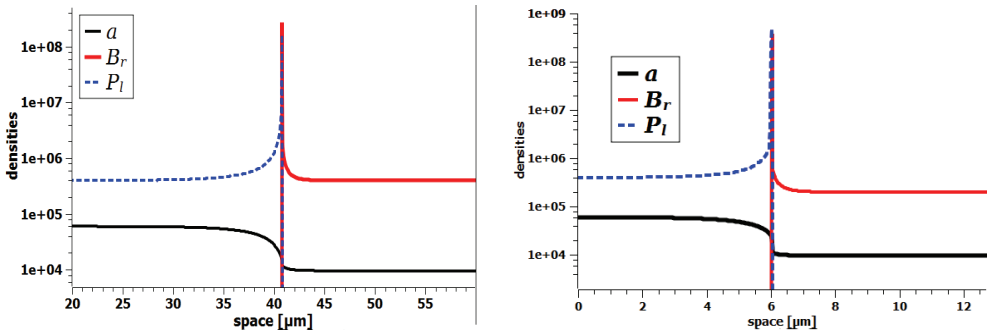

Figure 7.13: Examples of shock like solutions with plateaus in the end densities obtained by simulations using the upwind scheme for the end equations. *Left*: symmetric plateau values $4 \times 10^5\ \mu m^{-2}$, diffusion coefficient $D = 10\ \mu m^2 s^{-1}$, $\Delta x = 0.06\ \mu m$, $\Delta t = 0.0003\ s$. *Right*: asymmetric plateau values ($\mu = 0.5$), diffusion coefficient $D = 1\ \mu m^2 s^{-1}$, $\Delta x = 0.02\ \mu m$, $\Delta t = 0.0001\ s$. Notice that the densities are plotted on a logarithmic scale in order to capture both, the peaks and the plateaus!

to 30 $\mu m^2 s^{-1}$ at a spatial step size of $\Delta x = 0.01\ \mu m$ and always found both peaks to be located within these 0.01 μm. This is in strong contrast to the results obtained by the LAX-FRIEDRICHS scheme.

What we in fact observe are wider humps at the base of the peaks for larger diffusion coefficients. That means that the DIRAC-delta shaped peaks sit on top of wider profiles above the plateau levels which also carry more mass. Moreover, the filament tips also invade the region beyond the shock position more strongly if the diffusion coefficient is increased. These effects are accompanied by a monomer concentration showing smoothed approximation to the jump profile predicted for the fully hyperbolic system. Without being surprised we find that this smoothing effect is stronger the higher the diffusion coefficient is.

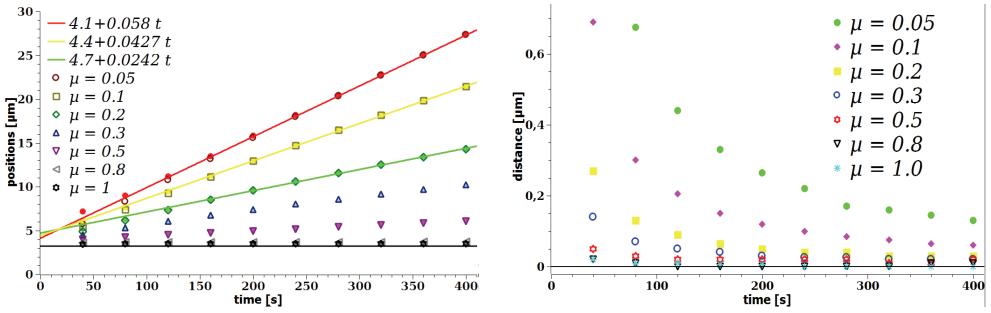

Figure 7.14: Positions of (*left*) and distances between (*right*) the barbed and pointed end peaks for shock like solutions with plateau for $D = 1\ \mu m^2 s^{-1}$. Shown is the evolution of both values over time for different values of the ratio μ between the plateau values for B_r and P_l. The colored lines on the left indicate the motion of the profile at asymptotically constant velocity for values of 0.05, 0.1, and 0.2 for the ratio μ

Again, we can ask for the movement of these shock like profiles depending on the

height of the plateaus for the barbed and pointed end densities. In figure 7.14, we depicted the temporal evolution of both, the peak positions and their respective distance over time for standard parameters and a rather small diffusion coefficient of $D = 1\ \mu m^2 s^{-1}$. Depending on the ratio μ between the plateau values we can estimate the following asymptotic velocities of the profile:

$$\begin{aligned} v = 0.0055 = 0.055 v_R \qquad & \text{for} \qquad \mu = 0.5 \\ v = 0.0139 = 0.139 v_R \qquad & \text{for} \qquad \mu = 0.3 \\ v = 0.0242 = 0.242 v_R \qquad & \text{for} \qquad \mu = 0.2 \\ v = 0.0427 = 0.427 v_R \qquad & \text{for} \qquad \mu = 0.1 \\ v = 0.058 = 0.58 v_R \qquad & \text{for} \qquad \mu = 0.05. \end{aligned}$$

These figures are not precisely the values we computed in subsection 5.2.1 but the qualitative relationship between μ and the velocity is recovered. More precisely, we observe that v is a monotonuously decaying, concave function of μ, and the velocities indeed lie between the retrograde flow velocity and 0. Also the order of magnitude of the velocities is as predicted although the monomer diffusion seems to slightly decrease them. This effect is obviously larger the closer μ is to 1.

We note that in contrast to the non-moving profiles obtained for equally high plateaus of barbed and pointed ends, we now find the peaks to be located at a finite distance from one another, and this distance is seen to increase with the velocity v.

This may also solve the seeming inconsistency between the results concerning the peak distances obtained from both types of simulations. We recall that in case of equal plateau values, the Lax-Fridrichs scheme suggested a finite distance between the barbed and the pointed end peak even in the limit of vanishing artificial diffusion whereas the finite volume scheme showed both peak positions to coincide. Now, we found that the distance between the peaks becomes nonzero whenever the whole profile is moving. Since the peaks indeed moved also for symmetric data under the effect of arbitrarily small artificial diffusion this may explain why also their distance is smaller.

Thinking of the situation in terms of viscosity limits leads to the following interpretation. The regularized system (7.1) with symmetric data seems to exhibit some type of generalized traveling wave solutions describing the transition from the left state

$$(P_l = B_0 > 0,\ B_r = 0,\ a = a_P)$$

to the right state

$$(P_l = 0,\ B_r = B_0,\ a = a_B)$$

via a profile of growing peaks moving at finite velocity and exhibiting very sharp but still bounded peaks in the end densities. As the regularizing artificial diffusion coefficient D_{num} is decreased to zero these profiles cease to exist and are replaced by the Dirac delta shaped peaks at a fixed and moreover coinciding position in space.

As opposed to the discussion of traveling wave profiles for the reduced model in the second part we observe the velocity of the profiles for the regularized system not to tend towards zero as the artificial diffusion is decreased. On the contrary, figure 7.12 indicates a velocity being roughly independent of the artificial diffusion coefficient. If the

regularizing term is completely removed which corresponds to the finite volume scheme this velocity should drop to zero and the accompanying finite distance between the peaks does so as well.

Chapter 8

Summary and Discussion I

Starting from the minimal cytoskeleton model deduced in [10] to investigate the polarization of a cell at rest we now formulated a free boundary problem that actually allows for movement of the cell. For the analysis and the simulations we imposed the simplest possible boundary condition corresponding to a membrane that does not exert any forces on the filaments so that any movement of leading filament tips results in a displacement of the boundary. The actin monomers are still supposed to be reflected at the membrane.

For the resulting moving boundary problem we showed well posedness for sufficiently small times if the initial and boundary conditions satisfy certain compatibility conditions. In particular, we were led to assume strict hyperbolicity for the end equations at least at the boundary in order to assure sufficient smoothness of the solutions. In that case we were able to prove the existence of solutions in the classical sense by employing a contraction principle and deduced certain estimates for the derivatives in suitable Hölder spaces.

After having treated the whole system with constant coefficients we saw that smooth variations of those did not substantially change the solvability. This is important since the actin dynamics in motile cells are regulated via a variety of mechanisms some of which drastically change the reaction rates and the critical monomer concentrations for the polymerization and depolymerization at the filament tips.

In case the strict hyperbolicity of the hyperbolic part cannot be assured we have to work with weak solutions of the problem but can still show local in time well posedness under rather mild assumptions. Also in that case the contraction mapping principle was the core element of the proof.

However, we were not able to show global well posedness since we could not exclude the possibility of blow-up or shock phenomena. From the hyperbolic equations we might have expected the development of Dirac measure type solutions corresponding to sharp fronts of filament tips moving at the same speed. The occurance of these measure valued solutions of the hyperbolic equations cannot be excluded to be accompanied by jumps in the monomer concentration − a phenomenon referred to as gradient blow-up for parabolic equations. This is a quite striking observation as all of the equations are in themselves linear and only contain bilinear coupling terms.

We also discussed the physical interpretation of these measure valued solutions for the hyperbolic equations as polymerization fronts of actin filaments. Precise pictures of

this correspondence are provided in subsections 2.4.2 and 5.2.1.

In fact, we did find exact solutions containing two types of δ-shocks. The first type consists of DIRAC measure valued solutions for the end densities and a continuous, piecewise smooth monomer profile with isolated jumps in the first spatial derivative. These profiles have been deduced as stationary or moving patterns.

The second type of shocks we found consists of at least two DIRAC peaks of filament tips at coincident position and of non-zero plateaus of the filament densities aside the shock. These profiles could be constructed in a way as to make the monomer concentration jump at the very position of the peaks but now, this concentration could only be viewed as piecewise solution of the parabolic equation since even for weak solutions we would have to require continuity and at least weak differentiability with respect to space. The existence of this type of shocks could hence only been shown for the purely hyperbolic system being obtained by formally putting the diffusion coefficient D in the parabolic equation to zero.

The question of whether any of these two shock type solutions could evolve from smooth initial data could not be addressed analytically, and we therefore performed some numerical simulations to investigate solutions which are at least close to these shocks.

In fact, we found the first type of fronts with continuous monomer concentration to evolve from a variety of suitable initial conditions and could even recover nicely the parameters of these solutions like the distance of the different peaks in dependence on the mass of the point measures and the model parameters.

The second type of shocks did not occur in the simulations but from analyzing the behavior of the numerical solutions we found that the diffusion seems to prevent the discontinuity in the monomer concentration. In fact, the predicted DIRAC measures for the end distributions indeed develop but their location does only coincide for non-moving profiles, and around these peaks the monomer density shows a large but still finite gradient.

Combining these two observations we may propose that the model allows for sharp fronts of polymerizing filament tips but that the profiles corresponding to those fronts are still weak solutions of the system. In particular, the suspected gradient blow-up in the parabolic equation does not seem to happen.

Nevertheless, the expected fronts of filament tips moving to one direction can be observed in the simulations as very sharp peaks in the filament densities. We note that our model is based on continuum limits and thus would lose its validity for discontinuous monomer densities. We can therefore use it to investigate the emergence of these sharp fronts but for the later stages of the evolution another model should be established. Similar arguments are for example known for blow-up phenomena in chemotaxis models as being discussed in [13].

To this end we should note that there is a reasonably large class of initial conditions and parameters for which we do not observe such concentration phenomena even over quite long simulation times. The front formation discussed above is therefore indeed dependent on both, the initial state of the cytoskeleton and the reaction kinetics which are regulated by additional control mechanisms.

Part II

Formulation and Analysis of a Reduced Model

In this second part of this thesis, we are going to derive and analyze a simplified model for the motion of the filaments at constant monomer density. Trying to get a glimpse of how our cytoskeleton model might react to additional diffusion and mutual alignment of filaments we derive in chapter 9 a model of two evolution equations for the total density of filaments and for the difference between right and left oriented filament densities. If being concerned with a finite spatial domain we additionally provide appropriate boundary conditions.

In chapters 10 and 11 we will discuss possible steady states of the system in a confined domain and investigate their stability against small perturbations. First, we linearize the system around these steady states in chapter 10 and will find linear stability criteria depending on the domain size and the model parameters which are the diffusivity and the strength of mutual alignment. Then we will ask for stability in terms of the energy method by employing an appropriate energy functional in chapter 11. We shall find that the precise shape of the alignment term determines whether both stability concepts yield the same stability criteria.

Considering the system on an infinite spatial domain, we may ask for solutions of traveling wave type which would correspond to fronts of filaments moving at constant speed and resembling steady motion of the system. This is done in chapters 13 and 14 where we explicitely find certain traveling waves for some reduced systems and then conclude the existence of traveling wave profiles for the full system by singular perturbation theory. In particular, depending on the model parameters we will discuss possible wave speeds and their relationship to the asymptotic states of the waves.

Finally, some simulations of the simplified system on bounded and on practically infinite domains are performed. On finite domains with boundary effects, we investigate the behavior of the system equipped with initial data close to the symmetric equilibrium, and the results are compared with the calculations from chapters 10 and 11.

Simulations on large spatial domains allow us to examine which of the predicted traveling wave solutions do in fact occur for our system. We observe two particular wave types, one given by saddle-node orbits in the phase space, and another one given by saddle-saddle connections. Together with pure diffusion fronts, several of these traveling waves can occur jointly to form different polarization patterns. Moreover, we will especially discuss the observed wave speeds and their connection to the model parameters.

Chapter 9

Derivation of the Reduced Model

9.1 General derivation

We recall the model (2.4a) - (2.4d), (2.15) for the cytoskeleton and now want to derive a reduced model that helps us understanding the effect of certain variations in the end equations such as diffusive behavior of filament tips and mutual alignment of filaments.

In order to get rid of the parabolic equation we make some strong assumptions on the behavior of monomers. Some of them are certainly not precisely met by the biological reality. However, we would like to note that the simplified model to be derived here is not intended to describe the cytoskeleton in vivo itself but rather the behavior of the end densities under certain settings with the goal to draw some conclusions for the original model. We will for instance find traveling wave solutions which motivate us to look for smoothed versions of the shock solutions found in subsections 2.4.2 and 5.2.1.

The precise simplifications to be made are the following ones.

1. Assume the monomer supply to be unlimited such that the monomer concentration a is constant over space and time. In that case we can omit the fifth equation. This assumption may be justified biologically if we assume rapid diffusion and arbitrary supply of monomers.

2. Assume further that for this particular monomer density the velocities for barbed and pointed ends coincide, $v_B = v_P =: v$. Without loss of generality we may set $v = 1$.

3. Assume the filaments to be very short, so that we have $B_r = P_r =: u_r$ and $B_l = P_l =: u_l$

This allows us to write a very simple system of equations describing the densities $u_r,\ u_l$ of right and left oriented filaments, respectively, which in the following for obvious reasons will occasionally also be called particles:

$$\begin{aligned} \partial_t u_r + \partial_x u_r &= 0 \\ \partial_t u_l - \partial_x u_l &= 0 \end{aligned}$$

These equations shall be assumed to be valid for $x \in (0, L)$ and $t > 0$. To provide boundary conditions we will assume that the particles turn around as soon as they

encounter a wall and thus obtain

$$u_r(t,x) \;=\; u_l(t,x) \qquad \text{for } x \in \{0, L\}.$$

This system could of course be solved explicitely but since we are interested in the effect of additional diffusion and alignment we shall proceed with the introduction of these mechanisms into the model.

Using the Kac trick we may readily rewrite the system to

$$\begin{aligned} \partial_t u + \partial_x w &= 0 \\ \partial_t w + \partial_x u &= 0 \end{aligned}$$

where we introduced the total particle density $u = u_r + u_l$ and the difference $w = w_r - w_l$ between right and left oriented filaments. This difference shall also be called polarization.

The boundary conditions translate into

$$w(t,x) \;=\; 0 \qquad \text{for } x \in \{0, L\}. \tag{9.1}$$

This system may be extended by dissipation of the difference w and mutual alignment of particles the mechanisms of which will be discussed more closely in section 9.2. By naively putting the dissipation into the equation for w we obtain the following system

$$\begin{aligned} \partial_t u + \partial_x w &= 0 && \text{(9.2a)} \\ \partial_t w + \partial_x u &= \varepsilon \partial_{xx} w + f(u,w). && \text{(9.2b)} \end{aligned}$$

Note that the retranslated form of this system is

$$\begin{aligned} &\partial_t \begin{pmatrix} u_r \\ u_l \end{pmatrix} + \begin{pmatrix} 1 & 0 \\ 0 & -1 \end{pmatrix} \partial_x \begin{pmatrix} u_r \\ u_l \end{pmatrix} \\ = \;& \tfrac{\varepsilon}{2} \begin{pmatrix} 1 & -1 \\ -1 & 1 \end{pmatrix} \partial_{xx} \begin{pmatrix} u_r \\ u_l \end{pmatrix} + \tfrac{1}{2} \begin{pmatrix} f(u_r + u_l,\; u_r - u_l) \\ -f(u_r + u_l,\; u_r - u_l) \end{pmatrix} \end{aligned} \tag{9.3}$$

with the diffusion matrix being only positive semidefinite. Positive definiteness may be reached by adding an arbitrarily small diffusion term $\delta \partial_{xx} u$ to the equation for the total density u. This model will in general still not preserve positivity of the partial densities u_r and u_l even if the reaction term f is well behaved. Moreover, it is hard to explain the biophysical meaning of this term beyond stating that it is an approximation to describe filaments randomly changing their direction.

This drawback is overcome by considering simple diffusion of the particles of either type, corresponding to the replacement of the diffusion matrix in 9.3 by a multiple of the identity matrix. From a biological point of view, this diffusion of filaments should in fact be expected if they are particularly short as we are assuming here.

The resulting model reads

$$\begin{aligned} \partial_t u + \partial_x w &= \varepsilon \partial_{xx} u && \text{(9.4a)} \\ \partial_t w + \partial_x u &= \varepsilon \partial_{xx} w + f(u,w) && \text{(9.4b)} \end{aligned}$$

Although model (9.2) does not guarantee positivity of the partial densities u_r and u_l, it is still of some interest from the mathematical point of view and provides some insights which are also useful to understand the behavior of model (9.4) in situations where analysis for the latter is not possible anymore. Since model (9.4) can also be understood to describe a polarizable medium having a certain density u of some physical quantity and a corresponding polarization w, we will investigate the properties of this model as well.

We note that both systems, (9.2) and (9.4), as well as their interpolates

$$\begin{aligned} \partial_t u + \partial_x w &= \theta\varepsilon\partial_{xx} u \\ \partial_t w + \partial_x u &= \varepsilon\partial_{xx} w + f(u,w), \end{aligned} \tag{9.5}$$

with $\theta \in (0,1)$ are special cases of the following class of diffusion advection problems:

$$\partial_t \begin{pmatrix} u \\ w \end{pmatrix} + \partial_x \begin{pmatrix} w \\ u \end{pmatrix} = \partial_x \left(B\partial_x \begin{pmatrix} u \\ w \end{pmatrix} \right) + F(u,w) \tag{9.6}$$

9.2 Properties of the alignment term

The nonlinear right hand side f is supposed to describe the mutual alignment of particles encountering each other in opposite direction. If the density of right and left moving particles are equal then none of them will be able to overcome the other and in that case the alignment term shall vanish:

$$f(u,0) = 0 \qquad \forall\ u \in [0,\infty) \tag{9.7}$$

indicating that on average as many left moving filaments are turned into right oriented ones as vice versa.

Furthermore, if all particles move in the same direction there will be no further alignment, thus we obtain

$$f(u,\pm u) = 0 \qquad \forall\ u \in [0,\infty). \tag{9.8}$$

Given a particular total density, say $u = 1$, we will consider the following three cases of nonlinearities whose cut in a $u = const$ plane is shown in figure 9.1.

1. **The bistable sublinear case**:

$$f(1,w) = \alpha w(1-w^2). \tag{9.9}$$

   The terminology *sublinear* means that the linearization of this function around $w = 0$ overestimates the absolute value of f. This version of the alignment term assumes that the aligning effect of an individual filament on the ones coming from the opposite direction is strongest when there are equally many right and left oriented filaments. This may be the case if we assume alignment to be due to single encounters of two filaments moving in opposite direction and one turning around the other by steric interactions.

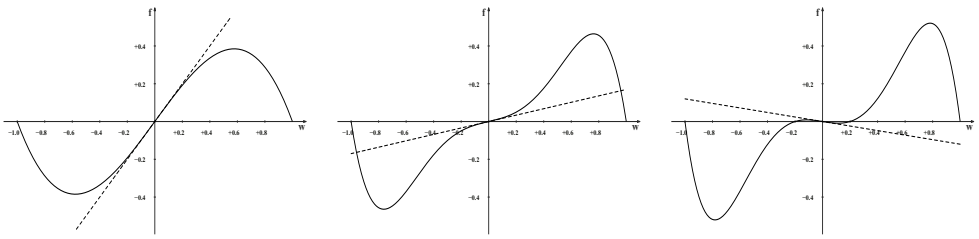

Figure 9.1: Different dependence of the nonlinearity f on the polarization w for fixed $u = 1$. *left*: sublinear bistable f according to (9.9), *middle*: sublinear bistable f according to (9.10), *right*: tristable f, according to (9.12). The black lines in the first two graphs show the linearization $\partial_w f(1,0)\, w$. Note that for $u \neq 1$, the outer zeros of f are given by $\pm u$ rather than ± 1.

2. **The bistable superlinear case**:

$$f(1,w) = \alpha w(1 + \nu w^2 - (\nu+1)w^4) \tag{9.10}$$

or

$$f(1,w) = \alpha w(1 + \nu|w| - (\nu+1)w^2) \tag{9.11}$$

with some $\nu > 1$. In practice, ν will typically be chosen to be of the order of magnitude of 10. For this superlinear right hand side, the linearization around $w = 0$ underestimates the absolute value of f. This term should be understood to describe cooperative effects of the alignment mechanism in the sense that those filaments being in majority can collectively turn around the ones coming from the opposite direction by joining forces. Thus, the alignment power of each individual particle is increased if it has as many collaborative partners. We would expect such a behavior if the possible turning of any arbitrarily chosen filament is assumed to be due to the interaction with several opposingly moving ones at a time rather than multiple encounters of single ones.

3. **The tristable case**:

$$f(1,w) = \alpha w(1 - w^2)(w^2 - \lambda^2) \tag{9.12}$$

or

$$f(1,w) = \alpha w(1 - |w|)(|w| - \lambda) \tag{9.13}$$

with some parameter $\lambda \in (0,1)$, typically being small compared with 1. In that case the term f even describes dealignment for small values of the polarization w. That means that close to the equilibrium state the system locally tends towards this equilibrium by itself. This alignment term is of rather small physical relevance but is used to illustrate the effect of the alignment term in the chapters 10 and 11 concerning the stability analysis.

In all of these cases, α is a positive parameter which we will call the *strength of alignment*.

Chapter 10

Linear Stability Analysis

In this chapter we are going to investigate the linear stability of the non-polarized homogeneous steady state characterized by $w = 0$ for both systems, (9.2) and (9.4). In sections 10.2 and 10.3 we will start with the linear stability analysis for the respective models. Here, the perturbations of the homogeneous steady state are assumed to be of similar shape for u and w, that is, we only consider perturbations, where both, the density and the polarization, have the same FOURIER modes. In section 10.4 we will compare the stability behavior of both models. Finally, in section 10.5, the stability against perturbations with different modes for u and w are discussed.

10.1 Preliminary calculations and remarks

For either system (9.2) or (9.4) we consider the constant equilibrium state

$$(u(t,x),\ w(t,x)) \equiv (\bar{u}, \bar{w})$$

satisfying the boundary conditions (9.1) and $f(\bar{u}, \bar{w}) = 0$. Such a pair will be called a homogeneous steady state. Due to the boundary conditions we necessarily find $\bar{w} = 0$, that is, we will be dealing with an equilibrium where the densities of right and left oriented particles are equal and the total density takes some certain fixed value $\bar{u} > 0$.

At this state, the derivative $F_u := \partial_u f(\bar{u}, 0)$ and any higher derivative with respect to u necessarily vanish by (9.7). For the linearization of the equations around the homogeneous steady state we thus only need to consider the derivative

$$F_w := \partial_w f(\bar{u}, 0)$$

with respect to w.

The linearization of the system (9.2) around this steady state reads

$$\partial_t \tilde{u} + \partial_x \tilde{w} = 0 \tag{10.1a}$$

$$\partial_t \tilde{w} + \partial_x \tilde{u} = \varepsilon \partial_{xx} \tilde{w} + F_w \tilde{w}. \tag{10.1b}$$

whereas system (9.4) has the following linearization:

$$\partial_t \tilde{u} + \partial_x \tilde{w} = \varepsilon \partial_{xx} \tilde{u} \tag{10.2a}$$
$$\partial_t \tilde{w} + \partial_x \tilde{u} = \varepsilon \partial_{xx} \tilde{w} + F_w \tilde{w}. \tag{10.2b}$$

Considering perturbations of the form

$$\tilde{u} = a_q \exp[\sigma_q t] \exp[\imath q x] \tag{10.3a}$$
$$\tilde{w} = b_q \exp[\sigma_q t] \exp[\imath q x] \tag{10.3b}$$

the linearized systems lead to the algebraic equations

$$\sigma a + \imath q b = 0 \tag{10.4a}$$
$$\sigma b + \imath q a = -\varepsilon q^2 b + F_w b \tag{10.4b}$$

or

$$\sigma a + \imath q b = -\varepsilon q^2 a \tag{10.5a}$$
$$\sigma b + \imath q a = -\varepsilon q^2 b + F_w b, \tag{10.5b}$$

for the respective models (9.2) and (9.4).

We only explicitely investigate linear stability of the designated steady state for alignment terms satisfying $F_w \geq 0$ – that is, the bistable ones. In fact, if the derivative F_w is negative then the diffusion and the nonlinearity tend to drive any sufficiently small perturbation to zero, and we necessarily obtain linear stability. We immediately conclude that the tristable alignment term leads to the homogeneous steady state being unconditionally linearly stable.

Thus the case of F_w being non-negative is the interesting one since here alignment and diffusion are in competition.

10.2 Linear stability analysis for model (9.2)

We start with analyzing the system (10.4a), (10.4b) and find that we have to distinguish two cases:

Case 1: $\sigma = 0$. From (10.4a) find

$$qb = 0$$

whereas (10.4b) yields

$$qa = 0 \qquad \text{and} \qquad \varepsilon q^2 b = F_w b.$$

That allows only the situations

$$a = b = 0 \qquad \text{(no perturbation at all)}$$

or

$$q = b = 0$$

which corresponds to a homogeneous displacement of the total density level to a new steady state $\bar{w} = 0,\ \bar{u} + a$.

This observation reflects the obvious ambiguity of the chosen steady state. It should be clear from physical considerations that adding or deducting a certain amount of (evenly oriented) particles will only lead to a new steady state the system will not evolve away from − at least if the addition or deduction is done homogeneously. The important information we obtain from this case is that a homogeneous change of the total density u without alteration of the zero polarization is the only possible perturbation the system will neither counteract nor enhance.

Case 2: $\sigma \neq 0$. In that case (10.4a) yields

$$a = -\frac{\imath q b}{\sigma}$$

which may be plugged into (10.4b) to find

$$\sigma b + \frac{q^2 b}{\sigma} + \left(\varepsilon q^2 - F_w\right) b = 0. \tag{10.6}$$

We now have to consider the following subcases:

Subcase 2a) $b = 0$. This in turn leads to

$$a = -\frac{\imath q \cdot 0}{\sigma} = 0$$

and we obtain no perturbation at all.

Subcase 2b) $b \neq 0$. Then we can divide (10.6) by b to find a quadratic equation for the growth rate σ:

$$\sigma^2 + \left(\varepsilon q^2 - F_w\right)\sigma + q^2 = 0$$

having the solutions

$$\sigma_\pm = \frac{1}{2}\left(\left(F_w - \varepsilon q^2\right) \pm \sqrt{(\varepsilon q^2 - F_w)^2 - 4q^2}\right). \tag{10.7}$$

For these solutions we observe different behaviors depending on the perturbing wave number q.

I. Purely imaginary roots − indicating oscillations around the underlying steady state − are found for precisely one nonzero wavelength:

$$q^2 = \frac{F_w}{\varepsilon}, \quad \Longrightarrow \quad \sigma_\pm = \pm\imath\frac{F_w}{\varepsilon}.$$

II. Purely real solutions are observed if the discriminant

$$D \equiv \left(\varepsilon q^2 - F_w\right)^2 - 4q^2$$

is positive. We compute the zeros of D:

$$\begin{aligned} 0 &= \left(\varepsilon q^2 - F_w\right)^2 - 4q^2 \\ &= q^4 - \frac{2}{\varepsilon^2}(\varepsilon F_w - 2)q^2 + \frac{F_w^2}{\varepsilon^2} \end{aligned}$$

and find

$$\begin{aligned} q_\pm^2 &= \frac{1}{\varepsilon}\left(\left(F_w - \frac{2}{\varepsilon}\right) \pm \frac{1}{\varepsilon}\sqrt{F_w^2 - \frac{4F_w}{\varepsilon} + \frac{4}{\varepsilon^2} - F_w}\right) \\ &= \frac{1}{\varepsilon}\left(\left(F_w - \frac{2}{\varepsilon}\right) \pm 2\sqrt{\frac{\frac{1}{\varepsilon^2} - F_w}{\varepsilon}}\right), \end{aligned}$$

and the respective wave numbers are

$$q_{\pm,1} = \pm\sqrt{\frac{2\sqrt{1 + F_w\varepsilon} + \varepsilon F_w + 2}{\varepsilon^2}} \in \mathbb{R} \tag{10.8}$$

$$q_{\pm,2} = \pm\sqrt{\frac{-2\sqrt{1 + F_w\varepsilon} + \varepsilon F_w + 2}{\varepsilon^2}} \in \mathbb{R}. \tag{10.9}$$

The roots $\sigma_\pm$ are not real if and only if

$$q_{+,1} < |q| < q_{+,2}. \tag{10.10}$$

III. We finally check the sign of the real part $\operatorname{Re}\sigma$ of the growth rate which will tell us the actual stability behavior. We already observed that only for the wave numbers

$$q^2 = \frac{F_w}{\varepsilon} \quad \text{and} \quad q = 0$$

the roots of (10.6) are purely imaginary. We easily see that $\operatorname{Re}\sigma > 0$ if and only if $q^2 < \frac{F_w}{\varepsilon}$. We further note that the critical wave number

$$q_{crit} = \sqrt{\frac{F_w}{\varepsilon}}$$

lies in the region of oscillating perturbations, that is

$$q_{+,1} \le q_{crit} \le q_{+,2} \tag{10.11}$$

with equality being only possible in the degenerate case $F_w\varepsilon = 0$ which corresponds to either vanishing diffusion or (at least to first order) vanishing nonlinearity.

Remark 10.1. *If the velocity v of the particles is different from one the condition for the real part of σ is not affected at all as v only enters the discriminant. In place of (10.6) we obtain*

$$\sigma b + q^2 v^2 \frac{b}{\sigma} + (\varepsilon q^2 - F_w)b = 0$$

which in case $b \neq 0$ has the solutions

$$\sigma_{\pm} = \frac{1}{2}\left(F_w - \varepsilon q^2 \pm \sqrt{\left(F_w - \varepsilon q^2\right)^2 - 4q^2v^2}\right). \tag{10.12}$$

The imaginary part of σ now becomes nonzero between the wave numbers

$$q_1 = \frac{1}{\varepsilon}\sqrt{-2v\sqrt{F_w\varepsilon + v^2} + \varepsilon F_w + 2v^2} \tag{10.13}$$

and

$$q_2 = \frac{1}{\varepsilon}\sqrt{2v\sqrt{F_w\varepsilon + v^2} + \varepsilon F_w + 2v^2}. \tag{10.14}$$

Again, both of these wave numbers are real and strictly positive whenever none of the parameters F_w, ε, and v does vanish. We note that the range of wave numbers resulting in genuinely complex growth coefficients σ increases with v for any given pair of ε and F_w. In figure 10.1 we depicted the values of the square roots depending on v and $a := \varepsilon F_w$.

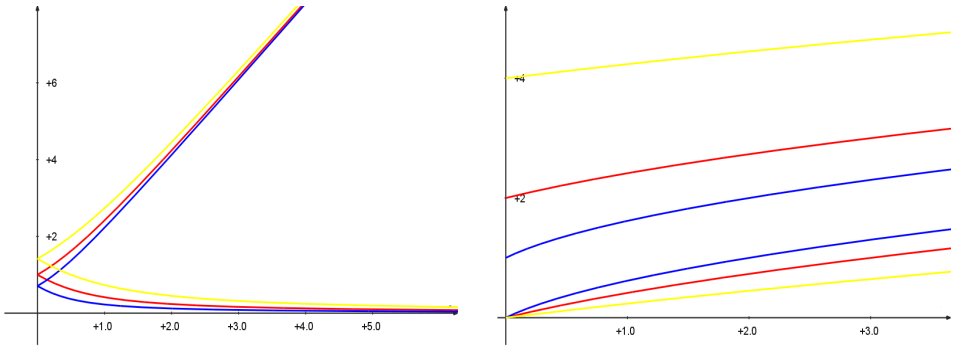

Figure 10.1: Scaled critical wave numbers $\varepsilon q_{1/2}$ depending on the particle velocity v (*right*) for fixed $a = 0.5$ (*blue*), $a = 1$ (*red*), and $a = 2$ (*yellow*), and depending on the parameter $a = \varepsilon F_w$ (*right*) for fixed $v = 0.5$ (*blue*), $v = 1$ (*red*), and $v = 2$ (*yellow*).

Using the boundary conditions we find that actually only a discrete set of wave numbers has to be considered. Besides the trivial perturbation

$$q = 0, \qquad b = 0, \qquad a \in [-\bar{u}, \infty)$$

that pushes the given steady state to a qualitatively equivalent one with a different total number of particles only perturbations with wave numbers

$$q_k = \frac{k\pi}{L} \qquad \text{for } k \in \mathbb{N}$$

are allowed. The interesting one is the smallest of these numbers, namely $q_1 = \frac{\pi}{L}$ corresponding to a wavelength of $2L$.

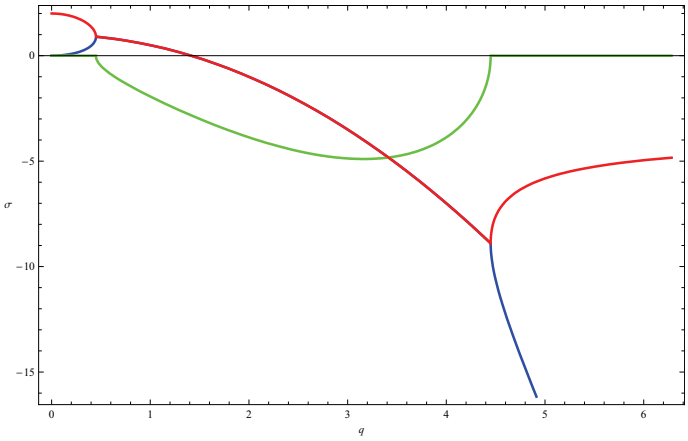

Figure 10.2: Growth rate σ plotted versus wave number q for $F_w = 1$, $\varepsilon = 0.5$.*red*: $\operatorname{Re}\sigma_+$, *blue*: $\operatorname{Re}\sigma_-$, *green*: $\operatorname{Im}\sigma_- = -\operatorname{Im}\sigma_+$.

If this minimal wave number lies in the region of stability, i.e. if

$$\frac{\pi}{L} > \sqrt{\frac{F_w}{\varepsilon}}$$

then all sufficiently small, non-homogeneous perturbations are predicted to decay by the linear stability analysis.

In figure 10.2, the dependence of the roots $\sigma_\pm$ on the wave number q is shown for fixed values of F_w and ε. Obviously, the real part of σ_+ is decreasing for $q \in [0, q_{crit}]$ from which we infer that whenever we have $q_1 \leq q_{crit}$ this is automatically the most unstable mode in the sense that $\operatorname{Re}\sigma_+(q_1) > \operatorname{Re}\sigma_+(q_k)$ for any integer $k \geq 2$.

We summarize our findings in the following proposition.

Proposition 10.2. *For the system (9.2) in $(0, L) \times (0, \infty)$ with boundary conditions*

$$w(0, t) = 0 = w(L, t) \ \forall t \geq 0$$

let us assume $\varepsilon > 0$ and condition (9.7).

(*i*) *Then the steady state*

$$w \equiv 0, \qquad u \equiv \bar{u} \geq 0$$

is linearly stable against perturbations with the same wave number for u and w if and only if either

(*a*)

$$F_w := \partial_w f(\bar{u}, 0) < 0$$

or

(*b*) $F_w \geq 0$ *and*

$$q_1 = \frac{\pi}{L} > \sqrt{\frac{F_w}{\varepsilon}} = q_{crit}$$

.

(*ii*) *If there are multiple unstable wave numbers $q_k = \frac{k\pi}{L}$ then always the minimal one q_1 exhibits the fastest growth. In particular, no mode selection can be expected.*

10.3 Linear stability analysis for model (9.4)

We now turn our attention to the system (9.4) and its linearization (10.5) which we rewrite to

$$\begin{aligned}(\sigma + \varepsilon q^2)a + \imath q b &= 0 && \text{(10.15a)}\\ (\sigma + \varepsilon q^2)b + \imath q a &= F_w b. && \text{(10.15b)}\end{aligned}$$

Before starting the exact calculations we remark that for the same reasons as above we only need to consider wave numbers $q_k = \frac{k\pi}{L}$ for $k \in \mathbb{N}_0$ and can thus concentrate on non-negative values for q. We now consider three cases.

Case 1: $q = 0$. This corresponds to a homogeneous perturbation and by the boundary conditions implies $b = 0$. The only remaining condition is now

$$\sigma a = 0$$

which allows arbitrary homogeneous perturbations a of the total density u with $\sigma = 0$ or no perturbations at all ($a = b = 0$) if σ shall be different from zero.

Case 2: $q \neq 0$ and $\sigma + \varepsilon q^2 = 0$. These conditions directly imply $\sigma < 0$ and from (10.15a) we readily infer $b = 0$. Plugging this into (10.15b) we also obtain $a = 0$.

Case 3: $q \neq 0$ and $\sigma + \varepsilon q^2 \neq 0$. This is now the truly interesting case where we can plug

$$a = -\frac{\imath q b}{\sigma + \varepsilon q^2} \tag{10.16}$$

obtained from (10.15a) into (10.15b) to find

$$\left(\sigma + \frac{q^2}{\sigma + \varepsilon q^2} + \varepsilon q^2 - F_w\right) b = 0.$$

In case $b = 0$, (10.16) immediately yields $a = 0$ and there is no perturbation at all. We thus may assume $b \neq 0$ and find the following quadratic equation for σ

$$0 \;=\; \sigma^2 + (2\varepsilon q^2 - F_w)\sigma + q^2\left(1 + \varepsilon(\varepsilon q^2 - F_w)\right)$$

having the solutions

$$\begin{aligned}\sigma_\pm &= \frac{1}{2}\left(F_w - 2\varepsilon q^2 \pm \sqrt{F_w^2 - 4F_w\varepsilon q^2 + 4\varepsilon^2 q^4 - 4(q^2 - \varepsilon^2 q^4 + \varepsilon q^2 F_w)}\right)\\ &= \frac{1}{2}\left(F_w - 2\varepsilon q^2 \pm \sqrt{F_w^2 - 4q^2}\right).\end{aligned} \tag{10.17}$$

For these roots we make the following observations:

(a) Real roots exist if $F_w^2 \geq 4q^2$ which is equivalent to

$$q \leq \frac{|F_w|}{2}.$$

(b) The real part of σ_+ is positive if one of the following is fulfilled

- $F_w > 2\varepsilon q^2$. Then the root

$$\sigma_+ = F_w - 2\varepsilon q^2 + \sqrt{F_w^2 - 4q^2} \geq F_w - 2\varepsilon q^2$$

  is clearly positive.

- $F_w \leq 2\varepsilon q^2$ and

$$F_w - 2\varepsilon q^2 + \sqrt{F_w^2 - 4q^2} > 0.$$

  In that case, the radicand

$$D = F_w^2 - 4q^2$$

  needs to be positive to ensure that the root $\sqrt{D}$ can contribute to the real part. This case reduces to

$$(2\varepsilon q^2 - F_w)^2 < F_w^2 - 4q^2.$$

  Equality holds if either $q = 0$ or

$$q = \frac{\sqrt{\varepsilon F_w - 1}}{\varepsilon}.$$

  We now easily find out that σ_+ is positive if

$$q < \frac{\sqrt{\varepsilon F_w - 1}}{\varepsilon}$$

  where we already used that only positive wave numbers are of interest to us.

Together we find that $\operatorname{Re}\sigma_+$ is positive if and only if

$$q < \max\{q_l, q_u\} = \max\left\{\sqrt{\frac{F_w}{2\varepsilon}}, \frac{\operatorname{Re}\sqrt{\varepsilon F_w - 1}}{\varepsilon}\right\} \tag{10.18}$$

where

$$q_l \left\{ \begin{array}{c} < \\ > \end{array} \right\} q_u \quad \Longleftrightarrow \quad \varepsilon F_w \left\{ \begin{array}{c} > \\ < \end{array} \right\} 2. \tag{10.19}$$

In fact, for $\varepsilon F_w = 2$ we have

$$\sqrt{\frac{F_w}{2\varepsilon}} = \frac{\sqrt{\varepsilon F_w - 1}}{\varepsilon} = \frac{1}{\varepsilon} = \frac{F_w}{2}. \tag{10.20}$$

Remark 10.3. *The effect of nontrivial velocities $v \neq 1$ is similar to that in system (9.2). The linearized equations in case*

$$q \neq 0 \neq \sigma + \varepsilon q^2 \quad \textit{and} \quad (a, b) \neq (0, 0)$$

now yield the equation

$$0 = \sigma^2 + (2\varepsilon q^2 - F_w)\sigma + q^2\left(v^2 + \varepsilon(\varepsilon q^2 - F_w)\right)$$

having the solutions

$$\sigma_\pm = \frac{1}{2}\left(F_w - 2\varepsilon q^2 \pm \sqrt{F_w^2 - 4q^2v^2}\right). \tag{10.21}$$

For the question of linear stability we only have to consider the case $F_w^2 > 4q^2v^2$ where the discriminant can affect the sign of the real part of σ_+. This is only of interest if in addition $F_w < 2\varepsilon q^2$, since otherwise this root has always a positive real part. We find

$$(2\varepsilon q^2 - F_w)^2 < F_w^2 - 4v^2q^2$$

from which we deduce

$$q < \frac{\sqrt{\varepsilon F_w - v^2}}{\varepsilon}. \tag{10.22}$$

Note that in the range of parameters under consideration the right hand side is real. We regain as stability condition

$$q < \max\{q_l,\ q_u\} \tag{10.23}$$

where

$$q_l = \sqrt{\frac{F_w}{2\varepsilon}}$$

is the same as before but now q_u is determined by (10.22). The transition between the ranges of validity of q_l and q_u now lies at $\varepsilon F_w = 2v^2$.

We finally note that in any case $\operatorname{Re}\sigma_+(q)$ attains its maximum $F_w + \sqrt{F_w^2}$ at $q = 0$ and that this maximum is only positive if F_w is. In particular, linear instability of the homogeneous steady state $(\bar{u}, 0)$ on finite domains is only possible for $F_w > 0$.

We conclude that again, only the bistable cases of our standard alignment terms can produce linear instability. Since, in addition, $\operatorname{Re}\sigma_+$ decreases with increasing q we conclude that the smallest wave number is the least stable one. We finally note that now the critical wave number not necessarily lies in the region where $\operatorname{Im}\sigma$ is different from zero but only in case $\varepsilon F_w < 2$.

The analogue of proposition 10.2 is

Proposition 10.4. *For the system (9.4) in $(0, L) \times (0, \infty)$ with boundary conditions*

$$w(0, t) = 0 = w(L, t)\ \forall t \geq 0$$

assume $\varepsilon > 0$ and (9.7).

(i) The steady state

$$w \equiv 0 \qquad u \equiv \bar{u} \geq 0$$

is linearly stable against perturbations with the same modes for u and w if and only if either

(a)

$$F_w := \partial_w f(\bar{u}, 0) < 0$$

or

(b) $F_w \geq 0$ *and*

$$q_1 = \frac{\pi}{L} > \left\{ \begin{array}{c} \frac{\sqrt{\varepsilon F_w - 1}}{\varepsilon} \\ \sqrt{\frac{F_w}{2\varepsilon}} \end{array} \right\} \quad \textit{if} \quad \varepsilon F_w \left\{ \begin{array}{c} > \\ < \end{array} \right\} 2 \tag{10.24}$$

(ii) If there are multiple unstable wave numbers $q_k = \frac{k\pi}{L}$ *then always the minimal one* q_1 *exhibits the fastest growth. In particular, no mode selection can be expected.*

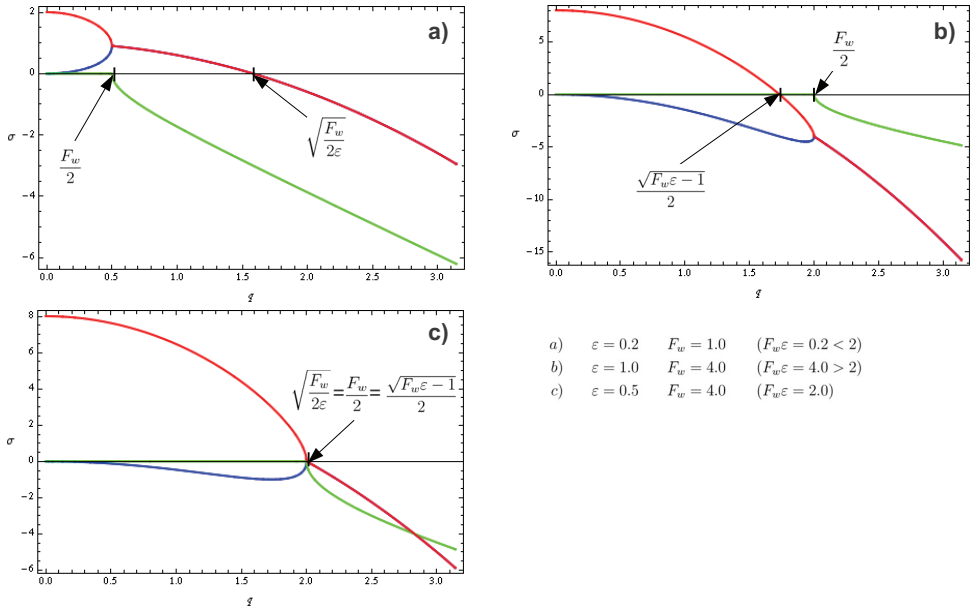

Figure 10.3: Growth rate σ according to the linearization of system (9.4) plotted versus wave number q. *red*: $\operatorname{Re}\sigma_+$, *Blue*: $\operatorname{Re}\sigma_-$, *green*: $\operatorname{Im}\sigma_- = -\operatorname{Im}\sigma_+$.

10.4 Comparison between the models

We want to conclude the previous two sections by pointing out some commonalities and differences of the considered models. In figure 10.4, the critical wave numbers for both models are plotted against F_w for an exemplary, fixed ε and vice versa.

We start with the common features of both models:

- In both cases, the homogeneous steady state $u = \bar{u}$, $w = 0$ is linearly stable whenever

  $$F_w \equiv \partial_w f(\bar{u}, 0) < 0.$$

  This does not come as a surprise as the diffusion term together with the homogeneous boundary conditions for w always tends to drive any perturbation to zero.

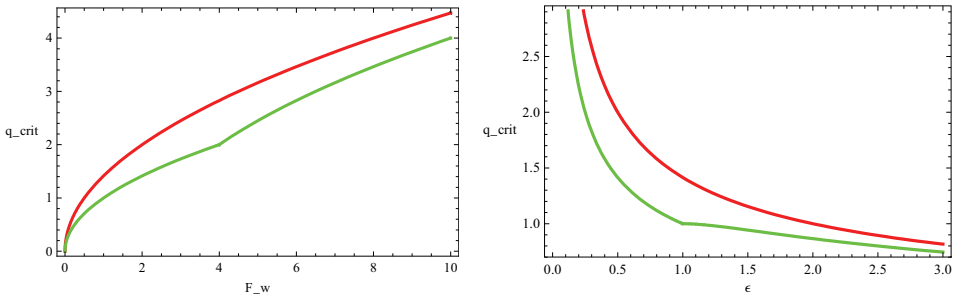

Figure 10.4: *left*: Critical wave number q_{crit} depending on F_w at $\varepsilon = 0.5$, *right*: q_{crit} depending on ε at $F_w = 2.0$. *red:* for model (9.2), *green:* for model (9.4)

If now $F_w < 0$ then also the alignment term will tend to dealign the particles for sufficiently small values of $|w|$ so that any small perturbation will become extinct.

- The largest real part of the growth rate σ always decreases with increasing wave number $q \geq 0$. This results in the smallest allowed wave number to be the least stable mode. In particular, any unstable perturbation containing this mode in its FOURIER expansion, will show strongest growth of this mode and finally end up with maximal wavelength.
- For any set of parameters $F_w > 0,\ \varepsilon > 0$, we obtain purely real growth rates if q is sufficiently small.

Possibly more interesting are the differences between the models:

- In case of model (9.2) we find a vanishing imaginary part of σ also if the wave number q is sufficiently large, whereas for model (9.4) the imaginary part grows to infinity as q does.
- For all $F_w > 0,\ \varepsilon > 0$, the critical wave number q_{crit} is larger for model (9.2) than for model (9.4). This is easily seen by direct computation:

Case 1: $\varepsilon F_w \leq 2$.

$$\sqrt{\frac{F_w}{\varepsilon}} > \sqrt{\frac{F_w}{2\varepsilon}}.$$

Case 2: $\varepsilon F_w > 2$.

$$\sqrt{\frac{F_w}{\varepsilon}} = \sqrt{\frac{\varepsilon F_w}{\varepsilon^2}} > \frac{\sqrt{\varepsilon F_w - 1}}{\varepsilon}.$$

However, we find that the limiting behavior for strong alignment $F_w \to \infty$ at fixed $\varepsilon > 0$ is the same:

$$\lim_{F_w \to \infty} \left(\sqrt{\frac{F_w}{\varepsilon}} - \frac{\sqrt{\varepsilon F_w - 1}}{\varepsilon} \right) = \frac{1}{\sqrt{\varepsilon}} \lim_{F_w \to \infty} \left(\sqrt{F_w} - \sqrt{F_w - \frac{1}{\varepsilon}} \right).$$

More precisely, the critical wave number always grows as

$$q_{crit} \sim \sqrt{\frac{F_w}{\varepsilon}}$$

for large F_w. Similarly, letting the diffusion coefficient grow to infinity yields

$$\lim_{\varepsilon\to\infty} \frac{\sqrt{\frac{F_w}{\varepsilon}}}{\frac{\sqrt{\varepsilon F_w - 1}}{\varepsilon}} = \lim_{\varepsilon\to\infty} \sqrt{\frac{\varepsilon F_w}{\varepsilon F_w - 1}} = 0.$$

- For model (9.2) the growth rate $\sigma(q_{crit})$ at the critical wave number always has a non-vanishing imaginary part. In case of model (9.4) this is only true for $\varepsilon F_w < 2$.

10.5 Different modes for u and w

The stability analysis of the previous sections assumes that the particle density u and the polarization w are perturbed by the same mode q. However, the perturbations of u and w can in general be different from one another. We will thus consider the following type of perturbations in place of (10.3):

$$\begin{aligned} \tilde{u} &= a_k \exp[\sigma_{kq} t] \exp[\imath k x] \\ \tilde{w} &= b_q \exp[\sigma_{kq} t] \exp[\imath q x] \end{aligned} \tag{10.25}$$

with different wave numbers k and q for u and w, respectively.

10.5.1 Stability for model (9.2)

We now have to investigate the following system of equations:

$$\sigma a + \imath q b = 0 \tag{10.26a}$$
$$\sigma b + \imath k a = -\varepsilon q^2 b + F_w b, \tag{10.26b}$$

for which we distinguish the following cases.

1. $\sigma = 0$. This case leads to $qb = 0$ which can be achieved by

   a) $q = 0$. Plugged into the second equation this leads to $F_w b = 0$ and $ak = 0$. The first of these conditions leads to $b = 0$ and the second one tells us that the perturbation of u is either identically zero ($a = 0$) or homogeneous ($k = 0$).

   b) $b = 0$. This again leads to $ak = 0$ which allows at most homogeneous perturbations of u.

   As before, we conclude that the only perturbation the system does not react to consists of a homogeneous change in the total density without altering the polarization at all.

2. $\sigma \neq 0$. This allows us to rewrite the first equation to

   $$a = -\frac{\imath q b}{\sigma}$$

   which in the second equation yields

   $$\sigma^2 + (\varepsilon q^2 - F_w)\sigma + qk = 0.$$

This has the roots

$$\sigma_{\pm} = \frac{1}{2}\left(F_w - \varepsilon q^2 \pm \sqrt{\left(\varepsilon q^2 - F_w\right)^2 - 4kq}\right) \tag{10.27}$$

which have both negative real part if and only if $F_w < \varepsilon q^2$. We thus recover the stability criterion from section 10.2.

We conclude that for model (9.2) the linear stability analysis does not change if the perturbations of u and w have different wave numbers.

10.5.2 Stability for model (9.4)

The respective linearized system in terms of the parameters of ansatz (10.25) now reads

$$\sigma a + \imath q b = -\varepsilon k^2 a \tag{10.28a}$$
$$\sigma b + \imath k a = -\varepsilon q^2 b + F_w b. \tag{10.28b}$$

Again, the usual distinction of cases is made:

1. $\sigma = 0$. This immediately leads to $qb = 0$ and $k^2 a = 0$. From the latter we conclude that only homogeneous perturbations of u are possible in that case whereas the first condition plugged into the second equation necessarily leads to $b = 0$.

2. $\sigma \neq 0$. We now can rewrite (10.28a) to

$$a = -\frac{\imath q b}{\sigma + \varepsilon k^2}$$

which can be put into (10.28b) to find

$$\sigma^2 + \left(\varepsilon\left(k^2 + q^2\right) - F_w\right)\sigma + kq + \varepsilon k^2\left(\varepsilon q^2 - F_w\right) = 0.$$

The roots of this equation can be written in the form

$$\sigma_{\pm} = \frac{1}{2}\left(F_w - \varepsilon(k^2 + q^2) \pm \sqrt{F_w^2 + \varepsilon(k^2 - q^2)(2F_w + \varepsilon) - 4kq}\right). \tag{10.29}$$

The upper root σ_+ has positive real part if

a) $F_w > \varepsilon(k^2 + q^2)$ which corresponds to the condition $F_w > 2\varepsilon q^2$ from section 10.3. If we allow for homogeneous perturbations of the particle density u (i.e., $k = 0$), the condition for linear stability reduces to

$$q_1 = \frac{\pi}{L} > \sqrt{\frac{F_w}{\varepsilon}} \tag{10.30}$$

which is the same as for model (9.2). For perturbations of u without homogeneous contribution, the minimal wave number is

$$k_1 = \frac{\pi}{L}$$

and the stability condition is the same as in section 10.3:

$$\frac{\pi}{L} > \sqrt{\frac{F_w}{2\varepsilon}}. \tag{10.31}$$

b) $F_w < \varepsilon(k^2 + q^2)$ and at the same time

$$kq + \varepsilon k^2 \left(\varepsilon q^2 - F_w\right) < 0.$$

Since k, q, and ε are non-negative, the latter can only be true if $\varepsilon q^2 - F_w$ is less than zero. This in turn is a contradiction to the first requirement and we can thus exclude this possibility.

We therefore find as stability criterion for this system again

$$F_w < 2\varepsilon \frac{\pi^2}{L^2},$$

but now for arbitrary values of the product $F_w\varepsilon$.

We can therefore merge propositions 10.2 and 10.4 into

Proposition 10.5. *For either system, (9.2) or (9.4), posed in* $(0, L) \times (0, \infty)$ *with boundary conditions*

$$w(0, t) = 0 = w(L, t) \ \forall t \geq 0$$

assume $\varepsilon > 0$ *and (9.7).*

(i) The steady state

$$w \equiv 0 \qquad u \equiv \bar{u} \geq 0 \tag{10.32}$$

is linearly stable against arbitrary small perturbations if and only if either

(a)

$$F_w := \partial_w f(\bar{u}, 0) < 0$$

or

(b) $F_w \geq 0$ *and*

$$q_1 = \frac{\pi}{L} > \sqrt{\frac{F_w}{\varepsilon}} \cdot \begin{cases} 1 & \text{in case of (9.2)} \\ \frac{1}{\sqrt{2}} & \text{in case of (9.4)} \end{cases}. \tag{10.33}$$

(ii) If there are multiple unstable wave numbers $q_k = \frac{k\pi}{L}$ *then always the minimal one* q_1 *exhibits the fastest growth. In particular, no mode selection can be expected.*

This proposition gives rise to the question whether we can find a single stability criterion for both systems and maybe even for their interpolates. We will clarify that in the following subsection.

10.5.3 Results for intermediate models

To close this chapter we are now going to discuss the interpolates (9.5) of systems (9.2) and (9.4). Plugging the FOURIER ansatz into these models we obtain

$$\sigma a + \imath q b = -\theta\varepsilon k^2 a \tag{10.34a}$$

$$\sigma b + \imath k a = -\varepsilon q^2 b + F_w b. \tag{10.34b}$$

The subsequent calculations are very much the same as for system (9.4) with the small difference that at every occurance k^2 has to be replaced by θk^2. We thus find the stability condition to be

$$F_w < \varepsilon(\theta k^2 - q^2)$$

and excluding changes in the total particle number this yields linear stability if

$$\frac{\pi}{L} > \sqrt{\frac{F_w}{(1+\theta)\varepsilon}}. \tag{10.35}$$

Denoting the diffusion coefficient in the equations for u and w by ε_u and ε_w, respectively, we can rewrite this condition to

$$\frac{\pi}{L} > \sqrt{\frac{F_w}{\varepsilon_u + \varepsilon_w}}. \tag{10.36}$$

Chapter 11

Nonlinear Stability Analysis

We now ask for nonlinear stability of the homogeneous steady state

$$(u = \bar{u},\ w = 0)$$

in dependence on the parameters ε, F_w, and L. The conditions to be found will be compared with those from the linear stability analysis. Throughout this section we assume that we only deal with classical solutions of the respective models. In particular, we assume w to be twice differentiable with respect to the spatial variable x, and we assume u to be once or twice differentiable with respect to x for systems (9.2) or (9.4), respectively.

11.1 Nonlinear stability for model (9.2)

An appropriate energy functional to investigate model (9.2) is given by the plain L_2-energy

$$E(t) = \frac{1}{2}\int_0^L w^2 + (u-\bar{u})^2 dx. \tag{11.1}$$

Multiplying the second equation of (9.2) by w, integrating over $(0, L)$, and noting that

$$\partial_x u = \partial_x(u-\bar{u}) \qquad \text{and} \qquad \partial_t u = \partial_t(u-\bar{u})$$

we find

$$\frac{1}{2}\frac{d}{dt}\int_0^L w^2 dx + \int_0^L w\partial_x u dx = \varepsilon\int_0^L w\partial_{xx} w dx + \int_0^L w\ f(w) dx \tag{11.2}$$

The second integral on the left hand side of (11.2) can be integrated by parts to obtain

$$\int_0^L w\partial_x u dx = -\int_0^L (u-\bar{u})\partial_x w dx = \int_0^L (u-\bar{u})\partial_t(u-\bar{u}) dx = \frac{1}{2}\frac{d}{dt}\int_0^L (u-\bar{u})^2 dx \tag{11.3}$$

where in the second step we used the first equation of (9.2).

The first integral on the right hand side of (11.2) is integrated by parts as well and

we find:

$$\begin{aligned}\frac{d}{dt}E(t) = \frac{1}{2}\frac{d}{dt}\int_0^L w^2 + (u-\bar{u})^2 dx \; &= -\varepsilon\int_0^L (\partial_x w)^2 dx + \int_0^L w f(w) dx \\ &\leq -\frac{\varepsilon}{C_1}\int_0^L w^2 dx + \int_0^L w f(w) dx\end{aligned} \tag{11.4}$$

where

$$C_1 = \frac{L^2}{\pi^2}$$

is the squared POINCARÉ constant for the domain $(0, L)$.

We consider now the particular alignment terms introduced in (9.9), (9.10), and (9.12).

1. **Bistable, sublinear:** $f(w) = \alpha w(1-w^2)$. For this type of f, (11.4) takes the form:

$$\begin{aligned}\frac{d}{dt}E(t) \; &\leq -\frac{\varepsilon\pi^2}{L^2}\int_0^L w^2 dx + \alpha\int_0^L w^2 dx - \alpha\int_0^L w^4 dx \\ &\leq \left(\alpha - \frac{\varepsilon\pi^2}{L^2}\right)\int_0^L w^2 dx.\end{aligned} \tag{11.5}$$

   The right hand side is not bigger than zero if and only if

$$\frac{\alpha}{\varepsilon} \leq \frac{\pi^2}{L^2} \tag{11.6}$$

   which is precisely the condition we found for linear stability in part (ii) of proposition 10.2. Since the POINCARÉ constant is optimal and arbitrary smooth perturbations are to be allowed we can conclude that for this particular type of alignment, linear and nonlinear stability coincide.

2. **Bistable, superlinear:** $f(w) = \alpha w(1 + \nu w^2 - (\nu+1)w^4)$. Now (11.4) becomes

$$\begin{aligned}\frac{d}{dt}E(t) \; &\leq -\frac{\varepsilon\pi^2}{L^2}\int_0^L w^2 dx + \alpha\int_0^L w^2 + \nu w^4 - (\nu+1)w^6 dx \\ &= \left(\alpha - \frac{\varepsilon\pi^2}{L^2}\right)\int_0^L w^2 dx + \alpha\nu\int_0^L w^4 dx - \alpha(\nu+1)\int_0^L w^6 dx.\end{aligned} \tag{11.7}$$

   We observe that the second term on the right hand side is now non-negative and dominates the third one for small absolute values of w. Thus for any perturbation w, no matter how small, we always find some

$$\alpha < \frac{\varepsilon\pi^2}{L^2}$$

   such that the right hand side is positive. Even more strikingly, if

$$\alpha = \frac{\varepsilon\pi^2}{L^2},$$

then the right hand side will be (strictly) positive for sufficiently small perturbations w not vanishing identically. We conclude that for superlinear alignment terms, nonlinear stability is genuinly stronger than linear stability.

3. **Tristable** $f(w) = \alpha w(1-w^2)(w^2-\lambda^2)$. Here we obtain

$$\begin{aligned} \frac{d}{dt}E(t) &\leq -\frac{\varepsilon\pi^2}{L2}\int_0^L w^2 dx + \alpha\int_0^L -\lambda^2 w^2 + (\lambda^2+1)w^4 - w^6 dx \\ &\leq -\left(\alpha\lambda^2 + \frac{\varepsilon\pi^2}{L^2}\right)\int_0^2 w^2 dx + \alpha\int_0^L w^4(\lambda^2+1+w^2)dx. \end{aligned} \tag{11.8}$$

In that case, the first term on the right hand side is always negative for all parameter settings and dominates the second, higher order term for sufficiently small values of w. That is, the right hand side is strictly negative for all sufficiently small perturbations w not vanishing identically, and we conclude that for this form of f we have unconditional nonlinear stability.

The difference between the sublinear and the superlinear bistable case can also be understood by a heuristic argumentation. In the sublinear case we have for small w:

$$|f(w)| \leq F_w|w| = \alpha|w| \tag{11.9}$$

such that for small perturbations the strongest tendency to align is present at $w = 0$, and precisely at that value the linear stability analysis operates. That explains why linear stability can imply nonlinear stability which investigates small neighborhoods of the steady state value. In contrast, for f being superlinear we have

$$|f(w)| > F_w|w| \tag{11.10}$$

for sufficiently small $|w| > 0$. Now the tendency to align increases as w deviates from zero, and this effect naturally cannot be captured by the linear stability analysis whereas the nonlinear exploration is sensitive to this superlinear growth.

11.2 Nonlinear stability for model (9.4)

To investigate nonlinear stability of the homogeneous steady state

$$(u = \bar{u},\ w = 0)$$

for (9.4) we will again employ the energy functional (11.1):

$$E(t) = \frac{1}{2}\int_0^L (u(x,t)-\bar{u})^2 + w(x,t)^2 dx.$$

Now we multiply the first equation of (9.4) by $(u-\bar{u})$ and the second equation by w, integrate over $(0, L)$ and add both equations up to:

$$\frac{d}{dt}E(t) + \int_0^L (u-\bar{u})\partial_x w + w\partial_x u dx = \varepsilon\int_0^L (u-\bar{u})\partial_{xx}u + w\partial_{xx}w dx + \int_0^L wf dx. \tag{11.11}$$

The integral on the left hand side vanishes due to the boundary conditions:

$$\int_0^L (u-\bar{u})\partial_x w + w\partial_x u dx = \int_0^L (u-\bar{u})\partial_x w - \partial_x w\ (u-\bar{u})dx + 0.$$

Next, we note that the reflecting boundary conditions also imply $\partial_x u$ to be zero at the boundary points so that we can integrate the first integral on the right hand side of (11.11) to obtain

$$\frac{d}{dt}E = -\varepsilon \int_0^L \left(\partial_x(u-\bar{u})\right)^2 + (\partial_x w)^2 dx + \int_0^L w f dx. \tag{11.12}$$

We end up with

$$\begin{aligned} \frac{d}{dt}E &\leq -\varepsilon \int_0^L \left(\partial_x(u-\bar{u})\right)^2 dx - \varepsilon \int_0^L (\partial_x w)^2 dx + \int_0^L w f dx \\ &\leq -\frac{\varepsilon\pi^2}{L^2}\int_0^L w^2 dx + \int_0^L w f dx. \end{aligned} \tag{11.13}$$

We have to take into account that there are possible perturbations of w that do not change u at all. Thus, we cannot expect the first integral in (11.13) to be strictly positive for arbitrary small perturbations. It follows that the nonlinear stability analysis for this model yields precisely the same results as for model (9.2).

We summarize the results in the following corollary.

Corollary 11.1. *For either system, (9.2) or (9.4), posed in $(0,L)\times(0,\infty)$ with boundary conditions*

$$w(0,t) = 0 = w(L,t)\ \forall t \geq 0$$

assume $\varepsilon > 0$ and (9.7).

(*i*) *If the nonlinearity f is bistable and sublinear in w (cf. (9.9)) then nonlinear and linear stability of the homogeneous steady state*

$$(w \equiv 0,\ u \equiv \bar{u})$$

coincide. More precisely, this state is linearly and nonlinearly stable if and only if

$$\frac{\alpha}{\varepsilon} < \frac{\pi^2}{L^2}.$$

(*ii*) *If the nonlinearity f is bistable and superlinear in w (cf. (9.10)) then nonlinear stability of the homogeneous steady state*

$$(w \equiv 0,\ u \equiv \bar{u})$$

implies its linear stability but the converse implication always fails.

(*iii*) *In case of the tristable alignment term ($\partial_w f(\bar{u},0) < 0$, cf. (9.12)), the homogeneous steady state*

$$(w \equiv 0,\ u \equiv \bar{u})$$

is always linearly and nonlinearly stable.

We should not forget to remark that, in fact, the first integral in (11.13) will become positive as we allow any perturbation of our homogeneous state to evolve in time. It may therefore be expected that we obtain an additional stabilizing contribution from this term which might induce stability even for larger alignment strengths than predicted by the corollary. We will discuss this effect when we investigate the stability behavior by simulations in section 15.2.

Chapter 12

Generalization to Alignment Terms Depending on the Total Particle Density

12.1 Basic assumptions on the alignment term

In section 9.2, we only considered the dependence of the alignment terms f on the polarization w for fixed values $\bar{u}$ of the total density. Moreover, we assumed that the zeros of f are besides $w = 0$ given by $w = \pm\bar{u}$.

We now want to consider also the u - dependence of the alignment term and allow for zeros $w = \pm\Lambda u$ with $\Lambda \neq 1$. The following properties for f shall always be assumed:

1. We require f to be continuous throughout its domain of interest

$$Q := \left\{(u, w) \in \mathbb{R}^2 \mid u \geq 0, w \in [-u, u]\right\}.$$

   In fact, we will most often consider such f that are continuously differentiable in the interior of Q and at least differentiable up to ∂Q.

2. To ensure that the states ($w = 0,\ u = const.$) are stationary we require

$$f(u, 0) = 0 \qquad \text{for each } \ u \geq 0. \tag{12.1}$$

3. For any $u \geq 0$ we assume the existence of at least one $w \in (0, u]$ satisfying

$$f(u, w) = f(u, -w) = 0. \tag{12.2}$$

4. To prevent the solutions of the purely hyperbolic system (without diffusion) from growing pointwise to infinity we further assume f to change its sign for large values of u (at fixed $\frac{w}{u}$) or at least to approach zero sufficiently fast as u grows to infinity. A physical explanation for this requirement is the following crowding effect. The higher the total density of particles in one place the harder it is to turn them around.

5. We finally assume f to be an odd function of w for any given value of u. This represents the symmetry of the model with respect to interchanging the roles of "left" and "right"

In the sequel we will encounter the following parameters

$$\begin{aligned} \alpha > 0 \quad &\ldots \quad \text{measures the strength of the alignment} \\ \Lambda \in (0,1] \quad &\ldots \quad \text{determines (outer) stable equilibria of } f \\ \lambda \in (0,\Lambda) \quad &\ldots \quad \text{determines possible additional equilibria (in the tristable case),} \end{aligned}$$

of which α and λ are already known from section 9.2. The parameters λ and Λ will typically satisfy $\lambda^2 \ll \Lambda^2 \approx 1$.

We present now some special examples of right hand sides.

1. **Hard cut off.** Here we consider such types of f for which w f becomes negative for large u. More precisely, we assume that there exists some $c > 0$ such that

$$wf(u,w) \leq 0 \qquad \text{for} \quad u^2 + w^2 \geq c^2.$$

(a) We start with an alignment term corresponding to the sublinear bistable case introduced in (9.9). We consider

$$f_{h,1}(u,w) := \alpha w \left(\Lambda^2 - \frac{w^2}{u^2}\right)\left(c^2 - (u^2+w^2)\right) \tag{12.3}$$

The case $\Lambda = 1$ corresponds to (9.9) where the stable equilibria of f are given for $w = \pm u$ − corresponding to all particles being oriented in the same direction.

(b) An alignment term corresponding to the bistable superlinear case (9.10) is

$$f_{h,2}(u,w) := \alpha w \left(\Lambda^2 + \nu\frac{w^2}{u^2} - (\nu+1)\frac{w^4}{\Lambda^2 u^4}\right)\left(c^2 - (u^2+w^2)\right). \tag{12.4}$$

As in section 9.2 we can alternatively consider

$$\tilde{f}_{h,2}(u,w) := \alpha w \left(\Lambda + \nu\frac{|w|}{u} - (\nu+1)\frac{w^2}{\Lambda u^2}\right)\left(c^2 - (u^2+w^2)\right). \tag{12.5}$$

Again, we recover (9.10) for $\Lambda = 1$. Recall that $\nu > 1$ is another parameter, typically being of the order of magnitude of 10.

(c) The tristable case (9.12) can be generalized to

$$f_{h,3}(u,w) := \alpha w \left(\Lambda^2 - \frac{w^2}{u^2}\right)\left(\frac{w^2}{u^2} - \lambda^2\right)\left(c^2 - (u^2+w^2)\right), \tag{12.6}$$

and a similar shape is reached by setting

$$\tilde{f}_{h,3}(u,w) := \alpha w \left(\Lambda - \frac{|w|}{u}\right)\left(\frac{|w|}{u} - \lambda\right)\left(c^2 - (u^2+w^2)\right). \tag{12.7}$$

2. **Soft decay.** We now consider $|f|$ decreasing to zero exponentially as u grows to infinity. This is done by replacing the term $(c^2-(u^2+w^2))$ by an exponential one. The rate of decline will be denoted by $\beta > 0$. We summarize the corresponding forms of f which correspond to the ones above.

   (a) The sublinear bistable alignment term now reads

$$f_{s,1}(u,w) := \alpha w \left(\Lambda^2 - \frac{w^2}{u^2}\right) \exp\left[-\beta^2 u^2\right] \tag{12.8}$$

   (b) The superlinear bistable version is

$$f_{s,2}(u,w) := \alpha w \left(\Lambda^2 + \nu\frac{w^2}{u^2} - (\nu+1)\frac{w^4}{\Lambda^2 u^4}\right) \exp\left[-\beta^2 u^2\right] \tag{12.9}$$

   or

$$\tilde{f}_{s,2}(u,w) := \alpha w \left(\Lambda + \nu\frac{|w|}{u} - (\nu+1)\frac{w^2}{\Lambda u^2}\right) \exp\left[-\beta^2 u^2\right] \tag{12.10}$$

   (c) And finally, the tristable case reads

$$f_{s,3}(u,w) := \alpha w \left(\Lambda^2 - \frac{w^2}{u^2}\right)\left(\frac{w^2}{u^2} - \lambda^2\right) \exp\left[-\beta^2 u^2\right] \tag{12.11}$$

   or

$$\tilde{f}_{s,3}(u,w) := \alpha w \left(\Lambda - \frac{|w|}{u}\right)\left(\frac{|w|}{u} - \lambda\right) \exp\left[-\beta^2 u^2\right]. \tag{12.12}$$

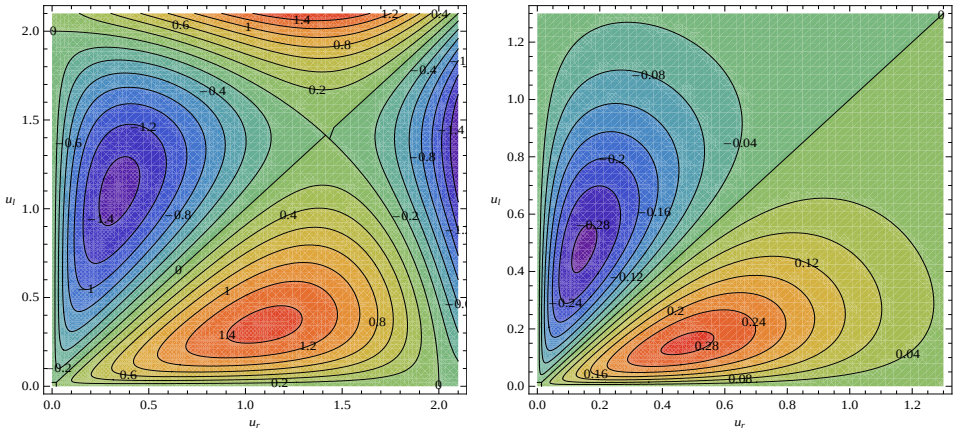

Figure 12.1: *Left*: $f_{h,1}$ with $\alpha = 0.5, \Lambda = 1, c = 2\sqrt{2}$. *Right*: $f_{s,1}$ with $\alpha = 2, \Lambda = 1, \beta^2 = 1$

The figures 12.1 - 12.3 exemplarily show the alignment strength f in dependence on its natural variables u_r and u_l rather than u and w. Note that the upper right quadrant in the u_r - u_l - plane coincides with Q. We further note that the sets $u = const.$ are the straight lines of slope -1 in the u_r - u_l - plane whereas the sets $w = const.u$ are the straight lines of positive slope passing through the origin.

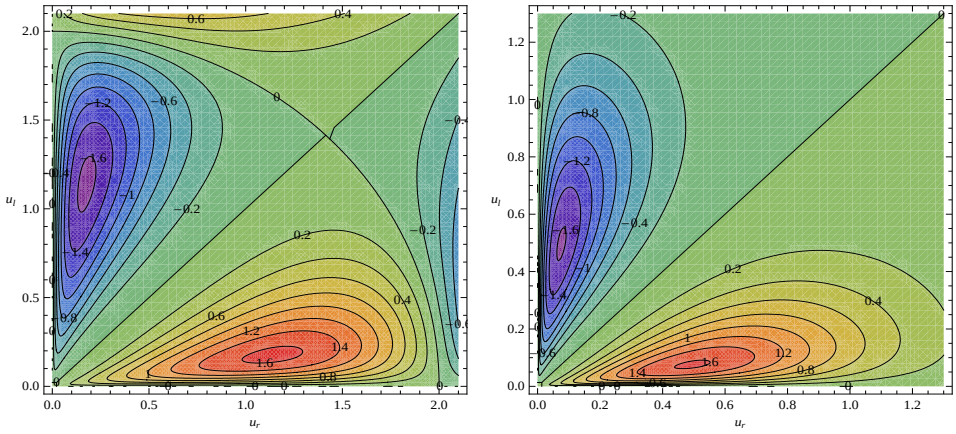

Figure 12.2: *Left*: $f_{h,2}$ with $\alpha = 0.1, \Lambda = 1, c = 2\sqrt{2}, \nu = 10$. *Right*: $f_{s,2}$ with $\alpha = 2, \Lambda = 1, \beta^2 = 1, \nu = 10$

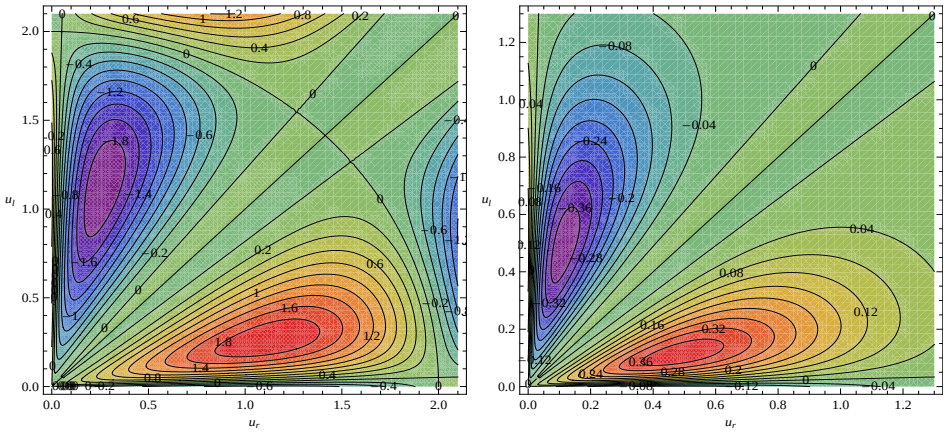

Figure 12.3: *Left*: $\tilde{f}_{h,3}$ with $\alpha = 2.5, \Lambda = 0.95, \lambda = 0.1, c = 2\sqrt{2}, \nu = 10$. *Right*: $\tilde{f}_{s,3}$ with $\alpha = 10, \Lambda = 0.95, \lambda = 0.1, \beta^2 = 1$

We finish this section pointing out that all of the above indeed satisfy the properties required in the beginning of this chapter and in section 9.2, in particular:

- $f = 0$ on $\{w = 0\} = \{u_r = u_l\}$,
- $f = 0$ on $\{w^2 = \Lambda^2 u^2\} = \left\{u_l = \frac{1 \pm \Lambda}{1 \mp \Lambda u_r}\right\}$, and
- in the tristable case we have additionally $f = 0$ on $\{w^2 = \lambda^2 u^2\} = \left\{u_l = \frac{1 \pm \lambda}{1 \mp \lambda u_r}\right\}$

12.2 Effects on linear stability

We immediately see that for the alignment terms introduced in section 12.1, the derivative $F_w = \partial_w f(\bar{u}, 0)$ strongly depends on the value of $\bar{u}$. We start with computing the partial derivatives of the above types of f with respect to u and w. To shorten the notation we introduce

$$C^2 := c^2 - (u^2 + w^2) \qquad \text{and} \qquad \mathcal{E} := \exp\left[-\beta^2 u^2\right]$$

and start with the sublinear bistable type:

$$\begin{aligned}
\partial_u f_{h,1} &= -2\alpha \frac{w}{u}\left(\Lambda^2 u^2 - (C^2 + u^2)\frac{w^2}{u^2}\right) \\
\partial_w f_{h,1} &= \alpha\left(\Lambda^2(C^2 - 2w^2) - (3C^2 - 2w^2)\frac{w^2}{u^2}\right) \\
\partial_u f_{s,1} &= -2\alpha \frac{w}{u}\left(\Lambda^2\beta^2 u^2 - (1 + \beta^2 u^2)\frac{w^2}{u^2}\right)\mathcal{E} \\
\partial_w f_{s,1} &= \alpha\left(\Lambda^2 - 3\frac{w^2}{u^2}\right)\mathcal{E}.
\end{aligned}$$

For the superlinear bistable terms we obtain:

$$\begin{aligned}
\partial_u f_{h,2} &= -2\alpha \frac{w}{u}\left(\Lambda^2 u^2 + \nu(c^2 - w^2)\frac{w^2}{u^2} - (\nu+1)(2c^2 - w^2)\frac{w^4}{\Lambda^2 u^4}\right) \\
\partial_w f_{h,2} &= \alpha\left(\Lambda^2(C^2 - 2w^2) + \nu(3C^2 - 2w^2)\frac{w^2}{u^2} - (\nu+1)(5C^2 - 2w^2)\frac{w^4}{\Lambda^2 u^4}\right) \\
\partial_u \tilde{f}_{h,2} &= -2\alpha \frac{w}{u}\left(\Lambda u^2 + \frac{\nu}{2}(C^2 + 2u^2)\frac{|w|}{u} - (\nu+1)(C^2 + u^2)\frac{w^2}{\Lambda u^2}\right) \\
\partial_w \tilde{f}_{h,2} &= \alpha\left(\Lambda(C^2 - 2w^2) + 2\nu(C^2 - w^2)\frac{|w|}{u} - (\nu+1)(3C^2 - 2w^2)\frac{w^2}{\Lambda u^2}\right)
\end{aligned}$$

and

$$\begin{aligned}
\partial_u f_{s,2} &= -2\alpha \frac{w}{u}\left(\Lambda^2\beta^2 u^2 + \nu(1 + u^2\beta^2)\frac{w^2}{u^2} - (\nu+1)(1 + \beta^2 u^2)\frac{w^4}{\Lambda^2 u^4}\right)\mathcal{E} \\
\partial_w f_{s,2} &= \alpha\left(\Lambda^2 + 3\nu\frac{w^2}{u^2} - 5(\nu+1)\frac{w^4}{\Lambda^2 u^4}\right)\mathcal{E} \\
\partial_u \tilde{f}_{s,2} &= -2\alpha \frac{w}{u}\left(\Lambda\beta^2 u^2 + \frac{\nu}{2}(1 + 2\beta^2 u^2)\frac{|w|}{u} - (1+\nu)(1 + \beta^2 u^2)\frac{w^2}{\Lambda u^2}\right)\mathcal{E} \\
\partial_w \tilde{f}_{s,2} &= \alpha\left(\Lambda + 2\nu\frac{|w|}{u} - 3(\nu+1)\frac{w^2}{\Lambda u^2}\right)\mathcal{E}.
\end{aligned}$$

To make the derivatives of the tristable alignment terms at least a little more readable we introduce the additional abbreviations

$$l^2 := \lambda^2 + \Lambda^2 \qquad \text{and} \qquad \tilde{l} = \lambda + \Lambda.$$

This allows us to write

$$\begin{aligned}
\partial_u f_{h,3} &= 2\alpha\frac{w}{u}\left(\Lambda^2\lambda^2u^2 - l^2(C^2+u^2)\frac{w^2}{u^2} + (2C^2+u^2)\frac{w^4}{u^4}\right)\\
\partial_w f_{h,3} &= -\alpha\left(\Lambda^2\lambda^2C^2 - l^2(3C^2-2w^2)\frac{w^2}{u^2} + 5(C^2+w^2)\frac{w^4}{u^4}\right)
\end{aligned}$$

$$\begin{aligned}
\partial_u \tilde{f}_{h,3} &= 2\alpha\frac{w}{u}\left(\lambda\Lambda u^2 - \tilde{l}(C^2+2u^2)\frac{|w|}{u} + 2(C^2+u^2)\frac{w^2}{u^2}\right)\\
\partial_w \tilde{f}_{h,3} &= -\alpha\left((C^2-2w^2)\lambda\Lambda - 2\tilde{l}(C^2-w^2)\frac{|w|}{u} + (3C^2-2w^2)\frac{w^2}{u^2}\right)
\end{aligned}$$

$$\begin{aligned}
\partial_u f_{s,3} &= 2\alpha\frac{w}{u}\left(\lambda^2\Lambda^2\beta^2u^2 - l^2(1+\beta^2u^2)\frac{w^2}{u^2} + (2+\beta^2u^2)\frac{w^4}{u^4}\right)\mathcal{E}\\
\partial_w f_{s,3} &= -\alpha\left(\lambda^2\Lambda^2 - 3l^2\frac{w^2}{u^2} + 5\frac{w^4}{u^4}\right)\mathcal{E}
\end{aligned}$$

$$\begin{aligned}
\partial_u \tilde{f}_{s,3} &= 2\alpha\frac{w}{u}\left(\lambda\Lambda\beta^2u^2 - \frac{1}{2}\tilde{l}(1+2\beta^2u^2)\frac{|w|}{u} + (1+\beta^2u^2)\frac{w^2}{u^2}\right)\mathcal{E}\\
\partial_w \tilde{f}_{s,3} &= -\alpha\left(\lambda\Lambda - 2\tilde{l}\frac{|w|}{u} - \frac{w^2}{u^2}\right)\mathcal{E}.
\end{aligned}$$

We first notice that all the derivatives indeed exist throughout Q and are continuous in its interior. At the steady state values

$$(w = 0,\ u = \bar{u} > 0)$$

we further observe that all the partial derivatives with respect to u vanish, since they contain a factor w. This is in fact no surprise as we already knew that $f \equiv 0$ along the line $w = 0$.

Let us now compute the particular values of $\partial_w f$ at $(\bar{u}, 0)$. For the sublinear bistable alignment terms these derivatives are given by

$$\begin{aligned}
\partial_w f_{h,1}(\bar{u},0) &= \alpha\Lambda^2(c^2-\bar{u}^2) &(12.13)\\
\partial_w f_{s,1}(\bar{u},0) &= \alpha\Lambda^2\exp\left[-\beta^2\bar{u}^2\right]. &(12.14)
\end{aligned}$$

For the different versions of the superlinear bistable alignment terms we obtain

$$\begin{aligned}
\partial_w f_{h,2}(\bar{u},0) &= \alpha\Lambda^2(c^2-\bar{u}^2) &(12.15)\\
\partial_w \tilde{f}_{h,2}(\bar{u},0) &= \alpha\Lambda(c^2-\bar{u}^2) &(12.16)\\
\partial_w f_{s,2}(\bar{u},0) &= \alpha\Lambda^2\exp\left[-\beta^2\bar{u}^2\right] &(12.17)\\
\partial_w \tilde{f}_{s,2}(\bar{u},0) &= \alpha\Lambda\exp\left[-\beta^2\bar{u}^2\right]. &(12.18)
\end{aligned}$$

We note that for the standard versions $f_{h,2}$ and $f_{s,2}$, these values which just represent the parameters F_w are the very same as for the corresponding sublinear alignment terms.

In particular, they do not depend on ν at all.

Finally, the tristable alignment terms yield

$$\begin{aligned}
\partial_w f_{h,3}(\bar{u},0) &= -\alpha\Lambda^2\lambda^2(c^2-\bar{u}^2) && (12.19)\\
\partial_w \tilde{f}_{h,3}(\bar{u},0) &= -\alpha\Lambda\lambda(c^2-\bar{u}^2) && (12.20)\\
\partial_w f_{s,3}(\bar{u},0) &= -\alpha\Lambda^2\lambda^2\exp\left[-\beta^2\bar{u}^2\right] && (12.21)\\
\partial_w \tilde{f}_{s,3}(\bar{u},0) &= -\alpha\Lambda\lambda\exp\left[-\beta^2\bar{u}^2\right] && (12.22)
\end{aligned}$$

The computations conducted in chapter 10 and in particular proposition 10.5 remain valid in that case. However, now the term $F_w = \partial_w f(\bar{u},0)$ not only depends on the parameters α, Λ, and λ but also explicitly on $\bar{u}$. We note that the values F_w above differ from their counterparts from chapter 10 only by the factors:

- Λ^2 or Λ, respectively, emerging from the adjustment of the outer zeros of f from $\pm u$ to $\pm\Lambda u$. We would also encounter these factors if we neglected the dependence of f on u.
- $(c^2-\bar{u}^2)$ or $\exp\left[-\beta^2\bar{u}^2\right]$ describing the dependence of f on u.

Significantly, the sign of F_w changes for the hard cut off versions of f as $\bar{u}$ exceeds c. This does not happen for the versions with exponential decay where F_w always has the same sign as its counterpart in chapter 10. We conclude that the exponentially decaying types of alignment terms exhibit qualitatively the same linear stability behavior of the homogeneous steady state ($w=0,\ u=\bar{u}$), and we can even recover the numerical values by choosing $\bar{u}$ appropriately. But even for the cut-off form of f we recover the linear stability analysis from chapter 10 if the steady state density $\bar{u}$ is smaller than c. This would clearly be the usual choice since c is supposed to bound u from above.

From the physical point of view the soft box versions are preferable over the hard box ones since it is not clear how at high densities of filaments the majority shall be turned around by the minority while at low densities this does not happen. A crowding effect where the relative power of both populations remains the same but the total amount of turning relative to the density decreases as there is less free space seems much more physically feasible. We will therefore for future considerations and in particular for the simulations in chapter 15 most often use the exponentially decaying versions of the alignment terms.

12.3 Effects on nonlinear stability

The abstract calculations for the nonlinear stability analysis remain the same as in chapter 11.

Recall first that for model (9.2) we found

$$\frac{d}{dt}E(t) \leq -\frac{\varepsilon\pi^2}{L^2}\int_0^L w^2dx + \int_0^L wf(w)dx \qquad (12.23)$$

from the energy estimates in chapter 11.

For the sake of easier computability we will investigate the effect of the hard box versions of the alignment term but not without noting that in the regime of u^2+w^2

being bounded away from 0 and c^2 there is no qualitative difference between hard and soft crowding terms.

We only have to reconsider the term

$$\int_0^L wf dx$$

where as before we need not make a difference between w and the perturbation $\tilde{w}$. We start with the sublinear bistable case:

$$\begin{aligned} wf_{h,1}(\bar{u}+\tilde{u},w) &= \alpha\frac{w^2}{(\bar{u}+\tilde{u})^2}\left(\Lambda^2(\bar{u}+\tilde{u})^2-w^2\right)\left(c^2-((\bar{u}+\tilde{u})^2+w^2)\right) \\ &= \alpha\left(\Lambda^2w^2-\frac{w^4}{(\bar{u}+\tilde{u})^2}\right)\left(c^2-((\bar{u}+\tilde{u})^2+w^2)\right). \end{aligned} \tag{12.24}$$

Keeping in mind that we would like to start with a steady state with $\bar{u}^2$ being bounded away from zero and from c^2 we find that for C^0-small perturbations we can assume

$$c^2-((\bar{u}+\tilde{u})^2+w^2)\geq 0$$

and conclude

$$\begin{aligned} &\int_0^L wf_{h,1}(\bar{u}+\tilde{u},w)dx \\ &=\int_0^L \alpha\left(\Lambda^2w^2-\frac{w^4}{(\bar{u}+\tilde{u})^2}\right)\left(c^2-((\bar{u}+\tilde{u})^2+w^2)\right)dx \\ &\leq \alpha\Lambda^2\int_0^L w^2\left(c^2-((\bar{u}+\tilde{u})^2+w^2)\right)dx \\ &\leq \alpha\Lambda^2\left((c^2-\bar{u}^2)\int_0^L w^2dx-2\bar{u}\int_0^L\tilde{u}w^2dx-\int_0^L w^2(\tilde{u}^2+w^2)dx\right) \\ &\leq \alpha\Lambda^2(c^2-\bar{u}^2)\int_0^L w^2dx-2\alpha\Lambda^2\bar{u}\int_0^L\tilde{u}w^2dx. \end{aligned}$$

The first term in the last line is just

$$F_w\int_0^L w^2dx$$

where $F_w=\partial_w f_{h,1}(\bar{u},0)$. This we already had in chapter 11. But now we have an additional term of which we cannot determine the sign since we do not know anything about the sign of $\tilde{u}$. As estimate for the growth of the energy functional E we have:

$$\frac{dE}{dt}\leq\left(\alpha\Lambda^2(c^2-\bar{u}^2)-\frac{\varepsilon\pi^2}{L^2}\right)\int_0^L w^2dx+2\alpha\Lambda^2\bar{u}\int_0^L|\tilde{u}|w^2dx. \tag{12.25}$$

We can only assert that for sufficiently small perturbations $(\tilde{u},\ w)$, the second term is small in comparison to the first one. However, we do not find an estimate as sharp as in (11.6) and thus cannot assert that linear stability implies nonlinear stability in this

case. The obvious reason is that the linear stability analysis misses the dependence of f on u.

The next case to be considered is the superlinear bistable one. Let us compute

$$\begin{aligned}
&\int_0^L w f_{h,2}(\bar{u}+\tilde{u},w)dx \\
&= \int_0^L \frac{\alpha w^2}{(\bar{u}+\tilde{u})^2}\left(\Lambda^2(\bar{u}+\tilde{u})^2+\nu w^2-(\nu+1)\frac{w^4}{(\bar{u}+\tilde{u})^2}\right)\left(c^2-((\bar{u}+\tilde{u})^2+w^2)\right)dx \\
&\leq \alpha\Lambda^2(c^2-\bar{u}^2)\int_0^L w^2dx+\alpha\nu(c^2-\bar{u}^2)\int_0^L \frac{w^4}{(\bar{u}+\tilde{u})^2}dx \\
&\quad -2\alpha\bar{u}\int_0^L \tilde{u}w^2(\Lambda^2+\nu\frac{w^2}{(\bar{u}+\tilde{u})^2})dx.
\end{aligned}$$

Again we find terms corresponding to those from chapter 11 and an additional term with unknown sign. But for this case we still recover the qualitative finding that nonlinear stability is not implied by linear stability.

The last case we want to discuss is the tristable one. Here we find

$$\begin{aligned}
&\int_0^L w f_{h,w}(\bar{u}+\tilde{u},w)dx \\
= \;& \alpha\int_0^L \frac{w^2}{(\bar{u}+\tilde{u})^4}\left(\Lambda^2(\bar{u}+\tilde{u})^2-w^2\right)\left(w^2-\lambda^2(\bar{u}+\tilde{u})^2\right)\left(c^2-((\bar{u}+\tilde{u})^2+w^2)\right)dx \\
\leq \;& -\alpha\Lambda^2\lambda^2\int_0^L w^2\left(c^2-((\bar{u}+\tilde{u})^2+w^2)\right)dx+\int_0^L \mathcal{O}(w^4)dx.
\end{aligned}$$

Noting that for sufficiently small perturbations the term

$$\left(c^2-((\bar{u}+\tilde{u})^2+w^2)\right)$$

remains bounded away from zero we see the higher order terms are small compared with the first integral. Thus we still find unconditional nonlinear stability for the tristable alignment term.

As already observed in chapter 11 the nonlinear stability analysis for both models, (9.2) and (9.4), yield the same stability results.

Chapter 13

Traveling Wave Solutions to the Auxiliary Problem

We will now ask for traveling wave solutions to our first reduced model (9.2). These traveling waves are to be understood as fronts of aligned filaments moving in a particular direction at a fixed speed. This may remind the reader of the polymerization fronts discussed in subsections 2.4.2 and 5.2.1 and being observed experimentally at lamellipodia and lamella of moving cells (cf. [26]).

For this first model we shall explicitely prove the existence of such waves. Moreover, we will find particular critical wave speeds depending on the precise parameters and on the type of the nonlinearity.

13.1 Derivation of the system of ordinary differential equations

Our goal is now to find solutions of the types

$$\begin{aligned} u(t,x) &= U(x-ct) \\ w(t,x) &= W(x-ct) \end{aligned} \tag{13.1}$$

where c is the velocity of the traveling wave and U and W describe the wave profile. This type of solutions has to be considered on the whole real line as spatial domain but it should be noted that this fact does not mean that the problem is spatially unbounded. By neglecting the boudnary we only assume that the evolving patterns are small compared to the domain size and are located away from the boudnary.

Plugging the ansatz (13.1) into (9.2) and writing $\xi := x - ct$ we find the following system of ordinary differential equations:

$$\begin{aligned} -cU'(\xi) + W'(\xi) &= 0 \\ -cW'(\xi) + U'(\xi) &= \varepsilon W''(\xi) + f(U,W) \end{aligned} \tag{13.2}$$

or with the abbreviation $\Phi = (U,\ W)^T$:

$$\varepsilon \begin{pmatrix} 0 & 0 \\ 0 & 1 \end{pmatrix} \Phi''(\xi) + \begin{pmatrix} -c & 1 \\ 1 & -c \end{pmatrix} \Phi'(\xi) = \begin{pmatrix} 0 \\ f \end{pmatrix}. \tag{13.3}$$

Multiplying the second equation of (13.2) by c we obtain

$$\begin{aligned} & -\varepsilon c W''(\xi) - c^2 W'(\xi) + c U'(\xi) \\ = \; & -\varepsilon c W''(\xi) + (1-c^2) W'(\xi) \; = \; c f(U, W) \end{aligned} \tag{13.4}$$

where we used the first equation of (13.2) to replace cU' by $-c^2 W'$.

Assuming that f is independent of u we thus have obtained a second order ordinary differential equation for W.

Remark 13.1. *Note that for $c \neq 0$ we also obtain an equation for W even if f depends on u, but now with an additional constant of integration C:*

$$-\varepsilon c W''(\xi) + (1-c^2) W'(\xi) = c f\left(\frac{W + C}{c}, W\right) \tag{13.5}$$

We also note that this is the generic case as $c = 0$ would correspond to a standing rather than a traveling wave.

Putting $V := W' \equiv -cU'$ we finally obtain a diagonalized system of first order equations:

$$\begin{aligned} W' - V \; &= 0 \\ V' - \frac{1}{\varepsilon}\left(\frac{1}{c} - c\right) V \; &= -\frac{1}{\varepsilon} f \end{aligned} \tag{13.6}$$

where we already assumed $c \neq 0$.

13.2 Special velocities

(1) $c = 0$. We immediately see from the first equation in (13.2) that $W(\xi) \equiv W_0 = const.$ The second equation then just reads

$$U'(\xi) = f(U, W_0)$$

which is now a first order equation for U. In the simplest case where we consider f to be independent of u this leads to

$$U(\xi) = U_0 + f(W_0)\xi.$$

This is unbounded and has no chance to converge to some finite values as $\xi \to \pm\infty$ unless $f(W_0) = 0$ in which case we recover the homogeneous steady states we already discussed in chapter 10.

(2) $c = \pm 1$. In that case we have from the first equation of (13.2)

$$U'(\xi) = \pm W'(\xi) \quad \Longrightarrow \quad U(\xi) = \pm W(\xi) + C$$

for some constant C whereas (13.4) simply reads

$$W''(\xi) = -\frac{1}{\varepsilon} f.$$

This may be more intriguing as it looks!

For all other values of c we obtain the following form of (13.4):

$$W''(\xi) + \mu W'(\xi) = -\frac{1}{\varepsilon} f \tag{13.7}$$

where the parameter

$$\mu := \frac{1}{\varepsilon}\left(c - \frac{1}{c}\right)$$

satisfies

$$\mu \left\{ \begin{array}{c} < \\ > \end{array} \right\} 0 \quad \Longleftrightarrow \quad c \in \left\{ \begin{array}{c} (-\infty, -1) \cup (0, 1) \\ (-1, 0) \cup (1, \infty) \end{array} \right\}. \tag{13.8}$$

Remark 13.2. *If the particle velocity v differs from 1 then the second order equation for the wave profile W in case $c \neq 0$ reads*

$$-\varepsilon c W''(\xi) + (v^2 - c^2) W'(\xi) = cf\left(\frac{v}{c}(W + C),\ W\right).$$

Obviously, the nonzero special velocities are given by $c = \pm v$, and the parameter μ takes the form

$$\tilde{\mu}(v) = \frac{1}{\varepsilon}\left(c - \frac{v^2}{c}\right).$$

Remarkably, the intervals of constant sign of $\tilde{\mu}$ are now $(-\infty, -v)$, $(-v, 0)$, $(0, v)$, (v, ∞). At $c = \pm v$, $\tilde{\mu}$ vanishes, whereas the singularity at $c = 0$ is preserved. The effect of this will become clear later.

13.3 Linearization around the equilibria

For the case $c = 0$ there is nothing to do so that we may assume throughout this section that $c \neq 0$. We thus consider the equation

$$W''(\xi) + \mu W'(\xi) + \frac{1}{\varepsilon} f = 0 \tag{13.9}$$

with

$$\mu = \frac{1}{\varepsilon}\left(c - \frac{1}{c}\right)$$

as above. As alignment term we first consider the sublinear bistable case independent of u which is given by

$$f(w) = \alpha w(\Lambda^2 - w^2), \tag{13.10}$$

having zeros at $W = 0$ and $W = \pm\Lambda$. Linearizing around these zeros yields:

1. $W = 0$. Here we find as linearized equation

$$W'' + \mu W' + \frac{F_w}{\varepsilon} W = 0$$

where we used the known abbreviation

$$F_w = \partial_w f \mid_{w=0} = \alpha\Lambda^2.$$

The characteristic eigenvalues of this equation are

$$\nu_{1,\pm} = -\frac{\mu}{2} \pm \sqrt{\frac{\mu^2}{4} - \frac{F_w}{\varepsilon}} = -\frac{\mu}{2} \pm \sqrt{\frac{\mu^2}{4} - \frac{\alpha\Lambda^2}{\varepsilon}}. \tag{13.11}$$

We have to distinguish two cases:

a) $\mu^2\varepsilon \geq 4F_w$. Then the roots are real and both have the opposite sign of μ. If strict inequality holds, then both roots have strictly the opposite sign of μ and we find a node at $W = W' = 0$ in the $W - W'$-plane (recall system (13.6)). The condition for the roots to be real can be rewritten as

$$\frac{1}{\varepsilon}\left(c - \frac{1}{c}\right)^2 = \varepsilon\mu^2 \geq 4F_w \tag{13.12}$$

or equivalently

$$c^4 - (4F_w\varepsilon + 2)c^2 + 1 \geq 0$$

which has the squared roots

$$c_\pm^2 = 2F_w\varepsilon + 1 \pm 2\sqrt{F_w\varepsilon(F_w\varepsilon + 1)}. \tag{13.13}$$

We thus obtain 4 critical velocities

$$\pm\, c_* = \pm\sqrt{2F_w\varepsilon + 1 - 2\sqrt{F_w\varepsilon(F_w\varepsilon + 1)}} \tag{13.14}$$

$$\pm c^* = \pm\sqrt{2F_w\varepsilon + 1 + 2\sqrt{F_w\varepsilon(F_w\varepsilon + 1)}}. \tag{13.15}$$

which are real whenever $F_w \geq 0$, and in case $F_w > 0$ satisfy $0 < c_* < 1 < c^*$. If we now recall the special form (13.10) of f and abbreviate

$$a := F_w\varepsilon = \alpha\Lambda^2\varepsilon$$

we may rewrite this to

$$\begin{aligned} \pm c_* &= \pm\sqrt{2a + 1 - 2\sqrt{a(a+1)}} \\ \pm c^* &= \pm\sqrt{2a + 1 + 2\sqrt{a(a+1)}} = \pm\frac{1}{c_*}. \end{aligned} \tag{13.16}$$

We should note that the critical velocity c^* arises in the same manner as the minimal traveling wave speed for the Fisher-KPP equation (cf. [32]). However, in our case, wave patterns oscillating around the trivial steady state $W = 0$ cannot be excluded since the polarization is allowed to take values of any sign. At this point we should note that the oscillations will always be of a form that ensures positivity of the single particle densities.

b) $\mu^2\varepsilon < 4F_w$. Now the roots have non vanishing imaginary part, and have the real parts

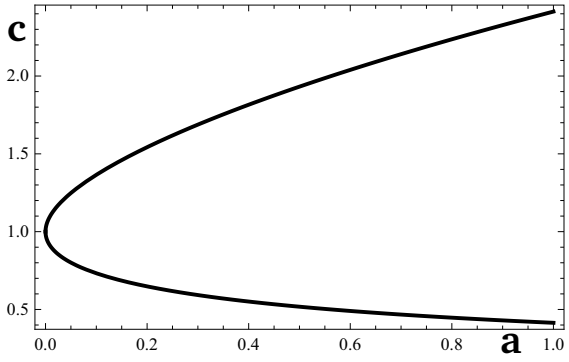

Figure 13.1: Critical wave velocities c^* (*upper branch*) and c_* (*lower branch*) in dependence on the product $a = \varepsilon F_w$. The space between the curves is forbidden if we seek monotone wave profiles as such c would lead to non-real eigenvalues.

$\mathrm{Re}\,\nu_\pm = -\frac{\mu}{2}$. We thus obtain a spiral point whose stability depends on the sign of μ.

In both cases, the corresponding eigenvectors may be represented as

$$\eta_{1,\pm} = \begin{pmatrix} -\frac{\varepsilon\mu}{2F_w} \mp \sqrt{\left(\frac{\varepsilon\mu}{2F_w}\right)^2 - \frac{\varepsilon}{F_w}} \\ 1 \end{pmatrix} = \begin{pmatrix} \frac{\varepsilon}{F_w}\nu_{1,\mp} \\ 1 \end{pmatrix} \tag{13.17}$$

or in the special case of f being given by (13.10):

$$\begin{pmatrix} -\frac{\varepsilon\mu}{2a\Lambda^2} \pm \sqrt{\left(\frac{\varepsilon\mu}{2\alpha\Lambda^2}\right)^2 - \frac{\varepsilon}{\alpha\Lambda^2}} \\ 1 \end{pmatrix} \tag{13.18}$$

2. $W = \Lambda$. We define $\tilde{W} := W - \Lambda$ and

$$\tilde{F}_w := \partial_w f \mid_{w=\Lambda}$$

to find the linearized equation

$$\tilde{W}'' + \mu\tilde{W}' + \frac{\tilde{F}_w}{\varepsilon}\tilde{W} = 0$$

where for f given by (13.10) the derivative is $\tilde{F}_w = -2\alpha\Lambda^2$.

The characteristic eigenvalues are the same as for $W = 0$ with $\tilde{F}_w$ replacing F_w:

$$\nu_{2,\pm} = -\frac{\mu}{2} \pm \sqrt{\frac{\mu^2}{4} + \frac{2\alpha\Lambda^2}{\varepsilon}}. \tag{13.19}$$

Both of them are real and have opposite signs so that we obtain a saddle at $(W = \Lambda, W' = 0)$ in the $W - W'$-plane. The corresponding eigenvectors are now given by

$$\eta_{2,\pm} = \begin{pmatrix} \frac{\varepsilon}{\tilde{F}_w}\nu_{2,\mp} \\ 1 \end{pmatrix} = \begin{pmatrix} \frac{\varepsilon}{4\alpha\Lambda^2}\left(\mu \pm \sqrt{\mu^2 + \frac{8\alpha\Lambda^2}{\varepsilon^2}}\right) \\ 1 \end{pmatrix} \tag{13.20}$$

3. $W = -\Lambda$. Putting now $\tilde{W} = W + \Lambda$ we find exactly the same linearization here as for $W = \Lambda$ which is just a consequence of f being an odd function of w. In particular, the states $(W = \pm\Lambda, W' = 0)$ are connected to $W = W' = 0$ along flow lines of the same shape.

Remark 13.3. *The dependence of the critical velocities c^* and c_* solely on the product εF_w is most easily appreciated if we write the alignment term as $f = \alpha f^0$ where f^0 determines the shape of the alignment term and α its strength. We can now rescale both, the time and space variables in the original equations by α:*

$$t \to \tilde{t} = \frac{t}{\alpha} \qquad \text{and} \qquad x \to \tilde{x} = \frac{x}{\alpha}.$$

This scaling does not change any velocities and the resulting system reads

$$\begin{aligned} \partial_{\tilde{t}} u + \partial_{\tilde{x}} w &= 0 \\ \partial_{\tilde{t}} w + \partial_{\tilde{x}} u &= \alpha\varepsilon \partial_{\tilde{x}\tilde{x}} w + f^0(u, w), \end{aligned} \tag{13.21}$$

and the only remaining parameter is just this product $\varepsilon\alpha$.

13.4 Existence of heteroclinic orbits

To find heteroclinic orbits connecting the equilibria of system (13.6) we analyze the behavior of the vector field

$$\Phi = \begin{pmatrix} V \\ -\mu V - \frac{1}{\varepsilon} f(W) \end{pmatrix} \tag{13.22}$$

in the W-V-plane and in particular in the triangles which are bounded by the W-axis and the lines through the equilibria being spanned by the eigenvectors of the linearization.

We start with the case $c > 1$ and the pair $W_1 = 0,\ W_2 = \Lambda$ of equilibria. Expecting an orbit connecting the point

$$(W_2 = \Lambda, V = 0)$$

to the point

$$(W_1 = 0, V = 0)$$

we are interested in the stable manifold of the fixed point at W_2. The triangle we want to show invariance for is thus given by the corner points $(0,0)^T$, $(W_2, 0)^T$ and $(W^s, V^s)^T$ which is given as the intersection of the straight lines through $(0,0)^T$ and $(W_2, 0)^T$ along the eigenvectors $\eta_{1,-}$ and $\eta_{2,+}$, respectively. This triangle is shown in figure 13.2.

Using the given values for the eigenvectors of the linearization we compute the (not normalized) inner normal to the eigenspace corresponding to the eigenvector $\eta_{1,+}$ at $(0,0)^T$ as

$$\mathfrak{n}_1 = \left(1, -\frac{\varepsilon}{F_w}\nu_{1,-}\right), \tag{13.23}$$

and the normal to the unstable eigenspace at $(W_2, 0)^T$ reads

$$\mathfrak{n}_2 = \left(-1, \frac{\varepsilon}{\tilde{F}_w}\nu_{2,-}\right). \tag{13.24}$$

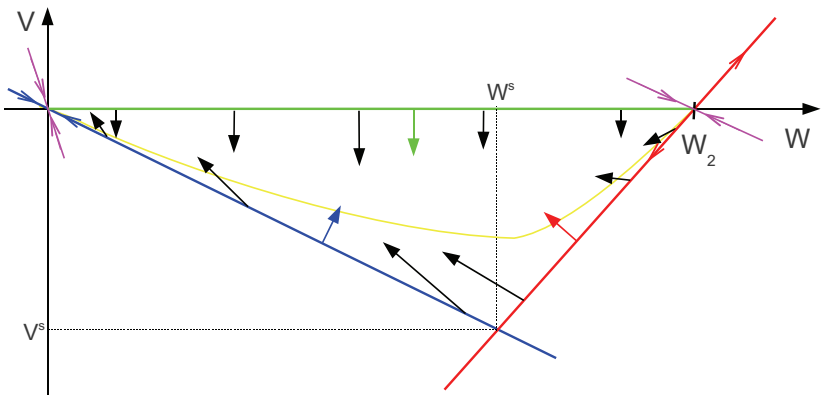

Figure 13.2: Invariant domain in phase plane for waves connecting $W_2 = U_2$ to $(W_1 = 0, U_1)$ with velocity $c > c^*$. The colored arrows denote the inner unit normals (*blue*: $\mathfrak{n}_1$ on the line corresponding to the eigenvector $\eta_{1,+}$ at the origin, *red*: $\mathfrak{n}_2$ along the unstable eigenspace of the linearization at $(W_2, 0)^T$, *green*: $\mathfrak{n}_0$ along the W-axis), the *black* arrows indicate the flow field along the boundary of the invariant triangle. *Magenta* arrows indicate the remaining eigenvectors. The curve $V' = 0$ is sketched as *yellow curve*.

Along the positive W-axis the field Φ has vanishing W-component and the V component is

$$-\frac{1}{\varepsilon} f(W) < 0$$

and the vector field clearly points into the triangle in question.

Along the unstable eigenspace attached to the point $(W_2, 0)^T$ we compute

$$\begin{aligned}
\mathfrak{n}_2\Phi &= -V - \frac{\varepsilon}{\tilde{F}_w}\nu_{2,-}\left(\mu V + \frac{1}{\varepsilon} f(W)\right) \\
&> -V - \frac{\varepsilon}{\tilde{F}_w}\nu_{2,-}\left(\mu V - \frac{1}{\varepsilon}\tilde{F}_w(W - W_2)\right) \\
&= -V\left(1 + \frac{\varepsilon}{\tilde{F}_w}\nu_{2,-}\left(\mu - \nu_{2,-}\right)\right) \\
&= -\underbrace{V}_{<0}\left(1 + \underbrace{\frac{\varepsilon}{\tilde{F}_w}\nu_{2,-}}_{>0}\left(\underbrace{\frac{3}{2}\mu + \sqrt{\frac{\mu^2}{4} - \frac{\tilde{F}_w}{\varepsilon}}}_{>0}\right)\right) \quad > \quad 0
\end{aligned}$$

where we used

- $0 < f(W) < -\tilde{F}_w(W - W_2)$ for $W \in (0, W_2)$,
- $W = W_2 + \frac{\varepsilon}{\tilde{F}_w}\nu_{2,-}V$ along the unstable eigenspace, and
- $\mu > 0$ since $c > 1$.

Finally, along the line corresponding to $\eta_{1,-}$ at $(0,0)^T$ we compute

$$\begin{aligned}
\mathfrak{n}_1\Phi &= V + \frac{\varepsilon}{F_w}\nu_{1,-}\left(\mu V + \frac{1}{\varepsilon}f(W)\right) \\
&> V + \frac{\varepsilon}{F_w}\nu_{1,-}\left(\mu V + \frac{F_w}{\varepsilon}W\right) \qquad (13.25)\\
&= V\left(1 + \frac{\varepsilon}{F_w}\nu_{1,-}\left(\mu + \nu_{1,-}\right)\right) \\
&= V\left(1 + \frac{\varepsilon}{F_w}\left(-\frac{\mu}{2} - \sqrt{\frac{\mu^2}{4} - \frac{F_w}{\varepsilon}}\right)\left(\frac{\mu}{2} - \sqrt{\frac{\mu^2}{4} - \frac{F_w}{\varepsilon}}\right)\right) \\
&= V\left(1 - \frac{\varepsilon}{F_w}\left(\frac{\mu^2}{4} - \left(\frac{\mu^2}{4} - \frac{F_w}{\varepsilon}\right)\right)\right) \;=\; 0
\end{aligned}$$

where now it has been used that

- $\frac{\varepsilon}{F_w}\nu_{2,-} < 0$,
- $W = \frac{\varepsilon}{F_w}\nu_{1,-}V$ along the line in question, and
- $f(W) < F_w W$ for any $W > 0$ which is at least true for the sublinear bistable alignment term $f_1(w) = \alpha w(\Lambda^2 - w^2)$.

We have hereby shown the positive (forward) invariance of the proposed triangle under the flow of the system. The same computations furthermore show that the unstable manifold of the point $(W_2, 0)^T$ lies between the corresponding unstable eigenspace and the W-axis at least for small negative values of $W - W_2$. Since there cannot be any fixed point in the interior of the investigated triangle, the unstable manifold of the point $(W_2, 0)^T$ has to reach the point $(0,0)^T$ and we have established the desired heteroclinic orbit.

The calculations for the other possible waves are very similar. We will briefly show how the invariant domains look like and how their invariance is shown.

For waves of velocity $c > c^*$ connecting the state $(W_3 = -\Lambda, 0)^T$ to $(0,0)^T$ we may choose the triangle being bounded by the negative W-axis, the line corresponding to the eigenvector $\eta_{1,+}$ at the origin and the unstable eigenspace at outer equilibrium point. The inner normals can be written as

$$\mathfrak{n}_0 = (0,1), \qquad \mathfrak{n}_1 = \left(-1, \tfrac{\varepsilon}{F_w}\nu_{1,-}\right), \qquad \mathfrak{n}_3 = \left(1, -\frac{\varepsilon}{\tilde{F}_w}\nu_{3,-}\right)$$

and we compute

$$\begin{aligned}
\mathfrak{n}_0\Phi &= -\mu V - \frac{1}{\varepsilon}f(W) \\
&> 0 \quad \text{for } V = 0, W < 0,
\end{aligned}$$

along the relevant part of the W-axis,

$$\begin{aligned}\mathfrak{n}_1\Phi &= -V - \frac{\varepsilon}{F_w}\underbrace{\nu_{1,-}}_{<0}\left(\mu V + \frac{1}{\varepsilon}\underbrace{f(W)}_{>F_w W=\varepsilon\nu_1 V}\right)\\ &> -V\left(1-\frac{\varepsilon}{F_w}\left(\frac{\mu}{2}+\sqrt{\frac{\mu^2}{4}-\frac{F_w}{\varepsilon}}\right)\left(\mu-\frac{\mu}{2}-\sqrt{\frac{\mu^2}{4}-\frac{F_w}{\varepsilon}}\right)\right) = 0,\end{aligned}$$

along the face corresponding to the eigenvector $\eta_{1,+}$, and finally

$$\begin{aligned}\mathfrak{n}_3\Phi &= V + \underbrace{\frac{\varepsilon}{\tilde{F}_w}\nu_{3,-}}_{>0}\left(\mu V + \frac{1}{\varepsilon}\underbrace{f(W)}_{>\tilde{F}_w(W-W_3)=\varepsilon\nu_{3,-}V}\right)\\ &> V\left(1+\frac{\varepsilon}{\tilde{F}_w}\nu_{3,-}\underbrace{(\mu+\nu_{3,-})}_{\geq 0 \text{ f. } c>c^*}\right)\\ &\geq V > 0,\end{aligned}$$

from which again positive invariance of the triangle follows.

We are next concerned with velocities $c \in (0, c_*)$ and waves connecting the non-polarized $W = 0$-state to the fully right aligned $W = W_2 = \Lambda$-state. Our invariant triangle now lies in the upper right quadrant of the W-V-plane and is bounded by the positive W-axis, the line given by the eigenvector $\eta_{1,-}$ at the origin and the stable eigenspace at the point $(W_2, 0)^T$. The non-normalized inner normals to these faces of the triangle read

$$\mathfrak{n}_0 = (0,1), \qquad \mathfrak{n}_1 = \left(1, -\tfrac{\varepsilon}{F_w}\nu_{1,+}\right), \qquad \mathfrak{n}_2 = \left(-1, \tfrac{\varepsilon}{\tilde{F}_w}\nu_{2,+}\right).$$

We now check for negative (backward) invariance by computing

$$\mathfrak{n}_0\Phi = -\mu V - \frac{1}{\varepsilon}f(W) < 0$$

along the W-axis,

$$\begin{aligned}\mathfrak{n}_1\Phi &= V + \frac{\varepsilon}{F_w}\nu_{1,+}\left(\mu V + \frac{1}{\varepsilon}\underbrace{f(W)}_{<F_w W=\varepsilon\nu_{1,+}V}\right)\\ &< V\left(1-\frac{\varepsilon}{F_w}\left(\frac{\mu}{2}-\sqrt{\frac{\mu^2}{4}-\frac{F_w}{\varepsilon}}\right)\left(\mu-\frac{\mu}{2}+\sqrt{\frac{\mu^2}{4}-\frac{F_w}{\varepsilon}}\right)\right)\\ &= V\left(1-\frac{\varepsilon}{F_w}\left(\frac{\mu^2}{4}-\frac{\mu^2}{4}+\frac{F_w}{\varepsilon}\right)\right) = 0,\end{aligned}$$

along the line corresponding to the eigenvector $\nu_{1,+}$, and along the line being determined

by the the eigenvector $\nu_{2,+}$ we find

$$\begin{aligned}
\mathfrak{n}_2\Phi &= -V\underbrace{-\frac{\varepsilon}{\tilde{F}_w}\nu_{2,+}}_{>0}\left(\mu V+\frac{1}{\varepsilon}\underbrace{f(W)}_{<\tilde{F}_w(W-W_2)=\varepsilon\nu_{2,+}V}\right)\\
&< -V\left(1+\frac{\varepsilon}{\tilde{F}_w}\nu_{2,+}\underbrace{(\mu+\nu_{2,+})}_{<0}\right)\\
&\leq -V \;<\; 0.
\end{aligned}$$

For the last calculation we used that for $0<c<1$ the parameter μ becomes negative and that $\nu_{2,+}$ is smaller than $-\mu$ if in addition $c<c_*$. We thus have found negative invariance of the triangle, and we conclude by time reversion that the left branch of the stable manifold at the saddle $(W_2,0)^T$ can only come from the origin.

The last case we will treat explicitely is the one of a wave with speed $c\in(0,c_*)$ connecting the $W=0$-state with the state $W=W_3=-\Lambda$. The triangle of interest is now bounded by the negative W-axis, the line given by the eigenvector $\eta_{1,-}$ at the origin and the stable eigenspace of the linearization at the point $(W_3,0)^T$.

The inner normals are now

$$\mathfrak{n}_0=(0,-1),\qquad \mathfrak{n}_1=\left(-1,\tfrac{\varepsilon}{F_w}\nu_{1,+}\right),\qquad \mathfrak{n}_2=\left(1,-\frac{\varepsilon}{\tilde{F}_w}\nu_{2,+}\right),$$

and the usual computations

$$\mathfrak{n}_0\Phi = \mu V+\frac{1}{\varepsilon}f(W)<0,$$

$$\begin{aligned}
\mathfrak{n}_1\Phi &= -V-\frac{\varepsilon}{F_w}\nu_{1,+}\left(\mu V+\frac{1}{\varepsilon}f(W)\right)\\
&< -V\left(1+\frac{\varepsilon}{F_w}\nu_{1,+}(\mu+\nu_{1,+})\right)\\
&= -V\left(1-\frac{\varepsilon}{F_w}\left(\frac{\mu}{2}-\sqrt{\frac{\mu^2}{4}-\frac{F_w}{\varepsilon}}\right)\left(\mu-\frac{\mu}{2}+\sqrt{\frac{\mu^2}{4}-\frac{F_w}{\varepsilon}}\right)\right) \;=\; 0,
\end{aligned}$$

and

$$\begin{aligned}
\mathfrak{n}_3\Phi &= V+\frac{\varepsilon}{\tilde{F}_w}\nu_{3,+}\left(\mu V+\frac{1}{\varepsilon}f(W)\right)\\
&< \underbrace{V}_{<0}\left(1+\underbrace{\frac{\varepsilon}{\tilde{F}_w}}_{<0}{}'\nu_{3,+}\underbrace{(\mu+\nu_{3,+})}_{<0}\right) \;<\; 0
\end{aligned}$$

again establish negative invariance of this triangle.

The cases with negative wave speeds will not be dealt with explicitely here, since

they are precise mirror images of those cases treated above.

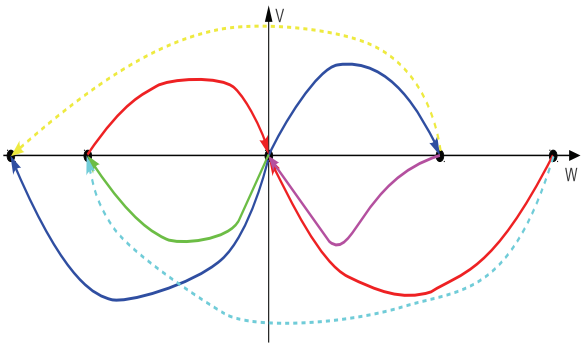

Figure 13.3: Sketch of possible traveling waves as heteroclinic orbits in the W-W'-plane. The variable U has to be considered as third dimension and U has to be calculated by $U = U_1 + \frac{W}{c}$. The colors code for the admissable velocities for these waves: $c < -c^* < c < 1 < -c_* < c < 0 < c < c_* < 1 < c < c^* < c$. Dashed arrows denote orbits whose existence is not shown, solid arrows correspond to orbits which are known to exist.

If the wave velocity lies in the oscillatory regime, $|c| \in (c_*,\ c^*)$, then we cannot conclude the existence of heteroclinic orbits by means of invariant domains. That means, that for such c we cannot assert the existence of heteroclinic orbits connecting any of the totally aligned states with the symmetric state $W = 0$. The possible non-existence of this type of orbits on the other hand allows for the existence of orbits connecting the different totally aligned states $W = \pm U$ with each other via a saddle-saddle connection.

Since there is no particular symmetric state involved in this picture it makes no sense to express the value of these states in terms of U_1. However, the equation

$$U = \frac{1}{c}(W + C)$$

with some constant C still has to be satisfied. We can therefore express the constant C in terms of the state $W_2 = U_2$ as

$$C = (c - 1)U_2$$

and thus compute

$$-W_3 = U_3 = \frac{c-1}{c+1}U_2 \tag{13.26}$$

from which we conclude that due to the requirement that U shall be positive these orbits can only exist for $|c| \in (1,\ c^*)$.

More precisely, there may exist an orbit connecting the state

$$W_2 = U_2 > 0$$

to the state

$$W_3 = -U_3 = -\frac{c-1}{c+1}U_2$$

for $-c^* < c < -1$ and an orbit connecting the state

$$W_2 = U_2 > 0$$

to the state

$$W_3 = -U_3 = -\frac{c-1}{c+1}U_2$$

for $1 < c < c^*$.

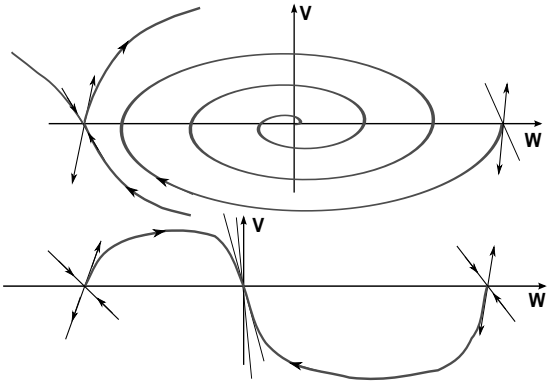

Figure 13.4: Illustration of the possible emergence of a heteroclinic orbit connecting the state $U_2 = W_2$ to the state $-W_3 = U_3 = (c-1)U_2/(c+1)$. The saddle-node connection existing for $c > c^*$ (*below*, for $c \gtrsim c^*$) turns into a spiral which may approach the stable manifold of the saddle at W_3 as c is decreased (*above*) and may finally merge with it to form the saddle-saddle orbit. The small arrows indicate the stable and unstable eigenspaces of the linearizations.

How this latter additional orbit will emerge for a certain wave velocity is sketched in figure 13.4. Once the node at $W = V = 0$ has turned into a spiral, the trajectory between the saddle at W_2 and this point will have to cross the W-axis. For a very particular velocity c it might do so at the appropriate counterpart equilibrium

$$-W_3 = \frac{c-1}{c+1} W_2$$

of opposite polarization and the saddle-saddle connection comes into existence.

All non-oscillatory heteroclinic orbits which are known to exist or whose existence cannot be excluded are shown in figure 13.3.

Remark 13.4. *We remark that here the value of the particle velocity v enters via the dependence on μ. Condition (13.12) for the eigenvalues of the linearization around the symmetric steady state to be real reads*

$$\frac{1}{\varepsilon}\left(c - \frac{v^2}{c}\right)^2 \geq 4\varepsilon F_w \tag{13.27}$$

and leads to the critical velocities

$$\pm\,\tilde{c}_*(v) \;=\; \pm\sqrt{2a + v^2 - 2\sqrt{a\,(a+v^2)}} \tag{13.28}$$

$$\pm\tilde{c}^*(v) \;=\; \pm\sqrt{2a + v^2 + 2\sqrt{a\,(a+v^2)}} \;=\; \pm\frac{v^2}{\tilde{c}_*(v)} \tag{13.29}$$

where a denotes the product

$$a = \varepsilon \partial_w f\,|_{W=0}\,.$$

These critical velocities show a similar behavior as for $v = 1$. In particular, as a tends to zero, both of them tend to v. To give an impression for the dependence of the curves $\tilde{c}^*(a;v)$ and $\tilde{c}_*(a;v)$ on a for different values of the velocity v, figure 13.5 shows them for $v = 0.5$ and $v = 2.5$.

Example. Let us briefly discuss the particular parameter setting

$$\alpha = \frac{1}{3}, \qquad \Lambda = 1, \qquad \varepsilon = 1$$

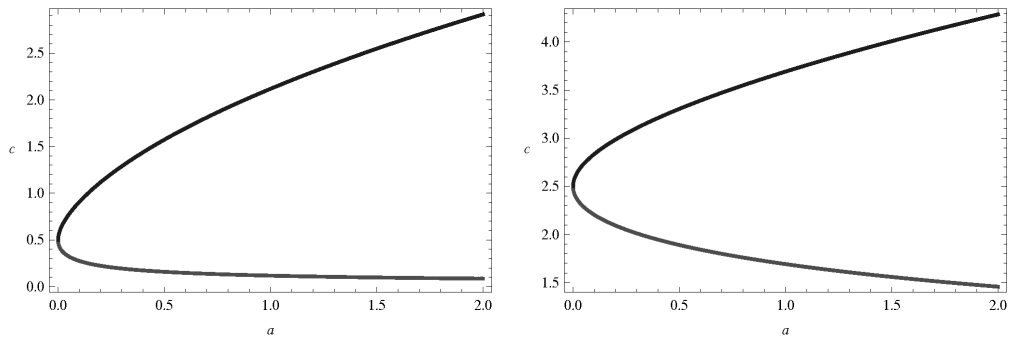

Figure 13.5: Dependence of $\tilde{c}^*$ (BLACK, UPPER BRANCH) and $\tilde{c}_*$ (GRAY, LOWER BRANCH) depending on $a = \varepsilon F_w$ for particle velocities $v = 0.5$ (*left*) and $v = 2.5$ (*right*).

to make the values computed above a little bit more accessible. We first find as critical velocities

$$\begin{aligned} c_* &= \sqrt{\frac{2}{3} + 1 - 2\sqrt{\frac{4}{9}}} = \frac{1}{\sqrt{3}} \\ c^* &= \sqrt{\frac{2}{3} + 1 + 2\sqrt{\frac{4}{9}}} = \sqrt{3}. \end{aligned}$$

We can now choose for example the velocities

$$\begin{aligned} c_1 = 1 + \sqrt{2} &> \sqrt{3} = c^* \\ c_2 = \sqrt{2} - 1 &< \frac{1}{\sqrt{3}} = c_* \end{aligned}$$

to obtain corresponding values of μ being

$$\mu_1 = 2 \quad \text{and} \quad \mu_2 = -2$$

For the eigenvalues of the linearized problem at $W = 0$ we now find

$$\begin{aligned} \nu_{\pm,1} &= -1 \pm \sqrt{\frac{2}{3}} < 0 \qquad \text{for } c = c_1 \\ \nu_{\pm,2} &= 1 \pm \sqrt{\frac{2}{3}} > 0 \qquad \text{for } c = c_2 \end{aligned}$$

and conclude that the origin is a stable node for $c = c_1$ and an unstable node in case of $c = c_2$. More generally, we find a stable node at zero whenever $c > c^*$ and an unstable one whenever $0 < c < c_*$.

The corresponding eigenvectors take the form

$$\eta_{\pm,1} = \begin{pmatrix} -3 \pm \sqrt{6} \\ 1 \end{pmatrix} = \begin{pmatrix} -3\left(1 \mp \sqrt{\frac{2}{3}}\right) \\ 1 \end{pmatrix} \qquad \text{for } c = c_1$$

$$\eta_{\pm,2} = \begin{pmatrix} 3 \pm \sqrt{6} \\ 1 \end{pmatrix} = \begin{pmatrix} 3\left(\pm\sqrt{\frac{2}{3}}\right) \\ 1 \end{pmatrix} \qquad \text{for } c = c_2$$

The linearization around $W = \pm\Lambda = \pm 1$ yields the eigenvalues

$$\tilde{\nu}_{\pm,1} = -1 \pm \sqrt{\frac{5}{3}} \qquad \text{for } c = c_1$$
$$\tilde{\nu}_{\pm,2} = 1 \pm \sqrt{\frac{5}{3}} \qquad \text{for } c = c_2.$$

and corresponding eigenvectors

$$\eta_{\pm,1} = \begin{pmatrix} \frac{3}{2} \pm \sqrt{\frac{20}{3}} \\ \\ 1 \end{pmatrix} = \begin{pmatrix} \frac{3}{2}\left(1 \pm \sqrt{\frac{5}{3}}\right) \\ \\ 1 \end{pmatrix} \qquad \text{for } c = c_1$$

$$\eta_{\pm,2} = \begin{pmatrix} -\frac{3}{2} \pm \sqrt{\frac{20}{3}} \\ \\ 1 \end{pmatrix} = \begin{pmatrix} -\frac{3}{2}\left(1 \mp \sqrt{\frac{5}{3}}\right) \\ \\ 1 \end{pmatrix} \qquad \text{for } c = c_2$$

In figure 13.6, we sketched the flow field of system (13.6) in the W-W'-plane for the parameters chosen above and positive velocities.

We summarize the results in the following proposition.

Proposition 13.5. *Consider system (9.2) on $\mathbb{R} \times (0, \infty)$ with*

$$f(u, w) = \alpha w(\Lambda^2 - w^2)$$

and parameters $\alpha, \Lambda, \varepsilon > 0$. Let $c_* > 1$ and $c^* \in (0, 1)$ be defined by (13.14) and (13.15), respectively. Then, the system allows traveling wave solutions of the following four types:

1. *fast waves traveling to the right with velocity $c > c^* > 1$, connecting one of the states $w = \pm\Lambda, u = \pm\frac{1}{c} + C$ with the state $w = 0, u = C$ for some constant $C \geq \frac{1}{c}$*
2. *slow waves traveling to the right with velocity $0 < c < c_* < 1$, connecting the state $w = 0, u = C$ with one of the states $w = \pm\Lambda, u = \pm\frac{1}{c} + C$ for some constant $C \geq c$*
3. *slow waves traveling to the left with velocity $-c_* < c < 0$, connecting one of the states $w = \pm\Lambda, u = \mp\frac{1}{c} + C$ with the state $w = 0, u = C$ for some constant $C \geq -\frac{1}{c}$*
4. *fast waves traveling to the left with velocity $c < -c^* < -1$, connecting the state $w = 0, u = C$ with one of the states $w = \pm\Lambda, u = \mp\frac{1}{c} + C$ for some constant $C \geq -\frac{1}{c}$*

Remark 13.6. *We finally note that by gluing together a slow and a fast wave, both traveling into the same direction with some plateau in between, we obtain a traveling hump of increasing width.*

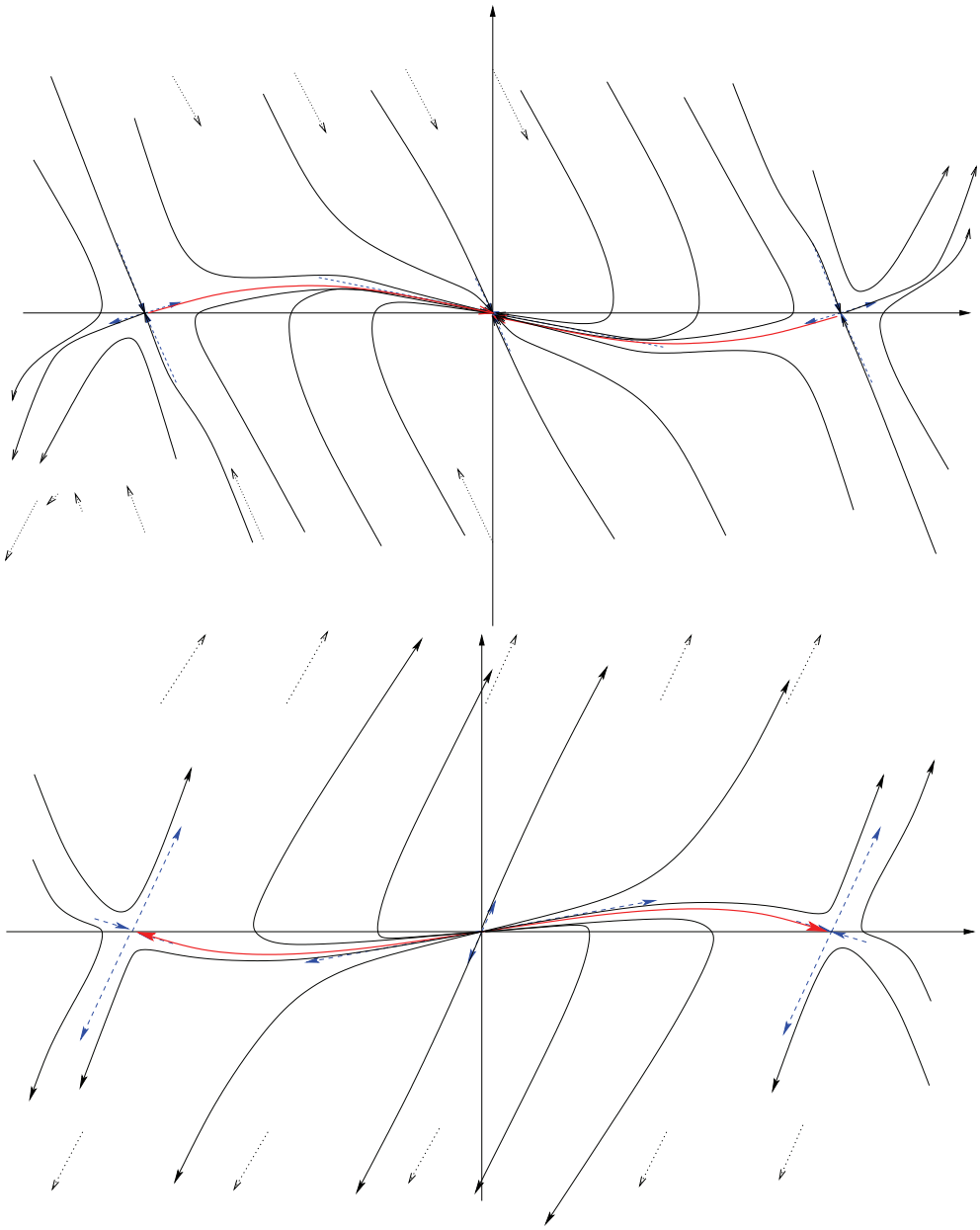

Figure 13.6: Flow fields for system (13.6) with parameter values $\varepsilon = 1, \Lambda = 1, \alpha = \frac{1}{3}$. *Above:* $\mu = 2$ ($c = \sqrt{2}+1$), *below:* $\mu = -2$ ($c = \sqrt{2}-1$). *Red*: Orbit connecting the stationary points. The *blue dotted* arrows indicate the eigenvectors of the linearizations around the equilibria.

13.5 Alignment terms depending on particle density

13.5.1 Equilibria of the system and compatible wave speeds

If we now allow f to depend on u then according to remark 13.1 we have to solve

$$W''(\xi) + \mu W'(\xi) + \frac{1}{\varepsilon} g(W) \tag{13.30}$$

or equivalently the system

$$\begin{array}{rcll} W' & = & & V \\ V' & = & -\frac{1}{\varepsilon} g(W) & -\mu V \end{array} \tag{13.31}$$

where

$$g(W) := f\left(\frac{W+C}{c}, W\right).$$

Our first goal will thus be to find the zeros of g. With the sublinear bistable form of f we find for example

$$\begin{aligned} 0 \ = g_{s,1}(W) \quad &\equiv \quad f_{s,1}\left(\frac{W+C}{c}, W\right) \\ &= \alpha W \left(1 - \left(\frac{cW}{W+C}\right)^2\right) \exp\left[-\frac{\beta^2}{c^2}(W+C)^2\right] \end{aligned}$$

where we have put Λ to one for simplicity of the calculations and recalling the fact that $\Lambda = 1$ corresponds to the natural case that the stable equilibria of f are just the totally aligned states $W = \pm U$ rather than $W = \pm \Lambda U$. More precisely, for $\Lambda = 1$, the equilibria correspond to the symmetric state

$$u_r = u_l = \frac{1}{2} U_1$$

and the totally aligned states

$$(u_r = 0, u_l = U_3 = -W_3 > 0) \quad \text{and} \quad (u_r = U_2 = W_2 > 0, u_l = 0).$$

We note that $g_{s,1}$ diverges at $W = -C$. We will see in an instant that C is determined by c and the value of U at the trivial equilibrium $W = 0$. The divergence of $g_{s,1}$ stems from that of $f_{s,1}$ as u approaches 0 along a path not belonging to the set $\{w \in [-u, u]\}$. Since we do not look for solutions in the regime $|W| > U$ this divergence is not an obstacle to our computations. The exponential term is always positive so that the zeros are given by

1. $W_1 = 0, U_1 > 0$, from which we deduce $C = cU_1$, and we find the point of divergence of $g_{s,1}$ at $W_* = -cU_1$. If we choose $U_1 = 1$, we obtain $C = c$.

2. $W_2 = U_2$. This yields
$$W_2 = \frac{W_2 + C}{c} = \frac{W_2 + cU_1}{c}$$

and thus

$$U_2 = W_2 = U_1 \frac{c}{c-1}. \tag{13.32}$$

We require $U_2 \geq 0$, and since $U_1 > 0$ we obtain as admissible velocities for this case:

$$c \in (-\infty, 0) \cup (1, \infty).$$

It should be noted that U_2 tends to infinity as c approaches 1 from above. We also note that for $c > 1$ we have $W_* < 0$ so that the divergence of $g_{s,1}$ cannot take place between $W_1 = 0$ and $W_2 > 0$ whereas for $c < 0$ we have

$$\frac{c}{c-1} < -c$$

which now assures that the equilibrium value W_2 lies between 0 and W_*.

3. $W_3 = -U_3$. We now find

$$cU_3 = W_3 + C = -U_3 + cU_1$$

or

$$-W_3 = U_3 = U_1 \frac{c}{c+1}, \tag{13.33}$$

which allows the following velocities to assure nonnegativity of U_3:

$$c \in (-\infty, -1) \cup (0, \infty), \tag{13.34}$$

where again U_3 grows to infinity as c approaches -1 from below. As in case 2 we find the critical point W_* for no admissible c lying between $W_1 = 0$ and W_3.

We conclude that we always find one fixed point at $W = 0$. If $|c| > 1$, we find two more equilibria whereas for $0 < |c| < 1$ there is only one further equilibrium.

Remark 13.7. *We note that the equilibria are completely independent of ε!*

13.5.2 Linearization around the equilibria

If we ask now for the linearization around the asymptotic states (U_i, W_i) $(i = 1, 2, 3)$ we have to compute the derivatives of g at the particular values W_i.

For the sublinear bistable alignment term with exponential decay we obtain

$$g'_{s,1}(W) = \alpha \left(1 - \frac{c^2 W^2}{(C+W)^2} \left(1 + \frac{2C}{C+W} \right) + 2\beta^2 \left(\frac{W^3}{C+W} - \frac{W(C+W)}{c^2} \right) \right) \mathcal{E}$$

where now $\mathcal{E}$ is an abbreviation for

$$\mathcal{E} = \exp\left[-\frac{\beta^2}{c^2} (W + C)^2 \right].$$

Inserting the equilibrium values computed above, we obtain the following values.

1. At $W_1 = 0$ we find

$$g'_{s,1}(0) = \alpha \exp\left[-\beta^2 U_1^2 \right] \tag{13.35}$$

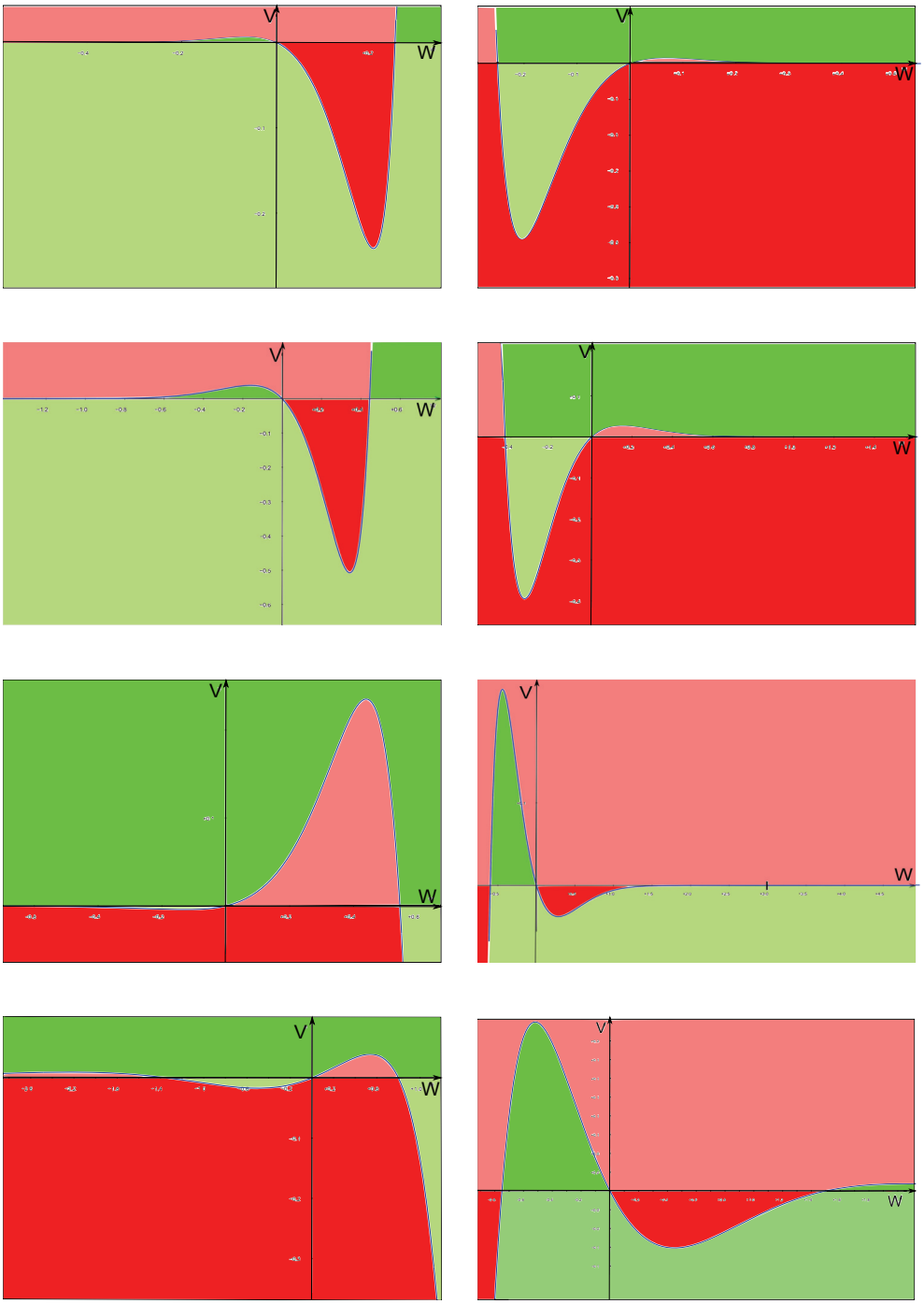

Figure 13.7: Null clines of $V' = -\mu V - \frac{1}{\varepsilon} g_{s,1}(W)$ in W-V-phase space. Parameters: $\alpha = \varepsilon = 2.0$, $\beta^2 = 2$, $U_1 = 1$, leading to $c^* \approx 1.94$. Colors code for the signs of V' and W': *green*: $W' > 0, V' > 0$, *pale green*: $W' < 0, V' > 0$, *pale red*: $W' > 0, V' < 0$, *red*: $W' < 0, V' < 0$. *left, from top*: $c = -\frac{1}{3} \in (-c_*, 0)$, $c = -\frac{4}{5} \in (-1, -c_*)$, $c = -\frac{6}{5} \in (-c^*, -1)$, $c = -4 < -c^*$. *right, from top*: $c = \frac{1}{3} \in (0, c_*)$, $c = \frac{3}{4} \in (c_*, 1)$, $c = \frac{3}{2} \in (1, c^*)$, $c = 3 > c^*$.

which is completely independent of the velocity c and always positive.

2. At $W_2 = U_2 = U_1 \frac{c}{c-1}$ we have

$$g'_{s,1}\left(U_1 \frac{c}{c-1}\right) = -2\alpha \frac{c-1}{c} \exp\left[-\beta^2 \frac{c^2}{(c-1)^2} U_1^2\right]. \tag{13.36}$$

Note that this is negative for the admissible values of c for this point.

3. At $W_3 = -U_3 = -U_1 \frac{c}{c+1}$ we finally find

$$g'_{s,1}\left(-U_1 \frac{c}{c+1}\right) = -2\alpha \frac{c+1}{c} \exp\left[-\beta^2 \frac{c^2}{(c+1)^2} U_1^2\right]. \tag{13.37}$$

This is again negative for the allowed values of c.

Let us now examine the linear stability of the found equilibria. As in section 13.3 we write

$$\mu = \frac{1}{\varepsilon}\left(c - \frac{1}{c}\right)$$

to obtain

$$W'' + \mu W' = -\frac{1}{\varepsilon} g(W) = -\frac{1}{\varepsilon} f\left(\frac{W+C}{c}, W\right) \tag{13.38}$$

and from this the linearizations around the equilibria W_i:

$$\tilde{W}'' + \mu \tilde{W}' = -\frac{1}{\varepsilon} g'(W_i)\tilde{W} \tag{13.39}$$

where $\tilde{W} = W - W_i$. If we abbreviate $G_i := g'(W_i)$ we readily rewrite equation (13.11) for the eigenvalues of the linearized equation at $W_1 = 0$ to

$$\nu_{1,\pm} \quad = \quad -\frac{\mu}{2} \pm \sqrt{\frac{\mu^2}{4} - \frac{G_1}{\varepsilon}} \quad = \quad -\frac{\mu}{2} \pm \sqrt{\frac{\mu^2}{4} - \frac{\alpha \mathcal{E}_1}{\varepsilon}} \tag{13.40}$$

where we used the additional abbreviation

$$\mathcal{E}_1 = \exp\left[-\beta^2 U_1^2\right].$$

We observe that the behavior of the eigenvalues now depends on the steady state value of U. Again, we are looking for real roots and thus have to require

$$\frac{\mu^2}{4} \geq \frac{G_i}{\varepsilon}$$

which now translates into

$$\frac{1}{\varepsilon}\left(c - \frac{1}{c}\right)^2 \geq 4\alpha \exp\left[-\beta^2 U_1^2\right]. \tag{13.41}$$

In contrast to the case of f being independent of U, this inequality can now be

fulfilled for any given $c \in \mathbb{R}\backslash\{-1,0,1\}$ if U_1 is only chosen large enough, namely:

$$U_1^2 > -\frac{1}{\beta^2}\left(2\log\left[\left|c-\frac{1}{c}\right|\right] - \log[4\alpha\varepsilon]\right) \tag{13.42}$$

which is trivially fulfilled if the right hand side is negative. In figure 13.8, we show the dependence of the right hand side of (13.42) on positive c and the product $\alpha\varepsilon$ and note that the picture is symmetric with respect to the $\alpha\varepsilon$-axis. If we are conversely given an asymptotic equilibrium value U_1 at $W_1 = 0$ we obtain again four critical velocities, depending on $\alpha\varepsilon$ and U_1 in the following way:

$$\pm c^* = \pm\sqrt{1+2\alpha\varepsilon\exp[-\beta^2U_1^2]\left(1+\sqrt{\frac{\exp[\beta^2U_1^2]}{\alpha\varepsilon}+1}\right)} \tag{13.43}$$

$$\pm c_* = \pm\sqrt{1+2\alpha\varepsilon\exp[-\beta^2U_1^2]\left(1-\sqrt{\frac{\exp[\beta^2U_1^2]}{\alpha\varepsilon}+1}\right)} = \pm\frac{1}{c^*}. \tag{13.44}$$

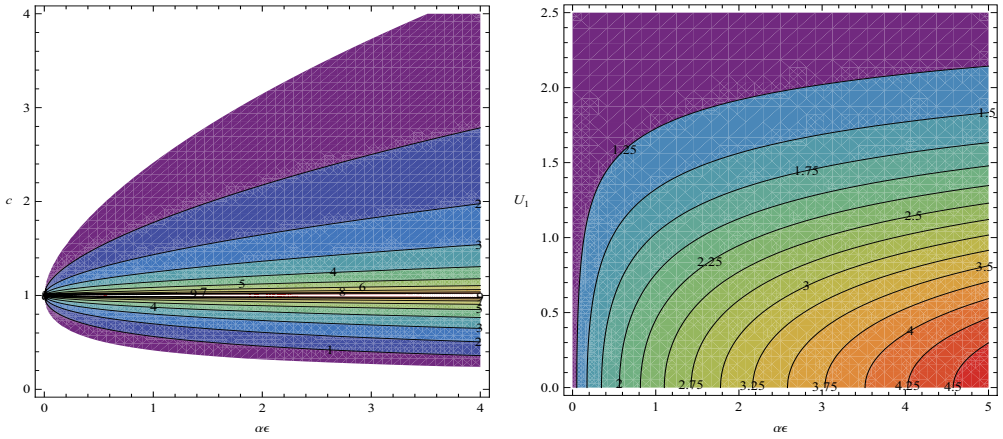

Figure 13.8: *Left*: minimal required value of U_1^2 depending on c and the product $\alpha\varepsilon$. In the white regions, the right hand side of (13.42) is negative so that any value of $U_1 > 0$ is allowed. *Right*: critical velocity c^* depending on U_1 and the product $\alpha\varepsilon$. In both cases: $\beta = 1$.

Again, if the eigenvalues $\nu_{1,\pm}$ are real, both have the same sign and we obtain a node whose stability depends on the wave speed c:

$$\nu_{1,\pm}\begin{Bmatrix}>\\<\end{Bmatrix}0 \iff \mu = \frac{1}{\varepsilon}\left(c-\frac{1}{c}\right)\begin{Bmatrix}<\\>\end{Bmatrix}0 \iff c \in \begin{Bmatrix}(-\infty,-1)\cup(0,1)\\(-1,0)\cup(1,\infty)\end{Bmatrix}. \tag{13.45}$$

To summarize the behavior of the eigenvalues in dependence on the wave speed c and the product $a = \varepsilon g'(\bar{W})$ we show a bifurcation diagram in figure 13.9.

Just for completeness we note that in case of non-real eigenvalues, the sign of their real parts again only depends on the sign of μ and we obtain a spiral point with stability depending on whether $|c|$ is bigger or smaller than 1.

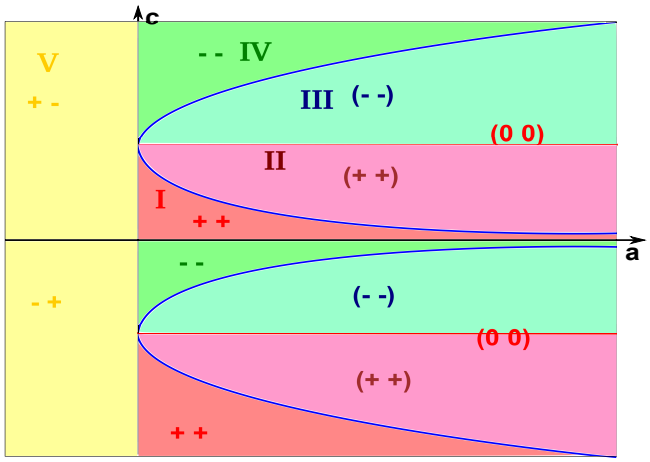

Figure 13.9: Behavior of the eigenvalues of the linearization at equilibria depending on $a = \varepsilon g'(\bar{W})$ and wave speed c. The signs of the real parts of the eigenvalues are indicated for each region where parentheses are used to indicate a pair of complex conjugate eigenvalues.

Asking for the eigenvalues of the equilibrium at

$$W_2 = \frac{c}{c-1} U_1$$

we obtain

$$\nu_{2,\pm} = -\frac{\mu}{2} \pm \sqrt{\frac{\mu^2}{4} - \frac{G_2}{\varepsilon}} = -\frac{\mu}{2} \pm \sqrt{\frac{\mu^2}{4} + 2\frac{\alpha}{\varepsilon}\frac{c-1}{c} \exp\left[-\beta^2 \frac{c^2}{(c-1)^2} U_1^2\right]}. \quad (13.46)$$

We recall that this equilibrium can only exist if the velocity satisfies

$$c \in (-\infty, 0) \cup (1, \infty)$$

which assures the positivity of the radicand and yields two real eigenvalues of opposite sign.

Similarly, we find at

$$W_3 = -\frac{c}{c+1} U_1$$

the eigenvalues

$$\nu_{3,\pm} = -\frac{\mu}{2} \pm \sqrt{\frac{\mu^2}{4} - \frac{G_3}{\varepsilon}} = -\frac{\mu}{2} \pm \sqrt{\frac{\mu^2}{4} + 2\frac{\alpha}{\varepsilon}\frac{c+1}{c} \exp\left[-\beta^2 \frac{c^2}{(c+1)^2} U_1^2\right]} \quad (13.47)$$

which are again real and of opposite sign for each velocity c that allows the existence of this equilibrium.

We finally note that the eigenvectors of equation (13.38) at the equilibrium point W_i can be written as

$$\begin{pmatrix} -\frac{\varepsilon\mu}{G_i} \pm \sqrt{\left(\frac{\varepsilon\mu}{2G_i}\right)^2 - \frac{\varepsilon}{G_i}} \\ 1 \end{pmatrix}$$

which is the same as

$$\begin{pmatrix} \frac{\varepsilon}{G_i}\nu_{i,\mp} \\ \\ 1 \end{pmatrix} \tag{13.48}$$

corresponding to the eigenvalues $\nu_{i,\pm}$.

Let us summarize the behavior of the eigenvalues in the different regimes of figure 13.9 and in particular upon crossing the lines where the character of the equilibria changes.

1. We start with $a = \varepsilon g'(\bar{W}) > 0$, that is, with the inner equilibrium $W = 0$ where the derivative of the alignment term with respect to W is positive.

   - Starting at large positive wave speeds $c > c^*(a)$ we are in region IV and observe two real negative eigenvalues. We are thus dealing with a stable node in this parameter regime.
   - Crossing the line $c = c^*(a)$ we enter region III where $1 < c < c^*(a)$ and there is a pair of complex conjugate eigenvalues with negative real part, corresponding to a stable spiral point.
   - As c decreases further and passes through one, the real part of the complex conjugate pair changes sign and we encounter a Hopf bifurcation with bifurcation parameter $1-c$. Whether this bifurcation is subcritical or supercritical depends on the higher order terms of the alignment term f. This can be seen by defining

     $$\omega_0 := \sqrt{\frac{g'(0)}{\varepsilon}} \qquad \text{and} \qquad \tilde{V} := \omega_0^{-1} V$$

     and rewriting system (13.31) in the form

     $$\begin{aligned} \frac{d}{d\xi}\begin{pmatrix}\tilde{V}\\ W\end{pmatrix} &= \begin{pmatrix} -\frac{1}{\varepsilon}\left(c - \frac{1}{c}\right)\tilde{V} - \frac{1}{\omega_0 \varepsilon} g(W) \\ \omega_0 \tilde{V} \end{pmatrix} \\ &= \begin{pmatrix} 0 & -\omega_0 \\ \omega_0 & 0 \end{pmatrix}\begin{pmatrix}\tilde{V}\\ W\end{pmatrix} + \begin{pmatrix} -\frac{1}{\varepsilon}\left(c - \frac{1}{c}\right)\tilde{V} + \omega_0 W - \frac{g(W)}{\omega_0 \varepsilon} \\ 0 \end{pmatrix} \\ &=: \begin{pmatrix} 0 & -\omega_0 \\ \omega_0 & 0 \end{pmatrix}\begin{pmatrix}\tilde{V}\\ W\end{pmatrix} + \begin{pmatrix}\phi(\tilde{V}, W)\\ 0\end{pmatrix}. \end{aligned}$$

     We already recognized that

     $$(W = 0, U = U_1 > 0)$$

     is an equilibrium point of the system whose linearization at this point has at the parameter value $c = 1$ a pair of purely imaginary eigenvalues $\pm\imath\omega_0$ which are nonzero as long as $g'(0) > 0$. For bilinear alignment terms this condition is always satisfied. We furthermore know that the real part of these eigenvalues for $c \neq 1$ is given by

     $$\frac{1}{\varepsilon}\left(\frac{1}{c} - c\right)$$

     and thus the pair crosses the imaginary axis transversally as c passes through one. We compute the first LYAPUNOV coefficient $l_1(0)$ to be zero (cf. appendix

B) at the bifurcation point and therefore, the bifurcation is degenerate.

That periodic orbits cannot exist for c different from one can also be deduced from physical considerations. Recalling the equation

$$\ddot{W} + \mu\dot{W} + \frac{1}{\varepsilon}g(W) = 0$$

for W and noting that $\mu = 0$ if and only if $c = \pm 1$ we observe that we deal with an equation describing an anharmonic oscillator which exhibits periodic orbits only in case of vanishing dissipation $\mu = 0$.

It should also be noted that a global bifurcation takes place at $c = 1$ since the positive equilibrium point characterized by

$$W_2 = U_2 = \frac{c}{c-1}U_1$$

vanishes to $W = \infty$ as c approaches one from above and is not present anymore for $c < 1$.

The flow field in the W-V-space for different c close to one is visualized in figure 13.10. It can be seen that there will always be a heteroclinic orbit connecting the equilibria at

$$W = W_3 = -\frac{c}{c+1}U_1$$

and the trivial equilibrium $W = 0$.

- Passing through the line $c = c_*(a)$ we enter region I where we have $a > 0$ and $0 < c < c_*(a)$. Here, the eigenvalues are real again and now are positive. We thus find an unstable node.
- Decreasing the wave speed further towards zero, one of the positive, real eigenvalues will decrease to zero whereas the other one diverges to $+\infty$ with order $\mathcal{O}(c^{-1})$.
- For negative speeds c we observe the symmetric behavior with all signs of the eigenvalues switched.

2. Let us now briefly discuss the behavior of the eigenvalues for $a < 0$ which corresponds to the linearization around the outer equilibria

$$W = \pm U \neq 0.$$

For any $c > 0$ we are in region V and there are two real eigenvalues of opposite sign and we therefore deal with a saddle. The negative eigenvalue will tend to zero as c does while the positive one grows to $+\infty$. as c passes through zero, both of these eigenvalues change their sign, and the saddle is recovered also for negative speeds.

3. Let us finally discuss the behavior close to the c-axis. We will assume that the derivative $g'(\bar{W})$ is fixed and examine the behavior of the eigenvalues as ε decreases to zero.

- Let us start with the case $g'(0) > 0,\ c > 1$. That is, we choose a fixed velocity larger than one and look at the linearization around the inner equilibrium $W = 0$. Starting at large values of ε we are in region III with a pair of complex conjugate eigenvalues with negative real part of increasing size. As ε decreases we reach the line $c = c^*(\varepsilon g'(0))$ and the eigenvalues merge and for further decreasing ε become distinct, real and negative as we enter domain IV. One of those now decreases and tends to $-\infty$ at rate $\mathcal{O}(\varepsilon^{-1})$. The other one increases but remains bounded away from zero tending to some finite negative value.
- Doing the same procedure for fixed $g'(0) > 0$ and $c \in (0, 1)$ we start in region II with an unstable focus with a pair of complex conjugate eigenvalues with positive real part. Passing through the line $c = c_*(\varepsilon g'(0))$ these eigenvalues become real and positive to give rise to an unstable node. As ε tends to zero, the larger of these eigenvalues tends to $+\infty$ at rate $\mathcal{O}(\varepsilon)$ whereas the smaller one remains bounded and approaches a finite positive value.
- Approaching the c-axis along the curve $c = c^*(\varepsilon g'(0))$ for fixed $g'(0) > 0$ we have a double negative eigenvalue which is given by

$$\begin{aligned}
\nu_\pm(\varepsilon) &= -\frac{1}{2\varepsilon}\left(c^*(\varepsilon g'(0)) - \frac{1}{c^*(\varepsilon g'(0))}\right) \\
&= -\frac{1}{2\varepsilon}\frac{1 + 2\varepsilon g'(0) + 2\sqrt{\varepsilon g'(0) + \varepsilon^2 g'(0)^2} - 1}{\sqrt{1 + 2\varepsilon g'(0) + 2\sqrt{\varepsilon g'(0) + \varepsilon^2 g'(0)^2}}} \\
&= -\frac{1}{2}\frac{2g'(0) + 2\sqrt{\frac{g'(0)}{\varepsilon} + g'(0)^2}}{\sqrt{1 + 2\varepsilon g'(0) + 2\sqrt{\varepsilon g'(0) + \varepsilon^2 g'(0)^2}}} \quad = \quad -\sqrt{\frac{g'(0)}{\varepsilon}}
\end{aligned}$$

  and therefore diverges to $-\infty$ at rate $\mathcal{O}(\varepsilon^{-\frac{1}{2}})$. The previous computation particularly shows that decreasing both, the alignment strength encoded in $g'(0)$ and the diffusion coefficient ε, at the same rate leads in the limit to a finite negative eigenvalue which would give rise to a stable node.
- Approaching the c-axis from the right along the line $c = 1$ there is a pair of purely imaginary eigenvalues having the values

$$\pm\imath\sqrt{\frac{g'(0)}{\varepsilon}}.$$

  We therefore may obtain as possible limits 0, $\pm\imath\infty$, or $\pm\imath \cdot const.$, depending on the way the limit $a \searrow 0$ is established. In the particular case of letting ε go to zero while holding α constant, this pair of eigenvalues gives rise to ever faster oscillatory behavior.

Remark 13.8. *The effect of particle velocities $v \neq 1$ now enters not only the parameter μ but also the right hand side g. We recall that the alignment term now reads*

$$g(w) = f\left(\frac{v}{c}(W + C),\ W\right).$$

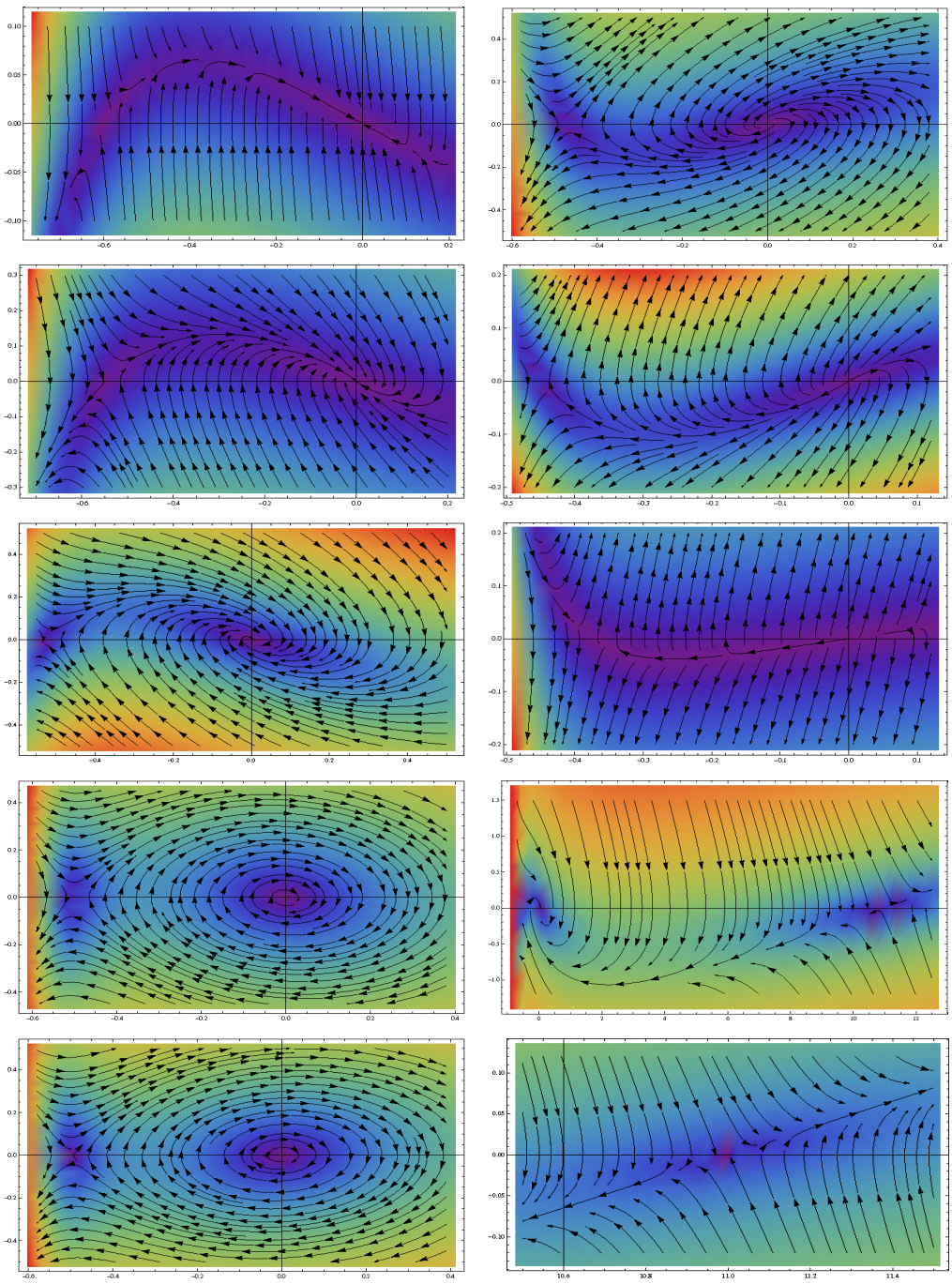

Figure 13.10: Flow field of system (13.31) in the $W-V$-plane. Parameters: $\alpha = 0.2$, $\varepsilon = 0.2$, $U_1 = 1.0$, leading to $c^* \approx 1.17$, $c_* \approx 0.85$, sublinear alignment term (12.8). *Left*: flow field around the equilibria at $W = 0$ and $W = W_3 = -\frac{c}{c+1}$ for $c = 1.5 > c^*$, $c = 1.2 \gtrsim c^*$, $1 < c = 1.1 < c^*$, $1 \lesssim c = 1.01 < c^*$, $c_* < c = 0.99 \lesssim 1$ (*from top*), *right*: flow field around $W = 0$ and $W = -\frac{c}{c+1}U_1$ for $c_* < c = 0.9 < 1$, $c = 0.82 \lesssim c_*$, $c = 0.6 < c_*$, and for completeness the whole flow field with all equilibria and the zoom around $W = W_2 = \frac{c}{c-1}U_1$ for $c = 1.1$, the latter two without exponential term for better visualization (*from top*). The heteroclinic orbits and the absence of periodic orbits can be easily seen in each of the images.

Clearly,

$$(U := U_1, W = 0)$$

is an equilibrium state, and we conclude that the constant of integration C takes the value

$$C = \frac{c}{v} U_1.$$

The other equilibria are given by

$$W_2 = U_2 = \frac{c}{c-v} U_1 \qquad \text{and} \qquad -W_3 = U_3 = \frac{c}{c+v} U_1.$$

The derivative of $g_{s,1}$ (corresponding to $f = f_{s,1}$) with respect to W is

$$\begin{aligned} & g'_{s,1}(W) \\ &= \alpha \left(1 + \frac{c^2}{v^2} \frac{W^2}{(W+C)^2} \left(\frac{2W}{W+C} - 3 \right) - 2\beta^2 W(W+C) \left(\frac{v^2}{c^2} - \frac{W^2}{(W+C)^2} \right) \right) \mathcal{E} \end{aligned}$$

where $\mathcal{E}$ denotes the exponential term

$$\mathcal{E} = \exp\left[-\beta^2 \frac{v^2}{c^2} (W+C)^2 \right].$$

Putting W to zero we find the following value

$$g'_{s,1}(0) = \alpha \exp\left[-\beta^2 U_1^2 \right]$$

which is the same as observed for $v = 1$.

At the outer equilibria $W_2 = U_2$ and $W_3 = -U_3$ we calculate

$$\begin{aligned} g'_{s,1}(W_2) &= \alpha \left(1 + \left(2\frac{v}{c} - 3 \right) \right) \exp[-\beta^2 U_2^2] \\ &= -2\alpha \frac{c-v}{c} \exp\left[-\beta^2 \frac{c^2}{(c-v)^2} U_1^2 \right] \end{aligned}$$

and

$$g'_{s,1}(W_3) = -2\alpha \frac{c+v}{c} \exp\left[-\beta^2 \frac{c^2}{(c+v)^2} U_1^2 \right].$$

It remains to calculate the critical wave speeds c^* and c_*. These are given by

$$\begin{aligned} \pm\, \tilde{c}^*(U_1, v) &= \pm \sqrt{ v^2 + 2a \left(1 + \sqrt{1 + \frac{v^2}{a}} \right) } \\ &= \pm \sqrt{ v^2 + 2\varepsilon\alpha \exp\left[-\beta^2 U_1^2 \right] \left(1 + \sqrt{1 + \frac{v^2 \exp\left[\beta^2 U_1^2 \right]}{\varepsilon\alpha}} \right) } \\ &= \frac{1}{\tilde{c}_*(U_1, v)}. \end{aligned} \tag{13.49}$$

We observe a similar symmetry as for $v = 1$ but now the forbidden velocities are $\pm v$.

13.5.3 Phase plane analysis

To conclude the existence of heteroclinic orbits we are now going to analyze the behavior of system (13.31) in the W-V-phase plane as already done for the alignment term without dependence on U in section 13.4.

We now choose a different invariant triangle which is still bounded by the positive W-axis and the line corresponding to the eigenvector $\eta_{1,+}$ at $(0,0)^T$ but now by the line $\{W = W_2\}$ rather than the unstable eigenspace of the linearization around $(W_2, 0)^T$. That this does not make a difference becomes immediately clear if we recall that the outer equilibria are always saddles and thus by the special form of the eigenvectors, the stable eigenspaces are always given by lines of positive slope whereas the unstable eigenspaces have negative slope. The situation is indicated in figure 13.11.

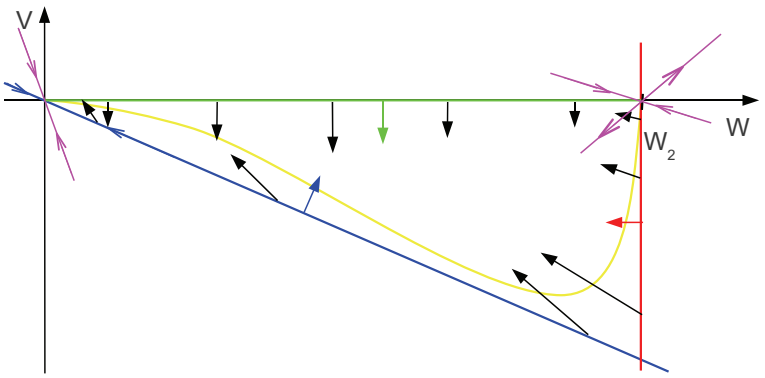

Figure 13.11: Invariant domain in phase plane for waves connecting $W_2 = U_2$ to $(W_1 = 0, U = U_1)$ with velocity $c > c^*(U_1)$. The colored arrows denote the inner unit normals (*blue*: $\mathfrak{n}_1$ on the line corresponding to the eigenvector $\eta_{1,+}$ at the origin, *red*: $\mathfrak{n}_2$ on the line $\{W = W_2\}$, *green*: $\mathfrak{n}_0$ on the W-axis), the *black* arrows indicate the flow field along the boundary of the invariant triangle. *Magenta* arrows indicate the remaining eigenvectors, the *yellow* curve shows $V' = 0$.

For the invariance along the first two segments we can employ the computations from section 13.4 with F_w being replaced by G_1 if we can establish the estimate

$$g(W) < G_1 W \qquad \text{for} \quad 0 < W < W_2.$$

We do so by calculating

$$\begin{aligned} g(W) &= \alpha W \underbrace{\left(1 - \left(\frac{cW}{W + cU_1}\right)^2\right)}_{<1 \ f.e. W>0} \underbrace{\exp\left[-\frac{\beta^2}{c^2}(W + cU_1)^2\right]}_{<\exp\left[-\frac{\beta^2}{c^2}c^2U_1^2\right] \ f.e. \ W>0} \\ &< \alpha W \exp\left[-\beta^2 U_1^2\right] \quad = \quad G_1 W. \end{aligned} \tag{13.50}$$

Along the line $\{W = W_2\}$ we observe that the inner normal is given by $\mathfrak{n}_2 = (-1, 0)$

and that we are in the lower half space and thus

$$\mathfrak{n}_2\Phi = -V > 0$$

along that line. Again, we conclude the existence of a heteroclinic orbit connecting $(W_2, 0)^T$ to the origin.

The modifications for the remaining cases are very similar, and we will not treat them in detail here.

A note on superlinear alignment terms

If we consider system (9.2) with a superlinear alignment term, the estimate in (13.25) fails since G is no longer bounded by its linearization around $W = 0$. Still trying to find an appropriate invariant domain we shall look for a line $V = -\tilde{G}_1 W$ with $\tilde{G}_1 > 0$ such that along this line, the vector field points towards the half plane above the line, that is

$$(\mu - \tilde{G}_1)\tilde{G}_1 W - \frac{1}{\varepsilon} g(W) > 0 \qquad \text{for each } W \in (0, W_2)$$

Let us for example consider the alignment term $\tilde{f}_{2,s}$ and omit the exponential term for these calculations as it only makes the alignment term smaller for positive particle densities. Thus, any estimate we obtain in the following also holds in the case with exponential crowding term.

We therefore have to check whether the following term remains positive for all $W \in (0, W_2)$:

$$\varphi(W) := \tilde{G}_1(\mu - \tilde{G}_1) - \frac{\alpha}{\varepsilon} - \frac{\alpha}{\varepsilon}\frac{cW}{W + cU_1}\left(\nu - (\nu+1)\frac{cW}{W + cU_1}\right).$$

In order to guarantee positivity for small W we first have to require

$$\tilde{G}_1(\mu - \tilde{G}_1) - \frac{\alpha}{\varepsilon} \geq 0$$

and deduce that we have to seek $\tilde{G}_1$ within the range of the eigenvalues:

$$0 < \frac{\mu}{2} - \sqrt{\frac{\mu^2}{4} - \frac{\alpha}{\varepsilon}} \;\leq\; \tilde{G}_1 \;\leq\; \frac{\mu}{2} - \sqrt{\frac{\mu^2}{4} - \frac{\alpha}{\varepsilon}} < \mu. \tag{13.51}$$

That these eigenvalues are real and positive is clear since we are in the velocity range $c > c^*$.

The next observation is that φ has precisely one local minimum between 0 and W_2 which is determined by

$$0 = \varphi'(W) \quad - \frac{\alpha}{\varepsilon}\frac{c^2 U_1}{(W + cU_1)^2}\left(\nu - 2(\nu+1)\frac{cW}{W + cU_1}\right).$$

For $cU_1 + W > 0$, this equation is equivalent to

$$\nu(W + cU_1) - 2(\nu+1)cW = 0$$

and has the solution

$$W_{min} = \frac{c\nu}{2(\nu+1)c-\nu}U_1 \quad \left(< \frac{c}{c-1}U_1 \equiv W_2 \right).$$

We are therefore on the safe side if we can assure that $\varphi(W_{min})$ is not smaller than zero. We first calculate

$$\begin{aligned}\frac{cW_{min}}{W_{min}+cU_1} &= \frac{\nu c^2 U_1}{(2(\nu+1)c-\nu)\left(\frac{c\nu}{2(\nu+1)c-\nu}U_1 + cU_1\right)} \\ &= \frac{\nu c}{\nu + (2(\nu+1)c-\nu)} \\ &= \frac{\nu}{2(\nu+1)}\end{aligned}$$

and plug this into φ:

$$\begin{aligned}\varphi(W_{min}) &= \tilde{G}_1(\mu-\tilde{G}_1) - \frac{\alpha}{\varepsilon} - \frac{\alpha}{\varepsilon}\frac{\nu}{2(\nu+1)}\left(\nu - (\nu+1)\frac{\nu}{2(\nu+1)}\right) \\ &= \tilde{G}_1(\mu-\tilde{G}_1) - \frac{\alpha}{\varepsilon} - \frac{\alpha}{\varepsilon}\frac{\nu^2}{4(\nu+1)}.\end{aligned}$$

This has to be non-negative,

$$0 \le -\tilde{G}_1^2 + \mu\tilde{G}_1 - \frac{\alpha}{\varepsilon}\left(1 + \frac{\nu^2}{4(\nu+1)}\right)$$

which is true if $\tilde{G}_1$ lies between the roots

$$\frac{\mu}{2} \pm \frac{1}{2}\sqrt{\mu^2 - 4\frac{\alpha}{\varepsilon}\left(1+\frac{\nu^2}{4(\nu+1)}\right)}.$$

This condition is just a further refinement of (13.51).

In order to find such a $\tilde{G}_1$ we have to require the positivity of the discriminant and obtain

$$\varepsilon\mu^2 \ge 4\alpha\left(1+\frac{\nu^2}{4(\nu+1)}\right)$$

which is just another version of (13.12) with $F_w = \alpha$ being replaced by the larger value

$$\alpha\left(1+\frac{\nu^2}{4(\nu+1)}\right).$$

In particular, we obtain the same shape for the critical velocity as in (13.16), namely

$$c^*_{sup} = \sqrt{1 + 2a_{sup} + 2\sqrt{a_{sup}(a_{sup}+1)}} \tag{13.52}$$

but now with a_{sup} being given by

$$a_{sup} = \alpha\varepsilon\left(1+\frac{\nu^2}{4(\nu+1)}\right) \tag{13.53}$$

rather than $a = \alpha\varepsilon$.

For the other types of waves connecting non-polarized with totally aligned states, we can do similar calculations yielding similar results.

We should finally note, that the condition $c > c^*_{sup}$ is a sufficient condition for the existence of a heteroclinic orbit for the superlinear alignment term. We have not checked for more complicated boundaries of a possible invariant domain than just a triangle. That means, that we cannot exclude the existence of such orbits for all velocities c between c^* and c^*_{sup} but we hope that it became clear that the superlinearity of f requires c to be genuinly larger than c^* for such f.

Example 1. Let us again consider a numerical example. We choose

$$\varepsilon = \alpha = 2 \qquad \beta = 1 \qquad U_1 = \tfrac{3}{4}.$$

and as velocity $c = 4$.

From these we obtain the following values:

$$\frac{c}{c-1} = \frac{4}{3}, \qquad \frac{c}{c+1} = \frac{4}{5}, \qquad \mu = \frac{15}{8}$$

and as equilibria apart from $W_1 = 0$:

$$W_2 = U_2 = 1 \qquad \text{and} \qquad W_3 = -U_3 = -\frac{3}{5}.$$

The derivatives of $g_{s,1}$ at these equilibria are

$$G_1 = 2\exp\left[-\frac{9}{16}\right], \qquad G_2 = -3\exp[-1], \qquad G_3 = -5\exp\left[-\frac{9}{25}\right]$$

yielding the eigenvalues

$$\nu_{1,\pm} = -\frac{15}{16} \pm \sqrt{\frac{225}{256} - \exp\left[-\frac{9}{16}\right]} \approx \begin{cases} -0.38 \\ -1.49 \end{cases}$$

$$\nu_{2,\pm} = -\frac{15}{16} \pm \sqrt{\frac{225}{256} + \frac{3}{2}\exp[-1]} \approx \begin{cases} 0.26 \\ -2.13 \end{cases}$$

$$\nu_{3,\pm} = -\frac{15}{16} \pm \sqrt{\frac{225}{256} + \frac{5}{2}\exp\left[-\frac{9}{25}\right]} \approx \begin{cases} 0.68 \\ -2.56 \end{cases}.$$

The corresponding eigenvectors are approximately given by

$$\text{at } W_1: \qquad \begin{pmatrix} -2.62 \\ 1 \end{pmatrix} \text{ and } \begin{pmatrix} -0.67 \\ 1 \end{pmatrix}$$

$$\text{at } W_2: \qquad \begin{pmatrix} 3.87 \\ 1 \end{pmatrix} \text{ and } \begin{pmatrix} -0.47 \\ 1 \end{pmatrix}$$

$$\text{at } W_3: \qquad \begin{pmatrix} 1.47 \\ 1 \end{pmatrix} \quad \text{and} \quad \begin{pmatrix} -0.39 \\ 1 \end{pmatrix}.$$

We obtain possible waves connecting either of the states

$$U_2 = W_2 = 1 \qquad \text{or} \qquad U_3 = -W_3 = \frac{3}{5}$$

with the state

$$(U_1 = \frac{3}{4}, W_1 = 0),$$

shown at the top of figure 13.12.

Example 2. Let us as second example consider a wave speed $c = \frac{1}{4}$ and an equilibrium value $U_1 = \frac{5}{4}$ with the other parameters given as above. The derived parameters are now

$$\frac{c}{c-1} = -\frac{1}{3}, \qquad \frac{c}{c+1} = \frac{1}{5}, \qquad \mu = -\frac{15}{8}.$$

We note that the second equilibrium does now not exist within the allowed range of values for U and W whereas the third one is given by

$$-W_3 = U_3 = \frac{1}{4}.$$

Furthermore we compute the derivatives at the remaining fixed points as

$$G_1 = 2\exp\left[-\frac{25}{16}\right] \qquad \text{and} \qquad G_3 = -20\exp\left[-\frac{1}{16}\right],$$

the resulting eigenvalues of equation (13.38) as

$$\nu_{1,\pm} \approx \begin{cases} 1.76 \\ 0.12 \end{cases} \qquad \text{and} \qquad \nu_{3,\pm} \approx \begin{cases} 5.37 \\ -3.50 \end{cases}$$

and finally the approximate corresponding eigenvectors as

$$\text{at } W_1: \qquad \begin{pmatrix} 0.57 \\ 1 \end{pmatrix} \quad \text{and} \quad \begin{pmatrix} 8.38 \\ 1 \end{pmatrix}$$

and

$$\text{at } W_3: \qquad \begin{pmatrix} 0.33 \\ 1 \end{pmatrix} \quad \text{and} \quad \begin{pmatrix} -0.50 \\ 1 \end{pmatrix}.$$

For this parameter setting we only obtain one possible wave connecting now the state

$$(U_1 = \frac{5}{4}, W_1 = 0)$$

with the state

$$U_3 = -W_3 = \frac{1}{4}.$$

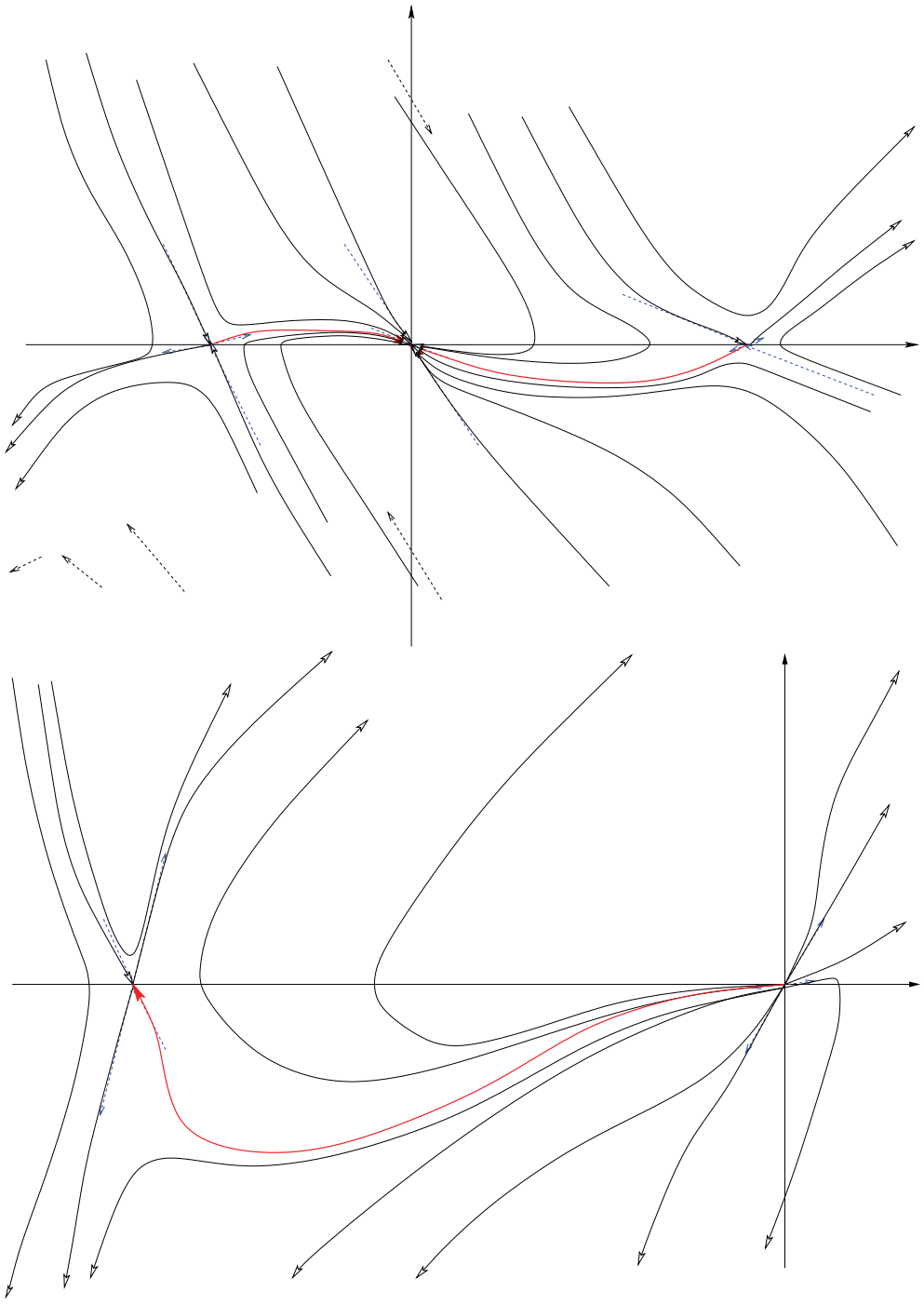

Figure 13.12: Flow fields for system (13.30) with $g = g_{s,1}$ and parameter values $\varepsilon = \alpha = 2, \beta = 1$. *Top:* $\mu = \frac{15}{8}$ $(c = 4), U_1 = \frac{3}{4}$, *Bottom:* $\mu = -\frac{15}{8}$ $(c = \frac{1}{4}), U_1 = \frac{5}{4}$. *Red*: Orbit connecting the stationary points. The *blue dotted* arrows denote the eigenvectors of the linearizations.

We conclude with a proposition summarizing the above results:

Proposition 13.9. *Consider system (9.2) on* $\mathbb{R} \times (0, \infty)$ *with*

$$f(u, w) = \alpha w \left(1 - \frac{w^2}{u^2}\right) \exp\left[-\beta^2 u^2\right]$$

and parameters $\alpha, \varepsilon > 0$. *Given* $U_1 > 0$ *set*

$$c^*(U_1) := \sqrt{1 + 2\alpha\varepsilon \exp[-\beta^2 U_1^2] \left(1 + \sqrt{\frac{\exp[\beta^2 U_1^2]}{\alpha\varepsilon} + 1}\right)}$$

Then, the system allows traveling wave solutions of the following types:

1. *Fast waves traveling to the right with velocity* $c > 1$, *connecting either of the states*

$$U = W = U_1 \frac{c}{c-1} \qquad \text{or} \qquad U = -W = U_1 \frac{c}{c+1}$$

with the state $(U = U_1, W = 0)$ *if* c *and* U_1 *satisfy*

$$c > c^*(U_1).$$

2. *Slow waves traveling to the right with velocity* $c \in (0, 1)$, *connecting the state* $(U = U_1, W = 0)$ *with the state*

$$U = -W = U_1 \frac{c}{c+1}$$

if c *and* U_1 *satisfy*

$$0 < c < \frac{1}{c^*(U_1)}.$$

3. *Slow waves traveling to the left with velocity* $c \in (-1, 0)$, *connecting the state*

$$U = W = U_1 \frac{c}{c-1}$$

with the state $(U = U_1, W = 0)$ *if* c *and* U_1 *satisfy*

$$-1 < c < -\frac{1}{c^*(U_1)}.$$

4. *Fast waves traveling to the left with velocity* $c < -1$, *connecting the state* $(U = U_1, W = 0)$ *with either of the states*

$$U = W = U_1 \frac{c}{c-1} \qquad \text{or} \qquad U = -W = U_1 \frac{c}{c+1}$$

if c *and* U_1 *satisfy*

$$c < -c^*(U_1).$$

13.6 Constructing a solution by gluing together traveling wave solutions

Let us now try to construct an approximate solution to (9.2) on $\mathbb{R} \times (0, \infty)$ and with $f = f_{s,1}$ consisting of two humps, one traveling to either direction and both increasing in width.

Since the asymptotic state as $x \to \pm\infty$ should be of the type

$$(U = U_1, W = 0)$$

with the same U_1, according to proposition 13.9 there is only one pattern to be expected:

1. The front of the right hump traveling with velocity $c_1 > 0$, connecting the state

$$U_3 = -W_3 = \frac{c_1}{c_1 + 1} U_1$$

with the state $(U = U_1, W = 0)$.

2. The rear of the right hump traveling with velocity $c_2 \in (0, 1)$, connecting the state

$$W = 0, \tilde{U}_1 = \frac{c_2 + 1}{c_2} U_3, \ W = 0$$

with the state $(U, W) = (U_3, -U_3)$.

3. The rear of the left hump traveling with velocity $c_3 \in (-1, 0)$, connecting the state

$$W_2 = U_2 = \frac{c_3}{c_3 - 1} \tilde{U}_1$$

with the state $(\tilde{U}_1, 0)$.

4. The front of the left hump traveling with velocity $c_4 < -1$, connecting the state $(U_1, 0)$ with the state (U_2, U_2) which implies

$$U_2 = \frac{c_4}{c_4 - 1} U_1.$$

We furthermore note, that monotone wave patterns require in addition

$$c_1 > c^*(U_1) \qquad c_2 < \frac{1}{c^*(\tilde{U}_1)}$$
$$c_3 > -\frac{1}{c^*(\tilde{U}_1)} \qquad c_4 < -c^*(U_1).$$

Example 1 - a symmetric pattern. Using parameters $\alpha = \varepsilon = 2$, $\beta = 1$ as above, we choose as asymptotic particle density at infinity $U_1 = \frac{3}{4}$. This leads to a critical velocity of

$$c^* = \sqrt{1 + 8 \exp\left[-\frac{9}{16}\right] \left(1 + \sqrt{\frac{\exp\left[\frac{9}{16}\right]}{4} + 1}\right)} \approx 3.32.$$

To obtain a symmetric solution (which is not at all necessary but convenient) let us furthermore assume $c_1 = -c_4$ and $c_2 = -c_3$. The following choices are admissible in the sense that they allow for monotone traveling wave solutions:

- $c_1 = 4 = -c_4$. This leads to the following values of U_2 and U_3:

$$\begin{aligned} U_2 &= \frac{c_4}{c_4 - 1} U_1 = \frac{-4}{-5}\,\frac{3}{4} = \frac{3}{5} \\ U_3 &= \frac{c_1}{c_1 + 1} U_1 = \frac{4}{5}\,\frac{3}{4} = \frac{3}{5}. \end{aligned}$$

- $c_2 = \frac{1}{2} = -c_3$. We find consistently:

$$\tilde{U}_1 = \frac{c_3 - 1}{c_3} U_2 = \frac{-\frac{3}{2}}{-\frac{1}{2}}\frac{3}{5} = \frac{9}{5} = \frac{\frac{3}{2}}{\frac{1}{2}}\frac{3}{5} = \frac{c_2 + 1}{c_2} U_3.$$

For the computations we note that the parameters μ are given by:

$$\begin{aligned} \mu_1 &= \frac{1}{\varepsilon}\left(c_1 - \frac{1}{c_1}\right) = \frac{15}{8} = -\mu_4 \\ -\mu_2 &= -\frac{1}{\varepsilon}\left(c_2 - \frac{1}{c_2}\right) = \frac{3}{4} = \mu_3. \end{aligned}$$

The wave profiles shown below are computed numerically by integrating equation (13.30) along the heteroclinic orbit from the saddle (U_2, U_2) or $(U_3, -U_3)$ to the node $(U_1, 0)$ or $(\tilde{U}_1, 0)$, respectively. That is, (13.30) is supplemented with initial conditions $W(\xi_0) = W_i$ and $W'(\xi_0) = 0$.

Of course, for waves emerging from an unstable node at $W = 0$ and ending at the saddle along the stable manifold of the latter we have to integrate the equation backward in ξ. We also should note that in fact, we cannot start exactly at the saddle (U_i, W_i) but have to shift the start value by some small δ towards 0 and calculate $W'(\xi_0)$ according to the eigenvectors obtained from the linearization around the respective saddle.

We finally choose the values ξ_0 in such a manner as to ensure that the waves are located in the appropriate order along the ξ-axis. The precise calculations are:

1. For the first wave front we choose find as starting point $W(\xi_{0,1}) = -\frac{3}{5} + \delta$ and note that the appropriate heteroclinic orbit emerges from the saddle along its unstable manifold and ends at the stable node in 0. For the eigenvector corresponding to the positive eigenvalue at W_3 we already computed in the example above:

$$\begin{pmatrix} 1.47 \\ 1 \end{pmatrix}.$$

   We thus choose as initial conditions

$$W(\xi_0) = -\frac{3}{5} + \delta \qquad \text{and} \qquad W'(\xi_0) = \frac{\delta}{1.47}.$$

   In figure 13.13, we show the wave pattern for this particular traveling wave solution.

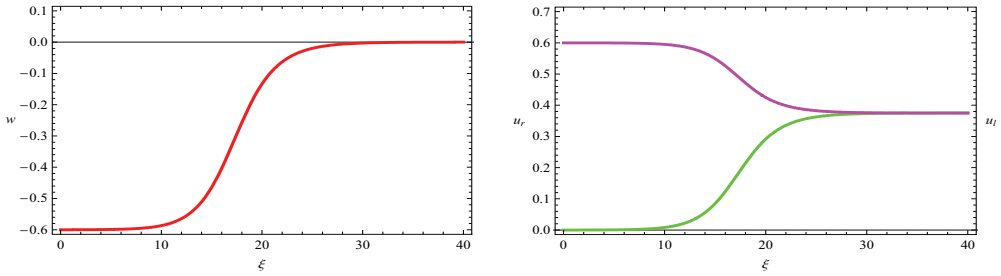

Figure 13.13: A traveling wave for system (9.2) connecting the states $W = -U = -\frac{3}{5}$ and $W = 0$, $U = \frac{3}{4}$ at a velocity of $c = 4$. *Left*: Wave pattern for W. *Right*: Corresponding values of U_r (green) and U_l (magenta).

2. The rear of the right hump is a wave front connecting the unstable node at $(\tilde{U}_1, 0)$ with the saddle at $(U_3, -U_3)$. We now have to compute the eigenvalues

$$G_3 = -2\alpha \frac{c_2 + 1}{c_2} \exp\left[-\frac{c_2^2}{(c_2+1)^2}\tilde{U}_1^2\right] = -12 \exp\left[-\frac{9}{25}\right],$$

$$\nu_{3,\pm} = -\frac{\mu_2}{2} \pm \sqrt{\frac{\mu_2^2}{2} - \frac{G_3}{\varepsilon}} = \frac{3}{8} \pm \sqrt{\frac{9}{64} + 6\exp\left[-\frac{9}{25}\right]} \approx \begin{cases} 2.46 \\ -1.71 \end{cases},$$

and finally as eigenvector corresponding now to the negative eigenvalue:

$$\begin{pmatrix} \frac{\varepsilon}{G_3}\nu_{3,+} \\ 1 \end{pmatrix} \approx \begin{pmatrix} -0.29 \\ 1 \end{pmatrix}.$$

The appropriate initial conditions are thus

$$W(\xi_{0,2}) = -\frac{3}{5} + \delta \qquad \text{and} \qquad W'(\xi_{0,2}) = -\frac{\delta}{0.29}.$$

3. At the rear of the left hump we have a wave connecting the state (U_2, U_2) with the state $(\tilde{U}_1, 0)$. We now calculate:

$$G_2 = -2\alpha \frac{c_3 - 1}{c_3} \exp\left[-\frac{c_3^2}{(c_3-1)^2}\tilde{U}_1^2\right] = -12 \exp\left[-\frac{9}{25}\right],$$

which is the same as G_3 from the previous wave.

The eigenvalues of the linearized system at (U_2, W_2) are thus given by:

$$\nu_{2,\pm} = -\frac{\mu_3}{2} \pm \sqrt{\frac{\mu_3^2}{2} - \frac{G_2}{\varepsilon}} = -\frac{3}{8} \pm \sqrt{\frac{9}{64} + 6\exp\left[-\frac{9}{25}\right]} \approx \begin{cases} 1.71 \\ -2.46 \end{cases},$$

and an eigenvector corresponding to the positive eigenvalue is

$$\begin{pmatrix} \frac{\varepsilon}{G_2}\nu_{2,-} \\ 1 \end{pmatrix} \approx \begin{pmatrix} 0.29 \\ 1 \end{pmatrix}.$$

We will thus choose as initial conditions

$$W(\xi_{0,3}) = \frac{3}{5} - \delta \qquad \text{and} \qquad W'(\xi_{0,3}) = -\frac{\delta}{0.29}.$$

4. The front of the left hump is treated completely complementarily to the front of the right hump. That is, our initial conditions are now given by

$$W(\xi_{0,4}) = \frac{3}{5} - \delta \qquad \text{and} \qquad W'(\xi_{0,4}) = -\frac{\delta}{1.47}.$$

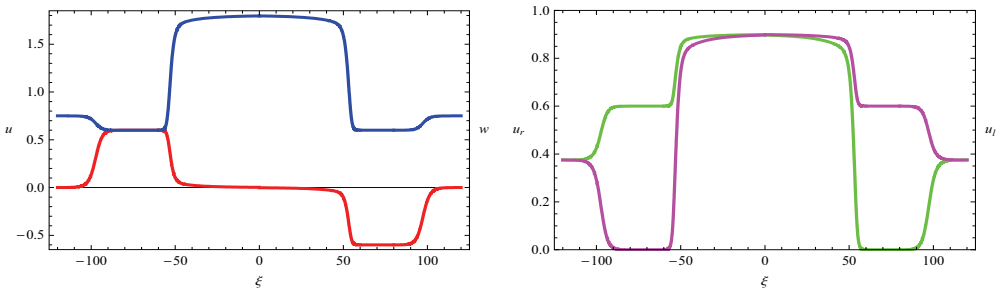

Figure 13.14: An approximate solution to (9.2) at some time t_0 constructed from four traveling waves. Velocities: $c = \pm 4$ at the outer fronts, $c = \pm\frac{1}{2}$ at the rears. *Left*: Wave pattern for U (blue) and W (red). *Right*: Corresponding values of U_r (green) and U_l (magenta).

We finally have to choose the start points $\xi_{0,i}$ according to the width of the wave fronts. This is effectively done by starting always at $\xi = 0$ and shifting the individual waves afterwards.

In figure 13.14, we show an example of the resulting pattern at some given instant t_0. Such a solution can be understood as some kind of contraction taking place in the center of the pattern. Here a high total density of non-aligned particles accumulates whereas in the moving humps totally aligned particles move at lower density towards the central region. We end up with an increasing region of high density and two recruitment zones moving outwards and also increasing in width.

Example 2 - a slightly asymmetric pattern. Let us now show an example of such a traveling wave solution with an asymmetric shape. This may be suspected to develop from asymmetric initial variations of the homogeneous steady state

$$(U = U_1, W = 0).$$

Here, we only show the possible existence of such a solution. However, we should already note that the simulations in chapter 15 will provide evidence that only very special wave speeds are selected and we therefore do not find such asymmetric patterns in the full simulations since the asymmetry is connected to a difference between the velocities of the right and left moving fronts.

We now choose $\varepsilon = \alpha = 0.2$ and an asymptotic particle density of $U_1 = 1$. This yields a critical wave speed of

$$c^* = \sqrt{1 + 0.08 \exp[-1] \left(1 + \sqrt{\frac{e}{0.04} + 1}\right)} \approx 1.097.$$

We may now choose the velocities closer to 1, say

$$c_1 = \frac{5}{4}, \qquad c_2 = \frac{3}{4}, \qquad c_3 = -\frac{4}{5}.$$

The last velocity has now to be determined from the requirement $U_1 = 1$ as asymptotic state as $\xi \to -\infty$. We calculate the respective values of interest to us. The right-most wave front has the parameters:

$$\begin{aligned}
\mu_1 &= 5\left(\frac{5}{4} - \frac{4}{5}\right) = \frac{9}{4} \\
U_3 &= \frac{\frac{5}{4}}{\frac{5}{4}+1} 1 = \frac{5}{9} \\
G_3 &= -2 \cdot 0.2 \frac{9}{5} \exp\left[-\frac{25}{81} 1\right] = -\frac{18}{25} \exp\left[-\frac{25}{81}\right],
\end{aligned}$$

and the resulting eigenpairs are given by

$$\begin{aligned}
\nu_{3,\pm} &= -\frac{9}{8} \pm \sqrt{\frac{81}{64} + \frac{18}{5} \exp\left[-\frac{25}{81}\right]} = \begin{cases} 0.85 \\ -3.10 \end{cases} \\
\eta_{3,+} &= \begin{pmatrix} 1.5 \\ 1 \end{pmatrix}
\end{aligned}$$

where we have written $\eta_{3,+}$ for the eigenvector corresponding to the positive eigenvalue.

At the rear of the right hump we compute

$$\mu_2 = -\frac{35}{12}, \qquad \tilde{U}_1 = \frac{35}{27}, \qquad G_3 = -\frac{14}{15} \exp\left[-\frac{25}{81}\right]$$

$$\nu_{3,\pm} \approx \begin{cases} 3.82 \\ -0.90 \end{cases}, \qquad \eta_{3,-} \approx \begin{pmatrix} -1.11 \\ 1 \end{pmatrix}.$$

For the slow wave front traveling to the left we find

$$\mu_3 = \frac{9}{4}, \qquad U_2 = \frac{140}{243}, \qquad G_2 = -\frac{9}{10} \exp\left[-\frac{19600}{59049}\right]$$

$$\nu_{2,\pm} \approx \begin{cases} 1.00 \\ -3.25 \end{cases}, \qquad \eta_{2,+} \approx \begin{pmatrix} 1.00 \\ 1 \end{pmatrix}.$$

For the fourth wave we have first to compute the wave speed from the requirement

$$1 \;=\; U_1 \;=\; \frac{c_4-1}{c_4}U_2 \;=\; \frac{c_4-1}{c_4}\frac{140}{243}$$

and find

$$c_4 = -\frac{140}{103} \approx -1.36\ , \qquad \mu_4 = -\frac{8991}{2884} \approx -3.1175, \qquad G_2 = -\frac{243}{350}\exp\left[-\frac{19600}{59049}\right]$$

$$\nu_{2,\pm} \approx \begin{cases} 3.78 \\ -0.66 \end{cases}, \qquad \eta_{2,-} \approx \begin{pmatrix} -0.78 \\ 1 \end{pmatrix}.$$

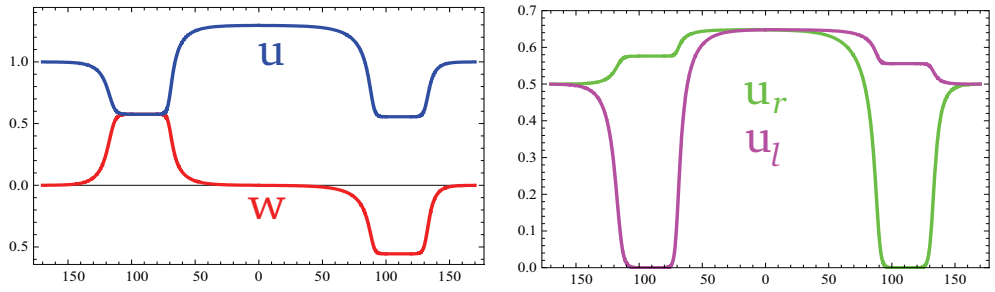

Figure 13.15: An approximate solution to (9.2) at some time t_0 constructed from four slightly asymmetric traveling waves. Velocities (from left to right): $c_4 = -\frac{140}{103}$, $c_3 = -\frac{4}{5}$, $c_2 = 34$, $c_1 = 54$. *Left*: Wave pattern for U (blue) and W (red). *Right*: Corresponding values of U_r (green) and U_l (magenta).

The resulting pattern is shown in figure 13.15 and can be seen to be very similar to the one obtained in example 1.

Example 3 - a strongly asymmetric pattern. Again we use $\alpha = \varepsilon = 0.2$ and $U_1 = 1$ but now velocities

$$c_1 = \frac{5}{4}, \qquad c_2 = \frac{1}{2}, \qquad c_3 = -\frac{9}{10}.$$

The values to be computed are now:

- At the front of the right hump:

$$\mu_1 = \frac{9}{4}\ , \qquad U_3 \;=\; \frac{9}{5}\ , \qquad G_3 = -\frac{18}{25}\exp\left[-\frac{25}{81}\right]$$

$$\nu_{3,\pm} \approx \begin{cases} 0.85 \\ -3.10 \end{cases}, \qquad \eta_{3,+} \approx \begin{pmatrix} 1.17 \\ 1 \end{pmatrix}.$$

- At the rear of the right hump:

$$\mu_2 = -\frac{15}{2}\,, \qquad \tilde{U}_1 \;=\; \frac{5}{3}\,, \qquad G_3 = -\frac{6}{5}\exp\left[-\frac{25}{81}\right]$$
$$\nu_{3,\pm} \approx \begin{cases} 8.05 \\ -0.55 \end{cases}, \qquad \eta_{3,-} \approx \begin{pmatrix} -1.83 \\ 1 \end{pmatrix}.$$

- At the rear of the left hump:

$$\mu_3 = \frac{19}{18}\,, \qquad U_2 \;=\; \frac{15}{19}\,, \qquad G_2 = -\frac{38}{45}\exp\left[-\frac{18225}{130321}\right]$$
$$\nu_{2,\pm} \approx \begin{cases} 1.46 \\ -2.52 \end{cases}, \qquad \eta_{2,+} \approx \begin{pmatrix} 0.69 \\ 1 \end{pmatrix}.$$

- At the front of the left hump:

$$c_4 = -\frac{15}{4}\,, \qquad \mu_2 \;=\; -\frac{209}{12}\,, \qquad G_2 = -\frac{38}{75}\exp\left[-\frac{225}{361}\right]$$
$$\nu_{2,\pm} \approx \begin{cases} 17.49 \\ -0.08 \end{cases}, \qquad \eta_{2,-} \approx \begin{pmatrix} -12.88 \\ 1 \end{pmatrix}.$$

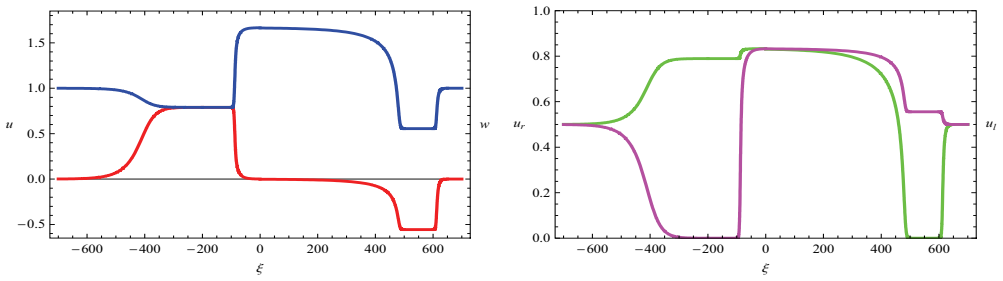

Figure 13.16: An approximate solution to (9.2) at some time t_0 constructed from four strongly asymmetric traveling waves. Velocities (from left to right): $c_4 = -\frac{15}{4}$, $c_3 = -\frac{9}{10}$, $c_2 = 12$, $c_1 = 54$. *Left*: Wave pattern for U (blue) and W (red). *Right*: Corresponding values of U_r (green) and U_l (magenta).

The resulting strongly asymmetric wave pattern is drawn in figure 13.16. Concerning the stability and hence the emergence of such a solution from perturbations of the homogeneous steady state the same reasoning as for the slightly asymmetric case applies. That means, that the selection of particular wave speeds prevents these patterns to emerge in simulations,

Apart from such solutions constructed from traveling waves glued together at their asymptotic states we can also construct the other types of traveling waves mentioned in proposition 13.9. As an example let us consider parameters $\alpha = \varepsilon = \beta = \Lambda = 1$ and an asymptotic state $U_1 = 1$. We would now like to construct a traveling wave of positive

velocity c connecting some state $W_2 = U_2$ to this asymptotic state. Choosing as velocity $c = 4$ we find

$$\mu = \frac{15}{4} \quad , \qquad U_2 = W_2 = \frac{4}{3} \quad , \qquad G_2 = -\frac{3}{2}\exp\left[-\frac{16}{9}\right]$$
$$\nu_{2,\pm} = \begin{cases} 0.07 \\ -3.82 \end{cases} \quad , \qquad \eta_{2,+} = \begin{pmatrix} 15.10 \\ 1 \end{pmatrix}.$$

We observe a very small eigenvalue indicating that the trajectory will be run through very slowly in the beginning. In figure 13.17 where the resulting wave pattern is drawn this slowness is reflected by the large interval along the ξ-axis.

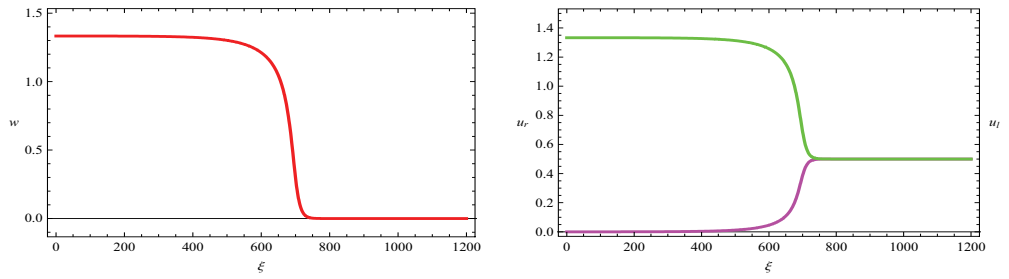

Figure 13.17: Traveling wave profile for W (*left*) and $U_{r,l}$ (*right*) for a wave connecting the state $W = U$ to the state $W = 0$ with parameters as indicated in the above example.

From this type of wave we cannot even construct a plateau like solution where the wave obtained above is glued together with one traveling to the left, since for the latter one we would require $U_2 < U_1$ which would be a contradiction to having $U_1 = 1$ as asymptotic state.

We finally note that the existence of such waves of positive polarization W_2 penetrating into a non-polarized state $W = 0$ does not rely in a crucial way on the exponential decay term in f. To see that, consider instead of $f_{s,1}$ the unbounded alignment term

$$f_1(U, W) = \alpha W \left(1 - \frac{W^2}{U^2}\right) \tag{13.54}$$

or, after replacing U by $\frac{1}{c}(W + C)$,

$$g_1(W) = \alpha W \left(1 - \frac{(cW)^2}{(W + C)^2}\right).$$

Its derivative is computed to be

$$g_1'(W) = \alpha\left(1 - \frac{c^2W^2}{(W + C)^3}(W + 3C)\right) = \alpha\left(1 - \frac{c^2W^2}{(W + C)^3}(W + 3C)\right) \tag{13.55}$$

whereas the zeros remain the same as for $g_{s,1}$. At these critical points the derivatives now read

- at $W_1 = 0$:

$$G_1 = \alpha \tag{13.56}$$

- at $W_2 = U_2 = \frac{c}{c-1}U_1$:

$$\begin{aligned} G_2 &= \alpha\left(1 - \frac{c^2W^2}{(W+C)^2}\frac{W+3C}{W+C}\right) \\ &= -\alpha\frac{2C}{W+C} \quad = \quad -2\alpha\frac{c-1}{c}. \end{aligned} \tag{13.57}$$

  where in the last step we additionally used $C = cU_1$.

- at $W_3 = -U_3 = -\frac{c}{c+1}U_3$:

$$G_3 = -2\alpha\frac{c+1}{c}. \tag{13.58}$$

Again, the precise steady states may be obtained by fixing the value of U_1. With the notation from section 13.5 we arrive at the following possible eigenvalues of the linearizations around the steady states:

$$\nu_{1,\pm} = -\frac{\mu}{2} \pm \sqrt{\frac{\mu^2}{4} - \frac{G_1}{\varepsilon}} = -\frac{\mu}{2} \pm \sqrt{\frac{\mu^2}{4} - \frac{\alpha}{\varepsilon}} \tag{13.59}$$

$$\nu_{2,\pm} = -\frac{\mu}{2} \pm \sqrt{\frac{\mu^2}{4} - \frac{G_2}{\varepsilon}} = -\frac{\mu}{2} \pm \sqrt{\frac{\mu^2}{4} + 2\frac{c-1}{c}\frac{\alpha}{\varepsilon}} \tag{13.60}$$

$$\nu_{3,\pm} = -\frac{\mu}{2} \pm \sqrt{\frac{\mu^2}{4} - \frac{G_3}{\varepsilon}} = -\frac{\mu}{2} \pm \sqrt{\frac{\mu^2}{4} + 2\frac{c+1}{c}\frac{\alpha}{\varepsilon}}. \tag{13.61}$$

We immediately observe that the points (U_2, U_2) and $(U_3, -U_3)$ are saddles whereas the point $(U_1, 0)$ is a node whenever

$$\frac{\mu^2}{4} > \frac{\alpha}{\varepsilon}$$

which is the case if and only if $|c| \notin [c_*, c^*]$ with c_* and c^* given by (13.16) with $a = \alpha\varepsilon$. We observe that the critical velocities do not depend on the chosen value of U_1 as it was the case for $f_{s,1}$ with exponential term.

13.7 Oscillating (quasi-) waves

Recall that the condition of $|c|$ being larger than $c^*(U_1)$ or smaller than $c_* = 1/c^*$ was due to the requirement that the eigenvalues of the linearized equations around the steady states should be real. This is necessary for obtaining monotone wave fronts.

One may ask whether there are possibly also wave patterns which are not monotone but oscillate into or out of their asymptotic states. We note that the eigenvalues at states of the type $W_2 = U_2$ or $W_3 = -U_3$ are automatically real whenever the velocity is such that these steady state values satisfy $U > 0$. Non-real eigenvalues can thus only occur around the state $(W_1 = 0,\ U_1 > 0)$ where oscillations of small amplitude do not cause the density of any type of particles to locally drop below zero.

This allows for formal traveling wave solutions to the system having oscillating tails at the non-polarized states. We will again construct such solutions by gluing together several of these wave trains but note that we were not able to find oscillating wave patterns in the simulations as they appear to be unstable. Again, this does not tell us that these solutions do not exist.

Example 1 - a pattern of waves with oscillations. We choose as parameters $\alpha = \varepsilon = \beta = 1$ and as asymptotic density $U_1 = 1$. The resulting critical velocity is now

$$c^* = \sqrt{1 + \frac{2}{e}\left(1 + \sqrt{e+1}\right)} \approx 1.78$$

and we deliberately choose as velocity for the front $c_1 = \frac{8}{7} < c^*$. This yields the following parameters:

$$\mu_1 = \frac{15}{56} \quad , \qquad -W_3 = U_3 = \frac{8}{15} \quad , \qquad G_3 = -\frac{15}{4}\exp\left[-\frac{64}{225}\right].$$

As eigenvalues of the linearized system at the steady states we now find:

$$\nu_{1,\pm} \approx -0.13 \pm 0.59\imath \quad , \qquad \nu_{3,\pm} = \begin{cases} 1.55 \\ -1.82 \end{cases} .$$

To obtain appropriate initial conditions we compute in addition the eigenvector at the state $-W_3 = U_3$ corresponding to the positive eigenvalue:

$$\eta_{3,+} = \begin{pmatrix} 0.64 \\ 1 \end{pmatrix}.$$

We show this wave train in figure 13.18.

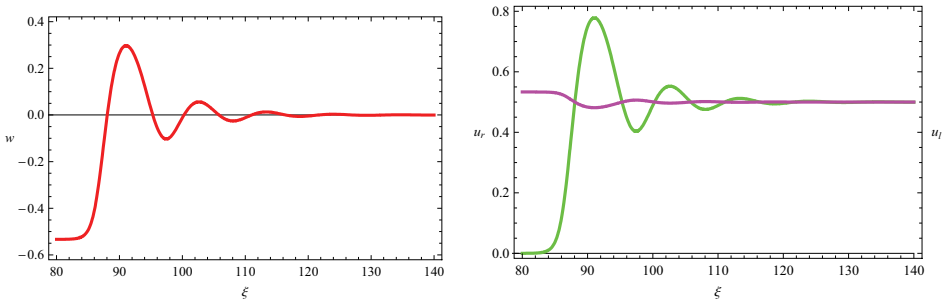

Figure 13.18: Oscillating (quasi-) traveling wave solution for (9.2) connecting the state $-W = U = \frac{8}{15}$ with the state $W = 0$, $U = 1$ at velocity $c = \frac{8}{7}$. *left*: Wave pattern for W. *right*: Corresponding values of U_r (green) and U_l (magenta).

To complete the picture we continue constructing an approximate solution to (9.2) by adding three further waves. Let us choose as velocities $c_2 = \frac{8}{13}$ and $c_3 = -\frac{3}{4}$. For

the second wave we find the following parameters:

$$\mu_2 = -\frac{105}{104}\ , \qquad \tilde{U}_1 = \frac{7}{5}$$
$$G_1 = \exp\left[-\frac{49}{25}\right]\ , \qquad G_3 = -\frac{21}{4}\exp\left[-\frac{64}{225}\right]$$

and as eigenvalues of the linearizations around the asymptotic states:

$$\nu_{1,\pm} \approx \begin{cases} 0.84 \\ 0.17 \end{cases}\ , \qquad \nu_{3,\pm} \approx \begin{cases} 2.56 \\ -1.55 \end{cases}\ .$$

We note that all the eigenvalues are now real and thus we deal with a genuine and in particular monotone traveling wave at this point. Finally the eigenvector at the state $-W_3 = U_3$ corresponding to the negative eigenvalue is found to be

$$\eta_{3,-} \approx \begin{pmatrix} -0.65 \\ 1 \end{pmatrix}.$$

For the third wave we compute

$$\mu_3 = \frac{7}{12}\ , \qquad U_2 = W_2 = \frac{3}{5}\ , \qquad G_2 = -\frac{14}{3}\exp\left[-\frac{9}{25}\right]$$

and the eigenvalues

$$\nu_{1,\pm} \approx -0.29 \pm 0.24\imath\ , \qquad \nu_{2,\pm} \approx \begin{cases} 1.54 \\ -2.12 \end{cases}$$

and as eigenvector corresponding to the positive eigenvalue at $W_2 = U_2$:

$$\eta_{2,+} \approx \begin{pmatrix} 0.65 \\ 1 \end{pmatrix}.$$

We finally have to compute the parameters for the last wave. We first find $c_4 = -\frac{3}{2}$ and from that the parameters

$$\mu_4 = -\frac{5}{6}\ , \qquad G_2 = -\frac{22}{5}\exp\left[-\frac{50}{121}\right],$$

the eigenvalues

$$\nu_{1,\pm} \approx 0.42 \pm 0.44\imath\ , \qquad \nu_{2,\pm} \approx \begin{cases} 2.35 \\ -1.52 \end{cases}$$

and as appropriate eigenvector at the state $U_2 = W_2$

$$\eta_{2,-} \approx \begin{pmatrix} -0.66 \\ 1 \end{pmatrix}.$$

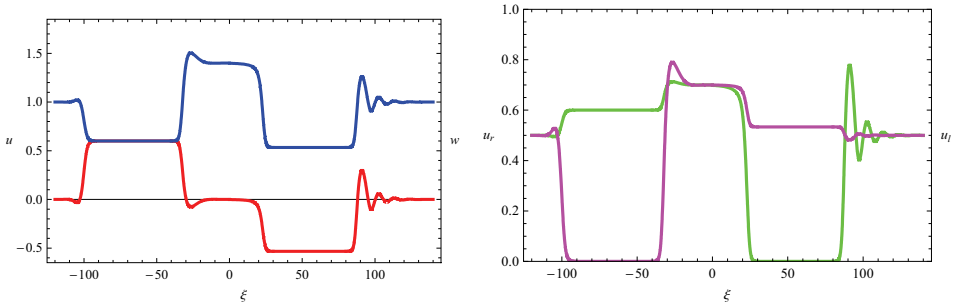

Figure 13.19: An approximate solution to (9.2) at some time t_0 constructed from one traveling wave and three oscillating (quasi-) waves. Velocities (from left to right): $c_4 = -\frac{3}{2}$, $c_3 = -\frac{3}{4}$, $c_2 = 8/13$, $c_1 = 8/7$. *Left*: Wave pattern for U (blue) and W (red), *right*: corresponding vales of U_r (green) and U_l (magenta).

We note that for the third and fourth wave train we find complex eigenvalues at the $W = 0$ - state which turns us to expect oscillations close to this state. The resulting pattern of all four waves glued together is shown in figure 13.19. Note the oscillations at all the wave trains except for the second one. We furthermore emphasize that the strength of the oscillations obviously increases with the ratio

$$\frac{|\operatorname{Im}\nu_1|}{|\Re\nu_1|}.$$

Chapter 14

Traveling Wave Solutions to the Full Probelm

Let us now consider solutions of the type

$$\begin{array}{rcl} u(t,x) & = & U(x-ct) \\ w(t,x) & = & W(x-ct) \end{array} \tag{14.1}$$

for model (9.4). We obtain a system of ordinary differential equations of the form

$$\begin{array}{ll} -cU'(\xi)+W'(\xi) & = \varepsilon U''(\xi) \\ -cW'(\xi)+U'(\xi) & = \varepsilon W''(\xi)+f(U,W) \end{array} \tag{14.2}$$

The first equation of (14.2) can be integrated once to yield

$$\varepsilon U'(\xi) = -cU(\xi)+W(\xi)+C, \tag{14.3}$$

where C is a constant of integration to be determined. Putting again $V(\xi) := W'(\xi)$ we can now derive from the second equation of (14.2):

$$\begin{array}{rl} \varepsilon V' \equiv \varepsilon W'' & = -cW'+U'-f(U,W) \\ & = -cV+\dfrac{1}{\varepsilon}\left(-cU+W+C\right)-f(U,W) \end{array} \tag{14.4}$$

and finally obtain the following system of three ordinary differential equations of first order:

$$\begin{array}{rcl} U'(\xi) & = & -\frac{c}{\varepsilon}U(\xi) \quad +\frac{1}{\varepsilon}W(\xi) \qquad\qquad +\frac{C}{\varepsilon} \\ W'(\xi) & = & \qquad\qquad\qquad V \\ V'(\xi) & = & -\frac{c}{\varepsilon^2}U \quad +\frac{1}{\varepsilon^2}W \quad -\frac{c}{\varepsilon}V \quad +\frac{C}{\varepsilon^2}-\frac{1}{\varepsilon}f(U,W). \end{array} \tag{14.5}$$

We ask for equilibria of this system and immediately find from the first two equations under the assumption of c being different from zero, $V=0$ and

$$-cU+W+C \quad = \quad 0 \tag{14.6}$$

which may be used in the third equation of (14.5) to find the conditions

$$0 = f(U,W) = f\left(\frac{W+C}{c}, W\right) = g(W). \tag{14.7}$$

We thus recover the problem of finding the zeros of f which may now be viewed as curves in the $V = 0$ - plane. Given the sublinear bistable version of the alignment term

$$f(U,W) = f_{s,1}(U,W) = \alpha W\left(1 - \frac{W^2}{U^2}\right)\exp\left[-\beta^2 U^2\right] \tag{14.8}$$

we find f to vanish along the lines $\{W = 0\}$ and $\{W = \pm U\}$. The same equilibria are found for the superlinear bistable version of f as well − always given $\Lambda = 1$.

14.1 Linearization around the equilibria

The linearization of system (14.5) around the steady state ($U = U_1,\ W = 0$) reads as follows:

$$\begin{aligned}
\tilde{U}' &= -\tfrac{c}{\varepsilon}\tilde{U} + \tfrac{1}{\varepsilon}\tilde{W} \\
\tilde{W}' &= \tilde{V} \\
\tilde{V}' &= -\tfrac{c}{\varepsilon^2}\tilde{U} + \tfrac{1}{\varepsilon}\left(\tfrac{1}{\varepsilon} - g'(0)\right)\tilde{W} - \tfrac{c}{\varepsilon}\tilde{V}
\end{aligned} \tag{14.9}$$

or in concise form

$$\begin{pmatrix}\tilde{U}'\\ \tilde{W}'\\ \tilde{V}'\end{pmatrix} = \frac{1}{\varepsilon}\begin{pmatrix}-c & 1 & 0\\ 0 & 0 & \varepsilon\\ -\frac{c}{\varepsilon} & \frac{1}{\varepsilon} - g'(0) & -c\end{pmatrix}\begin{pmatrix}\tilde{U}\\ \tilde{W}\\ \tilde{V}\end{pmatrix} =: A\begin{pmatrix}\tilde{U}\\ \tilde{W}\\ \tilde{V}\end{pmatrix} \tag{14.10}$$

where $\tilde{U},\ \tilde{W},\ \tilde{V}$ denote the deviations of $U,\ W,\ V$ from their equilibria:

$$\tilde{U} = U - U_1\ , \qquad \tilde{W} = W - 0 = W\ , \qquad \tilde{V} = V - 0 = V. \tag{14.11}$$

The corresponding characteristic polynomial takes the form

$$\det(\nu^\bullet - A) = \nu^3 + 2\frac{c}{\varepsilon}\nu^2 + \frac{1}{\varepsilon^2}\left(c^2 - 1 + \varepsilon g'(0)\right)\nu + \frac{c}{\varepsilon^2}g'(0). \tag{14.12}$$

Linearizing around a state of the form

$$(U = U_2,\ W = W_2 = U_2)$$

yields the equation

$$\begin{pmatrix}\tilde{U}'\\ \tilde{W}'\\ \tilde{V}'\end{pmatrix} = \frac{1}{\varepsilon}\begin{pmatrix}-c & 1 & 0\\ 0 & 0 & \varepsilon\\ -\frac{c}{\varepsilon} & \frac{1}{\varepsilon} - g'(W_2) & -c\end{pmatrix}\begin{pmatrix}\tilde{U}\\ \tilde{W}\\ \tilde{V}\end{pmatrix} =: A\begin{pmatrix}\tilde{U}\\ \tilde{W}\\ \tilde{V}\end{pmatrix}. \tag{14.13}$$

After some simple calculations under the assumption that ε is positive, the charac-

teristic equations turn out to have the shape

$$0 = \varepsilon\nu(\varepsilon\nu + c)^2 + (\varepsilon g'(\bar{W}) - 1)(\varepsilon\nu + c) + c. \tag{14.14}$$

Solving for the scaled eigenvalues $\varepsilon\nu$, the roots can be written down explicitly but are rather hard to analyze. Furthermore, the three dimensional system (14.5) does not allow for the deduction of closed heteroclinic orbits by simple analysis of the linearizations around the equilibria. We will therefore try to find such orbits by showing their existence for the model without diffusion and viewing this one as normally hyperbolic limit of the full system (9.4) which is done in the following subsection.

If we, however, know that at least for small ε the heteroclinic orbits corresponding to the wave profiles persist, we can still ask for the nature of the eigenvalues. Generically there will be three distinct ones, and our wave profiles can be monotone in U and W if all of them are real. Oscillatory behavior will emerge if two of them collapse into one and then form a pair of complex conjugate roots of the characteristic equation. The third one will of course always be real.

It is immediately obvious that the critical velocities will again only depend on the product

$$a = \varepsilon g'(\bar{W}),$$

and we can at least plot the sum of the imaginary parts

$$|\operatorname{Im}[\nu_1]| + |\Im[\nu_2]| + |\Im[\nu_3]|$$

to find the curves $c^*(a)$ and $c_*(a)$. This is done in figure 14.1.

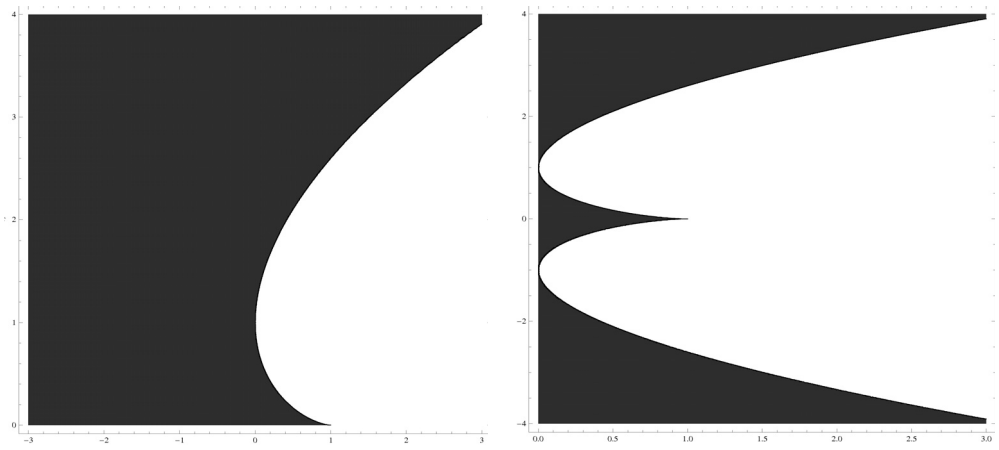

Figure 14.1: Illustration of the critical velocities c^* and c_* for the system with full diffusion. The eigenvalues of the linearization are real in the shaded region whereas in the white region two of them have non-vanishing imaginary part. *Left*: $a \in (-3, 3)$, $c \in (0, 4)$, *right*: $a \in (0, 3)$, $c \in (-4, 4)$.

Without knowing the precise functional relationship between a and the critical velocities we can observe the following properties:

1. Due to invariance under spatial reflection the picture is necessarily symmetric with

respect to $c = 0$.

2. For negative values a which are found at the outer equilibria $W = \pm U$, all eigenvalues are real no matter what value is assumed by the wave speed c. These are therefore always hyperbolic points as already was the case for system (9.2).

3. As soon as a becomes positive there emerges a neighborhood of $|c| = 1$ which is prohibited. As in the case for system (9.2), the derivatives

$$\frac{d}{da}c^*(a) \qquad \text{and} \qquad \frac{d}{da}c_*(a)$$

seem to diverge as a approaches zero from above.

4. In contrast to the observations in chapter 13, there are no monotone waves with $|c| < 1$ anymore if a becomes larger than 1. In particular the relation $c_* = 1/c^*$ does not hold anymore.

5. The critical velocity c^* behaves like

$$c^* \approx 1 + \sqrt{2a} \tag{14.15}$$

to leading order in $a > 0$. In fact, for $a < 3$ which is the region shown in figure 14.1, this approximation works so well that it is hard to see the difference by eye.

Asking in addition for the real parts of the eigenvalues we find another critical velocity $\hat{c}$ depending on $a > 0$. Recalling the calculations from section 13.5 we note that this velocity now plays the role of $c = 1$ for which the stability of the symmetric state $W = 0$ changed.

Now, the real part of the pair of complex conjugate eigenvalues changes sign at $c = \pm\hat{c}(a)$ which is in good pproximation given by

$$\hat{c} = \begin{cases} \sqrt{1 - \frac{a}{2}} & \text{if } a \in (0, 2) \\ 0 & \text{otherwise.} \end{cases} \tag{14.16}$$

In the following discussion we will see how that affects the existence of certain waves.

Taking into account all possible combinations of real and imaginary parts we obtain the bifurcation diagram for the dependence of the eigenvalues on c and a as shown in figure 14.2. More precisely, the signs of the real parts of $\varepsilon\nu$ are plotted in the a-c-plane. We will now briefly discuss the behavior of the eigenvalues across the bifurcation curves in figure 14.2.

1. We start with the negative a-axis and recall that

$$a = \varepsilon g'(\bar{W})$$

is only negative at the outer equilibria $W = \pm U$. Here, we always deal with saddle points, that is, we have three (distinct) real eigenvalues of different signs. More precisely, we have one eigenvalue of positive sign, one of negative sign, and a third one which has the opposite sign of the wave speed c.

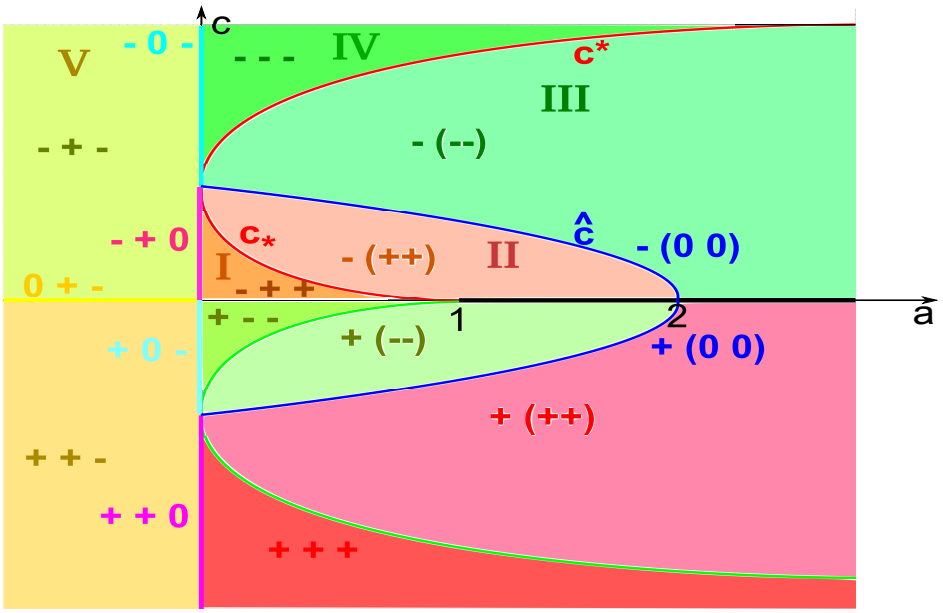

Figure 14.2: Bifurcation diagram for the eigenvalues of the linearizations around the steady states $(U_1, 0)$, (U_2, U_2), $(U_3, -U_3)$ depending on the wave speed c and the value $a = \varepsilon \partial_W f(\bar{U}, \bar{W})$. Note that a is positive at the point $(U_1, 0)$ and negative at the other two equilibria.

2. We now turn our attention to the region $0 < a < 1$ which corresponds to the situation at the interior equilibrium

$$(W = 0, U = U_1)$$

in case of small α and ε, or $-$ if using the damped alignment term with exponential decay $-$ to a large density U_1. Phenomenologically speaking, this is the case of weak diffusion and alignment strength, and we may expect a behavior which is dominated by the advection terms.

What we indeed observe is a situation very similar to that from figure 13.9 for model (9.2) with the special role of $c = 1$ being now replaced by $c = \hat{c}(a)$ and with an additional real eigenvalue having the same sign as c. Starting at large velocities $c > c^*(a)$ there are three distinct negative eigenvalues, one of them approaching zero as c increases the others growing approximately linearly with large c. We thus deal with a stable node in this parameter regime.

As c approaches c^* from above, the larger two of these real eigenvalues merge and form a pair of complex conjugate eigenvalues, still with negative real part, and the stable node turns into a stable focus. This corresponds to the oscillating waves discussed for model (9.2) in section 13.7.

Further decreasing c we approach the value $\hat{c}(a)$ at which the pair of complex conjugate eigenvalues passes through the imaginary axis. For $c \in (c_*(a), \hat{c}(a))$ the equilibrium state $W = 0$ thus has a one dimensional stable manifold corresponding

to the third eigenvalue which is still negative and a two-dimensional unstable manifold on which trajectories spiral away from that point.

For still smaller c we observe that at $c = c_*(a)$ the imaginary part of the complex conjugate pair shrinks to zero and both become real and distinct again, both remaining positive as long as c is positive. As the third eigenvalue is still negative we obtain a saddle with a one-dimensional stable and a two-dimensional unstable manifold.

As finally c approaches zero, one of the two positive eigenvalues passes through zero whereas the other one approaches $\nu_0(a) \in \left(0, \frac{1}{\varepsilon}\right)$ and upon sign change of c also changes it sign to become $-\nu_0(a)$. The third eigenvalue in turn approaches ν_0 from below and switches its sign as well. This results in two negative real eigenvalues and a third, positive eigenvalue for $c \in (-c_*, 0)$.

Further decreasing c simply yields a mirror image of the behavior discussed so far as each of the eigenvalues depends oddly on c.

3. As diffusion or alignment strength are increased to values resulting in $a \in (1, 2)$, the critical velocity $c_*(a)$ becomes zero, and there are no values of c left where the inner equilibrium is a saddle. The behavior for large c remains the same as for $a \in (0, 1)$, and the same is true for the passages of c through $c^*(a)$ and $\hat{c}(a)$. For decreasing c towards zero we see, that the (positive) real part of the pair of complex conjugate eigenvalues reaches a maximum and then shrinks again to reach zero as c does. The value of this maximum as well as the value of c where it is reached decreases for a getting closer to 2.

   The third eigenvalue also approaches zero as c does, and consequently all real parts of the eigenvalues pass transversally through zero as c goes through zero.

4. For even larger values of a, corresponding to fast diffusion and strong alignment, also the critical velocity $\hat{c}(a)$ becomes zero. For $a > 0$ we thus only have the regimes of nodes − stable for $c > c^*(a)$, unstable for $c < -c^*(a)$ − and foci − stable for $c \in (0, c^*(a))$, unstable for $c \in (-c^*(a), 0)$.

   As c passes through zero, all real parts of the eigenvalues smoothly and transversally pass through zero and do so with the opposite sign change of c.

5. Let us now consider the behavior of the eigenvalues while approaching the c-axis. Letting a go to zero corresponds to decreasing the diffusion coefficient to zero or changing the alignment term f in a way that it vanishes around the equilibria at least to linear order in W.

   The first case $\varepsilon \to 0$ is particularly delicate as we can only control the product of the eigenvalues with ε whereas the eigenvalues themselves (or at least one of them) explode with ε^{-1}. This limit corresponds to the transition from the full model (9.4) to its hyperbolic limit case. We will first discuss the situation of approaching $a = 0$ from positive values along lines $c = const.$ which corresponds to investigate the situation around the inner equilibrium $W = 0$.

   - For $c > 1$ there is a region of small positive a where all scaled eigenvalues $\varepsilon\nu$ are real and negative. One of them goes to zero with $\mathcal{O}(a)$ whereas the others

remain negative. In that case, we thus obtain one finite, negative eigenvalue and two diverging ones as ε decreases to zero at fixed $g'(0)$.

- For $c \in (0,1)$ we have one negative eigenvalue exploding to $-\infty$ and two positive eigenvalues one of whom remains bounded and the other one diverges to $+\infty$ as ε goes to zero.

- Along the line $c = 1$, we have a pair of complex conjugate eigenvalues with negative real part whose scaled versions approach zero linearly as a goes to zero. The real parts of the eigenvalues themselves therefore tend to some finite negative value. The imaginary part of the scaled eigenvalues tends to zero as a does, but only with order $\mathcal{O}(\sqrt{a})$, and thus in the limit $\varepsilon \to 0$ the rate of oscillations explodes.

- An interesting way to approach the c-axis is along the curve $c = c^*(a)$ which is suspected to be the regime of stable waves. Along this line we have a negative double eigenvalue and another one which is also negative. The simple one will diverge as the axis is approached by letting ε tend to zero, and does so as $\mathcal{O}(\varepsilon^{-1})$. The double eigenvalue also diverges but does so at a lower rate, namely $\mathcal{O}(\varepsilon^{-\frac{1}{2}})$. If the limit $a \to 0$ is accomplished by decreasing the diffusion coefficient ε and the alignment strength $g'(0)$ simultaneously in a way such that $\varepsilon^{-1}g'(0)$ approaches some finite value then the double eigenvalue also tends to some finite limit.

Let us now consider the case of negative a corresponding to the linearization around the outer equilibria. Now we have for arbitrary positive wave speeds c one positive and two negative eigenvalues. As a approaches 0 from below their behavior is the following.

- In case $c > 1$ the positive scaled eigenvalue goes linearly into zero whereas the negative ones tend to some finite negative values. For $\varepsilon \to 0$ at fixed $g'(\bar{W})$, we thus have two eigenvalues diverging to $-\infty$ and another one tending to some finite positive value.

- Along the line $c = 1$, there is one negative scaled eigenvalue being bounded away from zero and thus giving rise to an exploding eigenvalue tending to $-\infty$ with order $\mathcal{O}(\varepsilon^{-1})$ as ε tends to zero. There are furthermore two scaled eigenvalues approaching zero from opposite sides, both at rate $\mathcal{O}(\sqrt{-a})$. These correspond to exploding eigenvalues as well, but at lower rate $\mathcal{O}(\varepsilon^{-\frac{1}{2}})$, one of them to $+\infty$, the other one to $-\infty$.

- For $c \in (0,1)$ we still have one negative scaled eigenvalue being bounded away from zero and thus diverging to $-\infty$ at rate $\mathcal{O}(\varepsilon^{-1})$ as ε goes to zero. Furthermore there is a positive eigenvalue showing the same behavior. Finally we find a negative scaled eigenvalue tending to zero at linear rate thus giving rise to an eigenvalue tending to a finite negative value as ε shrinks to zero.

How the eigenvalues are located in the complex plane is shown in figure 14.3.

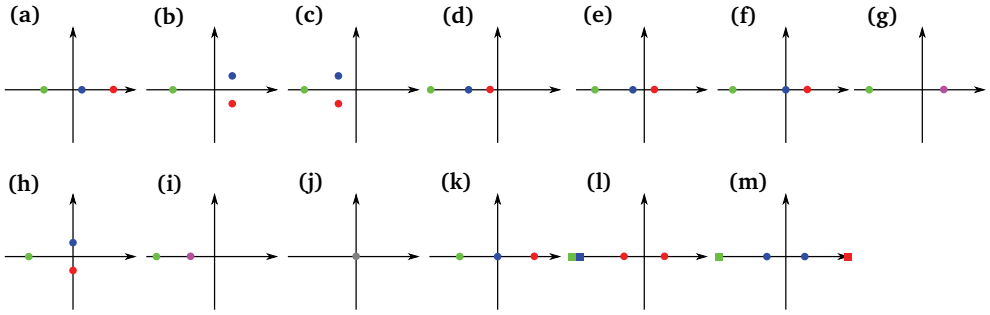

Figure 14.3: Sketch of the eigenvalues of the linearization of the full traveling wave system in the complex plane for different values of $a = \varepsilon g'(\bar{W})$ and c. Disks correspond to positions of eigenvalues, squares refer to infinite values. *pink* stands for a double eigenvalue (*red and blue*), *grey* for a triple eigenvalue. The parameter regimes are: *(a)*: $a > 0,\ 0 < c < c_*(a)$ (region I in figure 14.2), *(b)*: $a > 0,\ c_*(a) < c < \hat{c}(a)$ (region II), *(c)*: $a > 0,\ \hat{c}(a) < c < c^*(a)$ (region III), *(d)*: $a > 0,\ c > c^*(a)$ (region IV), *(e)*: $a < 0,\ c > 0$ (region V), *(f)*: $a \in (0,1),\ c = 0$, *(g)*: $a \in (0,1),\ c = c^*(a)$, *(h)*: $a \in (0,2),\ c = \hat{c}(a)$, *(i)*: $a > 0,\ c = c^*(a)$, *(j)*: $a \geq 1,\ c = 0$, *(k)*: $a < 0,\ c = 0$, *(l)*: $a = 0,\ c > 1$, *(m)*: $a = 0,\ c \in (0,1)$. Note in *(a)* - *(c)* that $c_*(a) = 0$ for $a > 1$ and $\hat{c}(a) = 0$ for $a > 2$

A note on the interpolate systems

Let us briefly review the calculation of the critical velocities for the interpolate systems (9.6) which we shall rewrite as

$$\partial_t u + \partial_x w = \theta\varepsilon\partial_{xx} u \tag{14.17a}$$
$$\partial_t w + \partial_x u = \varepsilon\partial_{xx} w + f(u,w) \tag{14.17b}$$

where θ is some number between 0 and 1.

The linearization of the resulting system of ordinary differential equations around the symmetric equilibrium $w \equiv 0$ reads

$$\begin{pmatrix} \tilde{U}' \\ \tilde{W}' \\ \tilde{V}' \end{pmatrix} = \frac{1}{\varepsilon} \begin{pmatrix} -\frac{c}{\theta} & \frac{1}{\theta} & 0 \\ 0 & 0 & \varepsilon \\ -\frac{c}{\theta\varepsilon} & \frac{1}{\theta\varepsilon} - g'(0) & -c \end{pmatrix} \begin{pmatrix} \tilde{U} \\ \tilde{W} \\ \tilde{V} \end{pmatrix} \tag{14.18}$$

where we reused the notation introduced above.

The resulting characteristic equation can again be written in terms of rescaled eigenvalues $\varepsilon\nu$ and then reads

$$0 = \left(\varepsilon\nu + \frac{c}{\theta}\right)(\varepsilon\nu + c)\,\varepsilon\nu + \left(\varepsilon\alpha - \frac{1}{\theta}\right)\left(\varepsilon\nu + \frac{c}{\theta}\right) + \frac{c}{\theta^2}. \tag{14.19}$$

Its roots have a rather complicated shape but we can plot the region where all of them are real. This is done in figure 14.4 for different values of θ. Looking closely at the graphs in the bottom row of this figure, we see that the upper critical velocity c^* slightly increases with θ.

More significant is the change in the maximal value a for which there exist velocities

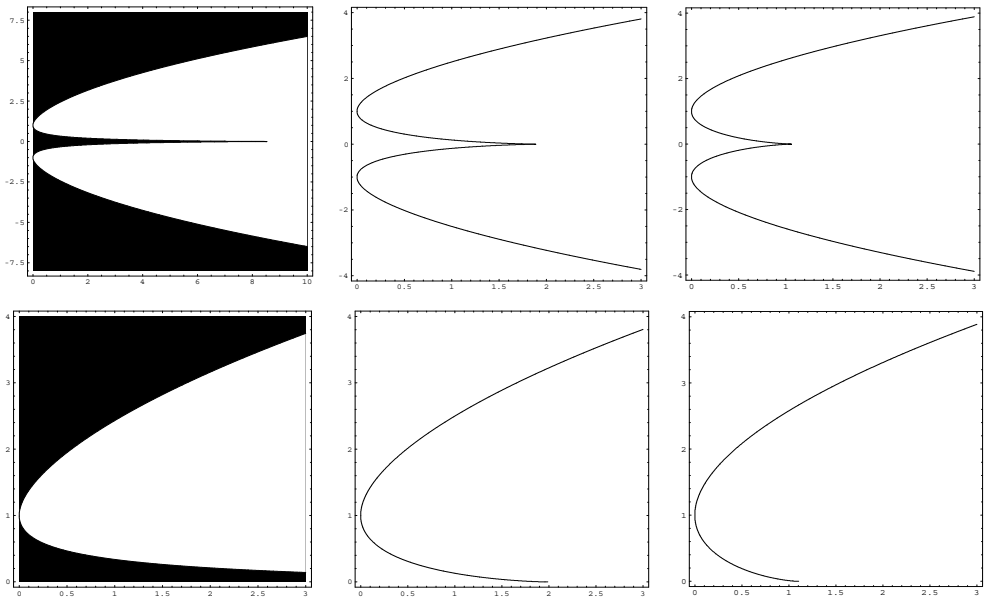

Figure 14.4: Critical velocities for the interpolate systems (14.17) for $\theta = 0.1$ (*left*), $\theta = 0.5$ (*middle*), and $\theta = 0.9$ (*right*). The scales reach from 0 to 3 for $a = \varepsilon g'(\bar{W})$ (except *top left*: from 0 to 10) and from -8 to 8 (*top left*), -4 to 4 (*top middle and right*), and 0 to 4 (*bottom row*) for c, respectively. For $\theta = 0.1$, we additionally indicated in black the region where all eigenvalues are real.

$c \in (-1, 1)$ leading to real eigenvalues. For $\theta = 1$, we found this maximal a_{max} to be 1, and examining the graphs, we observe it to behave like θ^{-1}. In particular, a_{max} converges to infinity as θ tends to zero which is compatible with the case $\theta = 0$ corresponding to (9.2) and being investigated in chapter 13.

14.2 Traveling waves for the hyperbolic system

If we consider the limiting case of model (9.2) or (9.4) with vanishing diffusion $\varepsilon = 0$, we obtain the hyperbolic system

$$\begin{aligned} \partial_t u + \partial_x w &= 0 \\ \partial_t w + \partial_x u &= f(u, w). \end{aligned} \tag{14.20}$$

Asking for solutions of constant shape we plug the ansatz

$$\begin{aligned} u(t, x) &= U(x - ct) \equiv U(\xi) \\ w(t, x) &= W(x - ct) \equiv W(\xi) \end{aligned} \tag{14.21}$$

into this system and deduce the following system of ordinary differential equations

$$-cU'(\xi) + W'(\xi) = 0 \tag{14.22}$$

$$-cW'(\xi) + U'(\xi) = f(U, W). \tag{14.23}$$

We start with the consideration of standing waves corresponding to a wave speed $c = 0$. We then obtain $W \equiv \bar{W} = const.$ and the second equation reduces to

$$U' = f(U, \bar{W}). \tag{14.24}$$

For any nonlinearity f with exponential decay term, this equation only has the single equilibrium $U = |\bar{W}|$ which is the minimal allowed value for U. Furthermore, the right hand side tends to zero as U tends to infinity but we cannot construct a wave profile of reasonable width from that. Recall that we observed the same effect during the construction of traveling waves for system (9.2) in chapter 13. We will thus again consider $c \neq 0$ in what follows.

Integrating (14.22) we obtain

$$cU = W + C$$

for some constant C. We use this to replace U' and U in (14.23) to find

$$\left(\frac{1}{c} - c\right) W' = g(W) := f\left(\frac{W + C}{c}, W\right) \tag{14.25}$$

from which we immediately see that − again in analogy with the construction for (9.2) − the wave speed cannot be taken to be ± 1, or rather $\pm v$ where v denotes the particle velocity, since otherwise the left hand side vanishes.

As we assume asymptotic states of the type

$$(W \equiv 0, U \equiv U_1)$$

we find the constant C to be $C = cU_1$ and can compute

$$g(W) = f\left(\frac{W + cU_1}{c}, W\right). \tag{14.26}$$

Choosing for example $f_{s,1}$ as alignment term we obtain

$$g_{s,1}(W) = \alpha W \left(1 - \left(\frac{cW}{W + C}\right)^2\right) \exp\left[-\beta^2 \frac{(W - cU_1)^2}{c^2}\right] \tag{14.27}$$

whose zeros and therewith the equilibria of (14.25) are just the usual

$$W_1 = 0, \qquad W_2 = U_2 = \frac{c}{c-1} U_1, \qquad -W_3 = U_3 = \frac{c}{c+1} U_1 \tag{14.28}$$

where the second one only exists for wave speeds

$$c \in (-\infty, 0) \cup (1, \infty)$$

and the third one only for

$$c \in (-\infty, -1) \cup (0, \infty)$$

which again perfectly corresponds to the situation from chapter 13 with the particular

critical velocities

$$c^* = c_* = 1.$$

There, by (13.15), c^* had been seen to behave like

$$c^* = \sqrt{1 + \mathcal{O}(\sqrt{\varepsilon})} \tag{14.29}$$

for small diffusion coefficients ε.

At this point we should also recall that for model (9.2) there were indeed wave profiles for any velocity $c \notin \{-1, 0, 1\}$ if we allowed for non-monotone waves.

Concerning the stability of the equilibria we observe precisely the same stability behavior. This is seen by just noting that the linearization around the $W = 0$ - state is given by

$$W'(\xi) = \frac{c}{1 - c^2} g'(0) W \tag{14.30}$$

and that we already computed for the bistable alignment term

$$g'_{s,1}(0) = \alpha \exp[-\beta^2 U_1^2] > 0 \tag{14.31}$$

and thus have the same stability condition for this equilibrium, namely:

$$(U_1, 0) \text{ is } \left\{ \begin{matrix} \text{stable} \\ \text{unstable} \end{matrix} \right\} \qquad \text{if and only if} \qquad \begin{cases} c \in (-1, 0) \cup (1, \infty) \\ c \in (-\infty, -1) \cup (0, 1) \end{cases} . \tag{14.32}$$

As we are in one dimension the other equilibria have the opposite stability properties of the inner one, and we obtain the same kind of waves as in proposition 13.9. We note, that now the orbits connecting the equilibria in phase space are just observed as intervals on the W-axis whereas in chapter 13 these orbits where seen in the $W - W'$-plane as some kind of deformed W-axis. In both cases the phase space is completed by additionally considering the U-component of the trajectory which is quite simple as it depends algebraically on W.

However, for the hyperbolic situation we are at least able to draw the complete phase portrait since we only have to deal with a total of two variables.

The possible wave trains can be summarized as follows.

1. For $c > 1$ there are waves connecting the fully left polarized state

   $$W = W_3 = -U_3 = -\frac{c}{c+1} U_1$$

   to the non-polarized state ($W = 0, U = U_1$) and waves connecting the non-polarized state ($W = 0, U = U_1$) to the fully right polarized state

   $$W = W_2 = U_2 = \frac{c}{c-1} U_1.$$

2. For $0 < c < 1$ there are waves connecting the non-polarized state ($W = 0, U = U_1$) to the fully left polarized state

   $$W = W_3 = -U_3 = -\frac{c}{c+1} U_1.$$

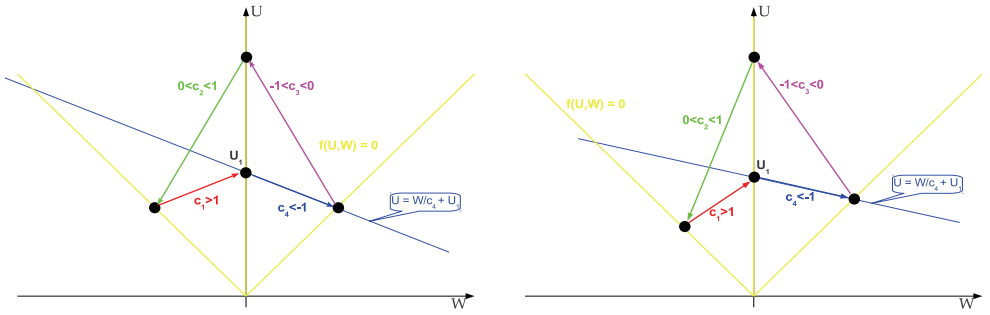

Figure 14.5: Phase portrait for system (14.22), (14.23). *Left*: corresponding to a symmetric pattern ($c3 = -c_2$, $c_4 = -c_1$), *right*: corresponding to an asymmetric pattern. The yellow lines are the three components of the equilibrium set $\{f = 0\}$. The arrows denote possible traveling fronts for different velocities c. Note, that starting from the point $(W, U) = (0, U_1)$ and going along all arrows subsequently, we arrive at a solution of the system which is composed of four traveling wave solutions being glued together at their asymptotic states (cf. section 13.6, figure 13.14 for the symmetric case, figure 13.16 for the asymmetric case). In fact, the same picture may be obtained by projecting the heteroclinic orbits for system (13.6) accompanied by $cU' = V$ from the $W - W' - U$ phase space to the $W - U$-plane.

3. For $-1 < c < 0$ there are waves connecting the fully right polarized state

$$W = W_2 = U_2 = \frac{c}{c-1} U_1$$

to the non-polarized state $(W = 0, U = U_1)$.

4. For $c < -1$ there are waves connecting the fully right polarized state

$$W = W_2 = U_2 = \frac{c}{c-1} U_1$$

to the non-polarized state $(W = 0, U = U_1)$ and waves connecting the non-polarized state $(W = 0, U = U_1)$ to the fully left polarized state

$$W = W_3 = -U_3 = -\frac{c}{c+1} U_1.$$

What happens if the wave speed c approaches the critical values ± 1? In that case the coefficient

$$c - \frac{1}{c}$$

tends to zero and the derivative W' takes large values wherever $g(W)$ does not vanish. We therefore expect a solution close to some shock profile. Of course, the stability of the asymptotic states switches as c goes through ± 1 and we may expect the following behavior.

$c \searrow 1$. The wave train connecting the fully right polarized state to the symmetric one will

become an approximate (weak) solution of the RIEMANN problem with data

$$\begin{aligned} u(0,x) &= \frac{1}{2}U_1\chi_{\{x<x_0\}} + U_1\chi_{\{x>x_0\}} \\ w(0,x) &= -\frac{1}{2}U_1\chi_{\{x<x_0\}} \end{aligned} \tag{14.33}$$

which corresponds to the following situation in terms of the individual particle densities u_r and u_l:

$$u_r(0,x) = \frac{1}{2}U_1\chi_{\{x>x_0\}}, \qquad u_l(0,x) \equiv \frac{1}{2}U_1. \tag{14.34}$$

$c \nearrow 1$. The wave profile should approach some weak solution of the corresponding RIEMANN problem with data

$$\begin{aligned} u(0,x) &= U_1\chi_{\{x<x_0\}} + \frac{1}{2}U_1\chi_{\{x>x_0\}} \\ w(0,x) &= -\frac{1}{2}U_1\chi_{\{x>x_0\}} \end{aligned} \tag{14.35}$$

or in terms of the individual densities:

$$u_r(0,x) = \frac{1}{2}U_1\chi_{\{x<x_0\}}, \qquad u_l(0,x) \equiv \frac{1}{2}U_1. \tag{14.36}$$

14.3 The hyperbolic model as hyperbolic limit

The striking analogies between the previous section and the findings in chapter 13 strongly suggest that system (9.4) exhibits very similar wave patterns. This expectation is also supplemented by simulations of the full systems of partial differential equations which are discussed in detail in chapter 15. Here we only point out that system (9.4) with diffusion coefficient ε behaves very similar to system (9.2) with diffusion coefficient put to 2ε.

This intuition can be made rigorous by using the theory of transversal heteroclinic orbits developed in [7] and [30]. We therefore rewrite (14.2) to

$$\begin{aligned} U'(\xi) &:= Z(\xi) \\ W'(\xi) &= V(\xi) \\ \varepsilon Z'(\xi) &= V(\xi) - cZ(\xi) \\ \varepsilon V'(\xi) &= Z(\xi) - cV(\xi) - f(U(\xi), W(\xi)). \end{aligned} \tag{14.37}$$

being defined on $\mathcal{M} \times \mathbb{R}$ with

$$\mathcal{M} = \left\{(U,W,Z,V)^T \in \mathbb{R}^4 \;\middle|\; U > 0, |W| < U\right\} \tag{14.38}$$

where the conditions $U > 0, |W| < U$ translate into the conditions $u_{r/l} > 0$.

The reduced system obtained by setting ε to zero is precisely the one we deduced for the hyperbolic model (14.20) and given by (14.25) supplemented by

$$cU = W + C.$$

This system acts on the set

$$\mathcal{S} := \left\{ (U,W,Z,V)^T \in \mathcal{M} \;\middle|\; V = \frac{c}{1-c^2} f(U,W),\ Z = \frac{1}{1-c^2} f(U,W) \right\} \tag{14.39}$$

The layer problem is obtained by setting ε to zero in the corresponding fast problem

$$\begin{array}{rcl} U'(\tau) & := & \varepsilon Z(\tau) \\ W'(\tau) & = & \varepsilon V(\tau) \\ Z'(\tau) & = & V(\tau) - cZ(\tau) \\ V'(\tau) & = & Z(\tau) - cV(\tau) - f(U(\tau),W(\tau)). \end{array} \tag{14.40}$$

which is just (14.37) rewritten in the new variable $\tau = \varepsilon^{-1}\xi$.

Thus, the layer problem reads

$$\begin{array}{rcl} U'(\tau) = 0 = W'(\tau) & & \\ Z'(\tau) & = & V(\tau) - cZ(\tau) \\ V'(\tau) & = & Z(\tau) - cV(\tau) - f(U(\tau),W(\tau)) \end{array} \tag{14.41}$$

and reduces to a simple linear system with constant coefficients by using

$$U \equiv \bar{U}, \qquad W \equiv \bar{W}, \qquad F := -f(\bar{U},\bar{W})$$

as notation. This linear system reads

$$\frac{d}{d\tau}\begin{pmatrix} Z \\ V \end{pmatrix} + \begin{pmatrix} c & -1 \\ -1 & c \end{pmatrix}\begin{pmatrix} Z \\ V \end{pmatrix} = \begin{pmatrix} 0 \\ F \end{pmatrix}. \tag{14.42}$$

For the extended fast system which is (14.40) supplemented by $\varepsilon' = 0$, let us denote the right hand side by Φ and compute its linearization to be

$$D\Phi = \begin{pmatrix} 0 & 0 & \varepsilon & 0 & Z \\ 0 & 0 & 0 & \varepsilon & V \\ 0 & 0 & -c & 1 & 0 \\ -\partial_U f & -\partial_W f & 1 & -c & 0 \\ 0 & 0 & 0 & 0 & 0 \end{pmatrix} \tag{14.43}$$

which, for $\varepsilon = 0$ has the trivial eigenvalues $\lambda_{1,2,3} = 0$ and the nontrivial ones $\lambda_{4,5} = -c \pm 1$. The corresponding eigenvectors can be chosen to be

$$\eta_{1,2,3} = \begin{pmatrix} 1 \\ 0 \\ \frac{1}{c^2-1}\partial_U f \\ \frac{c}{c^2-1}\partial_U f \\ 0 \end{pmatrix}, \begin{pmatrix} -\partial_W f \\ \partial_U f \\ 0 \\ 0 \\ 0 \end{pmatrix}, \begin{pmatrix} 0 \\ 0 \\ 0 \\ 0 \\ 1 \end{pmatrix}, \quad \eta_4 = \begin{pmatrix} 0 \\ 0 \\ -1 \\ 1 \\ 0 \end{pmatrix}, \quad \eta_5 = \begin{pmatrix} 0 \\ 0 \\ 1 \\ 1 \\ 0 \end{pmatrix}. \tag{14.44}$$

or even easier

$$\eta_{1,2,3} = \begin{pmatrix} 1 \\ 0 \\ 0 \\ 0 \\ 0 \end{pmatrix}, \begin{pmatrix} 0 \\ 1 \\ 0 \\ 0 \\ 0 \end{pmatrix}, \begin{pmatrix} 0 \\ 0 \\ 0 \\ 0 \\ 1 \end{pmatrix}, \quad \eta_4 = \begin{pmatrix} 0 \\ 0 \\ -1 \\ 1 \\ 0 \end{pmatrix}, \quad \eta_5 = \begin{pmatrix} 0 \\ 0 \\ 1 \\ 1 \\ 0 \end{pmatrix}. \tag{14.45}$$

We find that $D\Phi$ has its maximal possible rank 2 whenever $|c|$ is different from one and that the nontrivial eigenvalues are real and have

- both positive sign if $c < -1$,
- different signs if $-1 < c < 1$, and
- both negative sign if $c > 1$.

In particular, for $|c| \neq 1$, the whole invariant manifold $\mathcal{S}$ for the layer problem is normally hyperbolic and we conclude that for sufficiently small $\varepsilon > 0$, system (9.4) exhibits traveling wave solutions of the types discussed.

Proposition 14.1. *Assume the nonlinearity f to be of the form $f_{s,1}$ or $f_{s,2}$ given by (12.8) or (12.9), respectively, with $\alpha > 0$, $\Lambda = 1$, and $\beta \geq 0$. Then, for each*

$$c \in \mathbb{R} \backslash \{-v, 0, v\}$$

there exists $\varepsilon_0(c)$, depending also on α, β, v, and the shape of f, such that for any

$$\varepsilon \in (0, \varepsilon_0(c)),$$

the system

$$\begin{aligned} \partial_t u + v\partial_x w &= \varepsilon \partial_{xx} u \\ \partial_t w + v\partial_x u &= \varepsilon \partial_{xx} w + f \end{aligned}$$

exhibits at least one traveling wave solution with wave velocity c. Depending on the value of c, this solution connects the asymptotic states

a) $W = 0$ *to* $W = U$ *for* $c < -v$.

b) $W = U$ *to* $W = 0$ *for* $-v < c < 0$.

c) $W = 0$ *to* $W = -U$ *for* $0 < c < v$.

d) $W = -U$ *to* $W = 0$ *for* $c > 1$.

Here, v denotes the filament velocity.

We can now nicely interpret the behavior of the eigenvalues for the full problem (9.4) as ε tends to zero which has been discussed in section 14.1. Those eigenvalues which had been found to remain finite in the limit are those we also find for the hyperbolic system, namely with positive sign for $c \in (-1, 0) \cup (1, \infty)$ and with negative sign for $c \in (-\infty, -1) \cup (0, 1)$. The other ones which were observed to explode to infinity as ε decreases to zero are seen to describe the evolution of the fast system which becomes infinitely fast in the limit.

14.4 System (9.2) as hyperbolic limit of system (9.4)

Going via the interpolate systems (14.17), we can also view the traveling wave system (13.31) corresponding to system (9.2) as the reduced system of (14.5) which corresponds to traveling waves for (9.4), now viewed for fixed ε and taking θ as perturbation parameter.

In terms of the first order systems, we have

$$\begin{aligned} U' &= Z && (14.46a)\\ W' &= V && (14.46b)\\ V' &= -\frac{c}{\varepsilon}V + \frac{1}{\varepsilon}Z - \frac{1}{\varepsilon}f(U,W) && (14.46c)\\ \theta Z' &= -\frac{c}{\varepsilon}Z + \frac{1}{\varepsilon}V. && (14.46d) \end{aligned}$$

Putting θ to zero we indeed obtain (13.6) as reduced system by integrating the last equation and plugging it into the third one. The full system (14.5) corresponds to $\theta = 1$. Although the theory used in the previous section also works out in this situation it only yields persistence of the heteroclinic orbits − and thereby of traveling wave profiles − found in chapter 13 for small values of θ. Without knowing about the precise meaning of the term "small" we cannot assert the existence of particular traveling wave solutions for system (9.4).

14.5 Diffusion fronts

Let us very briefly note that there is another type of wave like pattern the system can produce. If there are only particles of one orientation the alignment terms with $\Lambda = 1$ vanish and any initial pattern undergoes a translation with the respective particle speed superimposed by diffusive spreading as described by the linear equation

$$\partial_t u_{r/l} \pm \partial_x u_{r/l} = \varepsilon \partial_{xx} u_{r/l}. \tag{14.47}$$

Considering any monotone initial conditions containing only one type of particles with saturation at $x \to \pm\infty$ we thus obtain a monotone front moving with velocity 1 or -1 and increasing in width. Such a front can possibly connect a fully polarized asymptotic state with the trivial state $u = 0$.

This type of pseudo-wave pattern allows us to construct solutions having the asymptotic state

$$(W = 0, U = U_1 > 0)$$

at $x \to \pm\infty$ into which two totally aligned humps invade which leave behind a depletion zone. More precisely, there may be a wave front with speed $c_1 > c^*$ traveling to the right and connecting the state

$$U_2 = W_2 = \frac{c}{c-1}U_1$$

to the state

$$(W = 0, U = U_1)$$

being followed by a trailing diffusive pseudo-wave front of speed 1 along which $U = W$ grows from zero to U_2.

In physical terms, these two profiles are the front and rear of a hump consisting only of right oriented particles that moves to the right and grows in width at the rate $c_1 - 1$.

This hump has a mirror image with left oriented particles moving to the left with speed $c_2 < -c^*$ at the front and $c = -1$ at the rear. The interpretation in terms of filament densities is the following. If this type of solution builds up from certain perturbations of the non-polarized state ($W \equiv 0, U \equiv U_1$) we found a setting where a large bulk of left oriented filaments moves to the left in a coordinated way, the same happens with right oriented filaments moving to the right, and in between there is a growing region without any filaments being present. We will indeed find this type of solutions in the simulation in section 15.3. Moreover, we find asymmetric solutions with only one hump running into one direction corresponding to a directed movement of the center of mass of the whole system as should be expected for a moving cell.

Chapter 15

Numerical Simulations for the Reduced Model

15.1 The numerical scheme

To solve the systems (9.2) and (9.4) as well as there interpolates numerically we first transform them back to the natural variables u_r and u_l and write the respective problem

$$(\partial_t + \partial_x)u_r = \frac{\varepsilon_u + \varepsilon_w}{2}\partial_{xx}u_r + \frac{\varepsilon_w - \varepsilon_u}{2}\partial_{xx}u_l + \frac{1}{2}f(u_r + u_l, u_r - u_l)$$
$$(\partial_t - \partial_x)u_l = \frac{\varepsilon_u + \varepsilon_w}{2}\partial_{xx}u_l - \frac{\varepsilon_w - \varepsilon_u}{2}\partial_{xx}u_r - \frac{1}{2}f(u_r + u_l, u_r - u_l)$$

which is then solved by a an explicite finite volume scheme. For notational convenience let us introduce the values

$$\varepsilon_+ := \frac{\varepsilon_u + \varepsilon_w}{2} \qquad \text{and} \qquad \varepsilon_- := \frac{\varepsilon_w - \varepsilon_u}{2}.$$

To discretize the first order space derivatives we use for obvious reasons an upwind flux. The second order terms contribute with their gradients to the flux, and we compute them by the difference of the values in the adjacent cells.

We briefly sketch the precise scheme for the right moving particles. The equations for the left moving ones are obtained by symmetry. First, let us write $u^k_{r,i}$ for the value of u_r at time $t_k = k\Delta t$ in the cell $\Omega_i = (x_i, x_{i+1})$ with $x_i = i\Delta x$. We consider an interior cell Ω_i at time t_k and compute the numerical flux through the end point x_i.

The contribution from the first order term is simply given by the influx from the left:

$$F^k_{r1,i} = u^k_{r,i-1}.$$

From the diffusive terms we obtain a contribution of

$$F^k_{r2,i} = -\frac{\varepsilon_+}{\Delta x}(u^k_{r,i} - u^k_{r,i-1}) - \frac{\varepsilon_-}{\Delta x}(u^k_{r,i} - u^k_{r,i-1}). \tag{15.1}$$

In addition, we have the alignment term f that is evaluated in each cell separately. Adding up the flux and the reaction terms we find the following evolution operator for

the density of right oriented filaments

$$\begin{aligned} u_{r,i}^{k+1} &= u_{r,i}^k + \frac{\Delta t}{\Delta x}\left(F_{r,i}^k - F_{r,i+1}^k\right) + \frac{\Delta t}{2} f(u_{r,i}^k - u_{l,i}^k, u_{r,i}^k - u_{l,i}^k) \\ &= \left(1 - \frac{\Delta t}{\Delta x}\right) u_{r,i}^k + \frac{\Delta t}{\Delta x} u_{r,i-1}^k + \varepsilon_+ \frac{\Delta t}{\Delta x^2}(u_{r,i+1}^k - 2u_{r,i}^k + u_{r,i-1}^k) \\ &\quad - \varepsilon_- \frac{\Delta t}{\Delta x^2}(u_{l,i+1}^k - 2u_{l,i}^k + u_{l,i-1}^k). \end{aligned} \tag{15.2}$$

15.2 Simulations on small domains and stability

From chapters 10 and 11 we recall the conditions for the linear and nonlinear stability of the homogeneous non-polarized steady state

$$(w \equiv 0,\ u \equiv u_1 = const).$$

Here, we will use simulations for both models with different alignment terms and initial conditions to provide a picture of what happens to small but also to larger perturbations of the homogeneous steady state.

Starting from any physically relevant initial conditions − meaning that

$$u(0,x) - |w(0,x)|$$

should be non-negative at each point x − we observe that the system approaches one of the following two asymptotic behaviors.

Either, every inhomogeneity is leveled out and the solution decays to the steady state

$$\left(w \equiv 0, u \equiv \int_0^L u(0,x)dx\right),$$

or the solution develops a nontrivial asymptotic state which flips back and forth. Both behaviors are sketched in figure 15.1.

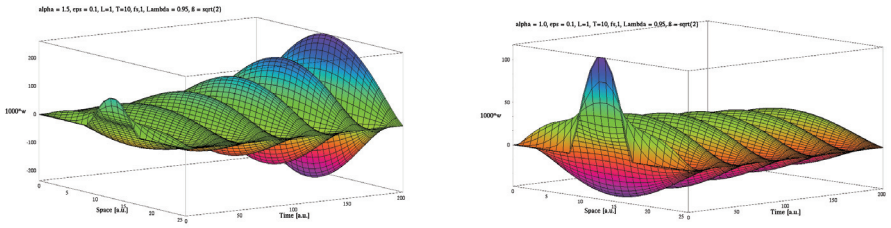

Figure 15.1: Evolution of the polarization w for system (9.4), alignment term $f_{s,1}$, data (15.3), and parameters $L = 1,\ T = 10,\ \varepsilon = 0.1, \Lambda = 0.95, \beta = \sqrt{2}$. *Left*: growth for strong alignment ($\alpha = 1.5$), *right*: decay for weak alignment ($\alpha = 1.0$). Note the different scales of the w-axes, both initial conditions are precisely the same.

For the simulations shown in figure 15.1, we used the following type of initial condi-

tion

$$w(0,x) = -h \ \sin\left[3\pi\frac{x}{L}\right] \ \chi_{(\frac{L}{3},\frac{2L}{3})} \tag{15.3}$$

with the total particle density u being kept constant. The latter means that the perturbation of the non-polarized state is achieved by turning around some existing filaments without adding or removing anything.

One may now suspect that the asymptotic shape of this flipping state shall depend on the shape of the initial conditions. However, this is not the case for generic data. Whenever the FOURIER series of the initial data contains a first mode contribution, then the system quickly develops a single sine shaped hump which is not surprising as the first mode has been calculated to be the least stable one. Only if the initial data are solely comprised of higher modes, then the smallest of those is selected as asymptotic shape.

To investigate the precise shape of the nontrivial asymptotic state we introduce the following quantities.

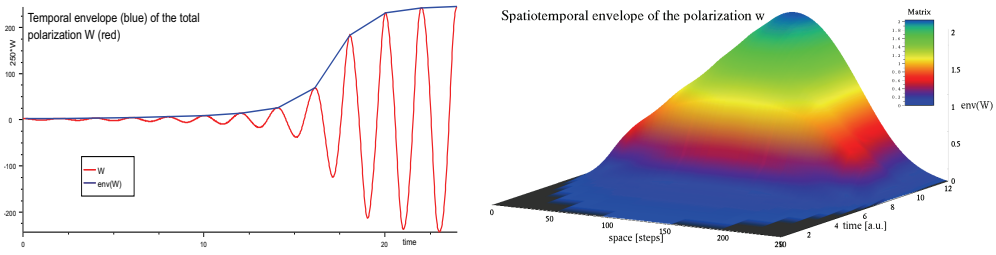

Figure 15.2: Illustration of the concept of the temporal envelope of the total polarization W (*left*) and spatiotemporal envelope of the polarization w (*right*).

Definition 15.2.1. *As the total polarization $W : [0,T] \to \mathbb{R}$ we define the spatial integral of the (local) polarization w:*

$$W(t) := \int_0^L w(t,x)dx. \tag{15.4}$$

As the temporal envelope of the total polarization (or short: envelope of the polarization) we define temporal evolution of the local maxima of W as indicated in figure 15.2.

The temporal envelope of the polarization allows us to precisely measure whether an initial perturbation decays towards the homogeneous steady state or approaches some nontrivial state flipping back and forth. The spatiotemporal envelope which is introduced in figure 15.2 provides a good impression of the shape of this flipping state.

15.2.1 Stability for system (9.2)

We start with the investigation under which conditions perturbations of the homogeneous steady state decay and in which situations they grow and achieve the asymptotic state flipping back and forth. These behaviors shall be denominated computational stability and computational instability, respectively.

The first observation we already expected concerns the critical alignment strength α_{crit}. For any given initial data and any bistable shape of the alignment term f we find a well defined value of α_{crit} which increases with the diffusion coefficient $\varepsilon = \varepsilon_w$ and characterizing the border between stability and instability. More precisely, we find some α_{crit} such that for $\alpha < \alpha_{crit}$, the total polarization W tends to zero as time tends to infinity whereas for $\alpha > \alpha_{crit}$, the temporal envelope of the total polarization approaches some finite value for large times. The latter case means that the solution tends to a nontrivial flipping state as described above.

Both, the rates of exponential decay or growth and the size of the possibly reached nontrivial asymptotic state, depend on the precise shape of the alignment term and the difference $\alpha - \alpha_{crit}$. The precise relationships for different alignment terms are shown in figures 15.3 and 15.4.

From the calculations in chapter 10 we know that the switch of stability happens in the oscillatory regime and from (10.7) we deduce that the real part of the growth rate σ_+ can be expected to behave like

$$\operatorname{Re}\sigma = \frac{1}{2}\left(F_w \pm \varepsilon\frac{\pi^2}{L^2}\right). \tag{15.5}$$

This linear dependence on F_w which is nothing else than α is nicely recovered by the simulations.

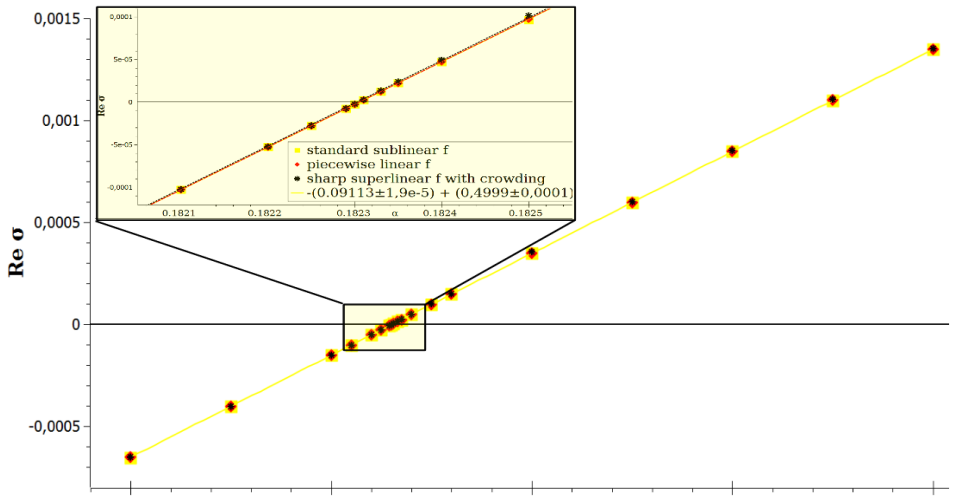

Figure 15.3: Dependence of the exponential growth rate $\operatorname{Re}\sigma_+$ on the alignment strength α close to α_{crit}. *Yellow squares*: standard sublinear alignment term according to (15.6), *red diamonds*: piecewise linear alignment term according to (15.8), *black stars*: sharp superlinear alignment term $\tilde{f}_{s,2}$ according to (12.10) with exponential crowding term.

For superlinear alignment, the behavior cannot completely be predicted from the linearization. For α being slightly larger than the critical value α_{crit}, the temporal envelope of the total polarization grows exponentially in time but at some point, the growth becomes superexponential until the final plateau is reached.

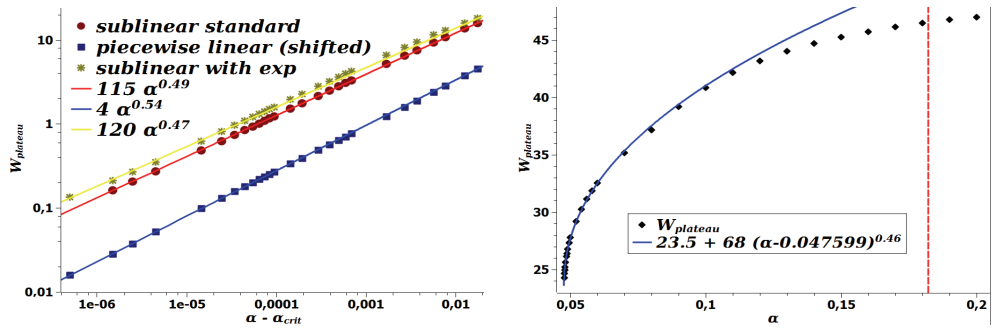

Figure 15.4: Asymptotic values of the temporal envelope of the total polarization for alignment strengths around α_{crit}. *Left*: For sublinear alignment terms, the plateau value is proportional to $\sqrt{\alpha - \alpha_{crit}}$ as is shown at the examples of the standard sublinear alignment term without (*red*, cf. (15.6)) and with (*yellow*, cf. (12.8)) exponential crowding term and the piecewise linear alignment term (*blue*, cf. (15.8)). In case of the latter, the plotted plateau values are corrected by an offset value of 20.157. For superlinear alignment as given by (12.10), there are also plateau values for $\alpha < \alpha_{crit}$ which are reached if the initial pertubation is large enough. The *dashed red* line indicates the value of α_{crit}.

If, in contrast, the alignment strength is slightly subcritical and the perturbation is appropriately small, an exponential decay similar to the sublinear case is observed. The latter behavior is not too surprising as the polarization remains very close to zero and thus in a range where the linearization provides a good approximation to the alignment term.

At this point, we should note that the initial behavior of the total polarization may seemingly contradict the true result. On the one hand, for large initial polarizations and slightly supercritical alignment strength, the nontrivial asymptotic state may exhibit smaller polarizations than the data. In that case, the temporal envelope of the total polarization decreases but does not approach zero.

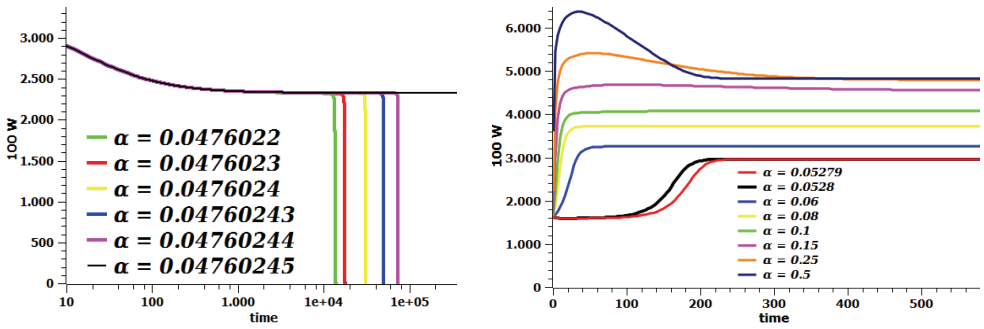

Figure 15.5: Illustration of some transient behaviors of the temporal envelope of the total polarization W. *Left*: Delayed decay to zero for subcritical alignment strengths $\alpha \lesssim \alpha_{crit}$ after apparent establishment of a plateau. Note the logarithmic scale for the time axis! *Right*: overshoot beyond the plateau value for strongly supercritical alignment strengths. In both cases, the alignment term was of superlinear type according to (12.10).

One the other hand, for most shapes of the initial conditions, if the alignment strength is only slightly smaller than its critical value, the temporal envelope of the total polarization may initially increase until the eigenshape is reached and then starts to decay to zero.

In case of superlinear alignment, we may even observe an apparently asymptotic plateau of the temporal envelope and then a sudden decay to zero. Some of these effects are depicted in figure 15.5.

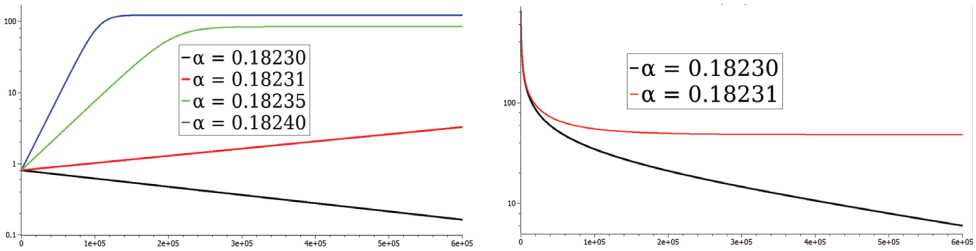

Figure 15.6: Typical large time behavior of the temporal envelope of the total polarization W for α being close to the critical value α_{crit} for sublinear alignment terms. Note the logarithmic scales for the ordinate! *Left*: In case of small initial data, the envelope exponentially decays to zero for subcritical α and exponentially grows until reaching its nontrivial final state for supercritical α. For short times, the envelope may behave differently while the solution develops its eigenshape. *Right*: If the initial polarization is large, the temporal envelope starts decaying independently of the stability. In case of supercritical α, this decay comes to halt when the nontrivial final state is reached whereas for subcritical alignment, the decay goes on and becomes exponentially for large times. *Parameters*: $\varepsilon_w = 0.15$, $L = \pi$, $\Delta x = 0.05$, $\Delta t = 0.004$, sublinear alignment term of type (15.6).

How the temporal envelope of the total polarization can be used to determine whether we are in the stable or unstable regime, is enlighted by figure 15.6. Moreover, different possible behaviors for large and small initial data become evident there. For superlinear alignment terms and sufficiently large alignment strengths α, an additional transient behavior may be observed. If the initial data are smaller than the asymptotic value, the temporal envelope of the total polarization increases, reaches a maximum and after this overshoot decays to its asymptotic value.

Let us now have a closer look at the dependence of the stability on the size of the initial polarization. As already indicated above, we have to distinguish between sublinear and superlinear bistable alignment terms.

1. For the sublinear versions of f, given any values of ε and L, we find a critical alignment strength α_{crit} such that for smaller α, any perturbation decays, regardless of its size. If the actual alignment strength is larger than the critical one, then any generic perturbation asymptotically approaches the oscillating state. The only exceptions are those initial data which do not contain the largest possible FOURIER mode. It is also notable that for different sublinear alignment terms, we find precisely the same stability behavior. In detail, we tried the following sublinear

alignment terms (the last of whom is in fact piecewise linear):

$$f(w,u) = \alpha w\left(1-\frac{w^2}{u^2}\right) \tag{15.6}$$

$$f(w,u) = \alpha w\left(1-\frac{|w|}{u}\right) \tag{15.7}$$

$$f(w,u) = \alpha w\chi_{\left\{|w|\leq\frac{u}{2}\right\}} + \alpha(1-w)\chi_{\left\{w>\frac{u}{2}\right\}} - \alpha(1+w)\chi_{\left\{w<-\frac{u}{2}\right\}}, \tag{15.8}$$

and for some tests also the versions with exponential crowding term. The critical alignment strength was found to be the same for all of these choices.

2. In case of the superlinear alignment terms, the critical alignment strength in addition depends monotonically on the size of the initial perturbation. For very small perturbations, we find the same α_{crit} as for the sublinear alignment term − at least within the considered range of accuracy. If then the height of the perturbation is increased without changing its shape, the alignment strength at which the switch from decay to growth occurs becomes smaller. This situation is plotted in figure 15.9. In our example with $\alpha_{crit} = 0.182306$ and the alignment term $\tilde{f}_{s,2}$ with $\nu = 12$, the largest alignment strength for which we found no initial perturbations not decaying to zero was $\alpha = 0.04760244$ which is only about one fourth of the critical value (cf. figure 15.5). This ratio indicates the importance of the shape of the nonlinearity for determining the true stability behavior as opposed to the predictions from the linearization.

For the plot in figure 15.9 showing the dependence of the critical alignment strength on the size of the perturbation we chose a diffusion coefficient of $\varepsilon_w = 0.2$, a domain size of $L = 5\pi$ and a perturbation of the shape

$$w(0,x) = 2h\ \sin\left(\pi\frac{x}{L}\right) \tag{15.9}$$

with constant particle density u. In terms of left and right particle densities this reads

$$u_r(0,x) = \frac{1}{2}u_0 + h\sin\left(\frac{x}{5}\right) \tag{15.10}$$

$$u_l(0,x) = \frac{1}{2}u_0 - h\sin\left(\frac{x}{5}\right). \tag{15.11}$$

In the particular case of figure 15.9, the total particle density u has been fixed to one in the initial data.

Let us finally comment on some numerical subtelties. First, we note that our scheme introduces some additional diffusion to the system whose size will depend on the numerical parameters Δx and Δt. We will discuss this dependence in more detail at the end of the next subsection where we compare the critical alignment strengths computed in chapter 10 with those found by the simulations. The discretization of the diffusion terms even adds artificial terms of higher order to the system. Moreover, the right hand side f also contributes to these additional terms.

We furthermore note that boundary artefacts cannot be excluded to play a role for very small domain size and thereby only few grid points. These are however not a major

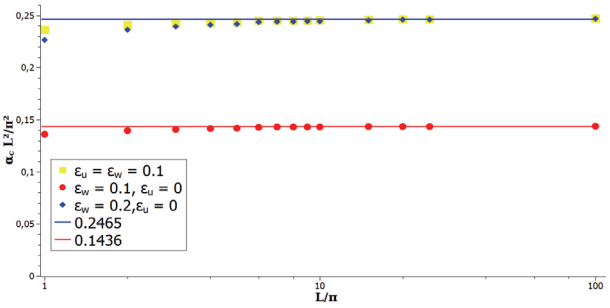

Figure 15.7: Dependence of the measured critical alignment strength on the domain size. *Abscissa*: domain length L in multiples of π (logarithmic scale), *ordinate*: critical alignment strength α_{crit} scaled by the domain length.

concern for reasonable choices of the numerical step sizes.

15.2.2 Stability for system (9.4)

With additional diffusion in the equation for the particle density u the basic features found in the previous subsection for system (9.2) remain the same.

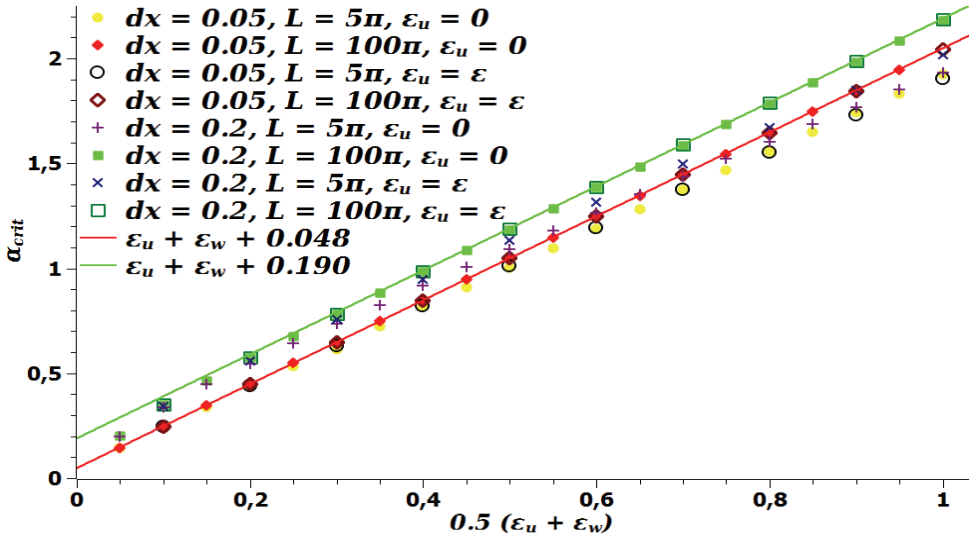

Figure 15.8: Dependence of the scaled critical alignment strength α_0 on the diffusion coefficient $\varepsilon_+ = \frac{\varepsilon}{2}$ for (9.2) and $\varepsilon_+ = \varepsilon$ for (9.4), respectively. Parameters: $L \in \{5\pi,\ 100\pi\}$, $\Delta t = 0.12\ \Delta x^2 {\varepsilon_+}^{-1}$, $\Delta x \in \{0.05,\ 0.1,\ 0.2\}$.

Again, the critical alignment strength increases with the diffusion coefficient

$$\varepsilon = \varepsilon_w = \varepsilon_u$$

as to be expected. The precise relationship between ε and the scaled value

$$\alpha_0 := \alpha_{crit} \frac{L^2}{\pi^2}$$

is depicted in figure 15.8 for both systems, (9.2) and (9.4), and for domain sizes of 5π

and 100π.

The initial perturbation used for these simulations was chosen to be a triangle shaped hat function

$$\begin{aligned} u_{r,0}(x) &= \frac{1}{2}u_0 + 2h\frac{x}{L}\chi_{[0,\frac{L}{2}]} + 2h\left(1-\frac{x}{L}\right)\chi_{[\frac{L}{2},L]} \\ u_{l,0}(x) &= \frac{1}{2}u_0 - 2h\frac{x}{L}\chi_{[0,\frac{L}{2}]} - 2h\left(1-\frac{x}{L}\right)\chi_{[\frac{L}{2},L]} \end{aligned}$$

but different initial conditions, also with perturbations of the total particle density, where checked to yield the same results.

As alignment term we chose the standard sublinear version given by (15.6) but as already found in subsection 15.2.1 for system (9.2), any other sublinear alignment term leads to the same critical alignment strengths.

By the analysis in chapter 10 we expect the scaled critical alignment strength α_0 to equal ε in case of system (9.2) and 2ε for system (9.4). In fact, we find a linear relationship between the critical alignment strength and the diffusion coefficient for ε being not too small, and the factor of proportionality is as expected, namely one for system (9.2) and two for system (9.4). In addition, there is some approximately constant offset which depends on the step size of the discretization is related to the numerical diffusion already being discussed in the previous subsection and being measured in more detail below.

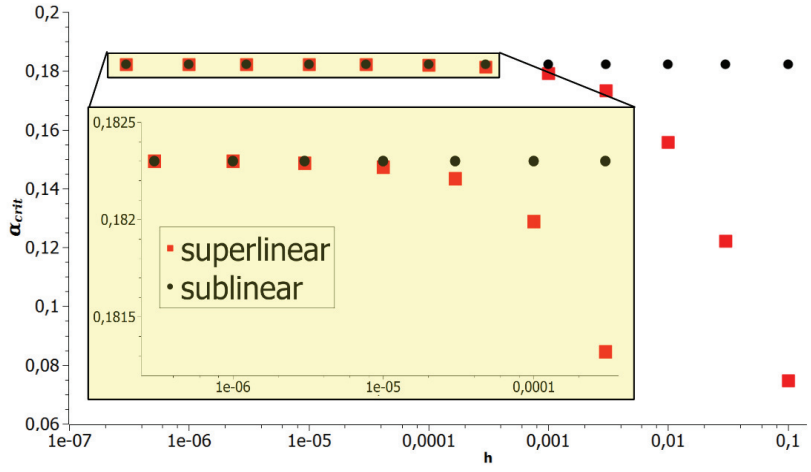

Figure 15.9: Dependence of the critical alignment strength on the size of the initial perturbation (measured in multiples of the total particle density u_0) at fixed shape of the perturbation and fixed model parameters. For the sublinear alignment terms (*black balls*), there is no dependence at all, whereas for the superlinear alignment term $\tilde{f}_{s,2}$ (*red squares*), α_{crit} decreases with increasing size of the perturbation. The zoom box shows that a perturbation size of $w = 10^{-4}u_0$, corresponding to less than 0.01 % of particles being turned around, already accounts for a change in the critical alignment strength by about 0.15%.

Moreover, we recover the dependence of the critical alignment strength on the size of the perturbation for superlinear alignment whereas for the sublinear version, this size

does not matter at all. This effect is shown in figure 15.9.

Concerning the observed offset which depends on the numerical step size we note that the found relation between the measured critical alignment strength and the given diffusion coefficients is approximately given by

$$\alpha_{crit,num} \sim \varepsilon_u + \varepsilon_w + const = \begin{cases} \varepsilon + const & \text{for system (9.2)} \\ 2\varepsilon + const & \text{for system (9.4),} \end{cases} \tag{15.12}$$

with the approximation being good if ε is not too small compared to Δx.

As we already noted the observed offset stems from the artificial diffusion and other superficial terms introduced by the numerical scheme. In the previous subsection we mentioned that the numerical diffusion coefficient depends on the spatial and temporal step sizes of the discretization. Moreover, we found the size of the spatial domain to play a role which we attributed to possible boundary artefacts or an effect of the alignment term and higher order terms.

Let us now analyze all the dependencies in more detail. Denoting the numerical diffusion coefficient by D_{num} we see that it enters the model as additional diffusion term in both equations which effectively are turned into

$$\begin{aligned} \partial_t u + \partial_x w &= (\varepsilon_u + D_{num})\partial_{xx} u \\ \partial_t w + \partial_x u &= (\varepsilon_w + D_{num})\partial_{xx} w + f(u,w) \end{aligned} \tag{15.13}$$

where we have $\varepsilon_u = 0$ for system (9.2) and $\varepsilon_u = \varepsilon$ for system (9.4), and in either case $\varepsilon_w = \varepsilon$.

To obtain functional relationships between the model parameters and the numerical grid sizes on the one hand and the numerical diffusion coefficient on the other hand we measure the value of the scaled critical alignment strength $\alpha_{0,num}$ obtained by the simulations depending on the different parameters we can control and ask for the difference between $\alpha_{0,num}$ and the predicted value

$$\alpha_0 = \alpha_{crit} \frac{L^2}{\pi^2} = 2\varepsilon_+.$$

First we find that keeping all else equal, the value of α_0 increases linearly as the temporal step size Δt is decreased to 0, and the factor of proportionality equals one:

$$\alpha_{0,num} = \bar{\alpha}_{0,num}(\varepsilon, \Delta x, L) - \Delta t,$$

at least for large domains.

The dependence of α_0 on the spatial step size is also in good approximation linear if we are concerned with large spatial domains. In fact, the artificial diffusion coefficient seems to behave like

$$D_{num} \approx \Delta x - \Delta t$$

if the domain is large enough, and the critical alignment strength therefore behaves like

$$\alpha_{crit,num} = \frac{\pi^2}{L^2}(\varepsilon_u + \varepsilon_w + \Delta x - \Delta t).$$

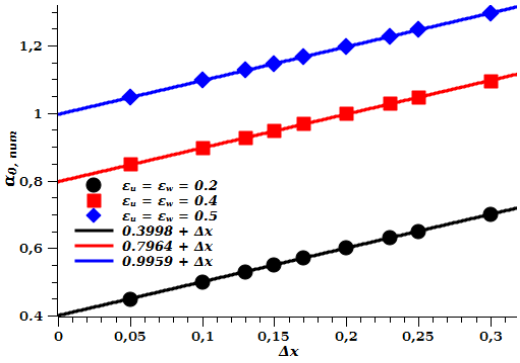

Figure 15.10: Dependence of the measured scaled critical alignment strength $\alpha_{0,num}$ on the spatial step size Δx for different values of the diffusion coefficients ε_u and ε_w, measured at domain size of $L = 100\ \pi$ and in the limit $\Delta t \searrow 0$. Note the linear relationship with asymptotic values being just equal to $\varepsilon_u + \varepsilon_w$.

This is in good agreement with the prediction for an explicite EULER scheme with upwind flux for the plain hyperbolic system without diffusion and alignment. Here, the artificial diffusion coefficient can be computed to be

$$D_{num,upwind} = v^2\ \Delta t + v\Delta x$$

where v is the particle velocity which is one in our case.

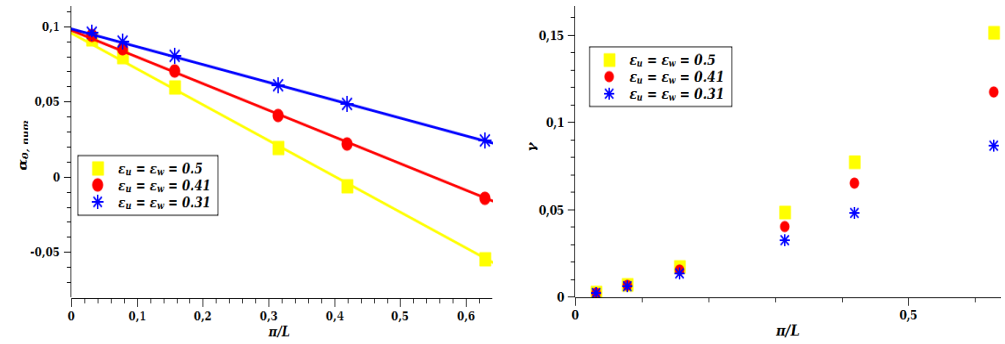

Figure 15.11: Dependence of the measured scaled critical alignment strength $\alpha_{0,num}$ in the limit $\Delta t \searrow 0$ (*left*) and the correction γ to the factor of proportionality in $D_{num} \sim \Delta t$ (*right*) on the invers domain size L^{-1}. The spatial step size was put to $\Delta x = 0.1$, the diffusion coefficients were chosen as $\varepsilon = 0.31,\ 0.41,\ 0.5$.

Not so easily appreciated is the dependence on the domain size, or rather on the alignment strength. What is always recovered in very good approximation is a linear dependence of the scaled critical alignment strength α_0 on the time step Δt of the shape

$$\alpha_{0,num} = \varepsilon_u + \varepsilon_w + D_{num,0} - (1 - \gamma)\Delta t$$

where γ quickly decreases to zero as the domain length grows. The constant $D_{num,0}$ is still independent of Δt, grows with Δx for fixed ε and L, and again approaches Δx from below as L is increased. Moreover, for fixed Δx and L, $D_{num,0}$ decreases as the diffusion coefficients $\varepsilon_{u/w}$ are increased.

In figure 15.11 we show the relationship between $D_{num,0}$ (which in fact also includes the higher order effects) and the domain size L for a fixed spatial step size and different diffusion coefficients. As L is decreased towards zero we observe a relationship of the

kind

$$D_{num,0} \sim L^{-1}.$$

The dependence of the correction factor γ in the linear relationship between $\alpha_{0,num}$ and Δt is also shown and we see that γ increases as the domain shrinks and approaches zero as L grows. It is however still not clear which amount of the nontrivial dependence of the deviation from the theoretical value α_0 is induced by boundary effects and which part is the contribution of the alignment term itself.

We conclude that at least for very small alignment strengths α, the numerical diffusion coefficient of the interior scheme (that is, without boundary effects) is in good approximation given by

$$D_{num} = \Delta x - \Delta t \tag{15.14}$$

and does not depend explicitely on ε itself. This is the artificial diffusion coefficient being introduced by the explicite EULER scheme with upwind flux which is the predominant discretization error for the advection dominated case $\alpha\varepsilon \ll 1$ (cf. remark 13.3).

Notably, if we put ε to zero and investigate virtually the whole system with only the numerical diffusion everything works out as predicted. That is, the measured scaled critical alignment strength is indeed given by $\Delta x - \Delta t$ with deviations only for very small domain sizes.

15.2.3 Interpretation of the results

The most striking observation is the dependence of the stability on the size of the perturbations for superlinear bistable alignment terms whereas for sublinear ones the homogeneous steady state is either stable against perturbations of any size or is unstable. This behavior can well be understood by recalling the stability results from chapters 10 and 11.

There, we found that for both models, the linear stability analysis yielded for any values of the diffusion coefficient and the domain length a critical alignment strength α_{crit} which marked the boundary between linear stability and instability.

For the sublinear versions of f, we found the same sharp stability boundary also in the nonlinear stability analysis. Using the superlinear alignment terms we instead did not find a sharp stability criterion and only could state that for alignment strengths larger than α_{crit}, the homogeneous steady state is nonlinearly unstable.

We argued that for α being slightly smaller than its critical value there should be some perturbations that will grow despite the predictions from the linear stability analysis. Moreover, we suspected that the larger a perturbation is, the smaller an alignment strength α is required to let it grow. And indeed, the simulations indicate that the critical alignment strength for a given shape of the perturbation decreases with its height increasing.

Thus, we find that our relatively simple system exhibits a symmetric steady state whose stability cannot be determined from the linearization but also depends on the higher orders of the nonlinearity.

We also recall that by the nonlinear stability analysis for system (9.4) we found a stability bound of $\alpha_0 = \varepsilon$ rather than $\alpha_0 = 2\varepsilon$ as predicted by the linear stability analysis and now observed in the simulations. This is not a contradiction as the result in chapter 11 took into account that possibly the total particle density might remain constant. The behavior observed in the simulations is somewhat different.

According to the prediction of the linear analysis, the system tends to select the minimal wave numbers from generic perturbations for both, the polarization and the particle density, as this combination is the one with the largest growth rate σ. In particular, any initial perturbation of the polarization at constant particle density will always from the beginning on produce variations in the particle density which contribute to the decay of the energy functional E. We have therefore reconciled with one another the different predictions from chapters 10 and 11.

15.3 Simulation on large domains and traveling waves

We will now consider the system on large spatial domains where the boundary conditions do not play a role. In that situation we choose different localized initial conditions on top of the trivial homogeneous steady state

$$(w \equiv 0,\ u \equiv U_1)$$

and examine which type of profiles will emerge from these data. Our main concern are traveling wave solutions emerging in the system. To assure that the homogeneous steady state can indeed be viewed as an asymptotic state of some wave pattern we will have to take the computational domain large enough to prevent the wave from reaching the boundary.

Since we have not been able to deduce any assertions about the stability of traveling wave solutions in chapters 13 and 14 we shall not expect to observe all kinds of wave profiles described there. The only patterns which are in fact observed in simulations should be the stable ones. We will in particular focus on the connection between the alignment strength α and the diffusion coefficients ε_u and ε_w on the one hand and the velocity of the evolving waves on the other hand.

15.3.1 Traveling waves for system (9.2)

Our first simulations started with initial conditions close to certain traveling wave profiles with well defined asymptotic states corresponding to well defined wave velocities. A particular example for such data is sketched in figure 15.12. In this example, the asymptotic states are chosen to be

$$(W_1 = 0,\ U_1 = 1)$$

on the right and

$$U_3 = -W_3 = \frac{2}{3}$$

to the left. These asymptotic states would correspond to a wave velocity of $c = 2$.

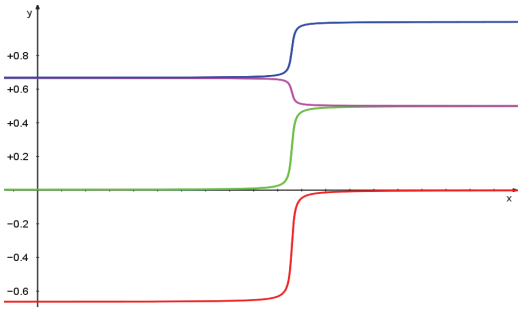

Figure 15.12: Typical shape of initial conditions for a traveling wave connecting the state $U_3 = -W_3$ to the symmetric state $W = 0$. *Red*: W, *blue*: U, *green*: U_r, *magenta*: U_l.

In fact, the system chooses its own wave velocity completely independent of the particular data and only according to the system parameters. As an example, figure 15.13 shows the temporal development of the polarization w for different initial conditions and different parameters.

We observe that the resulting traveling wave profile (the jump from the plateau in the center to that on the right) is independent of the asymptotic states encoded in the initial data but only depends on the parameters. In particular, these right moving waves have velocities larger than 1 which means that we work in the region above c^*.

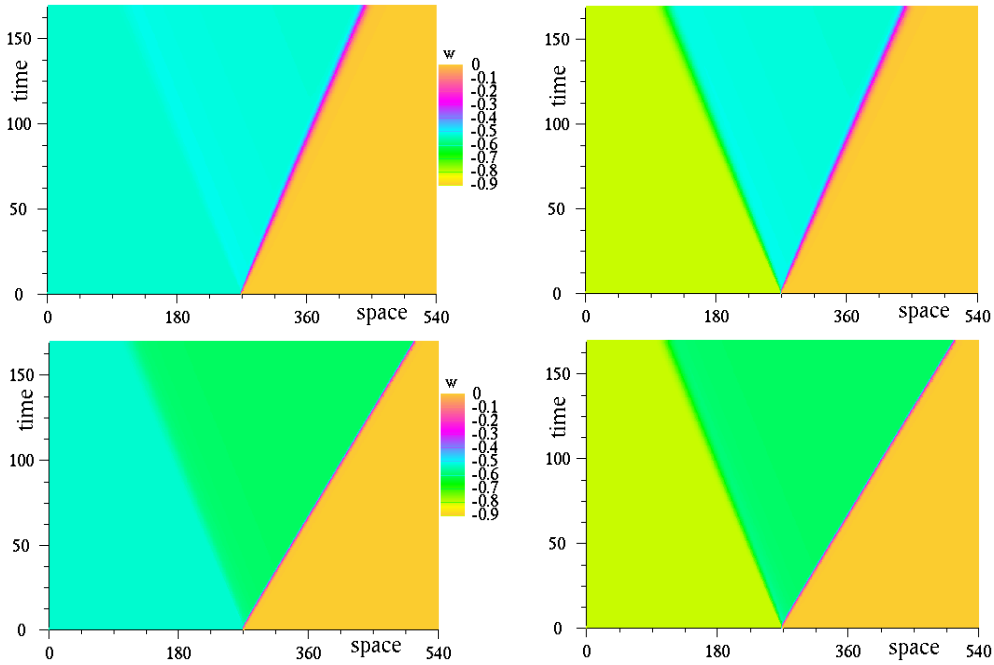

Figure 15.13: Single wave profiles moving to the right evolving from monotone initial conditions. *Top*: parameters corresponding to $c^* \approx 1.1$, *bottom*: $c^* \approx 1.5$, *left*: initial conditions corresponding to $c = 1.1$, *right*: intitial conditions corresponding to $c = 4$. Similar colors code for similar values of w. It is obvious that the asymptotic states of the right moving wave profile are those corresponding to the critical velocities c^* rather than to the initial conditions. At the rear, a diffusion profile moving to the left connects the left asymptotic state to the initial data on the left.

In addition, we find a secondary wave emerging to the left where the discrepancy between the left asymptotic states of the data and of the resulting traveling wave is corrected. These secondary waves are slower than the right moving ones and looking closer, we observe that their velocity is precisely 1. In fact, we are not dealing with traveling wave profiles but with the diffusion fronts discussed in section 14.5. In these fronts, two plateaus of totally left aligned states are connected.

Using qualitatively different initial conditions we also obtain traveling wave profiles of other types. In particular, choosing initial conditions similar to a wave profile connecting a state of the type $U_2 = W_2$ to a symmetric one of the type $W_1 = 0$ with $U_1 < U_2$, we find indeed a wave of this type moving to the right and behind that again a secondary diffusion profile which is now moving to the right at velocity 1.

Combining these different types of initial conditions one is tempted to produce a series of wave profiles as in section 13.6. However, the construction of these profiles fails as the waves with velocities $c \in (-1, 1)$ seem to be unstable. Still, there are two types of patterns we do observe, both of them containing diffusion fronts and a region of total

depletion of particles in the center of the domain.

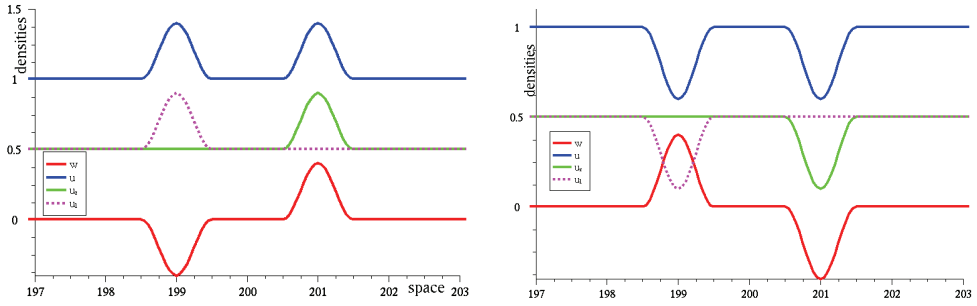

Figure 15.14: Typical initial conditions from which complex wave patterns evolve. *Left*: localized increase of densities of right and left oriented particles leading to two single humps emerging from the center of the domain, *right*: localized decrease of right and left oriented particles leading to two double humps emerging from the center. Note the zoom into the center of the spatial domain!

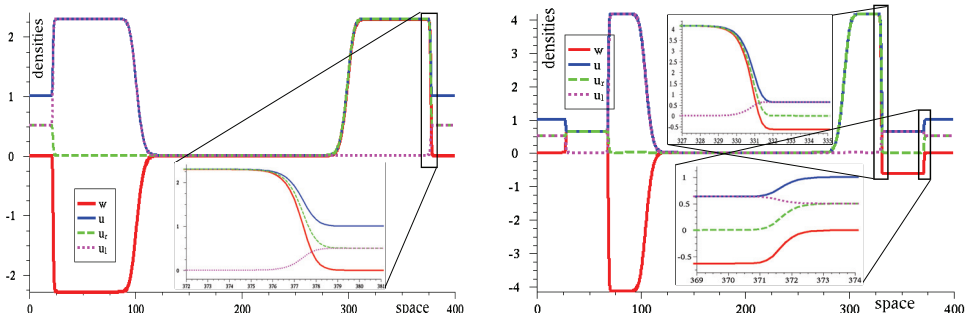

Figure 15.15: Typical wave patterns emerging from the initial conditions sketched in figure 15.14. *Left*: two single humps emerging from excess of particles as in figure 15.14 left, *right*: two double humps emerging from defects of particles as in figure 15.14. In both cases, the relevant wave patterns are shown in more detail in the zoom boxes.

1. The easiest symmetric pattern to be observed emerges from initial conditions where we put some additional right oriented particles slightly right to the center of the domain and some additional left oriented particles slightly left of the center (cf. figure 15.14, left). This results in a fast wave moving to the right at $c > c^*$ and connecting a totally right aligned state

$$U_2 = W_2 = \frac{c}{c-1} U_1$$

to the symmetric state $(W = 0, U = U_1)$, followed by a diffusion front along which the density $U = W$ falls from U_2 to zero. A mirror image of this profile moves to the left where at speed $-c$ the state $(W = 0, U = U_1)$ is connected to the totally

left aligned state

$$U_3 = -W_3 = \frac{c}{c-1}U_1 = \frac{-c}{-c+1}U_1.$$

Again, this wave profile is followed by a diffusion front bringing the particle density to the center value of zero. This type of solution has already been predicted in section 14.5 and will be referred to as single hump solutions in what follows.

2. If in contrast, we remove some right oriented particles on the right of the center and some left oriented particles on the left (cf. figure 15.14, right), we obtain a slightly more complicated profile which may also be understood in physical terms. The initially slight depletion of right oriented particles enables the majority of opposingly traveling left oriented particles to stop even more of them until finally a region with only left oriented particles is left.

   We therefore encounter a leading wave front connecting a state of type three (that is, $W_3 = -U_3$) to the outer symmetric state ($W = 0, U = U_1$) and moving at speed $c \geq c^*$. This wave is followed by a second one where the left oriented particles are met by a superior number of right oriented ones. This profile therefore connects a state of type two (that is, $U_2 = W_2$) to the type three state behind the leading front. The velocity of this wave lies between 1 and c^*. Recall that this type of wave connecting type two and type three states could not be predicted but there existence could neither be excluded (cf. the dotted yellow and cyan curves in figure 13.3). Yet, the existence of this type of waves was conjectured from the flow field pictures in phase space in figure 13.10. At the rear, we find a diffusion front with speed 1 behind which there are no particles left at all.

   Finally, the whole pattern is repeated symmetrically on the left. We will call these patterns double hump solutions for obvious reasons.

In figure 15.15, two typical wave patterns according to the two situations we discussed here are shown. In that example, the solution is shown after a simulation time $T = 100$ for parameters $\varepsilon_w = 0.2$, $\varepsilon_u = 0$ and $\alpha = 0.6$ with the superlinear alignment term

$$f(u, w) = \alpha w \left(1 + 12\frac{|w|}{u} - 13\frac{w^2}{u^2}\right).$$

If we allow for asymmetric perturbations, also the resulting wave patterns can become asymmetric. Let us consider data similar to case 1 above, but now the additional particles are only of one orientation. We will then obtain only one traveling and growing hump. At its rear, we have a diffusion profile at whose end there is no complete depletion from particles but rather a totally aligned state which is connected to the symmetric asymptotic state at the other end of the domain. An example of this phenomenon is depicted in figure 15.16.

We shall note that the use of other alignment terms leads to different shapes of the wave fronts but the basic pattern of single or double humps remains the same. In particular, the steepness of the wave fronts increases with the size of α, and superlinear alignment yields significantly sharper fronts than the sublinear f. Moreover, the time until a stable wave pattern is established is larger for the sublinear alignment term and for smaller values of α.

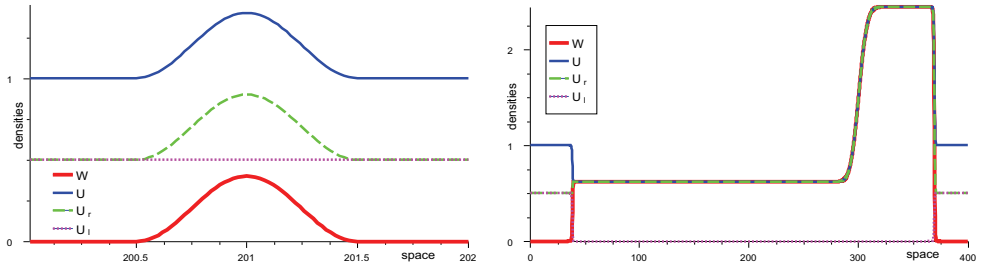

Figure 15.16: Typical asymmetric wave pattern (*right*) emerging from an initial perturbation (*left*) of the non-polarized state by local addition of right oriented particles. The rightmost front is a traveling wave profile similar to that in figure 15.15 *left*. On the outer left, there is a wave front corresponding to that in figure 15.15 *right*. The right asymptotic state of this wave is of totally right aligned type $W = U$ as is the left asymptotic state of the leading front on the right. The only difference lies in the amount of right oriented particles. These two states of the same type are connected by the diffusion profile at the rear of the right hump.

Another important finding is that the measured wave speeds and the plateau values of the asymptotic states indeed follow very precisely the predicted relationships we summarized in proposition 13.9. This also allows us to easily determine the velocity of a wave profile by just measuring the plateau values of the polarization in front of an behind the wave.

15.3.2 Traveling waves for system (9.4)

For this model, we only mention that the qualitative behavior of this system is the same as that of system (9.2) discussed in the previous subsection. Although the exact shapes of the wave fronts and the resulting values of the velocities are slightly different, we encounter precisely the same types of patterns from the same types of initial data as before.

In particular, the relation between wave speed and asymptotic states are precisely the same for this model. We therefore find good evidence for our conjecture that the full system (9.4) inherits the properties of its hyperbolic limit systems (9.2) and (14.20) not only for very small values of ε but in fact for a rather wide range of diffusion coefficients.

15.3.3 Dependence of wave velocities on parameters

The next step of our investigation is to find the precise relationship between the velocities of the evolving traveling waves on the one hand and the parameter values and the type of alignment term on the other hand. We already found that only three types of right moving wave profiles occur in the simulations. These are

1. waves with velocity $c > c^*$ connecting a state of type $U_2 = W_2$ to a state of type

$$(W = 0, U = U_1 = \frac{c-1}{c} U_2),$$

2. waves with velocity $c > c^*$ connecting a state of type $U_3 = -W_3$ to a state of type

$$(W = 0, U = U_1 = \frac{c+1}{c} U_3),$$

3. and waves with velocity $c \in (1, c^*)$ connecting a state of type $U_2 = W_2$ to a state of type

$$U_3 = -W_3 = \frac{c-1}{c+1} U_2.$$

Before examining the relationship between the parameters and the velocities in detail we shall note that the numerical diffusion coefficient has to be taken into account. We already observed that the full diffusion coefficients in the models are given by

$$\tilde{\varepsilon}_u = \varepsilon_u + D_{num} \qquad \text{and} \qquad \tilde{\varepsilon}_w = \varepsilon_w + D_{num},$$

respectively. In terms of our systems (9.2) and (9.4) this means that we will not be able to observe the true behavior of (9.2) since with numerical diffusion this one becomes

$$\begin{aligned} \partial_t u + \partial_x w &= D_{num} \partial_{xx} u \\ \partial_t w + \partial_x u &= (\varepsilon + D_{num}) \partial_{xx} w + f \end{aligned}$$

which is an interpolate model of type (14.17) with

$$\theta = \frac{D_{num}}{\varepsilon + D_{num}}.$$

For system (9.4) we obtain under consideration of the artificial diffusion effect the system

$$\begin{aligned} \partial_t u + \partial_x w &= (\varepsilon + D_{num}) \partial_{xx} u \\ \partial_t w + \partial_x u &= (\varepsilon + D_{num}) \partial_{xx} w + f \end{aligned}$$

which is just the same but with slightly different diffusion coefficient $\varepsilon + D_{num}$.

If we now recall that the artificial diffusion coefficient was found to be

$$D_{num} = \Delta x - \Delta t$$

we can try to establish a linear relationship between the original and the full diffusion coefficient by choosing the numerical step sizes as

$$\begin{aligned} \Delta x &= c_1 \varepsilon \\ \Delta t &= c_2 \Delta x \\ \tilde{\varepsilon} = \varepsilon + D_{num} &= (1 + c_1(1 - c_2))\varepsilon. \end{aligned}$$

Applying the same idea to system (9.2) we obtain an interpolate model of type (14.17) with

$$\theta = \frac{c_1(1-c_2)}{1 + c_1(1-c_2)} \qquad \text{independent of } \varepsilon$$

and

$$\tilde{\varepsilon} = \varepsilon(1 + c_1(1 - c_2)).$$

Having these choices of the step size at hand we can check the relationship between the observed wave velocities and the effective product

$$a_{eff} = \tilde{\varepsilon}\alpha = (1 + c_1(1 - c_2))\varepsilon\alpha.$$

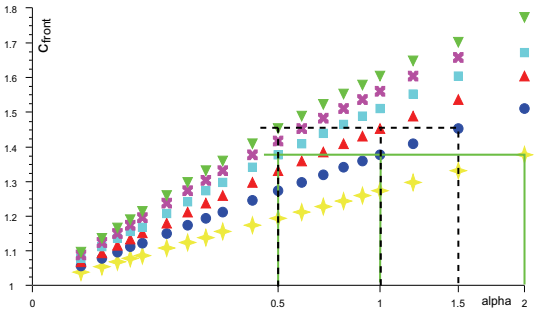

Figure 15.17: Velocity of the leading wave front for system (9.2) with standard sublinear alignment term depending on the alignment strength for different diffusion coefficients $\varepsilon = 0.05$ (*yellow stars*), $\varepsilon = 0.1$ (*blue balls*), $\varepsilon = 0.15$ (*red triangles*), $\varepsilon = 0.2$ (*cyan squares*), $\varepsilon = 0.25$ (*magenta crosses*), and $\varepsilon = 0.3$ (*green triangles*). Note the coincidence of wavespeeds for equal products of ε and α! The highlighted examples are $a = 0.15 = 0.1 \cdot 1.5 = 0.15 \cdot 1 = 0.3 \cdot 0.5$ (*black dashed line*) and $a = 0.1 = 0.05 \cdot 2 = 0.1 \cdot 0.1 = 0.2 \cdot 0.5$ (*green line*).

The most interesting profiles are the leading fronts whose velocities we calculated from the results of the simulations for different alignment terms.

These showed the following remarkable properties which are observed for both models, (9.2) and (9.4).

- Given any shape of the alignment term and any of the initial conditions being discussed above, the velocities indeed only depended on the product $\alpha\varepsilon$ and never on both parameters individually. This nicely fits to our calculations for the critical velocities c^* into whose formulas only the product $a = F_w\varepsilon$ entered. This effect is shown exemplarily in figure 15.17 for the sublinear alignment term.

- Using different sublinear alignment terms given by (15.6), (15.7), or (15.8), we always obtain the same velocities − depending on $\alpha\varepsilon$, of course. This supports the conjecture that for sublinear alignment terms, the critical velocities only depend on the linearization.

- In case of sublinear alignment, the velocities of the leading fronts in the solutions with one hump traveling in either direction and those of the solutions with two humps per direction coincide for given parameters (cf. figure 15.18). Recall that we analytically found both types of waves for the same velocity regime $|c| > c^*$. In case of superlinear alignment, the fronts of the single hump solutions are significantly faster than those of the double hump solutions. This indicates a nontrivial dependence of the velocity on the wave profile for superlinear alignment terms.

- The precise connection between the product $a = \alpha\varepsilon$ for any fixed alignment term and wave type is indeed of the shape

$$|c| - 1 \propto \sqrt{a}$$

for small values of a. We show this relationship in figure 15.18 for different alignment terms and different wave types.

- Given fixed parameters α and ε, the observed wave velocities are larger for superlinear than for sublinear alignment terms. Recall that this difference has already been predicted by the calculations in subsection 13.5.3. The calculations conducted there to find invariant domains in phase plane also give a glimpse why the wave speeds are different for different wave types in case of superlinear alignment terms.

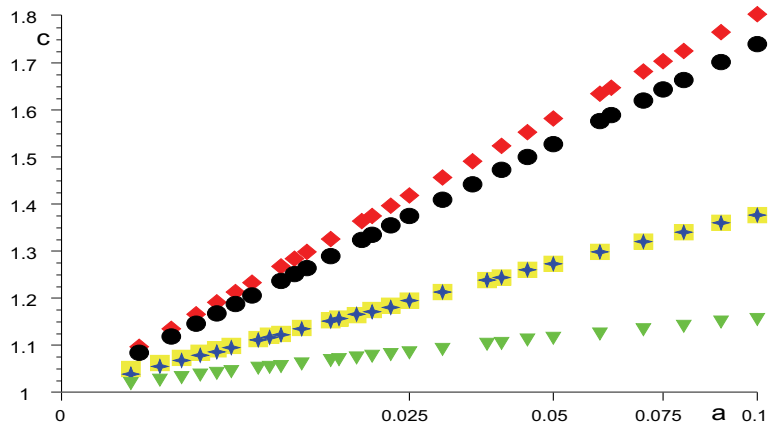

Figure 15.18: Precise dependence of the velocities of different waves occuring in model (9.4) for different alignment terms and different wave types on the product $a = \alpha\varepsilon$. The square root scale for the a-axis has been chosen to emphasize the linear relationship between c and $a = \sqrt{\alpha\varepsilon}$. Shown are the velocities of the outer fronts of single hump solutions for sublinear f (*yellow squares*) and superlinear f (*red diamonds*), of outer fronts of double hump solutions for sublinear (*blue stars*) and superlinear (*black balls*) alignment, and for comparison, the velocity of the second front in double hump solutions for sublinear f (*green triangles*). As sublinear alignment term the shape (15.6) is used, the superlinear term is $\tilde{f}_{s,2}$ according to (12.10) without exponential crowding term (i.e., $\beta = 0$) and $\nu = 12$.

Let us now have a closer look how the precise values of the velocities depend on the product $\alpha\varepsilon$ and try to deduce connections to the numerical diffusion coefficient. For these calculations we use fixed values of Δx and Δt and tune the alignment strength α for different diffusion coefficients ε.

Although we do not have an analytical relationship between $a = \alpha\varepsilon$ and the critical velocity c^* for the case of system (9.4), we can use the plot from figure 14.1 to graphically obtain the value of a from c^* and vice versa. This is used to find an effective value a_{eff} corresponding to given values of α, ε, Δx and Δt.

In figure 15.19, we show the measured and the predicted wave velocities for step sizes

$$\Delta x = 0.23 \qquad \text{and} \qquad \Delta t = 0.13\Delta x \approx 0.03.$$

According to our investigations in section 15.2, this should lead to a numerical diffusion coefficient of $D_{num} \approx 0.2$ and hence an effective diffusion coefficient $\varepsilon_{eff} = \varepsilon + 0.1$. Indeed, if the diffusion coefficient ε is put to zero, we observe a very good agreement

with the theory as the measured velocities are precisely those corresponding to $a = 0.1\alpha$. This coincidence becomes even more evident in the other graph in figure 15.19 which shows the calculated effective value a_{eff} together with the true value 0.1 α.

If we now choose ε different from zero, for example 0.1 or 0.2 in figure 15.19, then we find the velocities to be smaller than predicted, in particular as α increases. This observation provides some evidence for the conjecture that the alignment term itself has an impact on the numerical diffusion coefficient.

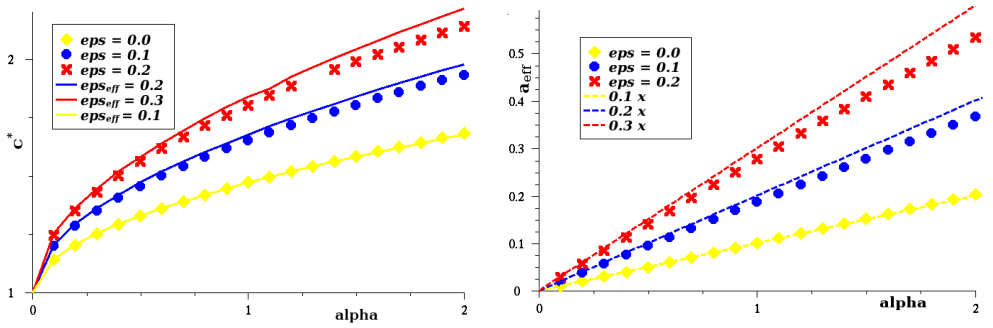

Figure 15.19: Measured and predicted wave velocities (*left*) and effective products a_{eff} (*right*) for numerical step sizes $\Delta x = 0.23$ and $\Delta t = 0.03$. Shown are the measured velocities for $\varepsilon = 0.0$ (*yellow diamonds*), $\varepsilon = 0.1$ (*blue balls*), and $\varepsilon = 0.2$ (*red crosses*) against the given alignment strength α, together with the predicted velocities c^* (as lines) for $a = \alpha(\varepsilon + 0.1)$. On the *right*, the symbols denote the values a_{eff} which are deduced from the measured velocities assuming these are the critical velocities c^*. For comparison, the dashed lines show the values $(\varepsilon + 1)\alpha$.

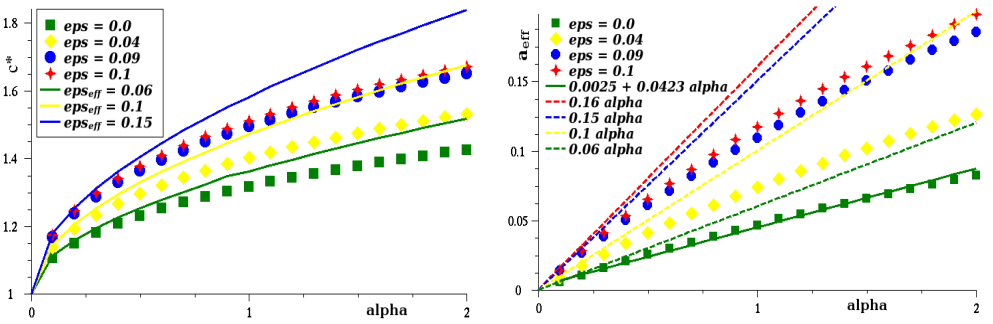

Figure 15.20: Measured and predicted wave velocities (*left*) and effective products a_{eff} (*right*) for numerical step sizes $\Delta x = 0.2$ and $\Delta t = 0.08$. Here, the measured velocities are given for $\varepsilon = 0.0$ (*green squares*), $\varepsilon = 0.04$ (*yellow diamonds*), and $\varepsilon = 0.09$ (*blue balls*) and $\varepsilon = 0.1$ (*red stars*). The curves of the same colors are the predicted critical velocities for $a = (\varepsilon + 0.06)\alpha$. The symbols on the right denote again the respective effective values a_{eff} for the measured velocities being assumed to be the critical ones. Again, we show the values $(\varepsilon+0.06)\alpha$ as dashed lines and for $\varepsilon = 0.0$ also the linear regression as *solid green line*.

Choosing different step sizes as is done for the simulations whose results are shown in figure 15.20, we also obtain a quantitatively different behavior. The precise parameters

are now taken to be

$$\Delta x = 0.2 \qquad \text{and} \qquad \Delta t = 0.4\Delta x = 0.08$$

resulting in a predicted numerical diffusion coefficient of 0.12 and a predicted effective diffusion coefficient of $\varepsilon_{eff} = \varepsilon + 0.06$.

Still the agreement of the predicted velocities with the measured ones is not too bad for small values of α but for each value we chose for the diffusion coefficient and for all investigated alignment strengths, the measured velocity was smaller than the predicted one. Moreover, the deviations are significantly larger as in the previously discussed setting. Again, the deviation increases with both, increasing α and ε.

It remains unclear why the predicted velocities are not precisely met by the simulations. Possible reasons for the differences are

- numerical errors beyond the artificial diffusion term $\Delta x - \Delta t$, most probably introduced by the discretization of the alignment term, or
- a deviation of the true critical wave speeds from the value predicted from the linearization. This would be surprising at least in case of the sublinear alignment term.

Still, the qualitative behavior of the wave speeds and in particular the dependence only on the product $\alpha\varepsilon_{eff}$ are nicely recovered in the simulations.

Chapter 16

Summary and Discussion II

The objective of this second part was a better understanding of the behavior of the hyperbolic part (2.13) of our cytoskeleton model upon additional effects like diffusive behavior and mutual alignment of filaments. Letting the monomer concentration a be constant and making certain assumptions on the parameters we found a family of reduced systems of two reaction diffusion equations.

This system (14.17) describes the motion of oriented particles − or particularly short filaments − in one space dimension at a fixed velocity superimposed with diffusive behavior and mutual alignment of right and left moving specimen. However, the final model is not formulated in terms of right and left oriented filaments but rather in terms of the total particle density u and the polarization w which is defined as the difference of the densities of particles moving to the right and left, respectively.

We introduced different types of alignment whose common feature are at least three equilibria. In particular, the alignment terms of major interest are of bistable type and take the value zero whenever the polarization vanishes or when it takes its maximal absolute value $w = \pm u$ indicating that all particles move into the same direction. The former equilibria we called symmetric or non-polarized states, the latter ones were dubbed totally aligned states.

The main difference between the alignment terms we considered is their behavior for small values of the polarization. The first type has been called sublinear, the second one superlinear alingment where the terminology meant the dependence on w for $w \approx 0$ and fixed particle density $u_0 > 0$. The sublinear version can be interpreted as filaments turning around one another by pure steric interactions between two filaments at a time whereas the superlinear alignment term incorporates possible cooperative effects in alignment.

This system confined to a finite spatial domain showed a continuum of homogeneous steady states being characterized by vanishing polarization $w \equiv 0$ and any non-negative particle density $u \equiv u_0 \geq 0$. In chapters 10 and 11 we considered the linear and nonlinear stability of these steady states against small perturbations.

First, we found the linear stability only to depend on the size L of the spatial domain and the ratio of the alignment strength α and the diffusion coefficient ε. It did not depend on the type of the alignment term at all since the linearization can by definition not distinguish between sublinear and superlinear right hand sides.

The nonlinear stability in terms of a suitable L_2-energy on the contrary revealed

a significant difference between sublinear and superlinear alignment. In case of the sublinear alignment term, the conditions for stability were found to be precisely the linear stability conditions whereas for the superlinear alignment terms, no sharp stability criterion could be found. The only assertion to be made for the latter case was that the linear stability condition is insufficient to guarantee nonlinear stability and that the stability behavior should depend on the shape and size of the perturbation.

All these predictions have been found to be confirmed by simulations whose outcomes are discussed in chapter 15. In particular, the dependence of the stability of the homogeneous non-polarized state on the size of the applied perturbations has been investigated, and a nontrivial dependence has been observed for the superlinear alignment terms. However, as the perturbations were made smaller and smaller, in the limit the stability conditions approached those found for the sublinear alignment terms. The particular importance of the shape of the nonlinearity for the stability behavior is stressed in subsection 15.2.3.

With a view to understanding polarization effects away from the boundary we considered the systems (9.2) and (9.4) on the whole real line as spatial domain and asked for traveling wave solutions. These were explicitely found for the purely hyperbolic system (14.20) without diffusion as well as for system (9.2). For system (9.4), the existence of traveling wave solutions could be asserted at least for small diffusion coefficients by viewing the according traveling wave system as a singular perturbation of the hyperbolic case (14.22), (14.23).

Since all totally aligned states and all non-polarized states (with arbitrary total densities) are equilibria of the system, there is a whole continuum of possible asymptotic states for the traveling waves. However, in contrast to typical scalar reaction diffusion equations, the choice of a pair of asymptotic states already fixes the velocity of the wave.

Moreover, we find critical velocities $c^* > 1$ and $c_* \in [0, 1)$, depending only on the product of linearization g_w of the alignment term at $w = 0$ by the diffusion coefficient ε. For wave speeds having an absolute value between c_* and c^* we cannot expect monotone wave profiles connecting the non-polarized state $w = 0$ to any of the totally aligned states $w = \pm u$. For the superlinear alignment terms, these critical velocities could not be determined explicitely but at least we could deduce upper bounds for c^*.

In fact, given two asymptotic states connected by any monotone profile as initial conditions, the solution develops a sequence of wave profiles and diffusion fronts to connect these asymptotic states. These profiles have particular velocities depending on the alignment strength and the diffusion coefficient. In fact, the velocities selected by the system depend on the parameters in a similar way as c^* does. Waves with velocities between -1 and 1, that is, slower than the particle velocity, are not observed in simulations. Neither are non-monotone wave profiles which are known to be unstable for most common reaction diffusion systems (cf. [33]).

Altogether, we obtained a rather basic reaction diffusion system describing the motion of aligning particles or alternatively a polarizable medium with stochastic equilibration effects.

Considering this system in a confined domain with reflecting boundary conditions, we found the stability of the symmetric, non-polarized equilibrium to depend on the domain

size, the diffusion coefficient and the strength of the alignment in a rather usual way. Strikingly, the linearization around this steady state could not appropriately predict the stability behavior in case of superlinear alignment terms. In fact, the stability was found to be determined by the whole nonlinearity.

Without spatial confinement we found arbitrary perturbations of the homogeneous non-polarized state to evolve into traveling profiles and eventually leading to propagating fronts of full polarization and often depletion zones without any particles being left.

Returning to the initial question of the behavior of the hyperbolic equations (2.13) at fixed monomer densities, these waves profiles remind us of fronts of aligned filament ends as they are observed in lamellipodia of moving cells. This suggests to incorporate effects like fluctuations of filament tips − by diffusion of whole filaments or by diffuse polymerization and depolymerization − and mutual alignment of filaments − by steric interaction or mediated by filament binding proteins such as α-actinin or fascin − into the model.

Allowing for alignment − or, in one space dimension, flipping − of filaments requires keeping track of the whole filaments rather than their tips. In particular, the length must be taken into account, and in such a model, filaments have to be characterized by their position (of one of the ends or of the center), their orientation, and their length as additional independent variable as has for example been done in [6].

Appendix A

Spaces for HÖLDER Estimates for Parabolic Equations

A.1 HÖLDER spaces

Before beginning with the introduction of parabolic HÖLDER spaces we note that we will occasionally encounter functions belonging to standard HÖLDER spaces. For that reasons we note that whenever a function is said to belong to $C^{k+\beta}$ with $k \in \mathbb{N}_0$ and $\beta \in (0,1]$, this function is assumed to have continuous derivatives of order k with respect to any collection of its arguments and that its derivatives of k^{th} order are HÖLDER continuous of exponent β, again with respect to all of its arguments. More precisely, we use the following notation.

Definition A.1.1. *1. Let $T > 0$, $\beta \in (0,1]$, and $k \in \mathbb{N}_0$ be given. We define the space $C^{k+\beta}([0,T])$ by*

$$C^{k+\beta}([0,T]) := \left\{ f \in C^k([0,T]) \mid H\ddot{o}l_\beta \left(\frac{d^k}{dt^k} f \right) < \infty \right\} \tag{A.1}$$

where for $g \in C^0([0,T])$, the HÖLDER constant is given by

$$H\ddot{o}l_\beta (g) = \sup_{0 \le s < t \le T} \frac{|g(t) - g(s)|}{(t-s)^\beta}. \tag{A.2}$$

We equip $C^{k+\beta}([0,T])$ with the norm

$$\|f\|_{C^{k+\beta}([0,T])} := \|f\|_{C^k([0,T])} + H\ddot{o}l_\beta \left(\frac{d^k}{dt^k} f \right) \tag{A.3}$$

where the C^k-norm is the sum of the supremum norms of all derivatives of f of orders $0, \dots, k$. We most often write $\|f\|_{C^{k+\beta}}$ rather than $\|f\|_{C^{k+\beta}([0,T])}$.

2. Given $T > 0$, $\beta \in (0,1]$, $k \in \mathbb{N}_0$, and a space-time domain

$$Q_T = \{(t,x) \mid 0 < t < T, l(t) < x < r(t)\},$$

we define the space $C^{k+\beta}(\overline{Q_T})$ *by*

$$C^{k+\beta}(\overline{Q_T}) = \left\{ f \in C^k(\overline{Q_T}) \mid H\ddot{o}l_\beta\left(\partial^\alpha f\right) < \infty \text{ for each } \alpha \text{ of length } k \right\}. \quad \text{(A.4)}$$

where the Hölder *constant for a continuous function* g *is now defined by*

$$\begin{aligned} H\ddot{o}l_\beta(g) :=& \; H\ddot{o}l_{t,\beta}(g) + H\ddot{o}l_{x,\beta}(g) \\ =& \sup_{(t,x),(s,x)\in\overline{Q_T},t\neq s} \frac{|g(s,x)-g(t,x)|}{|s-t|^\beta} + \sup_{(t,x),(t,y)\in\overline{Q_T},x\neq y} \frac{|g(t,y)-g(t,x)|}{|y-x|^\beta}. \end{aligned}$$

The norm is again given by

$$\|f\|_{C^{k+\beta}(\overline{Q_T})} := \|f\|_{C^k(\overline{QT})} + \sum_{|\alpha|=k} H\ddot{o}l_\beta\left(\partial^\alpha f\right). \quad \text{(A.5)}$$

Remark A.1. *It is well known that for* $0 < \beta_1 < \beta_2 \leq 1$ *and integers* $0 \leq l \leq k$*, the spaces* $C^{k+\beta_2}$ *compactly embed into* $C^{l+\beta_1}$*. We will occasionally require the embedding constant for the case* $k = l = 0$*.*

In the one dimensional case we find for $g \in C^{0+\beta_2}([0,T])$ *the follwing simple estimate:*

$$\begin{aligned} H\ddot{o}l_{\beta_1}(g) &= \sup_{0\leq s<t\leq T} \frac{|g(t)-g(s)|}{(t-s)^{\beta_1}} \\ &= \sup_{0\leq s<t\leq T} \frac{|g(t)-g(s)|}{(t-s)^{\beta_2}} (t-s)^{\beta_2-\beta 1} \\ &\leq H\ddot{o}l_{\beta_2} T^{\beta_2-\beta_1}. \end{aligned} \quad \text{(A.6)}$$

In the spatiotemporal case, we analogously obtain for $g \in C^{0+\beta_2}(\overline{Q_T})$*:*

$$H\ddot{o}l_{t,\beta_1}(g) \leq H\ddot{o}l_{t,\beta_2} T^{\beta_2-\beta_1} \quad \text{(A.7)}$$

$$H\ddot{o}l_{x,\beta_1}(g) \leq H\ddot{o}l_{x,\beta_2} L_{max}^{\beta_2-\beta_1} \quad \text{(A.8)}$$

with

$$L_{max} := \max_{t\in[0,T]} \mathcal{L}^1(\Sigma_t)$$

being the maximal length of a temporal section through Q_T*.*

For more information on Hölder spaces we refer to standard textbooks on real analysis and differential equations. A brief introduction can for instance be found in section 4.1 of [11].

For the interior estimates we slightly adapt the notation from the monograph [19] by Gary Lieberman concerning parabolic distances and interior Hölder norms. As we deal with a parabolic equation the notion of Hölder continuity is slightly more involved than in the usual definition.

We start with defining certain special subsets of $\mathbb{R} \times \mathbb{R}^n$ and some properties of the domain Q_T.

Definition A.1.2. *1. We define the (spatial) diameter of the domain* $Q_T \subset \mathbb{R} \times \mathbb{R}^n$

to be the spatial diameter of its projection to the space hyperplane $0 \times \mathbb{R}^n$*:*

$$\operatorname{diam} Q_T := \sup_{(t,x),(s,y)\in Q_T} |x-y| \tag{A.9}$$

2. *Given a point* $(t,x) \in \mathbb{R}\times\mathbb{R}^n$*, a set* $U \subset \mathbb{R}\times\mathbb{R}^n$ *and a radius* $R>0$ *let* $U[X,R]$ *denote the intersection of* U *with the parabolic cylinder of radius* R *below* (t,x)*:*

$$U[X,R] = U \cap \operatorname{Cyl}_R(t,x). \tag{A.10}$$

For the notion of parabolic cylinders we refer to subsection 2.2.2.

Having these notations at hand we can now proceed to define the global Hölder spaces which are used to measure the regularity of the functions in question throughout the whole domain and up to the boundary.

Definition A.1.3. *(Global* Hölder *spaces) Given a smooth function* $f \in C^\infty(\overline{Q_T})$ *and numbers* $k \in \mathbb{N}_0,\ \beta \in (0,1]$ *we define*

$$\|f\|_{C^{k+\beta,P}} := \sum_{m+2j\le k} \|\partial_x^m \partial_t^j f\|_{C^0} + [f]_{k+\beta} + \langle f\rangle_{k+\beta} \tag{A.11}$$

where

$$\begin{aligned} [f]_{k+\beta} &= \sum_{m+2j=k} \sup_{\substack{(t,x),(s,y)\in Q_T \\ (t,x)\neq(s,y)}} \frac{|\partial_x^m\partial_t^j f(t,x) - \partial_x^m\partial_t^j f(s,y)|}{|(t,x)-(s,y)|_P^\beta} \\ &\equiv \sum_{m+2j=k} H\ddot{o}l_{P,\beta}(\partial_x^m\partial_t^j f) \end{aligned} \tag{A.12}$$

and

$$\begin{aligned} \langle f\rangle_{k+\beta} &= \sum_{m+2j=k-1} \sup_{\substack{(t,x),(s,x)\in Q_T \\ s\neq t}} \frac{|\partial_x^m\partial_t^j f(t,x) - \partial_x^m\partial_t^j f(s,x)|}{|t-t_0|^{\frac{1+\beta}{2}}} \\ &\equiv \sum_{m+2j=k-1} H\ddot{o}l_{t,\frac{1+\beta}{2}}(\partial_x^m\partial_t^j f) \end{aligned} \tag{A.13}$$

are the parabolic and the temporal Hölder *constants of the highest relevant combinations of derivatives of* f*. A function* $f \in C^0(\overline{Q_T})$ *is called (globally) parabolically* Hölder *continuous with exponent* β *if* $\|f\|_{C^{0+\beta,P}} < \infty$*, and it is said to be of class* $C^{k+\beta,P}$ *if* $\|f\|_{C^{k+\beta,P}} < \infty$*.*

Let us remark that for small k the sums in the definition of the Hölder norm only contain a few terms. For example, the most commonly occuring versions are:

$$\|f\|_{C^{0+\beta,P}} = \|f\|_{C^0} + H\ddot{o}l_{P,\beta}(f), \tag{A.14}$$

$$\|f\|_{C^{1+\beta,P}} = \|f\|_{C^0} + \|\partial_x f\|_{C^0} + H\ddot{o}l_{P,\beta}(\partial_x f) + H\ddot{o}l_{t,\frac{1+\beta}{2}}(f), \tag{A.15}$$

$$\|f\|_{C^{2+\beta,P}} = \|f\|_{C^{2_x,1_t}} + H\ddot{o}l_{P,\beta}(\partial_{xx} f) + H\ddot{o}l_{P,\beta}(\partial_t f) + H\ddot{o}l_{t,\frac{1+\beta}{2}}(\partial_x f) \tag{A.16}$$

where

$$\|f\|_{C^{2_x,1_t}} = \|f\|_{C^0} + \|\partial_x f\|_{C^0} + \|\partial_{xx} f\|_{C^0} + \|\partial_t f\|_{C^0}. \tag{A.17}$$

To derive interior estimates the introduced HÖLDER norms are weighted by certain powers of the distance to the parabolic boundary of the domain. The corresponding definitions are as follows.

Definition A.1.4. *(Weighted* HÖLDER *spaces)*

1. *For any point $(t,x) \in Q_T$ we denote its parabolic distance to the parabolic boundary $\mathcal{P}Q_T$ by*

$$d_P((t,x)) := \inf_{\substack{(s,\,y)\,\in\,\mathcal{P}Q_T \\ s\,\le\,t}} |(t,x)-(s,y)|_P. \tag{A.18}$$

Given any two points $(t,x),\ (s,y) \in Q_T$ write

$$d_P((t,x),(s,y)) := \min\{d_P(t,x), d_P(s,y)\}.$$

2. *The oscillation of a function f over the domain Q_T is defined to be*

$$\operatorname{osc}_{Q_T}(f) := \sup_{(t,x)\in Q_T} f(t,x) - \inf_{(t,x)\in Q_T} f(t,x).$$

3. *Given a function $f \in C^0(Q_T)$ and a* non-negative *number b, define*

$$|f|_0^{(b)} := \|d_P^b f\|_{C^0} \equiv \sup_{(t,x)\in Q_T} |d_P(t,x)^b f(t,x)|. \tag{A.19}$$

4. *For $f \in C^0(Q_T)$ and a* negative *real number b we define*

$$|f|_0^{(b)} := (\operatorname{diam} Q_T)^b \|f\|_{C^0} \tag{A.20}$$

where $\operatorname{diam} Q_T$ denotes the spatial diameter of Q_T as defined above.

5. *Given $f \in C^\infty(Q_T)$ and numbers $k \in \mathbb{N}_0,\ \beta \in (0,1]$, and a real number $b \ge -k-\beta$ define the weighted* HÖLDER *norm*

$$|f|_{k+\beta}^{(b)} := \sum_{m+2j\le k} \left|\partial_x^m \partial_t^j f\right|_0^{(m+2j+b)} + [f]_{k+\beta}^{(b)} + \langle f\rangle_{k+\beta}^{(b)} \tag{A.21}$$

where in case $k+\beta+b \ge 0$:

$$[f]_{k+\beta}^{(b)} = \sup_{\substack{(t,\,x),\,(s,\,y)\,\in\,Q_T \\ (t,\,x)\,\neq\,(s,\,y)}} \sum_{m+2j=k} \left(d_P^{k+\beta+b} \frac{\left|\partial_x^m \partial_t^j f(t,x) - \partial_x^m \partial_t^j f(s,y)\right|}{|(t,x)-(s,y)|_P^\beta} \right) \tag{A.22}$$

and

$$\langle f\rangle^{(b)}_{k+\beta} = \sup_{\substack{(t,x),(s,x)\in Q_T\\ t\neq s}} \sum_{m+2j=k-1} \left(d_P^{k+\beta+b} \frac{\left|\partial_x^m\partial_t^j f(t,x) - \partial_x^m\partial_t^j f(s,y)\right|}{|t-s|^{\frac{1+\beta}{2}}} \right). \tag{A.23}$$

In the last two formulas we abbreviated both, $d_P((t,x),(s,y))$ and $d_P((t,x),(s,x))$, by d_P.

In case $k+\beta+b<0$, $[f]^{(b)}_{k+\beta}$ and $\langle f\rangle^{(b)}_{k+\beta}$ are defined by

$$[f]^{(b)}_{k+\beta} = \sup_{\substack{(t,x),(s,y)\in Q_T\\ (t,x)\neq(s,y)}} \sum_{m+2j=k} \left(d^{k+\beta+b} \frac{\left|\partial_x^m\partial_t^j f(t,x) - \partial_x^m\partial_t^j f(s,y)\right|}{|(t,x)-(s,y)|_P^{\beta}} \right) \tag{A.24}$$

and

$$\langle f\rangle^{(b)}_{k+\beta} = \sup_{\substack{(t,x),(s,x)\in Q_T\\ t\neq s}} \sum_{m+2j=k-1} \left(d^{k+\beta+b} \frac{\left|\partial_x^m\partial_t^j f(t,x) - \partial_x^m\partial_t^j f(s,y)\right|}{|t-s|^{\frac{1+\beta}{2}}} \right) \tag{A.25}$$

with d denoting the (spatial) diameter of Q_T.

A function $f\in C^0(Q_T)$ is said to belong to $C^{k+\beta}_{(b)}(Q_T)$ if the norm $|f|^{(b)}_{k+\beta}$ is finite.

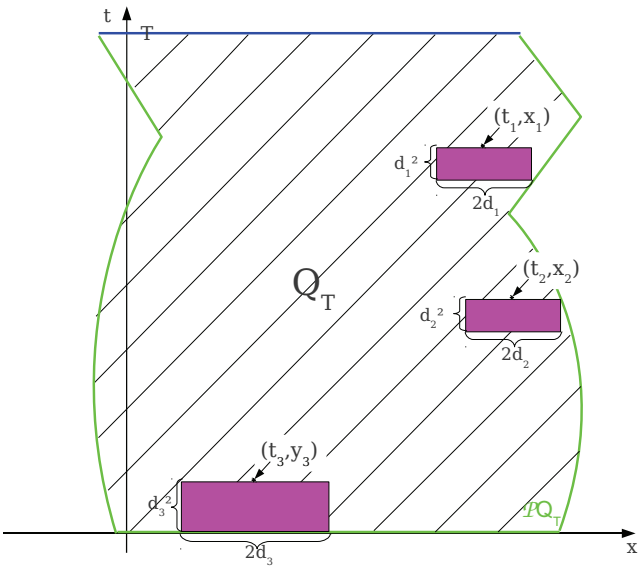

Figure A.1: Illustration of the parabolic distance for different points in Q_T. Here: $d_1 = d_P((t_1,x_1))$, $d_2 = d_P((t_2,x_2))$, $d_3 = d_P((t_3,x_3))$.

Remark A.2. *The parabolic distance of a point (t,x) to the parabolic boundary is just the radius of the largest parabolic cylinder beneath (t,x) that is completely contained in Q_T. The weighted norms thus suppress large changes in the relevant derivatives close to the parabolic boundary.*

HÖLDER norms for the lowest regularities

As for our purposes the cases $k \in \{0,1,2\}$ are the most relevant ones we write the explicite forms of the weighted HÖLDER norms for these k. The general forms are the following:

$$\begin{aligned}
|f|^{(b)}_{0+\beta} &= |f|^{(b)}_{0} + [f]^{(b)}_{0+\beta}, \\
|f|^{(b)}_{1+\beta} &= |f|^{(b)}_{0} + |\partial_x f|^{(1+b)}_{0} + [f]^{(b)}_{1+\beta} + \langle f\rangle^{(b)}_{1+\beta}, \\
|f|^{(b)}_{2+\beta} &= |f|^{(b)}_{0} + |\partial_x f|^{(1+b)}_{0} + |\partial_{xx} f|^{(2+b)}_{0} + |\partial_t f|^{(2+b)}_{0} + [f]^{(b)}_{2+\beta} + \langle f\rangle^{(b)}_{2+\beta}.
\end{aligned}$$

For particular values of b and β we find for $|f|^{(b)}_{0+\beta}$ the following:

$$|f|^{(b)}_{0+\beta} = \|d_P^b f\|_{C^0} + \sup_{(t,x)\neq(s,y)} d_P^{b+\beta} \frac{|f(t,x)-f(s,y)}{|(t,x)-(s,y)|_P^\beta} \qquad \text{for } b \geq 0,$$

$$|f|^{(b)}_{0+\beta} = (\operatorname{diam} Q_T)^b \|f\|_{C^0} + \sup_{(t,x)\neq(s,y)} d_P^{b+\beta} \frac{|f(t,x)-f(s,y)}{|(t,x)-(s,y)|_P^\beta} \qquad \text{for } 0 > b \geq -\beta,$$

$$|f|^{(b)}_{0+\beta} = (\operatorname{diam} Q_T)^b \|f\|_{C^0} + (\operatorname{diam} Q_T)^{b+\beta} \sup_{(t,x)\neq(s,y)} \frac{|f(t,x)-f(s,y)}{|(t,x)-(s,y)|_P^\beta} \qquad \text{for } b < -\beta.$$

For $k = 1$ we can distinguish the following cases:

$$\begin{aligned}
|f|^{(b)}_{1+\beta} = \|d_P^b f\|_{C^0} + \|d_P^{1+b}\partial_x f\|_{C^0} &+ \sup_{(t,x)\neq(s,y)} d_P^{1+b+\beta} \frac{|\partial_x f(t,x)-\partial_x f(s,y)}{|(t,x)-(s,y)|_P^\beta} \\
&+ \sup_{(t,x)\neq(s,x)} d_P^{1+b+\beta} \frac{|f(t,x)-f(s,x)|}{|t-s|^{\frac{1+\beta}{2}}} \qquad \text{for } b \geq 0,
\end{aligned}$$

$$\begin{aligned}
|f|^{(b)}_{1+\beta} = (\operatorname{diam} Q_T)^b \|f\|_{C^0} + \|d_P^{1+b}\partial_x f\|_{C^0} &+ \sup_{(t,x)\neq(s,y)} d_P^{1+b+\beta} \frac{|\partial_x f(t,x)-\partial_x f(s,y)}{|(t,x)-(s,y)|_P^\beta} \\
&+ \sup_{(t,x)\neq(s,x)} d_P^{1+b+\beta} \frac{|f(t,x)-f(s,x)|}{|t-s|^{\frac{1+\beta}{2}}} \qquad \text{for } 0 > b \geq -1,
\end{aligned}$$

$$\begin{aligned}
|f|^{(b)}_{1+\beta} = (\operatorname{diam} Q_T)^b \|f\|_{C^0} &+ (\operatorname{diam} Q_T)^{(1+b)} \|\partial_x f\|_{C^0} \\
&+ \sup_{(t,x)\neq(s,y)} d_P^{1+b+\beta} \frac{|\partial_x f(t,x)-\partial_x f(s,y)}{|(t,x)-(s,y)|_P^\beta} \\
&+ \sup_{(t,x)\neq(s,x)} d_P^{1+b+\beta} \frac{|f(t,x)-f(s,x)|}{|t-s|^{\frac{1+\beta}{2}}} \qquad \text{for } -1 > b \geq -1-\beta,
\end{aligned}$$

and finally

$$
\begin{aligned}
|f|^{(b)}_{1+\beta} \;=\; & (\operatorname{diam} Q_T)^b \|f\|_{C^0} + (\operatorname{diam} Q_T)^{(1+b)} \|\partial_x f\|_{C^0} \\
& + (\operatorname{diam} Q_T)^{1+b+\beta} \sup_{(t,x)\neq(s,y)} \frac{|\partial_x f(t,x) - \partial_x f(s,y)}{|(t,x)-(s,y)|_P^\beta} \\
& + (\operatorname{diam} Q_T)^{1+b+\beta} \sup_{(t,x)\neq(s,x)} \frac{|f(t,x)-f(s,x)|}{|t-s|^{\frac{1+\beta}{2}}} \qquad \text{for } b < -1-\beta.
\end{aligned}
$$

Here, as always, by $\partial_x f$ and $\partial_t f$ we denote the derivative of f with respect to the spatial variable and the time variable, respectively, no matter at what point it is evaluated. The term $\partial_x f(s,y)$ for example, has to be read as

$$
(\partial_x f(t,x))\,|_{(t,x)=(s,y)}\ .
$$

Similarly, we find for $k=2$ different expressions for the cases

$$
b>0, \quad b\in[-1,0), \quad b\in[-2,-1), \quad b\in[-2-\beta,-2), \quad \text{and} \quad b<-2-\beta.
$$

We only write down the following explicite expressions for those cases which are of interest to us.

$$
\begin{aligned}
|f|^{(b)}_{2+\beta} \;=\; & \|d_P^b f\|_{C^0} + \|d_P^{1+b}\partial_x f\|_{C^0} + \|d_P^{2+b}\partial_{xx} f\|_{C^0} + \|d_P^{2+b}\partial_t f\|_{C^0} \\
& + \sup_{(t,x)\neq(s,y)} d_P^{2+b+\beta} \frac{|\partial_{xx} f(t,x) - \partial_{xx} f(s,y)}{|(t,x)-(s,y)|_P^\beta} \\
& + \sup_{(t,x)\neq(s,y)} d_P^{2+b+\beta} \frac{|\partial_t f(t,x) - \partial_t f(s,y)}{|(t,x)-(s,y)|_P^\beta} \\
& + \sup_{(t,x)\neq(s,x)} d_P^{2+b+\beta} \frac{|\partial_x f(t,x) - \partial_x f(s,x)|}{|t-s|^{\frac{1+\beta}{2}}} \qquad \text{for } b>0,
\end{aligned}
$$

$$
\begin{aligned}
|f|^{(b)}_{2+\beta} \;=\; & (\operatorname{diam} Q_T)^b \|f\| + (\operatorname{diam} Q_T)^{1+b} \|\partial_x f\| + \|d_P^{2+b}\partial_{xx} f\| + \|d_P^{2+b}\partial_t f\| \\
& + \sup_{(t,x)\neq(s,y)} d_P^{2+b+\beta} \frac{|\partial_{xx} f(t,x) - \partial_{xx} f(s,y)}{|(t,x)-(s,y)|_P^\beta} \\
& + \sup_{(t,x)\neq(s,y)} d_P^{2+b+\beta} \frac{|\partial_t f(t,x) - \partial_t f(s,y)}{|(t,x)-(s,y)|_P^\beta} \\
& + \sup_{(t,x)\neq(s,x)} d_P^{2+b+\beta} \frac{|\partial_x f(t,x) - \partial_x f(s,x)|}{|t-s|^{\frac{1+\beta}{2}}} \qquad \text{for } b\in[-2,-1)
\end{aligned}
$$

with all norms in the first line being the supremum norms $\|\cdot\|_{C^0}$, and

$$\begin{aligned}
|f|^{(b)}_{2+\beta} &= (\operatorname{diam} Q_T)^b \|f\|_{C^0} + (\operatorname{diam} Q_T)^{1+b} \|\partial_x f\|_{C^0} \\
&\quad + (\operatorname{diam} Q_T)^{2+b} \|\partial_{xx} f\|_{C^0} + (\operatorname{diam} Q_T)^{2+b} \|\partial_t f\|_{C^0} \\
&\quad + \sup_{(t,x)\neq(s,y)} d_P^{2+b+\beta} \frac{|\partial_{xx} f(t,x) - \partial_{xx} f(s,y)}{|(t,x)-(s,y)|_P^\beta} \\
&\quad + \sup_{(t,x)\neq(s,y)} d_P^{2+b+\beta} \frac{|\partial_t f(t,x) - \partial_t f(s,y)}{|(t,x)-(s,y)|_P^\beta} \\
&\quad + \sup_{(t,x)\neq(s,x)} d_P^{2+b+\beta} \frac{|\partial_x f(t,x) - \partial_x f(s,x)|}{|t-s|^{\frac{1+\beta}{2}}} \qquad \text{for } b \in [-2-\beta, -2).
\end{aligned}$$

A.2 Morrey spaces

We will also use the global and weighted Morrey spaces being introduced in [19] as well. We shall therefore cite their definition and then give some explicite examples how the according norms look like for certain values of the relevant exponents p, θ, and b.

Definition A.2.1. *1. Given $f \in C^{0+1,P}(Q_T)$ and numbers $p \in [1,\infty)$, $\theta > 1$ we define*

$$\|f\|_{M_{p,\theta}} := \sup_{(t,x)\in Q_T, r<\operatorname{diam} Q_T} \left(r^{-\theta} \int_{Q_T[(t,x),r]} |f|^p ds dy \right)^{\frac{1}{p}}. \tag{A.26}$$

The function f is said to belong to $M_{p,\theta}(Q_T)$ if this supremum is finite.

2. Given $f \in L_1^{loc}(Q_T)$ and numbers $\theta \in [0,3]$, $b \geq 3-\theta$ we define

$$\|f\|_{M^{(b)}_{p,\theta}} := \sup_{\substack{(t,x)\in Q_T \\ r \in \left[0, \frac{d_P(t,x)}{2}\right]}} \left(r^{-\theta} d_P((t,x))^{pb+\theta-3} \int_{\mathrm{Cyl}_r(t,x)} |f|^p ds dy \right)^{\frac{1}{p}} \tag{A.27}$$

and say f belongs to $M^{(b)}_{p,\theta}(Q_T)$ if this value is finite.

We will at some point require that cU and $\tilde{c}U$ belong to $M_{1,2+\beta}$ or to $M^{(2)}_{1,2+\beta}$ for some $\beta \in (0,1)$. Let us therefore explicitely calculate the corresponding norms for a function f:

$$\begin{aligned}
\|f\|_{M_{1,2+\beta}} &= \sup_{(t,x)\in Q_T, r<\operatorname{diam} Q_T} \left(r^{-2-\beta} \int_{Q_T[(t,x),r]} |f(s,y)| ds dy \right) \\
&\leq \sup_{(t,x)\in Q_T, r<\operatorname{diam} Q_T} \left(r^{-2-\beta} r^2 \int_{B_r(x)} |f(t,y)| dy \right) \\
&\leq (\operatorname{diam} Q_T)^{1-\beta} \|f\|_{C^0} \quad \leq \quad (L + 2T v_{max})^{1-\beta} \|f\|_{C^0}
\end{aligned}$$

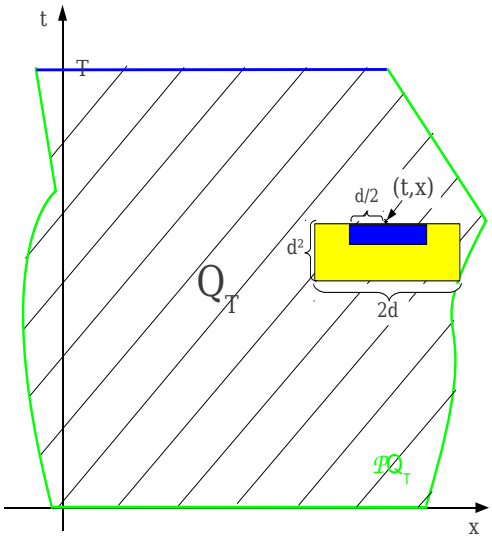

Figure A.2: Illustration of the region of integration for the weighted Morrey norm $\|\cdot\|_{M^{(b)}_{p,\theta}}$. The supremum is taken over all points $(t,x) \in Q_T$ and then the integral has to be taken over parabolic cylinders being bounded away from the parabolic boundary of Q_T. Here d denotes the parabolic distance $d_P((t,x))$ of the point (t,x) to the parabolic boundary (the corresponding parabolic cylinder indicated in yellow). The integral is now to be evaluated over all parabolic cylinders beneath (t,x) of diameter less than $\frac{d}{2}$, that is, at most over the blue area.

for the global norm and

$$\|f\|_{M^{(2)}_{1,2+\beta}} = \sup_{\substack{(t,x)\in Q_T \\ r\in\left[0,\frac{d_P(t,x)}{2}\right]}} \left(r^{-2-\beta} d_P((t,x))^{1+\beta} \int_{\mathrm{Cyl}_r(t,x)} |f(s,y)| d(s,y) \right)$$

for the weighted version.

Appendix B

Computation of the LYAPUNOV Coefficient

In section 13.5, we noticed that the non-polarized equilibrium state

$$(W = 0, U = U_1 > 0)$$

undergoes a Hopf bifurcation as the wave speed c passes through one. We stated that the first LYAPUNOV coefficient $l_1(0)$ at the bifurcation point vanishes which we will now demonstrate.

At the critical velocity $c = 1$ the system (13.31) reads

$$\begin{aligned}
\frac{d}{d\xi}\begin{pmatrix} W \\ V \end{pmatrix} &= \begin{pmatrix} V \\ -\frac{1}{\varepsilon} g(W) \end{pmatrix} \\
&= \begin{pmatrix} 0 & 1 \\ -\omega_0^2 & 0 \end{pmatrix}\begin{pmatrix} W \\ V \end{pmatrix} + \frac{1}{2}\begin{pmatrix} 0 \\ -\frac{g''(0)}{\varepsilon} W^2 \end{pmatrix} + \frac{1}{6}\begin{pmatrix} 0 \\ -\frac{g'''(0)}{\varepsilon} W^3 \end{pmatrix} + \mathcal{O}(W^4) \\
&=: A\begin{pmatrix} W \\ V \end{pmatrix} + \frac{1}{2}\begin{pmatrix} W & V \end{pmatrix} B\begin{pmatrix} W \\ V \end{pmatrix} + \frac{1}{6} C\left(\begin{pmatrix} W \\ V \end{pmatrix}, \begin{pmatrix} W \\ V \end{pmatrix}, \begin{pmatrix} W \\ V \end{pmatrix}\right) + \mathcal{O}(W^4).
\end{aligned}$$

where we introduced the first order frequnecy

$$\omega_0^2 = \frac{g'(0)}{\varepsilon}. \tag{B.1}$$

Here, the quadratic form B is given by

$$(x_1, y_1) B\begin{pmatrix} x_2 \\ y_2 \end{pmatrix} = \begin{pmatrix} 0 \\ -\frac{g''(0)}{\varepsilon} x_1 x_2 \end{pmatrix}$$

and the third order form C reads

$$C\left(\begin{pmatrix} x_1 \\ y_1 \end{pmatrix}, \begin{pmatrix} x_2 \\ y_2 \end{pmatrix}, \begin{pmatrix} x_3 \\ y_3 \end{pmatrix}\right) = \begin{pmatrix} 0 \\ -\frac{g'''(0)}{\varepsilon} x_1 x_2 x_3 \end{pmatrix}.$$

The coefficient matrix of the linear part clearly has the eigenvalues

$$\nu_{0,\pm} = \pm \imath\omega_0 \tag{B.2}$$

and the associated normalized eigenvectors

$$\eta_\pm = \frac{1}{\sqrt{2}} \begin{pmatrix} \pm\frac{1}{\imath\omega_0} \\ 1 \end{pmatrix}. \tag{B.3}$$

The corresponding eigenvectors of the transposed matrix are

$$\zeta_\pm = \frac{1}{\sqrt{2}} \begin{pmatrix} \pm\imath\omega_0 \\ 1 \end{pmatrix} \tag{B.4}$$

and we find their complex scalar product to be $\langle \eta_+, \zeta_- \rangle = 1$.

The first LYAPUNOV coefficient (up to a positive factor) can therefore be computed by

$$\begin{aligned} l_1(0) &= \frac{1}{2\omega_0^2} \operatorname{Re}\left[\langle \zeta_-, C(\eta_+, \eta_+, \eta_-\rangle - 2\left\langle p, \eta_+^T B(A^{-1}\eta_+^T B\eta_-)\right\rangle \right. \\ &\quad \left. + \left\langle \zeta_+, \eta_-^T B((2\imath\omega_0 \bullet - A)^{-1}(\eta_+^T B\eta_+))\right\rangle \right] \\ &= \frac{1}{2\omega_0^2} \operatorname{Re}\left[\frac{\imath}{4}\frac{g'''(0)}{\varepsilon\omega_0^3} + \frac{\imath g''(0)^2}{2\varepsilon^2\omega_0^5} + \frac{\imath}{\sqrt{2}}\frac{g''(0)}{6\varepsilon\omega_0^3} - \frac{\imath g''(0)}{3\varepsilon\omega_0^3} \right] \end{aligned} \tag{B.5}$$

which is indeed zero since the term in the brackets is purely imaginary.

List of Figures

Bibliography

[1] Bamburg J R, Bernstein B W, *Roles of ADF/cofilin in actin polymerization and beyond*, F1000 Biol Reports **2**:62 (2010)

[2] Bugyi B, Carlier M-F, *Control of actin filament treadmilling in cell motility*, Annu Rev Biophys **39** (2010), 449–470

[3] Cannon J R, *The one dimensional heat eqution*, Addison-Wesley Publishing Company, Reading (1984)

[4] Crank J, *Free and moving boundary problems*, Oxford University Press, Oxford (1984)

[5] DiPerna R J, Lions P-L, *Ordinary differential equations, transport theory and Sobolev spaces*, Invent Math **98** (1989), 511–547

[6] Doubrovinski K, Kruse K, *Self-alignment in systems of treadmilling filaments*, Eur Phys J E **31** (2010), 95–104

[7] Fenichel N, *Geometric singular perturbation theory*, J Diff Eq **31** (1979), 53–98

[8] Friedman A, *Variational principles and free boundary problems*, John Wiley & sons, New York (1982)

[9] Fuhrmann J, *Actin dynamics and cell motility*, Diploma Thesis (2007)

[10] Fuhrmann J, Käs J, Stevens A, *Initiation of cytoskeletal asymmetry for cell polarization and movement*, J Theor Biol **249** (2007), 278–288

[11] Gilbarg D, Trudinger N S, *Elliptic partial differential equations of second order* (reprint of the 2nd ed.), Grundlehren der Mathematischen Wissenschaft **224**, Springer, Berlin Heidelberg New York (1983)

[12] Guckenheimer J, Holmes P, *Nonlinear oscillations, dynamical systems, and bifurcations of vector fields* (corrected 7th printing), Applied Mathematical Sciences **42**, Springer, New York (2002)

[13] Jäger W, Luckhaus S, *On explosions of solutions to a system of partial differential equations modelling chemotaxis*, Trans Amer Math Soc **329** (1992), 819–824

[14] Kawashima S, *Systems of a hyperbolic-parabolic composite type, with applications to the equations of magnetohydrodynamics*, Thesis, Kyoto University (1983)

[15] Kuznetsov Y A, *Elements of applied bifurcation theory*, Springer, New York (1995)

[16] Ladyženskaja O A, Solonnikov V A, Ural'ceva N N, *Linear and quasilinear equations of parabolic type* (corrected reprint), Translations of Mathematical Monographs, American Mathematical Society, Providence, R.I. (1988)

[17] LeVeque R J, *Finite volume methods for hyperbolic problems*, Cambridge University Press, Cambridge (2004)

[18] Li Ta-tsien, Yu Wen-ci, *Boundary value problems for quasilinear hyperbolic systems*, Duke University Mathematics Series V, Duke University, Durham (1985)

[19] Lieberman G M, *Second order parabolic differential equations*, World Scientific Publishing, Singapore (1996)

[20] Lunardi A, *Analytic semigroups and optimal regularity in parabolic problems*, Birkhäuser, Basel (1995)

[21] MacCluer C R, *Boundary value problems and Fourier expansions* (Revised ed.), Dover Publications, Mineola, NY (2004)

[22] Mori Y, Jilkine A, Edelstein-Keshet L, *Wave-pinning and cell polarity from a bistable reaction-diffusion system*, Biophys J **94**.9 (2008), 3684–3697

[23] Perthame B, *Transport equations in biology*, Birkhäuser, Basel (2007)

[24] Plastino J, Lelidis I, Prost J, Sykes C, *The Effect of Diffusion, Depolymerization and Nucleation Promoting Factors on Actin Gel Growth*, Eur Biophys J **33** (2004), 310-320

[25] Pollard T D, *Rate constants for the reactions of ATP- and ADP-actin with the ends of actin filaments*, J Cell Biol **103** (1986), 2747–2754

[26] Ponti A et al, *Two Distinct Actin Networks Drive the Protrusion of Migrating Cells*, Science **305**.5691 (2004), 1782–1786

[27] Romero S et al, *Formin is a processive motor that requires profilin to accelerate actin assembly and associated ATP hydrolysis*, Cell **119**.3 (2004), 419–429

[28] Shelkovich V M, *The Riemann problem admitting δ-, δ'-shocks, and vacuum states (the vanishing viscosity approach)*, J Diff Eq **231**.2 (2006), 459–500

[29] Smoller J, *Shock waves and reaction diffusion equations* (2^{nd} ed.), Springer, New York (1994)

[30] Szmolyan P, *Transversal heteroclinic and homoclinic orbits in singular perturbation problems*, J Diff Eq **92**.2 (1991), 252–281

[31] Thomas J W, *Numerical Partial Differential Equations* (TAM **22**), Springer, New York (1995)

[32] Volpert V, Petrovskii S, *Reaction-diffusion waves in biology*, Physics of Life Reviews **6** (2009), 267–310

[33] Volpert A I, Volpert V A, Volpert V A, *Traveling wave solutions of parabolic systems* (corrected reprint), Translations of Mathematical Monographs, American Mathematical Society, Providence, R.I. (2000)

[34] Wilson C A et al, *Myosin II contributes to cell-scale actin network treadmilling through network disassembly*, Nature **465**.7296 (2010), 373–377